Multiscale chemomechanics of polymer deformation under contact: Predicting structure-property correlations from the bulk to the interphase

by

CATHERINE ANNE TWEEDIE

Bachelor of Science, Materials Science and Engineering
Massachusetts Institute of Technology, Cambridge, Massachusetts, 2003

Submitted to the Department of Materials Science and Engineering
In partial fulfillment of the requirements for the degree of

DOCTOR OF PHILOSOPHY IN MATERIALS SCIENCE AND ENGINEERING
at the
MASSACHUSETTS INSTITUTE OF TECHNOLOGY

February 2008
Presented: 6 November 2007

Signature of Author: _____
Department of Materials Science and Engineering
7 November 2007

Certified by: _____
Krystyn J. Van Vliet
Thomas Lord Assistant Professor of Materials Science and Engineering
Thesis Advisor

Accepted by: _____
Samuel M. Allen
POSCO Professor of Physical Metallurgy
Chair, Departmental Committee on Graduate Students

Multiscale chemomechanics of polymer deformation under contact: Predicting structure-property correlations from the bulk to the interphase

By
Catherine Anne Tweedie

Submitted to the Department of Materials Science and Engineering
on 7 November 2007 in partial fulfillment of the
requirements for the degree of Doctor of Philosophy in
Materials Science and Engineering

Presented on 6 November 2007

ABSTRACT

The development of nanoscale polymeric materials for mechanical applications necessitates advances in small-volume experimental techniques and analyses that reflect the viscoelastoplastic behavior of such materials. In this thesis, the time-dependence and response of homogeneous engineering polymers under confined contact loading are characterized as a function of polymer physical and structural properties. The validity of the time-independent metric indentation hardness H_i is evaluated through the combination of nanoindentation and atomic force microscopy imaging. In addition, the classic, time-dependent metric creep compliance $J(t)$ is used to establish the experimental conditions necessary for linear elastic behavior for a set of thermoplastic and thermoset materials. For large indentations ($h_{max} > 1$ um), properties are tacitly assumed to reflect the properties of bulk polymer; however, this assumption does not hold within 100 nm of a free surface or interface of amorphous polymers such as polystyrene and polycarbonate. The contact deformation mechanism near an amorphous polymer surface is found to scale with the surface area of contact, suggesting the dynamic formation of a structural interphase region. Chemical probe functionalization experiments are developed to explore the effects of probe surface charge on the probe-polymer interface and contribute to the understanding of the interphase that dominates nanocomposite material response. A

technique to rapidly screen mechanical response of combinatorial polymer libraries is presented, to establish structure-property-processing relationships of such chemomechanically defined interfaces before nanoscale deformation mechanisms in confined polymers are fully understood. Finally, material design for elastic, viscoelastic, and viscoelastoplastic mechanical properties is discussed in terms of polymer physical length and time scales.

Thesis supervisor: Krystyn J. Van Vliet
Assistant Professor of Materials Science and Engineering

Acknowledgements

I am deeply indebted to a number of people for their help, encouragement, and friendship throughout my graduate studies. First, however, I will thank my advisor Krystyn Van Vliet who took me on as one of her first students when I barely knew anything about research and spent untold hours with me while I learned how to use and troubleshoot the nanoindenter, how to read research literature, and finally how to write papers. We have shared victories and disappointments and learned countless lessons including "Back-up your data!" and "how to build an effective research group dynamic." Thank you for how hard you have worked on my behalf and for always maintaining high standards for my work.

I would like to thank my thesis committee including Professors David Roylance, Subra Suresh, Christopher Schuh, and Anne Mayes for their support and very helpful discussions related to research, classes and life. I am also very grateful to Professors Michael Rubner, Michael Cima, and Robert Cohen for their constructive criticisms that helped guide my research.

To my colleagues in the materials science department, and especially within the Van Vliet group, I owe a special debt of gratitude for creating a community with whom I could share my life. Within the Van Vliet group I absolutely need to thank Binu Oommen, Todd Thompson, Solar Olugebefola, Sunyoung Lee, Sezen Curgul, Emily Walton, Jack Milwid, Dessy Nikova, Georgios Constantinides, John Maloney, Timothy Lau, Ranjani Krishnan, Ilke Kalcioglu, and Emilio Silva. My lab group has meant so much to me that I can only pray that I will once again get to work with a group as wonderful as the one I have been blessed with here at MIT. Support and friendships extended outside the lab group as well and I would be remiss not to thank Alicia Jackson, Rachel Pytel, Andy Detor, Lauren Frick and Jonathan Varsanik for all the mid-day hallway talks and lunch dates.

I have also been hugely lucky in the number of fantastic collaborators I have had on my research projects both within and outside of MIT. First of all I thank James Smith of MicroMaterials, Ltd. for teaching me about his nanoindenter, listening to my dreams, and reminding me of Santa Claus. I thank Stephen Goodes of MicroMaterials, Ltd. for

enabling the software modifications to the nanoindenter. Importantly, I gratefully acknowledge support from the DuPont-MIT Alliance, and thank Greg Blackman of DuPont Central Research & Development for all the hard work on his end to make our collaboration a success. I would also like to gratefully acknowledge Y. Brun, K. Sharp, M. Wetzel, and B. Bennett for helping to synthesize and characterize the smoothest polymer samples ever. Of course I would also like to thank Mark Van Landingham and Thomas Juliano of the Army Research Laboratory for their collaborations and valuable discussions. Within MIT, I would like to thank Dan Anderson in the Langer Laboratory for sharing his polymer combinatorial libraries that led to fruitful project collaborations.

I am so thankful to have had access to such fantastic equipment while doing my research at MIT. A huge thank you goes to Alan Schwartzman for putting up with my persistent presence and borrowing of items from the Nanolab. I also thank the Shared Experimental Facilities supported by the MRSEC Program of the National Science Foundation (DMR 02-13282) for extensive use of the profilometer. Further, I am not sure where I would be now without the help of DMSE's Kathy Farrell, Juliette Braun, Angelita Mireles, and Stephanie Bright from the head office for holding my hand through the administrative aspects of the doctoral process.

I would also like to thank the MIT Athletic Center, the MIT track team, and in particular the MIT pole vaulting squad for teaching me that anything is possible. Nothing melted my research worries like the grin of one of my workout buddies. Special thanks go to Nathan Ball, Patrick Barragan, and Vanessa Li. Eric Abel, you were the best coach I have ever had.

To my undergraduate MIT roommates and best friends, Julie Pinkston and Monica Morrison, I can't imagine my life without you both.

Finally, I want to acknowledge the love and support of my family. To my parents, Christina and William Tweedie, I can not thank you enough for giving me all the tools I would need in my life to be happy. To my little sister, Alexandra, I toast to our lifetime of friendship.

This thesis is dedicated to my grandparents: Tish and Roy Tweedie and Jim, Jean, and Signe Allen. I love you all.

Table of Contents

ABSTRACT..... 2

ACKNOWLEDGEMENTS..... 4

TABLE OF CONTENTS.....6

LIST OF FIGURES..... 9

LIST OF TABLES.....16

CHAPTER 1 INTRODUCTION..... 17
1.1 MOTIVATION 17
1.2 MECHANICAL TESTING OF BULK POLYMERS, POLYMER FILMS, AND POLYMER SURFACES 19
1.3 CONVENTIONAL NANOINDENTATION 21
1.4 ALTERNATIVE NANOINDENTATION APPROACHES 25
1.5 CURRENT INTERPRETATIONS OF POLYMER NANOINDENTATION 27
1.6 APPLICATION OF MOLECULAR DYNAMICS TO POLYMER MECHANICS 29
1.7 HIGH-THROUGHPUT MECHANICAL SCREENING 32
REFERENCES

CHAPTER 2 CONTACT MECHANICS OF POLYMERS..... 40
2.1 INTRODUCTION 40
2.2 NANOMECHANICAL QUANTIFICATION OF POLYMER ENERGY ABSORPTION 41
2.2.1 Introduction 41
2.2.2 Experimental details 42
2.2.2.1 Nanoindentation-based approaches 43
2.2.2.2 Materials 44
2.2.3 Results and Discussion 46
2.2.3.1 Conventional nanoindentation of polymers 46
2.2.3.1.1 Composition and loading rate dependence 46
2.2.3.1.2 Probe shape effect on analytical fitting constants 47
2.2.3.1.3 Challenges to relating time-independent metrics of quasistatic polymer response to polymer physical attributes 48
2.2.3.2 Specific energy absorption 49
2.2.4 Conclusions 51
2.3 CONTACT CREEP COMPLIANCE 53
2.3.1 Introduction 53
2.3.2 Basis and implementation of contact creep compliance solutions 57
2.3.2.1 Solutions for spherical indenter geometry 57
2.3.2.2 Solutions for conical indenter geometry 58
2.3.2.3 Extensions and applications of creep compliance models 59

2.3.3 Experiments 62
2.3.3.1 Materials 62
2.3.3.2 Instrumented indenter-enabled contact creep testing 63
2.3.4 Results and Discussion 64
2.3.4.1 Nanoindentation contact creep with a sharp indenter 64
2.3.4.1.1 Nonlinear viscoelastic deformation 64
2.3.4.1.2 Effect of loading rate 66
2.3.4.2 Nanoindentation contact creep with a spherical indenter 67
2.3.4.3 Structural and physical determinants of creep compliance 70
2.3.5 Conclusions 75
2.3 INDENTATION RECOVERY RATES VIA SCANNING PROBE MICROSCOPY 76
2.3.1 Introduction 76
2.3.2 Experimental 78
2.3.2.1 Materials 78
2.3.2.1 Indentation, imaging, and image analysis 79
2.3.3 Results and discussion 82
2.3.3.1 Viscoelastic recovery progression 82
2.3.3.2 Comparison among polymers and loading conditions 85
2.3.3.3 Implications for indentation hardness of viscoelastic surfaces 89
2.3.4 Conclusions 90
2.4 CONCLUSIONS 91
REFERENCES 92

CHAPTER 3 CONTACT MECHANICS OF CONFINED POLYMER VOLUMES 95
3.1 INTRODUCTION 95
3.2 ENHANCED STIFFNESS OF AMORPHOUS POLYMER SURFACES UNDER CONFINEMENT OF LOCALIZED CONTACT LOADS 95
3.2.1 Introduction 96
3.2.2 Experimental 97
3.2.2.1 Polymer synthesis and characterization 97
3.2.2.2 Nanoindentation experiments and analysis 98
3.2.3 Results and discussion 100
3.2.4 Conclusions 110
3.3 MODIFIED PROBE SURFACE CHEMISTRY 111
3.3.1 Introduction 111
3.3.2 Material and methods 112
3.3.3 Experimental Protocol 113
3.3.3.1 Design and assembly of spherical, nanoindentation probe 114
3.3.3.2 Chemical functionalization 115
3.3.3.1 Results and discussion 117
3.4 REACTIVE POTENTIAL MOLECULAR DYNAMICS (MD) OF POLYMER SURFACE INDENTATION 119
3.4.1 Motivation and background 120
3.4.2 Simulation details and analysis 120

3.4.3 Results and discussion 124
3.4.4 Conclusions 128

3.5 CONCLUSIONS 129
REFERENCES 130

CHAPTER 4 COMBINATORIAL SCREENING OF MECHANICAL RESPONSE 137
4.1 MOTIVATION AND BACKGROUND 137
4.2 HIGH-THROUGHPUT POLYMER SYNTHESIS AND NANOMECHANICAL SCREENING 138
4.2.1 Introduction and enabling experimental technologies 138
4.2.2 Experimental details 142
4.2.2.1 Combinatorial Array Preparation 142
4.2.2.2 Nanoindentation 142
4.2.3 Results and discussion 143
4.2.4 Conclusions 147
4.3 COMBINATORIAL SCREENING OF MECHANICAL RESPONSE CASE STUDY: PHOTOCROSSLINKABLE AND DEGRADABLE MATERIALS 148
4.3.1 Methods and materials 148
4.3.1.1 Macromer synthesis and characterization 148
4.3.1.2 Polymerization and degradation 149
4.3.1.3 Mechanical properties characterization 150
4.3.2 Results and discussion 151
4.4 CONCLUSIONS 153
REFERENCES 154

CHAPTER 5 CONCLUSIONS AND DIRECTIONS FOR FUTURE RESEARCH 157
5.1 THESIS SUMMARY 157
5.2 CORRELATION OF MECHANICAL AND STRUCTURAL PROPERTIES 159
5.3 SUGGESTIONS FOR FUTURE RESEARCH 168
5.3.1 Larger molecular dynamics studies on polymer surface mechanics 168
5.3.2 Model nanocomposite interfaces using molecular dynamics 169
5.3.3 Nonlinear viscoelastoplastic analysis of model nanocomposites materials 169
5.3.4 Contact deformation of hydrated (biological) materials using fluid cell 171
5.3.5 Apply impulse experimental technique to develop protective / barrier coating materials 172
REFERENCES 175

APPENDIX A. GENERAL FRAMEWORK OF EXISTING SOLUTION FOR J(T) 176

List of Figures

Figure 1.1 Devices including small volumes of time-dependent materials that require quantitative mechanical characterization for development: (a) DVD, (b) hip replacements, and (c) microchip development. Images from (a) http://www.avx.be/nl/dvd/faq.html, (b) http://www.zircotec.com/ortho.html , (c) http://www.gersteltec.ch/.

Figure 1.2 (a) Atomic force microscopy image of Berkovich tip indentation in a metal and schematics of (b) Berkovich and (c) spherical tips.

Figure 1.3 Typical polymeric nanoindentation response and associated nomenclature. The plastic work of indentation W_p is the area between the loading and unloading curves. The total work W_t is equal to the area under the loading curve or W_p plus the elastic work of indentation W_e.

Figure 1.4 a) All-atom schematic of a polystyrene monomer with polymerization sites circled. b) 384-atom unit cell of amorphous, atactic polystyrene with periodic boundary conditions.

Figure 2.1 Figure of Micro Materials Ltd. nanoindenter pendulum test set-up.

Figure 2.2 Nanoindentation testing techniques: a) quasistatic loading, Q; b) chain momentum evaluation, c); impulse testing (I).

Figure 2.3 Load-displacement curves for indentations in a glassy, amorphous polymer performed on two nanoindention instruments: MicroMaterials (○) and Hysitron (●).

Figure 2.4 Reponses of polyethylene (PE) (blues) and polystyrene (pinks) to maximum load of 15 mN demonstrating variation in polymeric response for three loading rates: 0.15 mN/s (lightest), 0.5 mN/s (second lightest), 1.5 mN/s (darkest).

Figure 2.5 Values of the fitting parameters a) C and b) x in Eq. 2.1 for five maximum indentation depths between 300 nm and 3000 nm in Plexiglass® and for four loading rates of 0.05 mN/s (○), 0.15 mN/s (□), 0.5 mN/s (Δ) and 1.5 mN/s (Δ). Error bars represent standard deviations among five experiments.

Figure 2.6 Indentation hardness H for six polymeric materials loaded to a maximum load of 15 mN at two loading rates: 1.5 mN/s (black) and 0.05 mN/s (cross-hatch). There are two poly(methyl methacrylate) materials with trade names Plexiglass (Plexi) and Lucite, polycarbonate (PC) and polypropylene (PP).

Figure 2.7 a) Energy absorption per unit volume (W_p / V) of polystyrene as a function of loading rate dP/dt for Q-loading experiments; b) Quasistatic W_p / V as a function of weight average molecular weight M_w for PE (polyethylene), PP(polypropylene), PS(polystyrene), LU(Lucite) and PL(plexiglass).

Figure 2.8 a) C-loading of all polymers. Displacement of indenter Δh during hold at $0.5P_{max}$ for 60s. Prior positive creep of the indenter into the surface at P_{max} for 60s (cross-hatch), 30s (solid) and 0s (striped) shows that recovery increases with increasing deformed volume V: Energy dissipation at P_{max} did not result in decreased work against the indenter at $0.5P_{max}$. b) Energy absorption per unit volume W_p / V for PE for two Q-loading rates (0.056 and 1.5 mN/s) versus for I-loading (theoretically infinite rate).

Figure 2.9 (a) Ideal linear viscoelastic behavior is illustrated as strain ε as a function of time during creep t_c for three instantaneous and constant levels of applied stress σ_i. (b) The creep compliance $J(t)$ for a linear viscoelastic material is characteristic of that material and independent of σ_i.

Figure 2.10 Contact creep compliance $J_c(t)$ under ramp loading of 0.5 mN/s via Berkovich (sharp) probe. (a) Plexiglas (PL) shows typical dependence on creep load for P_o: 3 mN (light grey), 15 mN (dark grey) and 30 mN (black). (b) Comparison among all polymers at $J_c(t = 10\text{ s})$ for P_o: 3 mN (black) and 15 mN (grey) indicates increasing $J_c(t)$ with decreasing steric hindrance. Polymer abbreviations are as follows: PMMA Plexiglas (PL), PMMA Lucite (LU), polystyrene (PS), polycarbonate (PC), polypropylene (PP), polyethylene (PE) and two epoxies: E3 and E8.

Figure 2.11 a) Contact creep compliance $J_c(t)$ under ramp loading (0.5 mN/s) to 30 mN via Berkovich (sharp) probe for (a) six polymers as a function of t_c. (b) The rate of creep compliance $dJ_c(t) / dt$ increases with molecular weight M_w for the amorphous polymers tested in (a): polycarbonate (PC), polystyrene (PS), Lucite (LU) and Plexiglass (PL). Though monomer structure and physical properties also differ among these polymers, LU and PL differ principally in M_w.

Figure 2.12 Schematic illustrations of high (left) and low (right) molecular weight polymer samples (a) before and (b) after loading via a sharp indenter. Actual contact radii a ranged from 0.8 μm to 4.8 μm, while contour lengths L of the amorphous polymers of highest and lowest M_w were 0.7 μm (PS) and 7.3 μm (PMMA), respectively. The star * in (b) indicates a region of high intramolecular tension, which causes continued molecular displacement to reduce the internal strain.

Figure 2.13 Comparison of creep compliance $J_c(t)$ for step (black) and ramp (grey) loading for a single epoxy (E3) indented with a Berkovich indenter at three maximum loads: 1 mN, 5 mN and 15 mN. (b) Comparison of $J_c(t)$ for two epoxies differing in molecular weight between crosslinks M_c ramp loaded with a Berkovich indenter to three maximum loads: 1 mN, 5 mN and 15 mN. The average M_c is twice as high for E8 (black) than for E3 (grey).

Figure 2.14 Load-displacement response for epoxy (E3) ramp loaded to a maximum load of 15 mN for both a Berkovich indenter (grey) and a spherical indenter of radius $R = 500$ μm (black). Here, the creep segment at maximum load has been removed.

Figure 2.15 (a) Comparison of creep compliance $J_c(t)$ for step (black) and ramp (grey) loading measured with a spherical indenter of radius R = 500 μm for a single epoxy (E3). $J_c(t)$ is not dependent on load or loading rate, as shown in the overlap among step and ramp loading for three maximum loads: 1 mN, 5 mN and 15 mN. (b) Comparison of $J_c(t)$ for two epoxies differing in molecular weight between crosslinks M_c, under ramp loading with a spherical indenter of R = 500 μm to three maximum loads: 1 mN, 5 mN and 15 mN. M_c of E8 (black) is twice that of E3 (grey).

Figure 2.16 a) Creep compliance measurements of the three epoxy samples at 25°C using indentation. Error bars show one standard deviation between three separate test runs. Each measurement is within scatter of one another. b) Creep compliance measurement of the three epoxy samples at 55°C using indentation. Error bars show one standard deviation between three separate test runs. These measurements agree qualitatively with bulk torsion experiments.

Figure 2.17 (a) Hysitron nanoindenter and Quesant scanning probe microscope (SPM)

Figure 2.18 (a) Load-displacement curves for indentations in polystyrene (light gray), polycarbonate (dark gray) and polyethylene (black) to approximately the same depth. (b) Tapping mode scanning probe microscopy amplitude image of an indentation in polyethylene to 7 mN at 48 h post-indentation. Sidewall bowing at the surface is delineated at the loss of contact (straight, solid lines), at 4 min (curved, dashed lines) and at 48 h (curved, solid lines) post-indentation.

Figure 2.19 Polymer surface recovery is detected immediately upon unloading via a low-load holding phase (loading profile pictured in inset of plot (a)). (a) Normalized depth h / h_o recovery of polyethylene (PE) during hold segment after loading to 1.6 mN. (b) Scanning probe microscopy line traces through the minimum of an indentation to 7 mN in PE at 4 min (black), 136 min (dark gray), 24 h (light gray) and 48 h (lightest gray). (c) Normalized depth h / h_o and volume V / V_o as a function of $t > t_o$ for PE loaded to 1.6 mN. Note: star represents h_o / h_o and V_o / V_o, which are measured and calculated via Eq. 4, respectively, from the last point of indentation unloading. Error bars represent standard deviation among triplicate experiments.

Figure 2.20 (a) Normalized recovered volume V / V_o for indentations to h_{max} = 1200 nm in polyethylene (square), polystyrene (triangle) and polycarbonate (circle). (b) Normalized depth recovery of indentations to P_{max} = 7 mN in polyethylene (square), polystyrene (triangle) and polycarbonate (circle); decaying exponential or Burgers model fit shown as black lines. (c) Normalized depth h / h_o recovery in polyethylene during hold segment for three different unloading rates. The material was loaded to 1.6 mN at 0.5 mN/s and unloaded at 0.1 mN/s (dark gray), 0.5 mN/s (light gray) or 2.5 mN/s (lighter gray). Note: star represents V_o / V_o, where $V(t)$ is calculated via Eq. 4 from the last point of indentation unloading. Error bars represent standard deviation among triplicate experiments.

Figure 3.1 Stiffening of polymer surfaces under contact. a) Schematic of a nanoindentation probe (image reconstructed from atomic force microscopy, scalebar = 500 nm) approaching an amorphous polymer surface with higher molecular mobility over the first ~40 nm from the surface. b) Representative indentation load-displacement curves to five maximum loads P corresponding to a range of indentation depths h are displayed alternately in black and grey. c) The indentation elastic modulus E increases with decreasing indentation depth h_c in compression molded polystyrene, molecular weight M_w = 12 kg/mol. Error bars represent one standard deviation and may be smaller than the symbol.

Figure 3.2 Dependence of apparent stiffness under contact loading on polymer processing, structure and physical environment. a) Compression molded polystyrene (PS) samples with M_w = 12 kg/mol (●) and M_w = 197 kg/mol (●) as well polycarbonate, PC with M_w = 18 kg/mol (●) exhibit statistically equivalent stiffening trends toward the surface, while poly(methyl methacrylate), PMMA with M_w = 15 kg/mol stiffened at the surface to a lesser extent (●). Data are normalized for each material with respect to E_a measured at h_c ~ 200 nm for clarity, as the plateau stiffness of PMMA overlaps with the decreasing stiffness trends of PS and PC. b) Apparent stiffness E_a increases with decreasing contact depth h_c in PS (molecular weight M_w = 12 kg/mol) for compression molded (●), injection molded (Δ), spin coated (□) and annealed / spin coated (■) PS. Both spin coated samples appear stiffer for $h_c \geq 20$ nm than for other processing routes because of the Si substrate contribution to the mechanical response. c) There is no effect of relative humidity (% RH) on the extent of stiffening at the surface of compression molded PS: 42% RH before oven drying (●), 10% RH after oven drying (Δ), 42% RH after oven drying (half-filled square). d) Quasistatic nanoindentation (●) and nanoscale dynamic mechanical analysis at an oscillation frequency of 90 Hz (▲) of polystyrene (PS-12k) both demonstrate significant stiffening of the amorphous polymer surface for contact deformation experiments. Error bars represent one standard deviation and may be smaller than the symbol.

Figure 3.3 Lack of surface stiffening for non-polymeric materials. No increase in elastic modulus E is observed in soft, single crystal gold (open cross) or hard, borosilicate glass (closed diamond) over contact depths ranging 5 nm to 200 nm from the free surface. Note: the decrease in E of the gold surface for the indentation of contact depth ~ 5 nm is likely due to the presence of a well-documented thin organic layer (~ 1 nm) that adsorbs to gold surfaces under ambient conditions.[53]

Figure 3.4 Possible mechanisms for mechanical stiffening of the contacted surface. a) The free surface could be a mechanically distinct, thin layer of thickness t. Analytical theory for contact deformation of a bilayer mechanical model (inset) predicts that the composite elastic modulus $E(E_1, E_2, t)$ should vary as a function of contact radius a, but not of indenter radius R. Fits of this model (lines) to experimental data obtained with two probes of effective radii R_{eff} = 487 nm (○) and R_{eff} = 8724 nm (■) for polystyrene (PS-12k) do not coincide and thus do not support this model. b) A mechanically distinct phase could be formed in the material immediately adjacent to the probe surface, scaling with the surface area of contact SA_c for any probe radius R. These data show that E increases with decreasing surface area of contact SA_c for these probes, consistent with the

formation of an interface at the region defined by probe-surface contact. Error bars represent one standard deviation and may be smaller than the symbol.

Figure 3.5 a) Schematic of the indenter probe assembly using an atomic force microscopy probe. b) Schematic of the top of the assembled probe. c) Top down optical microscopy image of cantilever glued onto the glass with zoom-in inset of spherical probe. **d)** Three-dimensional topography from atomic force microscopy image of probe surface.

Figure 3.6 Contact angle measurements of a drop of water on a borosilicate glass slide were performed to evaluate stability of the amine functionalization over time.

Figure 3.7 a) Load-displacement *P-h* hystereses of amorphous, atactic polystyrene indented by three probes of varying radii. The data for the assembled probe of radius R = 2500 nm (●) is bounded by the induced responses from two conospherical, diamond probes of R = 9000 nm (●) and R = 500 nm (●). **b)** Representative *P-h* responses for contact deformation experiments on an instrumented nanoindenter with an amine group functionalized probe of R = 2500 nm before (●) and after (○) surface chemistry are indistinguishable over this range of loads and depths. *P-h* responses at alternating maximum loads are highlighted (●) such that the smaller maximum loads / depths may be distinguished. **c)** Representative *P-h* responses for contact deformation experiments on an atomic force microscope, with a carboxyl group functionalized probe of R = 2500 nm before (●) and after (●) surface chemistry to P_{max} of 40 μN, demonstrates a stiffer response than the bare borosilicate sphere.

Figure 3.8 a) A polystyrene (PS) thin film surface with periodic boundary conditions in the x-y plane is deformed with an indenter (rigid-carbon lattice) functionalized with carboxyl (COOH) groups that are presented toward the polymer surface with a net negative charge. The polymer-indenter simulations were repeated with two other probe surface functionalizations: b) hydrogen-capped for a net neutral charge and c) amine (NH_2) group functionalized for a net positive charge. d) A smaller simulation system was used to determine the range of feasible initial velocities for the approaching indenter

Figure 3.9 Maximum probe indentation depth for a flat probe with carboxyl group functionalization indenting a polystyrene surface (see Fig. 3.8d) as a function of initial probe approach velocity v.

Figure 3.10 Maximum indentation depths h_{max} on a polystyrene surface for probes with three different chemical functionalizations: carboxyl groups (COOH), amine groups (NH_2) and hydrogen atoms. The results are presented for two initial probe velocities: a) 0.5 km/s and b) 2 km/s. Error bars represent one standard deviation among three repeats of the same simulation beginning with different starting structures.

Figure 3.11. The local orientation parameter P can range between -0.5 (randomly coiled molecule) and 0.5 (straight molecule). The orientation parameter was calculated for each molecule in each time-frame and is plotted b) for a single indentation simulation with an amine group (NH_2) functionalized probe at an initial velocity of 2 km/s over 200 time

frames, equal to 2.5 ps. In c), the time-averaged orientation parameter for the average over all the molecules is shown over 2.5 ps during equilibration (black), indentation with an initial velocity of 0.5 km/s (gray), and indentation with an initial velocity of 2km/s (blue). The d) time-averaged orientation parameter averaged over all the molecules in the simulation and then over the three repetitions of the simulation for three probe surface functionaliztions: hydrogen atoms (gray), amine groups (blue), and carboxyl groups (red). Error bars represent one standard deviation among three repeats of the same simulation beginning with different starting structures.

Figure 3.12 a) Side-view of polystyrene film with each molecule depicted in a distinct color. Vertically-long rectangles highlight regions of the film relative to the indenter position within which the local orientation parameter was calculated. b) Depicts the change in the local orientation parameter over time 200 time frames, or 2.5 ps, for three molecules averaged over 3 repetitions of the simulation in different positions in the polymer film relative to the indenter probe: under the indenter (red), away from the indenter (green), and split over the boundary condition (purple).

Figure 4.1 Discrete polymer arrays. (**a**) Three 576-spot libraries comprised of pairwise combinations of 24 monomers printed on a glass slide. (**b**) Differential contrast interference image depicts spots of 300 μm diameter and 15 μm thickness printed on a square lattice with 740 μm spacing. (**c**) Monomer unit structure notation. Note that monoacrilate * was added at 30 vol% instead of monomer 17 to increase hydrophilicity.

Figure 4.2 Load-displacement (P – h) responses from the borosilicate glass (solid line); a stiff polymer spot (dashed line) and the most compliant polymer spot (dotted line).

Figure 4.3 Nanoindentation determination of elastic modulus *E* for 576-spot array. (a) Nanoindentation data was acquired in 48 hrs with precision and accuracy. (b) Subarrays of major monomer 8 (black); monomer 11 (grey); and monomer 22 (white). Error bars represent the maximum observed standard deviation of 7.5% among the triplicate subarrays (shown only on major monomer 22). Asterisks mark polymer spots with minimum and maximum *E*.

Figure 4.4 General polymerization scheme and chemical structures. Diacrylated macromers were synthesized by the condensation polymerization of an amine with a diacrylate (top). The various monomers used included 12 amines and 10 diacrylates (bottom) to produce a library of 120 photopolymerizable macromers. The macromers were crosslinked into polymers with exposure to ~10 mW/cm^2 ultraviolet light (365 nm) for 5 minutes.

Figure 4.5 Mechanical behavior of polymers fabricated from the macromer library. The elastic modulus (*E*), determined with a nanoindentation method, is reported for 79 of the candidate polymers from the macromer library. These polymers exhibit a range of E ranging from ~4 to ~350 MPa (note the log scale on the y-axis).

Figure 5.1 Elastic modulus E as inferred from instrumented indentation on the μm-scale as a function of polymeric structural length-scales, time-scales, and physical properties. Data for E as a function of weight average molecular weight (M_w), persistence length (L_p), characteristic retardation time (τ), and glass transition temperature (T_g) is given as available for an array of amorphous (polystyrene (PS), poly(methyle methacrylate) (LU and PL), polycarbonate (PC)) and semi-crystalline (polyethylene (PE), polypropylene (PP)) polymers.

Figure 5.2 Apparent elastic modulus of near-surface polymeric material E_{surf} as inferred from instrumented indentation on the nm-scale as a function of polymeric structural length-scales, time-scales, and physical properties. Data for E_{surf} as a function of weight average molecular weight (M_w), persistence length (L_p), characteristic retardation time (τ), and glass transition temperature (T_g) is given as available for an array of amorphous (polystyrene (PS), poly(methyle methacrylate) (LU and PL), polycarbonate (PC)) and semi-crystalline (polyethylene (PE), polypropylene (PP)) polymers.

Figure 5.3 Contact creep compliance J_c as a function of polymeric structural length-scales, time-scales, and physical properties. Data for J_c as a function of weight average molecular weight (M_w), persistence length (L_p), characteristic retardation time (τ), and glass transition temperature (T_g) is given as available for an array of amorphous (polystyrene (PS), poly(methyle methacrylate) (LU and PL), polycarbonate (PC)) and semi-crystalline (polyethylene (PE), polypropylene (PP)) polymers.

Figure 5.4 Extent of recovery post indentation $\Delta h/h_{max}$ as a function of polymeric structural length-scales, time-scales, and physical properties. Data for $\Delta h/h_{max}$ as a function of weight average molecular weight (M_w), persistence length (L_p), characteristic retardation time (τ), and glass transition temperature (T_g) is given as available for an array of amorphous (polystyrene (PS), poly(methyle methacrylate) (LU and PL), polycarbonate (PC)) and semi-crystalline (polyethylene (PE), polypropylene (PP)) polymers.

Figure 5.5 Much larger system sizes can be simulated with united atoms molecular dynamics (MD) run on parallel processes than for all-atom reactive MD (ReaxFF) simulations that allow for bond breaking and reforming.

Figure 5.6 Schematics of three polymer nanocomposites systems. In each schematic the yellow color represents the nanoparticle and the blue represents the surrounding amorphous polymer matrix. In a) the thickness d of the nanoparticle is less than the radius of gyration R_g of the polymer matrix, while in b) the thickness d exceeds R_g. In c) the asymmetric nanoparticle has one dimension greater than R_g and another smaller than R_g.

Figure 5.7 Mapping of nanocomposites through sharp probe contact deformation, schematically represented in a), may provide multi-dimensional mapping of several mechanical paramenters. In b), the apparent stiffness and viscosity are represented as a function of mechanical mapping in the x-direction.

Figure 5.8 a) Schematic and image of nanoindentation fluid cell installed on the Van Vliet Lab MicroMaterials Ltd. instrumented nanoindenter. b) Change in load-displacement response for a viscoelastic material as a function of hydration time.

Figure 5.9 a) Schematic of impulse experimental apparatus as installed on the Micro Materials Ltd. instrumented nanoindenter. b) Representative impulse response on glassy polymeric material, where c) diagrams the important parameters measured during the first contact with the surface.

Figure 5.10 Coefficient of restitution e for glassy polymers as a function of testing temperature normalized by the polymer glass transition temperature T / T_g.

List of Tables

Table 2.1 Proposed model polymer systems

Table 2.2 Polymer monomer structure and physical properties

Table 3.1 Experimental parameter scale comparison between reactive molecular dynamics simulations and physical experiment

Table 5.1 Synthesis of polymer property data for the mechanical metrics studied rigorously in this thesis.

CHAPTER 1 INTRODUCTION

1.1 MOTIVATION

Mechanical characterization of polymeric thin films and small volume structures is critical to device development in industrial applications ranging from low-k dielectric microelectronic packaging films to synthetic and natural biological substrata. There is currently no established, physics-based, quantitative analysis for testing of small volumes of time-dependent materials. This lack of quantifiable properties is a hindrance to the development of applications with polymers in small or complex volumes such as thin films, fibers, composite matrices, and biological scaffolds (Fig. 1.1). Nanoindentation represents one of the best nondestructive, nanoscale mechanical testing approaches available. Although this technique has the potential to quantify mechanical properties of polymeric systems, most researchers use nanoindentation to calculate metrics developed for metals and ceramics, such as material hardness and Young's elastic modulus. These metrics do not capture all aspects of polymer viscoelastoplastic deformation and are therefore only useful for studying polymer behavior when experimental conditions are carefully taken into account. Despite the lack of nanoscale mechanical testing standards for polymers, nanoindentation experiments and analyses are published with increasing regularity due to the high demand for nanomechanical behavior and properties of small polymer volumes. This thesis research will develop experimental and analytical avenues to characterize the nanomechanics of finite-volume, time-dependent materials. The goal of this research is enable the extraction of meaningful mechanical properties through contact deformation of polymer surfaces by systematically addressing challenges unique to testing polymers at the nano-scale.

Despite the rigorously developed analytical framework for bulk polymer testing found in ISO and ASTM standards, there is no parallel schema for quantifying the performance of confined volumes of polymers such as deposited thin films or fibers in a composite. To establish such standards, appropriate experimental instrumentation must be identified and the physics-based analytical interpretation of multiaxial mechanical testing of

viscoelastoplastic materials must be developed. Nanoindentation can be used to mechanically deform thin and confined volumes of material, as well as to perform quality control of bulk polymers. Instrumented nanoindentation continuously outputs displacement as a function of applied load, and thus provides potentially quantitative mechanical characterization of polymers as a function of maximum load and loading rate.

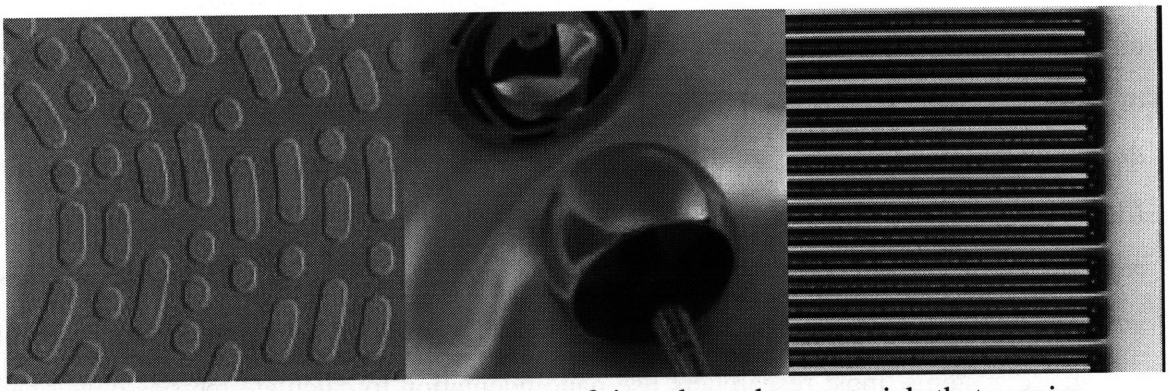

Figure 1.1 Devices including small volumes of time-dependent materials that require quantitative mechanical characterization for development: (**a**) DVD, (**b**) hip replacements, and (**c**) microchip development. Images from (**a**) http://www.avx.be/nl/dvd/faq.html, (**b**) http://www.zircotec.com/ortho.html, (**c**) http://www.gersteltec.ch/.

This Introduction lays the foundation for the current state of mechanical testing of polymers in bulk and thin film or confined geometries (Section 1.2); conventional nanoindentation experiments and the generally accepted time-independent theory by which these experiments are used to estimate bulk mechanical properties (Section 1.3); new nanoindentation-enabled experiments (Section 1.4) and analyses (Section 1.5); molecular dynamics as a tool to understand the nano-scale deformation response of polymers (Section 1.6); and high-throughput mechanical screening of combinatorial polymer libraries as a potential application for mechanical testing of small volumes of time-dependent materials (Section 1.7). Investigation of current nanoindentation and simulation options, combined with a critical review of the rich history of polymer physics / mechanics, will lead to an understanding of how key mechanical parameters of confined polymers relate to physical properties differently than bulk polymers.

Although bulk mechanical tests are not feasible for extremely small volumes of material, the polymer physics / mechanics derived from these tests can be extended and applied to nanoindentation, but only for indentation depths > 100 nm from the polymer free surface.[1] The dynamics of polymer macromolecule chains within 100 nm of free surfaces or within confined volumes have been shown to vary, sometimes significantly, from those of the bulk polymer. Improved understanding of confinement mechanics of polymers has been hindered by challenges unique to performing contact mechanics experiments on (1) time dependent materials and (2) the nanometer length scale. This thesis systematically addresses these two areas of uncertainty in the field of polymer contact mechanics and additionally presents a technique to rapidly obtain target chemomechanical responses of polymers on the nanoscale in cases where structural determinants of polymer mechanical behavior and chemical stability are not fully understood.

1.2 MECHANICAL TESTING OF BULK POLYMERS, POLYMER FILMS, AND POLYMER SURFACES

The range of mechanical properties and specific strength (strength / volume) attainable with polymers is the major driving force for the size and growth of the commercial polymer market. Polymers are robust engineering materials because of their relatively low density (usually on the order of 1 g/cm^3), tunable mechanical properties, and economically favorable processability.[2] For this reason, mechanical characterization of polymers is integral to many polymer product applications. Bulk polymer mechanical testing techniques include uniaxial / biaxial tension and compression, dynamic mechanical analysis (DMA), impact testing, and rheological approaches. Uniaxial tension and compression tests output stress-strain relationships, and thus the tensile and compressive elastic moduli, while impact testing identifies the polymer impact strength. DMA is a thermal technique which measures the storage modulus E' (elastic response) and the loss modulus E'' (viscous response). The viscous response is assessed via the material damping of an oscillatory force applied to the material.

Testing techniques to characterize physical and structural characteristics of polymers include Differential Scanning Calorimetry (DSC), Gel Permeation Chromatography (GPC), and Nuclear Magnetic Resonance (NMR).[2] DSC can detect the melting and glass transition temperatures of a polymer, as well as the enthalpies related to those transitions, while scanning through a selected temperature range. GPC is the most commonly used method of determining the molecular weight distribution of a polymer. Molecular structures on the order of 2-200 Å[2] can be measured using NMR, including polymer microstructure, chain conformation and chain dynamics.[2] NMR can quantify the relative amounts of each monomer present and the sequence distribution of these monomers, thus increasing understanding of the effects of polymer morphology on macroscopic properties. The main spectroscopy techniques used for elemental analysis of polymers include atomic absorption spectrometry (AAS), atomic emission spectrometry (AES), X-ray fluorescence spectrometry (XRF), and atomic mass spectrometry.[2]

The polymer characterization techniques listed above are all well-developed and indispensable for bulk samples. However, the mechanical characterization approaches are not designed to characterize the small, structurally complex volumes that are typical of nano-composites and thin films. In order to meet the demand for quantified mechanical metrics in applications such as microelectronic thin films or mechanically robust composites, nanoscale mechanical testing and analysis theory must be pursued and developed.

The tool set necessary for nanoscale mechanical testing of polymer films and polymer surfaces requires characterization of sample topography as well as mechanical behavior. High-resolution imaging techniques must be coupled with nanomechanical testing to confirm the applicability of geometry-dependent analyses, since the precise geometry and roughness of nm- or μm-scale samples cannot be determined by eye or with most optical microscopes. Analysis of polymer thin-film mechanical testing requires knowledge of the film thickness t_f to ensure that mechanical contributions from the underlying substrate are either avoided or taken into account. Film thickness is the average height difference between the surface of the substrate and the polymer film surface and can be measured

via several techniques including ellipsometry, profilometry, and scanning probe microscopy (SPM). SPM is primarily used for surface imaging, which allows users to choose specific indentation sites as well as image the post-indentation surface, a necessary feature for investigating specific phases of composite materials. Further, non-contact mechanical testing techniques have been developed to test the elastic[3] and viscoelastic[4] properties of polymer thin films. However, both techniques require flat film geometries and therefore are not able to distinguish spatial distributions of mechanical response or characterize thick materials with nm-scale phase dimensions, as would be applicable to polymer-based nanocomposites or microelectronics. This thesis aims to pursue quantitative experimental and analytical approaches capable of being adapted to varied sample geometries. Instrumented nanoindentation is the experimental platform chosen to perform this research, the current mechanics and analysis of which will be discussed in the Sections 1.3-1.5.

1.3 CONVENTIONAL NANOINDENTATION

Instrumented nanoindentation was originally developed for the high-performance microelectronics industry[5] as a modified hardness test for the mechanical characterization of ceramic and metallic thin films. Nanoindention applies a normal force to the sample surface with a relatively rigid indenter of known geometry and mechanical properties, while nano-scratch testing uses the same instrument to apply a lateral (frictional) force. The indenter is typically fabricated from diamond, a natural material exhibiting high elastic stiffness and hardness, and can be shaped into many geometries having varying influences on the applied stress as a function of indentation depth. The most common tip geometries include: faceted pyramids (analyzed as sharp conical nanoindentation), blunted cones, spheres of micrometer-scale radii (spherical nanoindentation), and flat-ended cylinders (punch nanoindentation). Sharp and spherical indenters (depicted in Figure 2b-c) are often modeled via analytical formulations[6] and simulations[7,8] because the indenter geometries induce very different stress states within the material. As with any conical indenter, the Berkovich indenter geometry maintains a constant height-to-cross-sectional-area ratio during indentation:

$$A_{Berkovich}(h) = 24.56h^2 \tag{1.1}$$

where A is the geometrically idealized area of indentation cross-section at the indentation depth h. However, the finite sharpness of the conical tip induces large plastic strains in the indented material; these strains change significantly as a function of distance from the sharp tip, obfuscating closed-form analytical interpretations of the nanoindentation response. A spherical indenter, while having a non-constant relationship between depth and area

$$A_{Sphere}(h) = \pi\left(R - h^2\right), \tag{1.2}$$

is capable of low initial stresses and thus may demonstrate elastic to plastic material response transitions, where R is the radius of the spherical tip.

Nanoindentation is usually force-controlled and capable of continuously measuring or calculating force and indenter displacement throughout the loading, holding and unloading portions of the indentation. Forces (nN- through mN-scales) can be applied at rates that vary from quasi-static rates of < 1 nm/s, similar to continuum-level computational simulation, to dynamic rates of > 1 mm/s, applicable to end-use application testing.

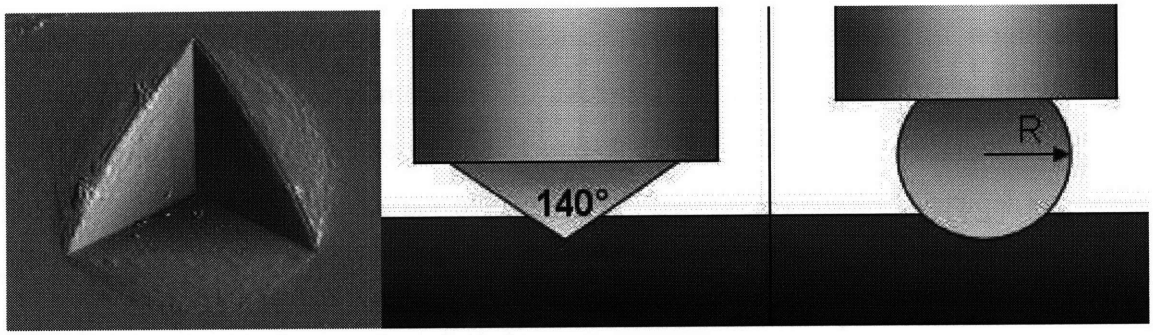

Figure 1.2 (**a**) Atomic force microscopy image of Berkovich tip indentation in a metal and schematics of (**b**) Berkovich and (**c**) spherical tips.

Recently, displacement-controlled quasi-static experiments and dynamic polymer nanoindentation have been performed using scanning probe microscopy (SPM).[9-11] While the pN- to nN-scale loading of SPM is advantageous, quantitative measurements of normal / lateral stress are complicated by the cantilevered probe geometry, and thus such experiments currently yield only qualitative comparison of samples. In addition, higher maximum loads are required to deform a glassy, amorphous polymer with a spherical probe to maximum depths between 0 and >100 nm from the surface, the depth range of interest for confined polymers.

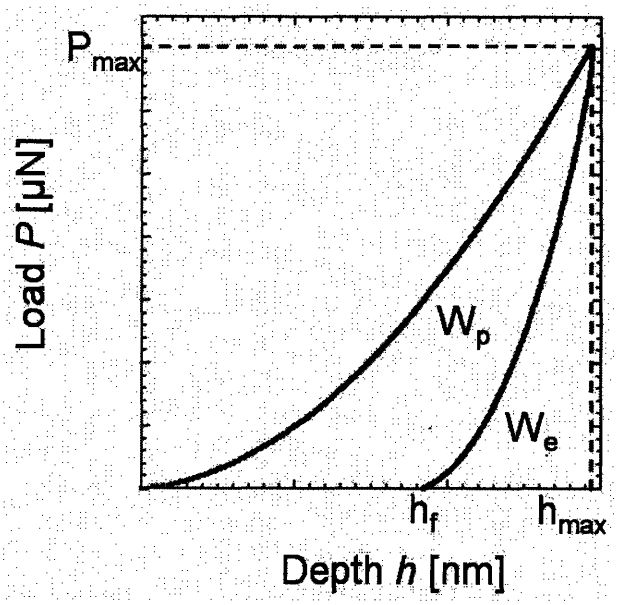

Figure 1.3 Typical polymeric nanoindentation response and associated nomenclature. The plastic work of indentation W_p is the area between the loading and unloading curves. The total work W_t is equal to the area under the loading curve or W_p plus the elastic work of indentation W_e.

Nanoindentation has been applied to polymers with increasing frequency to estimate elastic mechanical properties such as Young's modulus E and quasi-properties such as nanoindentation hardness H_i.[12] Despite the prevalence of such experiments in the open literature and in industrial application, the attainment and interpretation of polymer nanoindentation is based on a framework developed for *time-independent* materials. That is, load-displacement data sets are analyzed following closed-form, semi-empirical equations based in contact mechanics for linear elastic, Von Mises yielding materials,

such as metals, to obtain E, H_i[13] and yield strength σ_y.[8] If the rigid indenter geometry can be approximated as a sharp cone and the indented material can be approximated as a linear elastic-plastic solid, then

$$E = \frac{\sqrt{\pi}}{2}\left[\frac{(dP/dh)\big|_{P_{max}}}{\sqrt{A_c(h_c)}}\right] \tag{1.3}$$

$$H = \frac{P_{max}}{A_c(h_c)} \tag{1.4}$$

where $\frac{\sqrt{\pi}}{2}$ is a geometrical constant related to the apex angle of the indenter, $dP/dh|_{Pmax}$ is the slope of the unloading curve at the maximum load P_{max} and $A_c(h_c)$ is the maximum projected indentation contact area, which changes with h as defined in Eq. (1.1) but is evaluated at the contact depth h_c, where

$$h_c = h_{max} - \varepsilon\left[\frac{P_{max}}{(dP/dh)\big|_{P_{max}}}\right] \tag{1.5}$$

where ε is a constant usually equal to 0.75.[13,14]

Van Vliet et al. have extended nanoindentation analysis to the discrete defect nucleation events that precipitate mechanical failure in crystalline films, and have created interpretive models to analyze these data.[15-18] One important limitation of current interpretations is a historical reliance on hardness as a surrogate metric of yield strength. Nanoindentation hardness H_i is not a true mechanical property of any material including polymers, because it is a measure related to - but not quantitatively equal to - the average stress sustained by the indented material surface. Hardness is thus dependent upon geometrical details that induce stress discontinuities. This distinction is especially important in the context of polymers, for which H_i varies significantly with load, loading rate and recovery time. Nevertheless, the current industry metric for polymeric coating characterization is nanoindentation "hardness" of polymer coatings under normal or

lateral loading at arbitrary load, loading rates, and dwell times. Such a measurement does not reflect quantitative, physically meaningful mechanical behavior of the polymer in actual applications and is not demonstrative of whether / how the polymeric coating is irreversibly damaged upon mechanical loading. However, given the dearth of alternative metrics, many researchers accept H_i to make qualitative comparisons among a wide field of bulk polymers subjected to different processing and aging histories.[19-25] In Section 2.4, the variation in H_i for three polymers post-indentation as a function of loading rate is demonstrated.

There are two primary arguments against using the above, convenient analysis to extract E and H_i from polymer nanoindentation experiments. First, the time-independent model requires a positive initial slope of the unloading curve, as always observed in materials such as metals and ceramics. However, due to the time-dependent nature of polymer nanoindentation response, either a fast unloading segment is needed or a "holding period", or dwell time, at maximum load is necessary to ensure the response will conform to the model. If there is no dwell segment at P_{max}, the beginning of the unloading curve may exhibit a negative slope, indicating that the polymer is continuing to "creep" further despite a decrease in applied load. Second, the time-independent properties E and H are of limited utility in the design of viscoelastoplastic polymers and polymer applications. These points motivate consideration of new experimental options and interpretations, or at least more conscientious treatment of time-independent properties.

1.4 ALTERNATIVE NANOINDENTATION APPROACHES

Alternative nanoindentation-enabled approaches have been developed explicitly to capture time-dependent material behavior. These include nanoindentation impact testing, dynamic nanoindentation,[26,27] nanoindentation creep and relaxation.[28,29] While experimentally feasible, these approaches lack a quantitative, physical interpretation. These approaches typically idealize the polymers as a configuration of spring and dashpot elements,[19] as in dynamic mechanical analysis of bulk polymers. Nanoindentation impact testing applies a delta distribution of normal force to the polymer surface at high

loading rates, and can be used to measure resonance and energy dissipation, as well as the delamination of polymeric thin films.

Dynamic nanoindentation involves application of a cyclic load to estimate storage and loss moduli (E', E'') from the amplitude and phase shift in the damped cyclic response. As the majority of essential industrial polymers display strain-rate sensitivity, creep, and anelastic deformation upon unloading, time-independent metrics such as E and H and simplified-model metrics such as E' and E'' can be incomplete measures of polymer behavior. Although E' and E'' might approximate the polymer response, they are continuum descriptors based on a phenomenological model unrelated to atomistics and uncorrelated to polymer microstructure. Thus, an analytical model for nanoindentation is needed that connects the physical and microstructural properties of polymers to relevant mechanical parameters. Early efforts toward this end include the experimental analysis of Klapperich et al.[30] regarding qualitative connections between nanomechanical behavior and polymer structure, crystallinity, and molecular weight for quasistatic nanoindentation, as well as the theoretical analysis of Anand et al. relating energy, loading conditions, and continuum polymer properties.[31] The results discussed in Chapter 2 outline the development of several types of nanoindentation-based experiments that characterize aspects of polymer viscoelastoplastic behavior and application of these approaches for a set of well-characterized amorphous polymers.

Nanoindentation creep has been used to measure deformation of both metals and polymers under near-constant applied load for a range of temperatures.[22,28,32,33] These tests typically utilize punch nanoindentation, which creates stress singularities at the punch perimeter and thus obfuscates analytical interpretation. However, phenomenological models have been developed for creep under sharp and spherical indenter geometries.[34-38] As polymers are known to creep and relax at different rates as a function of load and loading rate, several investigations have studied the *relaxation rates* for 'large' polymer indentations (h_f = 20 μm).[39-43] Chang et al. demonstrated that a polymer indented with a large spherical indenter and heated above its glass transition temperature T_g would relax almost entirely to the pre-indentation configuration.[41] This

result is expected because polymer chains can move more freely above the glass transition temperature. However, significant changes in depth after penetration with a sharp indenter at room temperature would have direct implications regarding the suitability of hardness values for polymeric materials. Lorenzo et al. subsequently related the relaxation of indentations made with a Vickers (sharp conical) microhardness tester to the microstructure of low and high density polyethylene (PE), demonstrating that the final fractional recovery is greater for polymers comprising shorter molecules.[40] Despite the ability to perform these experiments, time-dependent analytical solutions for mechanical behavior based on polymer physical properties are still in development.

1.5 CURRENT INTERPRETATIONS OF POLYMER NANOINDENTATION

Current semi-empirical and empirical models exist to extract mechanical properties from traditional nanoindentation,[38,44] nanoindentation creep,[35,37,44,45] and dynamic nanoindentation.[26,27] The model for quasistatic sharp nanoindentation by Cheng et al.[44] predicts the ratio of h_f / h_{max} , where h_f is the final unloading depth and h_{max} is the maximum depth, based on the ratio of plastic work of indentation W_p over the total work of indentation W_{tot}, as diagrammed in Figure 1.3.

$$\frac{W_p}{W_{tot}} = 1 - \left[\frac{1 - 3(h_f / h_m)^2 + 2(h_f / h_m)^3}{1 - (h_f / h_m)^2} \right] \tag{1.6}$$

This model is independent of indenter apex angle and mechanical properties, but does assume the self-similarity of conical indenters. Closed-form relationships for indenter load as a function of time are derived for a standard linear viscoelastic solid model under a quasi-static constant indenter displacement rate condition and a constant indentation strain rate condition. However, outside of these specific loading and phenomenological model material assumptions, there are no closed-form analytical solutions for polymer nanoindentation. Dimensional analysis has been used to develop interpretations of mechanical experiments but requires simulation to obtain fitting constants.

The time-dependent mechanical deformation mechanism of creep has been studied extensively for metals as a function of time and temperature.[45,46] The creep strain rate for metals is a function of the specific creep mechanism, applied stress, grain size and temperature.[45] Most metals creep only when employed in high-temperature applications via diffusion controlled creep or under very high stresses via dislocation creep while polymers will creep at room temperature under low stress conditions as a function of entirely distinct structural parameters.

As discussed in more detail in Section 2.3, Ting et al.[35] have developed functional relationships for the creep and relaxation compliance ($J(t)$ and $G(t)$) for conical and paraboloidal indentation tip geometries where the creep compliance is:

$$J(t) = \beta \frac{A(t)}{P_0 \tan\theta} \tag{1.7}$$

and β is a constant of proportionality usually equal to 1.0, A(t) is the contact area as a function of time, which can be obtained from Eq. (1.1) and the prescribed loading rate dP / dt, P_0 is the maximum load in a Heaviside step function, and θ is the indenter apex half-angle. Vandamme et al.[36] have derived a phenomenological model based on two, three and four element spring-dashpot models for trapezoidal load histories. Cheng et al.[44] proposed a semi-empirical model for spherical indentation, idealizing the polymer to a three-element spring-and-dashpot model (standard linear solid) from which material properties can be extracted from a creep test by fitting experimental data.

$$\delta(t) = \left(\frac{3}{4}\sqrt[3]{\frac{3P_0^2}{4RE_1^2}}\right)\left(-\left(\frac{E_1}{E_2}\right)e^{-\left(\frac{E_2 t}{3\eta}\right)} + \left(\frac{E_1 + E_2}{E_2}\right)\right)^{2/3} \tag{1.8}$$

In this model $\delta(t)$ is the depth of the indentation as a function of time, P_0 is the maximum step-load, E_1 and E_2 are the Young's moduli of the two springs, and η is the viscosity of the dashpot. In a juxtaposition of the Vandamme and Cheng models, the indentation load and contact area development in conical indentation of a Kelvin-Voigt material were overlaid. Vandamme's model compared to Cheng's FEA showed excellent agreement

while the contact area was increasing, but diverged after the time of maximum load as the Vandamme model does not hold for decreasing contact areas.[36]

Oyen et al.[38] developed a semi-empirical analysis for sharp indentation that decouples plastic, viscous and elastic deformation, as shown in Eq. (1.9)-(1.10).

$$h^{LOAD}(t) = \dot{P}_A^{1/2} t^{1/2} \frac{2t}{3(\alpha_3 \eta_Q)^{1/2}} + \frac{1}{(\alpha_2 E')^{1/2}} + \frac{1}{(\alpha_1 H)^{1/2}} \tag{1.9}$$

$$h^{UNLOAD}(t) = \dot{P}_A^{1/2} \frac{t_R^{3/2} - (2t_R - t)^{3/2}}{3/2(\alpha_3 \eta_Q)^{1/2}} + \frac{(2t_R - t)^{1/2} - t_R^{1/2}}{(\alpha_2 E')^{1/2}} + h^{LOAD}(t_R) \tag{1.10}$$

Where $\dot{P}_A$ is the un- / loading rate, α_i are geometrical terms, $\alpha_3\eta_Q$ is the viscosity term, E' is the plain strain modulus, H is the hardness, and t_R is the time at P_{max}. Since the equations for the loading (1.9) and unloading (1.10) portions of the load profile are fit to the experimental load-displacement data with three unknown variables, there is no unique solution. The solution is therefore obtained by curve matching, indicating that the material response cannot be predicted by the material properties alone since only forward solutions are possible. Nevertheless, Oyen et al. demonstrates fairly accurate mechanical property calculations for a range of polymer test-cases. This analysis may enable the mapping of mechanical properties (E', $\alpha_3\eta_Q$, and H) across a composite material surface with a sharp indenter probe, as discussed further in Section 5.3.

The models above extend analysis capabilities to paraboloidal, conical, and spherical tip geometries and allow the extraction of the creep compliance as well as moduli related to the springs assumed in the linear viscoelastic models. Outside of Eq. (1.6), which does not predict any material properties, all the models treat the indented material as a continuum comprising spring and dashpot elements. Therefore, these approaches idealize the time-dependent behavior and neglect explicit dependence on physical properties, microstructure, and chemical composition of the polymers. In the following section, molecular dynamics will be introduced as a tool to relate nanoindentation to the

mechanical properties of polymers through the study of molecular motion during contact deformation with a chemically defined probe surface.

1.6 APPLICATION OF MOLECULAR DYNAMICS TO POLYMER MECHANICS

The current polymer simulation literature explores length scales that span nine orders of magnitude through modeling techniques that each access a unique microstructural range. These simulation tools include finite element modeling (FEM) on the continuum scale, molecular dynamics (MD) on the molecular scale, first principles approaches such as *ab initio* calculations on the atomic scale, and Monte Carlo (MC) simulations for less restricted ranges of system length scale. Interest in multi-scale materials modeling has surged because small-scale detail can be added to larger-scale simulations without the prohibitive computational cost of performing detailed simulations for a large system. One of the aims of this thesis is to study the effect of molecular movement and molecular interactions on the mechanical response of polymeric materials. Continuum constitutive equations used in FEM do not extend to molecular scale polymer behavior, while *ab initio* calculations alone cannot yet be applied to a system as large as a polymer network. Monte Carlo modeling is often used to study relaxation and conformational changes in molecules for variations in chain geometry. However, mechanical studies of polymer molecules as well as glassy and melted polymer networks via MC modeling has been limited, in part due to high levels of simulation noise that impede meaningful interpretation of results.[47-49] Monte Carlo simulations of glassy polymers are also computationally expensive, and although intermolecular force fields for specific polymeric systems exist for MC,[50] they are generally less proven through comparison with experiment than force fields in MD literature. This section will introduce the evolution of MD mechanical simulations of glassy polystyrene, which is not only a relatively well-studied material but also very relevant to the experiments and modeling treated in this thesis. Polystyrene, a fully amorphous polymer, is frequently used in simulation and experimental polymer physics literature for the development of more accurate mechanical models, and is used in numerous industrial applications.

In the early 1990s, a few all-atom and united atom force field models were parameterized for polystyrene,[51-53] which gave way to the progressive refinement of these initial force fields as well as additional force fields with alternative functional forms. "All-atom" models explicitly include all the atoms in the molecule (Fig.1.4a) which enables detailed studies of molecular motions, such as flipping dynamics of the polystyrene phenyl ring,[54] while "united atom" models lump sub-groups of atoms, which decreases computational demands and increases accessible model system sizes.[52] Both approaches have been used to investigate the molecular structure and dynamics of polystyrene (PS) as a function of temperature[55,56] as well as to study gaseous and solvent diffusion through PS.[53,57] Further, a branch of chemically reactive force fields have been developed for hydrocarbons that include electrostatic potentials in all-atom simulations that direct bond-breaking and reformation during the simulation experiment.[58,59] This reactive potential approach is discussed further in Section 3.3.3.

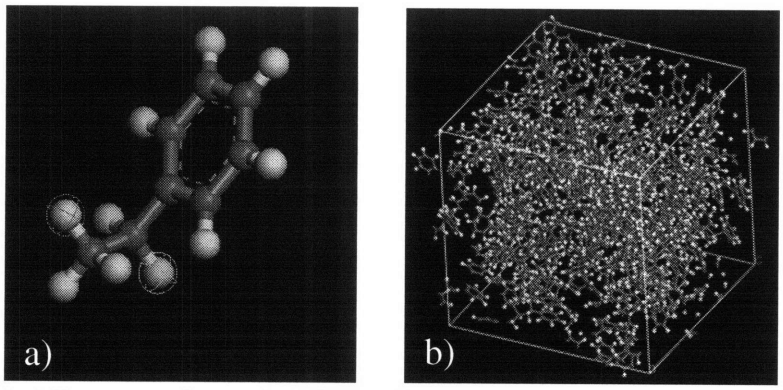

Figure 1.4 a) All-atom schematic of a polystyrene monomer with polymerization sites circled. b) 384-atom unit cell of amorphous, atactic polystyrene with periodic boundary conditions.

From this array of evolving polystyrene, potentials the choice of force field for modeling mechanical testing depends on the size and electrostatic needs of the polymer system to be simulated. Although several studies have investigated the nanomechanics of non-specific polymer networks though elastic compression of nanostructures,[60] fracture,[61]

and shear forces,[62] only Lyulin et al. have performed united-atom molecular dynamic simulations of uniaxial tensile tests of glassy polystyrene to obtain Young's moduli and yield stresses that agree well with experimental data. Such results attest to the potential of molecular dynamics to mechanistically explain and predict mechanical behavior of nano-scale polymer systems.

1.7 HIGH-THROUGHPUT MECHANICAL SCREENING

While a mechanistic understanding of confined polymer behavior is in development, high-throughput mechanical sensing presents an alternative route to rapid material discovery. Combinatorial materials science has existed as an experimental concept for over forty years, but has only recently been enabled by technological progress as a viable option for rapid screening of potential materials. Polymer printing technology and nanoindentation technology have become feasible, reliable and relatively time-efficient experimental tools,[63] and combination has great potential for identifying dependencies of polymer mechanical properties on polymer structure. Recently developed polymer deposition techniques are capable of printing higher molecular weight polymers than ever before and can create discrete polymer spot arrays with precise and accurate spatial resolution.[64] This advancement in small-volume processing of polymers will facilitate nanoindentation-based investigations of mechanical properties as a function of molecular weight, crosslink density, glass transition temperature, complexity of monomer structure, and variations in monomer combination. In the context of nanoindentation, discrete polymer libraries enable rapid mechanical characterization previously unparalleled in experimental nanoindentation.

Combinatorial materials characterization enables rapid discovery and optimization of functional materials. High-throughput examination of structure-property-processing relationships as a function of the constituent monomers and processing / operating conditions for nL and μL volumes will be applicable to fields ranging from biological materials to microelectronic insulators.[65-67] Precise quantification of mechanical properties for any volume of material is an integral part of the discovery and development of new materials. Although Section 1.2 highlighted major mechanical characterization

techniques for bulk polymeric materials, parallel accuracy for mechanical analysis of thin films and small, complex volumes (nm^3 to μm^3) does not exist. The evolution and creation of many polymer-enabled applications are dependent in part on the accuracy and speed of mechanical testing performed on small volumes of material. Such applications include low-k dielectric thin films and metal interconnect lines in microelectronics;[68] abrasion resistant palliative coatings;[69] photonics-compatible adhesives;[70] and polymeric biomaterials.[67,71,72] It is anticipated that the mechanical characterization of material libraries enabled by research in this thesis will not only create an accurate and efficient testing approach for small material volumes, but also offer a time-efficient alternative to testing individual bulk samples. Perhaps more importantly, nanoindentation can thus be applied to combinatorial material libraries to develop quantitative analyses of polymer nanoindentation response and mechanical properties as a function of microstructure. Such an approach will serve as a valuable proof of concept for the analytical and experimental developments in the time-dependent nanomechanics of materials.

This thesis aims to develop the capacity of nanomechanical tools and analyses to measure quantitatively useful time-dependent mechanical properties of materials as a function of polymer micro- and monomer structure. The goal is to advance nanoindentation-related experiments and analyses that relate the mechanical behavior and physical properties of small material volumes including thin films and nanocomposites. Molecular dynamics will be investigated as a tool capable of relating the contact deformation response to molecular motion at the polymer surface. Combinatorial polymer libraries will be demonstrated as an efficient, accurate technique for rapidly screening materials as a function of polymer structure variations. This integrated approach provides methods of rapid discovery and more accurate mechanical characterization for confined polymer volumes.

Chapter 1 included motivation for this thesis research as well as a review of established mechanical testing techniques for bulk polymers and polymer films. Conventional nanoindentation and analysis were introduced, followed by a discussion of alternative

nanoindentation approaches and current analytical techniques. Molecular dynamics simulations were put forward as a tool to compliment the mechanical testing of confined polymers. Finally, the potential of high-throughput mechanical screening for the advancement of material discovery and development was discussed. Chapter 2 includes three studies related to contact mechanics of *polymers* while Chapter 3 uses experiments and simulation to study the contact mechanics of *confined volumes* of polymer. Building upon the fundamentals discussed in Chapters 2 and 3, Chapter 4 presents two case studies in combinatorial screening of mechanical response in polymer libraries. Chapter 5 will present the salient conclusions and suggest directions for future research.

REFERENCES

1. Forrest J.A., Dalnoki-Veress K., Stevens J.R., Dutcher J.R.; Effect of free surfaces on the glass transition temperature of thin polymer films. *Physical Review Letters* **1996**; 77, (10), 2002-2005.
2. Berry G. In Comprehensive Desk Reference of Polymer Characterization and Analysis; Brady, R. F., Ed.; Oxford University Press: New York, 2003.
3. Stafford C.M., Harrison C., Beers K.L., Karim A., Amis E.J., Vanlandingham M.R., Kim H.C., Volksen W., Miller R.D., Simonyi E.E.; A buckling-based metrology for measuring the elastic moduli of polymeric thin films. *Nature Materials* **2004**; 3, (8), 545-550.
4. O'Connell P.A., McKenna G.B.; Rheological measurements of the thermoviscoelastic response of ultrathin polymer films (vol 307, pg 1760, 2005). *Science* **2005**; 310, (5753), 1431-1431.
5. Nix W.D.; Elastic and plastic properties of thin films on substrates: nanoindentation techniques. *Materials Science and Engineering A-Structural Materials Properties Microstructure and Processing* **1997**; 234, 37-44.
6. Malzbender J., de With G.; Indentation load-displacement curve, plastic deformation, and energy. *Journal of Materials Research* **2002**; 17, (2), 502-511.
7. Kogut L., Komvopoulos K.; Analysis of the spherical indentation cycle for elastic-perfectly plastic solids. *Journal of Materials Research* **2004**; 19, (12), 3641-3653.
8. Dao M., Chollacoop N., Van Vliet K.J., Venkatesh T.A., Suresh S.; Computational modeling of the forward and reverse problems in instrumented sharp indentation. *Acta Materialia* **2001**; 49, (19), 3899-3918.
9. Domke J., Radmacher M.; Measuring the elastic properties of thin polymer films with the atomic force microscope. *Langmuir* **1998**; 14, (12), 3320-3325.
10. Du B.Y., Tsui O.K.C., Zhang Q.L., He T.B.; Study of elastic modulus and yield strength of polymer thin films using atomic force microscopy. *Langmuir* **2001**; 17, (11), 3286-3291.
11. Bar G., Ganter M., Brandsch R., Delineau L., Whangbo M.H.; Examination of butadiene/styrene-co-butadiene rubber blends by tapping mode atomic force microscopy. Importance of the indentation depth and reduced tip-sample energy dissipation in tapping mode atomic force microscopy study of elastomers. *Langmuir* **2000**; 16, (13), 5702-5711.
12. VanLandingham M.R., Villarrubia J.S., Guthrie W.F., Meyers G.F.; Nanoindentation of polymers: An overview. *Macromolecular Symposia* **2001**; 167, 15-43.
13. Oliver W.C., Pharr G.M.; An Improved Technique for Determining Hardness and Elastic-Modulus Using Load and Displacement Sensing Indentation Experiments. *Journal of Materials Research* **1992**; 7, (6), 1564-1583.
14. Sneddon I.N.; The relation between load and penetration in the axisymmetric Boussinesq problem for a punch of arbitrary profile. *International Journal of Engineering Science* **1965**; 3, (1), 47.
15. Van Vliet K.J., Gouldstone A.; First prize - Mechanical properties of thin films quantified via instrumented indentation. *Surface Engineering* **2001**; 17, (2), 140-145.
16. Van Vliet K.J., Bao G., Suresh S.; The biomechanics toolbox: experimental approaches for living cells and biomolecules. *Acta Materialia* **2003**; 51, (19), 5881-5905.

17. Gouldstone A., Van Vliet K.J., Suresh S.; Nanoindentation - Simulation of defect nucleation in a crystal. *Nature* **2001**; 411, (6838), 656-656.
18. van Melick H., van Dijken A., den Toonder J., Govaert L., Meijer H.; Near-surface mechanical properties of amorphous polymers. *Philosophical Magazine a-Physics of Condensed Matter Structure Defects and Mechanical Properties* **2002**; 82, (10), 2093-2102.
19. Park K., Mishra S., Lewis G., Losby J., Fan Z.F., Park J.B.; Quasi-static and dynamic nanoindentation studies on highly crosslinked ultra-high-molecular-weight polyethylene. *Biomaterials* **2004**; 25, (12), 2427-2436.
20. Mina M.F., Ania F., Calleja F.J.B., Asano T.; Microhardness studies of PMMA/natural rubber blends. *Journal of Applied Polymer Science* **2004**; 91, (1), 205-210.
21. Mailhot B., Bussiere P.O., Rivaton A., Morlat-Therias S., Gardette J.L.; Depth profiling by AFM nanoindentations and micro-FTIR spectroscopy for the study of polymer ageing. *Macromolecular Rapid Communications* **2004**; 25, (2), 436-440.
22. Kolarik J., Pegoretti A.; Indentation creep of heterogeneous blends of poly(ethylene terephthalate)/impact modifier. *Polymer Testing* **2004**; 23, (1), 113-121.
23. Soloukhin V.A., Brokken-Zijp J.C.M., van Asselen O.L.J., de With G.; Physical aging of polycarbonate: Elastic modulus, hardness, creep, endothermic peak, molecular weight distribution, and infrared data. *Macromolecules* **2003**; 36, (20), 7585-7597.
24. Signor A.W., VanLandingham M.R., Chin J.W.; Effects of ultraviolet radiation exposure on vinyl ester resins: characterization of chemical, physical and mechanical damage. *Polymer Degradation and Stability* **2003**; 79, (2), 359-368.
25. Matzelle T.R., Geuskens G., Kruse N.; Elastic properties of poly(N-isopropylacrylamide) and poly(acrylamide) hydrogels studied by scanning force microscopy. *Macromolecules* **2003**; 36, (8), 2926-2931.
26. Loubet J.L., Oliver W.C., Lucas B.N.; Measurement of the loss tangent of low-density polyethylene with a nanoindentation technique. *Journal of Materials Research* **2000**; 15, (5), 1195-1198.
27. Asif S.A.S., Wahl K.J., Colton R.J., Warren O.L.; Quantitative imaging of nanoscale mechanical properties using hybrid nanoindentation and force modulation. *Journal of Applied Physics* **2001**; 90, (3), 1192-1200.
28. Lu H., Wang B., Ma J., Huang G., Viswanathan H.; Measurement of creep compliance of solid polymers by nanoindentation. *Mechanics of Time-Dependent Materials* **2003**; 7, (3-4), 189-207.
29. Ngan A.H.W., Tang B.; Viscoelastic effects during unloading in depth-sensing indentation. *Journal of Materials Research* **2002**; 17, (10), 2604-2610.
30. Klapperich C., Komvopoulos K., Pruitt L.; Nanomechanical properties of polymers determined from nanoindentation experiments. *Journal of Tribology-Transactions of the Asme* **2001**; 123, (3), 624-631.
31. Anand L., Gurtin M.E.; A theory of amorphous solids undergoing large deformations, with application to polymeric glasses. *International Journal of Solids and Structures* **2003**; 40, (6), 1465-1487.
32. Asif S.A.S., Pethica J.B.; Nano-scale indentation creep-testing at non-ambient temperature. *Journal of Adhesion* **1998**; 67, (1-4), 153-165.

33. Cheng L., Xia X., Yu W., Scriven L.E., Gerberich W.W.; Flat-punch indentation of viscoelastic material. *Journal of Polymer Science Part B-Polymer Physics* **2000**; 38, (1), 10-22.
34. Fischer-Cripps A.C.; A simple phenomenological approach to nanoindentation creep. *Materials Science and Engineering a-Structural Materials Properties Microstructure and Processing* **2004**; 385, (1-2), 74-82.
35. Ting T.C.T.; The contact stresses between a rigid indentor and a viscoelastic half-space. *Journal of Applied Mechanics* **1966**; 88, 845-854.
36. Vandamme M., Ulm F.J.; Viscoelastic solutions for conical indentation. *International Journal of Solids and Structures* **2006**; 43, (10), 3142-3165.
37. Oyen M.L.; Spherical indentation creep following ramp loading. *Journal of Materials Research* **2005**; 20, (8), 2094-2100.
38. Oyen M.L., Cook R.F.; Load-displacement behavior during sharp indentation of viscous-elastic-plastic materials. *Journal of Materials Research* **2003**; 18, (1), 139-150.
39. Lorenzo V., Perena J.M., Fatou J.M.G., Mendezmorales J.A., Aznarez J.A.; Interference Microscopy Measurements of Depth at Vickers Hardness Indentations in Polyethylene. *Journal of Materials Science Letters* **1987**; 6, (7), 756-758.
40. Lorenzo V., Perena J.M., Fatou J.G., Mendezmorales J.A., Aznarez J.A.; Delayed Elastic Recovery of Hardness Indentations in Polyethylene. *Journal of Materials Science* **1988**; 23, (9), 3168-3172.
41. Chang B.T.A., Li J.C.M.; Indentation Recovery of Atactic Polystyrene. *Journal of Materials Science* **1980**; 15, (6), 1364-1370.
42. Bansal A., Yang H.C., Li C.Z., Cho K.W., Benicewicz B.C., Kumar S.K., Schadler L.S.; Quantitative equivalence between polymer nanocomposites and thin polymer films. *Nature Materials* **2005**; 4, (9), 693-698.
43. Kung T.M., Li J.C.M.; Recovery Processes in Amorphous Polymers. *Journal of Materials Science* **1987**; 22, (10), 3620-3630.
44. Cheng Y.T., Cheng C.M.; Scaling, dimensional analysis, and indentation measurements. *Materials Science & Engineering R-Reports* **2004**; 44, (4-5), 91-149.
45. Frost H.J., Ashby M.F. Deformation-Mechanism Maps: The Plasticity and Creep of Metals and Ceramics; Pergamon Press, 1982.
46. Lucas B.N., Oliver W.C.; Indentation power-law creep of high-purity indium. *Metallurgical and Materials Transactions a-Physical Metallurgy and Materials Science* **1999**; 30, (3), 601-610.
47. Aumann F., Lankas F., Caudron M.W., Langowski J.; Monte Carlo simulation of chromatin stretching. *Physical Review E* **2006**; 73, (4), -.
48. Bhawe D.M., Cohen C., Escobedo F.A.; Formation and characterization of semiflexible polymer networks via Monte Carlo simulations. *Macromolecules* **2004**; 37, (10), 3924-3933.
49. Rosa A., Marenduzzo D., Kumar S.; Stretching a self-interacting semiflexible polymer. *Europhysics Letters* **2006**; 75, (5), 818-824.
50. Rapold R.F., Suter U.W., Theodorou D.N.; Static Atomistic Modeling of the Structure and Ring Dynamics of Bulk Amorphous Polystyrene. *Macromolecular Theory and Simulations* **1994**; 3, (1), 19-43.

51. Khare R., Paulaitis M.E., Lustig S.R.; Generation of Glass Structures for Molecular Simulations of Polymers Containing Large Monomer Units - Application to Polystyrene. *Macromolecules* **1993**; 26, (26), 7203-7209.
52. Mondello M., Yang H.J., Furuya H., Roe R.J.; Molecular-Dynamics Simulation of Atactic Polystyrene .1. Comparison with X-Ray-Scattering Data. *Macromolecules* **1994**; 27, (13), 3566-3574.
53. MullerPlathe F.; Local structure and dynamics in solvent-swollen polymers. *Macromolecules* **1996**; 29, (13), 4782-4791.
54. Khare R., Paulaitis M.E.; Molecular Simulations of Cooperative Ring Flip Motions in Single Chains of Polystyrene. *Chemical Engineering Science* **1994**; 49, (17), 2867-2879.
55. Lyulin A.V., Balabaev N.K., Michels M.A.J.; Correlated segmental dynamics in amorphous atactic polystyrene: A molecular dynamics simulation study. *Macromolecules* **2002**; 35, (25), 9595-9604.
56. Sun Q., Faller R.; Dynamic behavior of polystyrene by mesoscale modeling. *Abstracts of Papers of the American Chemical Society* **2006**; 231, -.
57. Han J., Gee R.H., Boyd R.H.; Glass-Transition Temperatures of Polymers from Molecular-Dynamics Simulations. *Macromolecules* **1994**; 27, (26), 7781-7784.
58. Stuart S.J., Tutein A.B., Harrison J.A.; A reactive potential for hydrocarbons with intermolecular interactions. *Journal of Chemical Physics* **2000**; 112, (14), 6472-6486.
59. van Duin A.C.T., Dasgupta S., Lorant F., Goddard W.A.; ReaxFF: A reactive force field for hydrocarbons. *Journal of Physical Chemistry A* **2001**; 105, (41), 9396-9409.
60. Van Workum K., de Pablo J.J.; Computer simulation of the mechanical properties of amorphous polymer nanostructures. *Nano Letters* **2003**; 3, (10), 1405-1410.
61. Buxton G.A., Balazs A.C.; Modeling the dynamic fracture of polymer blends processed under shear. *Physical Review B* **2004**; 69, (5), -.
62. Everaers R., Kremer K.; Elastic properties of polymer networks. *Journal of Molecular Modeling* **1996**; 2, (9), 293-299.
63. Schmatloch S., Schubert U.S.; Techniques and instrumentation for combinatorial and high-throughput polymer research: Recent developments. *Macromolecular Rapid Communications* **2004**; 25, (1), 69-76.
64. Anderson D.G., Levenberg S., Langer R.; Nanoliter-scale synthesis of arrayed biomaterials and application to human embryonic stem cells. *Nature Biotechnology* **2004**; 22, (7), 863-866.
65. Meredith J.C., Karim A., Amis E.J.; Combinatorial methods for investigations in polymer materials science. *Mrs Bulletin* **2002**; 27, (4), 330-335.
66. Stoykovich M.P., Cao H.B., Yoshimoto K., Ocola L.E., Nealey P.F.; Deformation of nanoscopic polymer structures in response to well-defined capillary forces. *Advanced Materials* **2003**; 15, (14), 1180-+.
67. Tweedie C.A., Anderson D.G., Langer R., Van Vliet K.J.; Combinatorial material mechanics: High-throughput polymer synthesis and nanomechanical screening. *Advanced Materials* **2005**; 17, (21), 2599-+.
68. Itano K., Choi J.Y., Rubner M.F.; Mechanism of the pH-induced discontinuous swelling/deswelling transitions of poly(allylamine hydrochloride)-containing polyelectrolyte multilayer films. *Macromolecules* **2005**; 38, (8), 3450-3460.

69. Chan C.M., Cao G.Z., Fong H., Sarikaya M., Robinson T., Nelson L.; Nanoindentation and adhesion of sol-gel-derived hard coatings on polyester. *J. Mater. Res.* **2000**; 15, 148-154.
70. Yacobi B.G., Martin S., Davis K., Hudson A., Hubert M.; Adhesive bonding in microelectronics and photonics. *Journal of Applied Physics* **2002**; 91, (10), 6227-6262.
71. Engler A.J., Richert L., Wong J.Y., Picart C., Discher D.E.; Surface probe measurements of the elasticity of sectioned tissue, thin gels and polyelectrolyte multilayer films: Correlations between substrate stiffness and cell adhesion. *Surface Science* **2004**; 570, 142-154.
72. Thompson M., Berg M., Tobias I., Rubner M., Van Vliet K.; Tuning compliance of polyelectrolyte multilayers to modulate cell adhesion. *Biomaterials* **2005**; in press,

CHAPTER 2 CONTACT MECHANICS OF POLYMERS

2.1 INTRODUCTION

This thesis aims to relate mechanical metrics of confined polymers to polymer structure to benefit mechanistic understanding of the nm-scale polymer mechanics. This understanding will lead to characterization and predictive development of complex polymeric materials such as nanocomposites. For contact deformation applications such as protective coatings, nanoindentation is the most promising route to quantify the mechanical response of confined polymers in a wide range of geometries. However, before nanoindentation can be applied to confined polymer systems, the experimental and analytical aspects of nanoindentation unique to testing time-dependent material properties must be investigated. To this end, a set of common engineering polymers, both thermoplastics and thermosets, with relatively simple monomer structures were tested using several nanoindentation techniques. In Section 2.2 the limitations of classically analyzed quasistatic indentation are introduced, followed by a discussion of energy absorption per unit volume as a model-free mode of analyzing polymer response. In Section 2.3 contact creep compliance experiments are used to characterize time-dependent deformation as a function of experimental parameters such as loading rate and probe geometry as well as microstructural parameters of the polymer such as molecular weight between crosslinks for thermosets or monomer steric hindrance. Section 2.4 investigates indentation recovery rates via scanning probe miscroscopy imaging of the surface post-indentation and thereby evaluates the validity of indentation hardness as a metric for polymer-application development.

2.2 NANOMECHANICAL QUANTIFICATION OF POLYMER ENERGY ABSORPTION

Parts of the following study were published in 2005 with co-author James F. Smith[1]

Although nanoindentation has the potential to quantify mechanical properties of polymeric systems, the established analyses developed for metals and ceramics (e.g., calculation of hardness and Young's modulus) do not capture all aspects of viscoelastoplastic deformation and are therefore of limited value. Here, we present a set of complementary, nanoscale contact-based experimental approaches that together characterize specific energy absorption as a unique mechanical characteristic of polymers and provide examples for a set of amorphous and semi-crystalline engineering polymers.

2.2.1 Introduction

A quantitative, polymer structure / properties-based framework to interpret the mechanical behavior of time-dependent materials coupled with accurate nanomechanical experiments is motivated by developments in areas such as nanocomposites, thin films, and biological substrates and scaffolds. Despite established bulk polymer physics and rheology (for example, creep as a function of time and temperature[2]), there is currently no standard method for characterizing the mechanical behavior of polymers confined to small volumes. A standard semi-analytical model exists for time-independent materials, from which indentation elastic modulus E and indentation hardness H are calculated from the unloading portion of an instrumented indentation experiment.[3] As there exists no parallel analysis for time-dependent materials, this method is increasingly employed to quantify the mechanical properties of polymers.[4-6] However, it is difficult to derive general principles or polymer mechanical properties from these reported experiments for three reasons. First, the inherent time dependency of the polymer nanoindentation response necessitates a "hold period" at maximum load prior to unloading, or sufficiently fast unloading so that the unloading response can be approximated by a line of positive slope, as assumed and observed in the nanoindentation response of metals and ceramics. In the absence of such a holding segment in polymers, a so-called "nose effect" or initially negative slope upon unloading may be observed. Second, the materials

considered vary in basic molecular composition, molecular weight, and degree of crystallinity, all of which are known to affect polymer properties. Third, time-independent properties such as E and H do not fully describe viscoelastoplastic polymer behavior and are therefore of limited use in design of polymer-based devices.

This section outlines the development and application of three types of nanoindentation-based experiments to characterize polymer energy absorption as a unique metric of polymer mechanical performance, as well as preliminary results for a set of well-characterized amorphous polymers. The goal of this systematic study of nanoindentation-based energy absorption is to consider a structure / properties-based analysis of polymer energy absorption as a function of confined loading conditions and physical / microstructural properties.

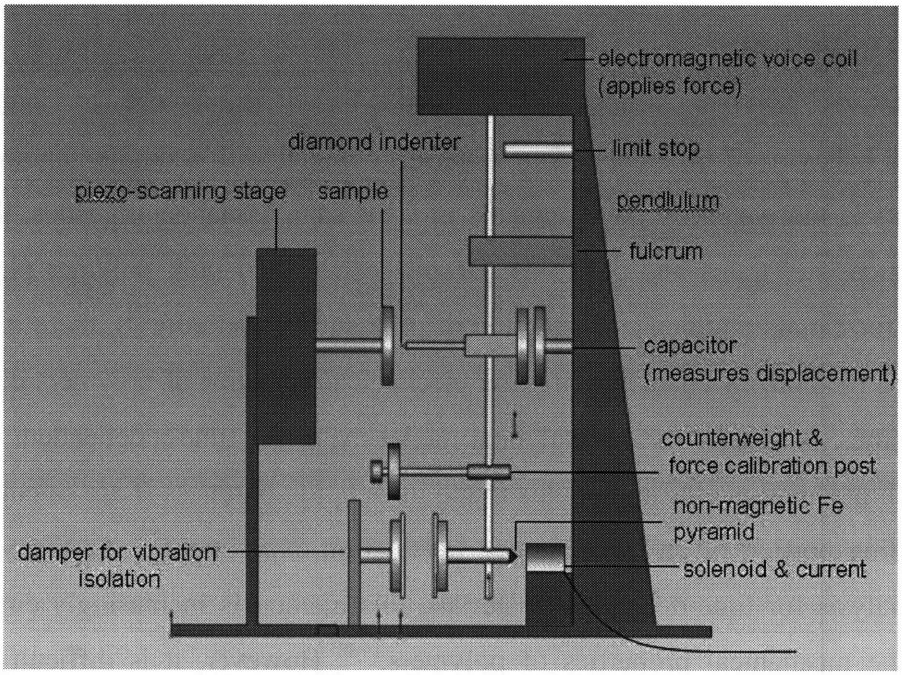

Figure 2.1 Figure of Micro Materials Ltd. nanoindenter pendulum test set-up.

2.2.1 Experimental details

An instrumented nanoindenter (NanoTest600, MicroMaterials Limited) including a Berkovich diamond indenter of nominal tip radius $R < 100$ nm was used for all experiments, Figure 2.2. All experiments were conducted in air at ambient temperature ($T = 22°C$) and relative humidity ($RH < 50\%$). For each sample listed in Table 2.1, the three

types of experiments described schematically in Fig. 2.2 were conducted, with five trials for each experimental condition (specific maximum load and / or loading rate) in each sample; the average and standard deviation are reported.

2.2.1.1 Nanoindentation-based approaches

The continuous load-displacement ($P - h$) response measured in conventional, quasistatic nanoindentation loading (Q) was evaluated to calculate the energy absorbed by the polymers as a function of load, loading rate, and polymer microstructure. Figure 2.2a) diagrams quasistatic behavior, where the gray area is the absorbed energy due to indentation loading, or the plastic work of indentation W_p. In metals, the energy absorbed per unit volume of material deformed (W_p / V) is a constant unique to the material.[7] Therefore, such parameterization of polymer Q-loading enables comparison with time-independent deformation response and suggests a potential metric to quantify polymer energy absorption. For each polymer, Q-loading was conducted for five maximum loads (1 mN, 3 mN, 7 mN, 15 mN and 30 mN), each at four loading / unloading rates (0.056 mN/s, 0.167 mN/s, 0.5 mN/s and 1.5 mN/s) with a holding period of 10 s at the maximum load. For this arbitrary holding period and matrix of maximum loads and loading rates, "nose effects" were not observed. To ensure that the indentation results were characteristic of the sample and not affected by instrument artifacts related to poor calibration, an identical indentation loading profile was performed 5 times on the same glassy polymer sample on a second instrumented nanoindentation apparatus (TriboIndenter, Hysitron, Minneapolis, MN), see Fig. 2.3. Analysis of these P-h curves via the Oliver and Pharr analysis[3] for the two instruments as outlined in Section 1.3 resulted in agreement of the Young's moduli within 7%.

Chain momentum (C) experiments were used to assess the change in indentation depth at 50 percent of P_{max} and to quantify the relaxation or reverse plasticity of the deformed volume. After this stress history, the polymer may either "creep" (an increase in depth with time) or exhibit reverse plasticity (a decrease in depth with time as the polymer "pushes" the indenter out of the sample). The measurement of depth increase with time is not a true creep experiment because the applied load is not strictly maintained constant by

the instrument. Here, chain momentum experiments were conducted by holding the load at 0.5 P_{max} for 60s, as depicted in Figure 2.2b, after a hold period of 0 s, 30 s, or 60 s at P_{max}. The gray area corresponds to the energy released by the polymer when recovering to its equilibrium depth, in the case of depth decreasing with time.

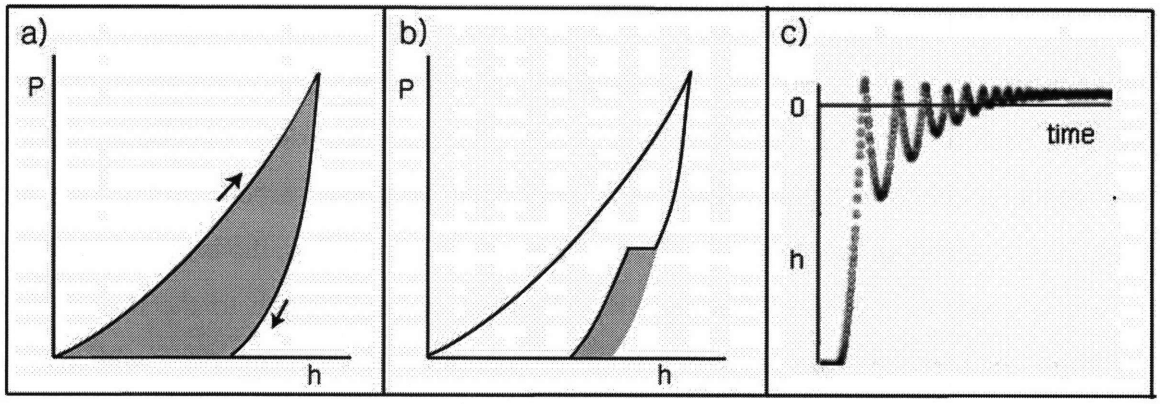

Figure 2.2 Nanoindentation testing techniques: a) quasistatic loading, Q; b) chain momentum evaluation, c); impulse testing (I).

Impulse experiments (I) were analyzed to evaluate the energy absorbed under multiaxial loading at rates far exceeding Q-loading conditions. Such experiments allow consideration of the relevance of Q-loading analysis for polymers that will be used for high frequency applications, and is enabled by the pendulum design of this particular nanoindenter. Here, the indenter is held away from the sample surface by a current maintained between a stationary solenoid and non-magnetic iron attached to the pendulum free end. When the solenoid current is terminated, the pendulum of effective mass m_p impacts the sample surface with a nominal force equal to the "preload" applied by the force transducer. Pendulum displacement is recorded as a function of time and kinetic energy before and after the force impulse is calculated from the corresponding velocities v. As shown in Fig. 2.2c, the applied energy is fully damped after several oscillations on the surface and the absorbed energy W_p is calculated upon the first impulse by $W_p = \frac{1}{2} m_p \left(v_{in}^2 - v_{out}^2 \right)$.

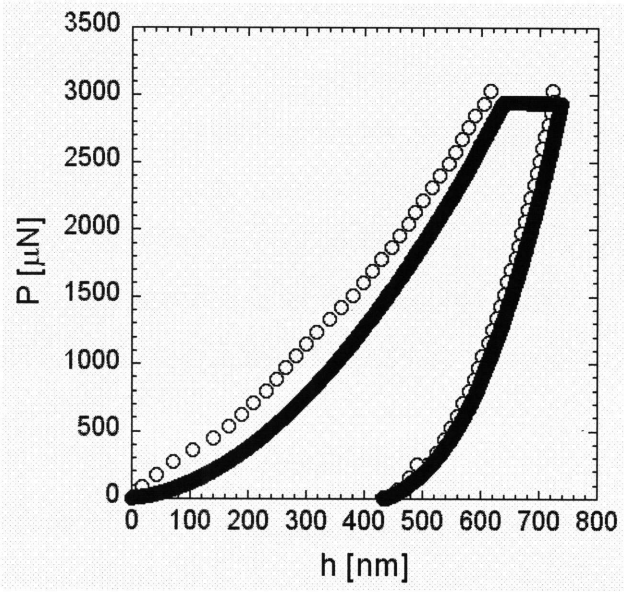

Figure 2.3 Load-displacement curves for indentations in a glassy, amorphous polymer performed on two nanoindentation instruments: MicroMaterials (○) and Hysitron (●) under identical conditions demonstrating relative consistency between instrumented indenters.

2.2.1.1 Materials

Five polymers, selected as model systems to examine the behavior of small volumes, were injection molded by DuPont into smooth discs. Three of these samples were fully amorphous, allowing analysis in the absence of microstructural complications such as percent crystallinity. The weight average molecular weight (M_w) was measured by DuPont via GPC and the glass transition temperature (T_g) was measured at MIT via DSC. The five characterized samples are shown with the polymer chain structure in Table 2.1.

Table 2.1 Proposed model polymer systems

POLYMER NAME	STRUCTURAL FORMULA[1]	T_g [°C]	M_w [g/mol]
Polyethylene PE	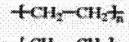	-30	85,195
Polypropylene PP	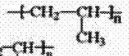	4.6	343,326
Polystyrene PS		103	248,670
Poly(methyl methacrylate) LU: Lucite®[2]	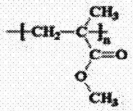	114	1,042,916
PL: Plexiglas®[3]		117	2,588,744
Polycarbonate PC	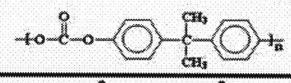	145	18,000

[1] Images from http://www.psrc.usm.edu/macrog/index.htm; [2] Rohm and Haas; [3] Ineos Acrylics

This polymer system allows comparison of certain physical and structural characteristics of amorphous polymers. For example, Plexiglas® (PL) and Lucite® (LU) are two types of poly(methyl methacrylate) (PMMA) that exhibit essentially the same T_g but almost a three-fold difference in weight averaged molecular weight, and poly(styrene) (PS) and poly(propylene) (PP) exhibit very similar molecular weight but very different degrees of steric hindrance of chain motion due to backbone rigidity, side-group size, and percent crystallinity.

The polymer materials set developed for the experiments in Chapter 3, also made by DuPont, improve upon the above set in that they systematically vary individual properties, so that mechanical property effects can be isolated and directly linked to changes in microstructure. The new materials set is designed such that direct comparisons can be made between materials responses where only one microstructural parameter is varied: molecular weight, glass transition temperature, or side-group size. Nevertheless, the materials set introduced above and used for experiments throughout Chapter 2 provides an excellent baseline for investigating polymer specific properties through nanoindentation in terms of microstructure.

2.2.3 Results and Discussion

2.2.3.1 Conventional nanoindentation of polymers

The rapid adaptation of instrumented nanoindentation to materials sets such as glassy polymers resulted in direct application of time-independent experimental approaches to time-dependent materials systems. In Section 2.2.3.1, conventional quasistatic testing and analysis will be discussed as a tool to investigate mechanical response dependence on polymer composition and experimental parameters, while Section 2.2.3.2 will extend the interpretation of nanoindentation responses to energy absorption per unit volume.

2.2.3.1.1 Composition and loading rate dependence

Figure 2.4 depicts the displacement responses of two representative polymers to identical loading that demonstrate the possible response variation among common engineering

polymers with relatively simple monomer structures (see Table 2.1). Figure 2.4 illustrates loading rate dependence of these two polymers for loading rates between 0.05 mN/s and 1.5 mN/s.

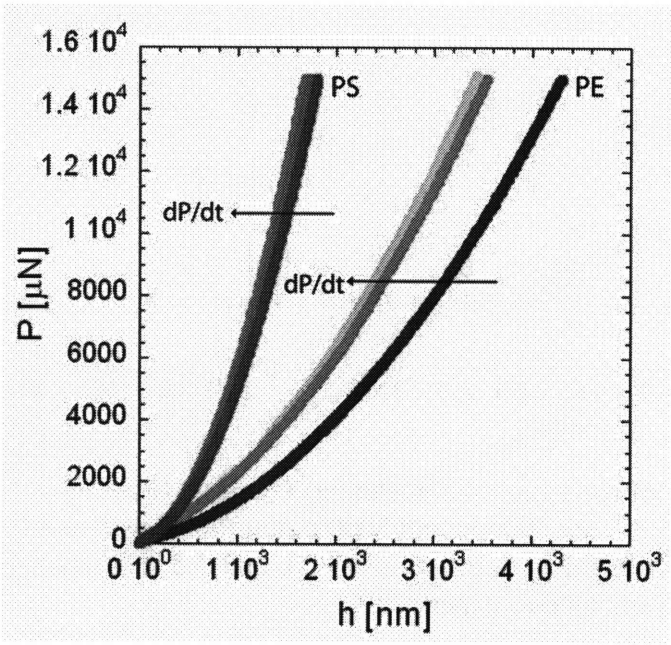

Figure 2.4 Reponses of polyethylene (PE) (blues) and polystyrene (pinks) to maximum load of 15 mN demonstrating variation in polymeric response for three loading rates: 0.15mN/s (lightest), 0.5 mN/s (second lightest), 1.5 mN/s (darkest).

2.2.3.1.2 Probe shape effect on analytical fitting constants

As introduced in Section 1.3, the stress state induced by the probe tip shape strongly influences the polymer mechanical response. In fact, the loading portion of an indentation curve, such as those in Figure 2.4, can be fit to a power law of the form

$$P = Ch^x, \tag{2.1}$$

where C is a fitting constant and x is a power related to the tip geometry. Sneddon was the first to report the values of x for various axisymmetric tip shapes: $x = 1$ for a flat punch, $x = 2$ for a sharp cone, and $x = 3/2$ for a sphere.[8] Figure 2.5 depicts fitted values for the parameters C and x for five maximum loads and four loading rates with a Berkovich indentation probe in Plexiglass®. The power-law fitting parameters, C and x, for the loading segment of this polymer appear to be independent to changes in loading

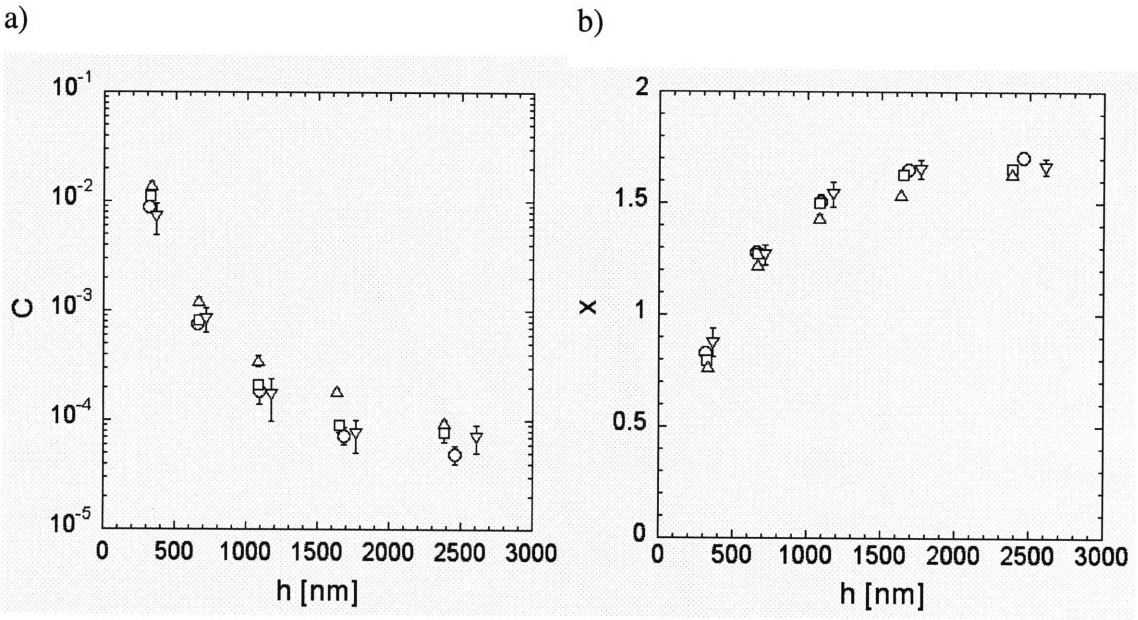

Figure 2.5 Values of the fitting parameters a) C and b) x in Eq. 2.1 for five maximum indentation depths between 300 nm and 3000 nm in Plexiglass® and for four loading rates of 0.05 mN/s (○), 0.15 mN/s (□), 0.5 mN/s (Δ), and 1.5 mN/s (Δ). Error bars represent standard deviations among five experiments.

rate between 0.05 mN/s and 1.5 mN/s. Figure 2.5b) depicts the evolution of the fitting parameter x with indentation depth. For the shallowest indentation depths, the fitting power is close to one and increases to a value between 1.5 and 2. This increase correlates with a progression of the probe geometry with indentation depth: the finite radius near the tip interacts with surface essentially as a flat punch and transitions toward a conical geometry.

2.2.3.1.3 Challenges to relating time-independent metrics of quasistatic polymer response to polymer physical attributes

Indentations to a single P_{max} in six polymers were analyzed using the method of Oliver and Pharr[3,8] for indentation hardness H values for two loading rates, and the results plotted in Fig. 2.6. A qualitative comparison of these six polymers suggests that the most simple monomer structures (and semi-crystalline samples), in this case PP and PE, may exhibit the least resistance to plastic deformation. However, a conclusive statement about indentation hardness as a function of molecular structure cannot be made for two reasons: (1) there are several interdependent variables that control crystallinity, chain packing, and

orientation and (2) indentation hardness is not an invariant material property but instead changes as a function of experimental conditions as well as with time after unloading. This example distills the two challenges in mechanically characterizing polymers via nanoindentation in terms of polymer structure: polymer structural variables are not independent of one another, making the ability to attribute changes in mechanical response to a change in the polymer physics or architecture very limited. Furthermore, the metrics that quantify the mechanical response of polymers were often designed for non-time-dependent materials, resulting in parameters that depend on testing conditions. The validity of indentation hardness as a metric for polymers will be treated in detail in Section 2.4.

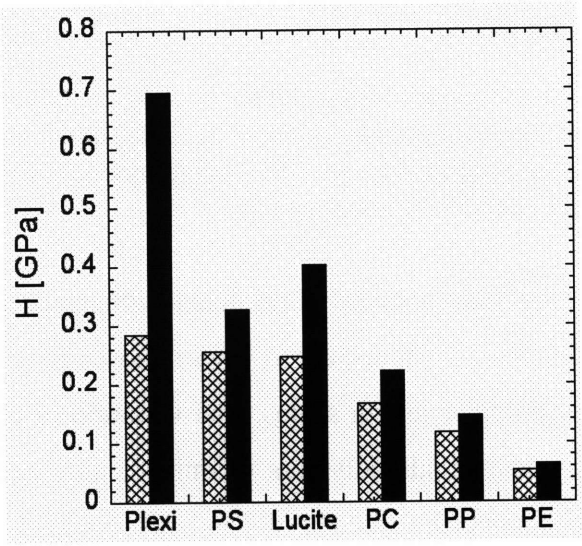

Figure 2.6 Indentation hardness H for six polymeric materials loaded to a maximum load of 15 mN at two loading rates: 1.5 mN/s (black) and 0.05 mN/s (cross-hatch). There are two poly(methyl methacrylate) materials with trade names Plexiglass (PL) and Lucite, polycarbonate (PC), and polypropylene (PP).

2.2.3.2 Specific energy absorption

The goal of this study of nanoindentation-based energy absorption was to develop an analysis based on the polymer structure as a function of confined loading conditions and physical / microstructural properties. Figure 2.7a) depicts specific energy absorption (W_p / V) as a decreasing function of loading rate for quasistatic loading experiments in PS, where indentation volume is calculated through the geometry of the Berkovich indenter

as:

$$V = 8.12h_{max}^3 \tag{2.2}$$

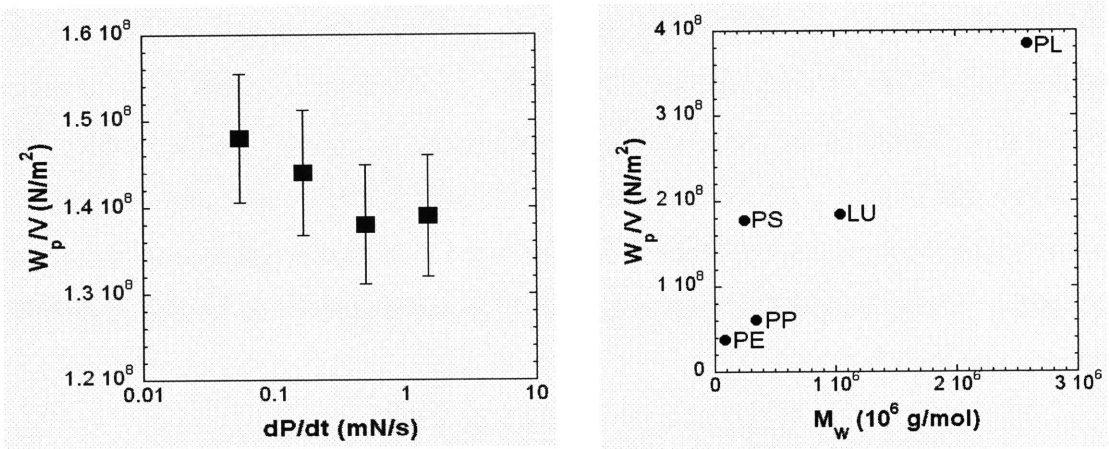

Figure 2.7 a) Energy absorption per unit volume (W_p / V) of polystyrene as a function of loading rate dP / dt for Q-loading experiments; b) Quasistatic W_p / V as a function of weight average molecular weight M_w for PE (polyethylene), PP (polypropylene), PS (polystyrene), LU (Lucite) and PL (Plexiglass).

Although absorbed energy may also be normalized with respect to the total applied energy W_{tot}, here normalization with respect to V was chosen to identify any size effects associated with inherent polymer length scales. The variation of energy absorption with loading rate in PS is typical of all polymers examined, although the strength of this correlation varies. It is noteworthy that the dependence on loading rate in Oliver and Pharr-type analysis of H is greater for the polymers with higher H values (Fig. 2.6). Others have reported Oliver and Pharr-type time-independent analysis of quasistatic loading experiments in ultra high molecular weight polyethylene (UHMWPE), polymethyl methacrylate (PMMA), polycarbonate (PC), and polystyrene (PS).[6,9,10] Among attempts to determine loading-rate dependence with a time-independent model, the experimental results do not agree; although Klapperich et al. found that E and H have opposite trends in relation to increasing indention volume V in such quasistatic experiments, Briscoe et al. and Dreschler et al. found that both E and H decrease with increasing V.[5,9] Figure 2.7b) illustrates that W_p / V increases with increasing M_w in the polymers considered; however, monomer structure strongly affects specific energy absorption as well (compare PS and PP). The glass transition temperature was not

observed to induce any clear trends with energy absorption over the range of loads and loading rates considered.

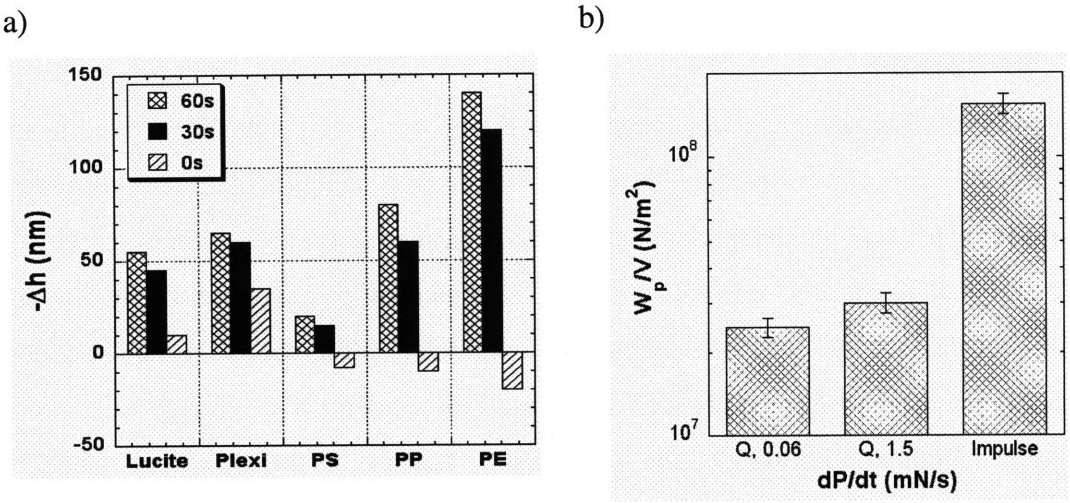

Figure 2.8 a) C-loading of all polymers. Displacement of indenter Δh during hold at $0.5P_{max}$ for 60 s. Prior positive creep of the indenter into the surface at P_{max} for 60 s (cross-hatch), 30 s (solid), and 0 s (striped) shows that recovery increases with increasing deformed volume V: Energy dissipation at P_{max} did not result in decreased work against the indenter at 0.5 P_{max}. b) Energy absorption per unit volume W_p / V for PE for two Q-loading rates (0.056 and 1.5 mN/s) versus for I-loading (theoretically infinite rate).

Figure 2.8a shows the behavior of the five polymers under C-loading, quantified as the change in indentation depth Δh over 60 s at $0.5P_{max}$ for three different hold periods at P_{max}. Most polymers essentially push the indenter out of the surface, and this work against the indenter actually increases as hold time at P_{max} increases from 0 s to 60 s. Thus, the longer the polymer creeps at P_{max}, the more the polymer deformation lessens during the hold segment during unloading. This finding suggests that the recovery scales with the size of the deformed polymer volume. The logarithmic decrease in h with time appears to be a strong function of monomer steric hindrance and a weaker function of molecular weight, as seen through comparison of PS, PL, and PE. Figure 2.8b compares W_p / V for the extreme loading rates of quasistatic loading experiments with that measured under I-loading for the polymer of simplest monomer structure and lowest M_w. For all polymers considered, W_p / V increased by approximately one order of magnitude under I-loading. Further, no clear correlation was observed between specific energy

absorption under Q- and I-loading. That is, the ranking by W_p / V shown in Fig. 2.7b (PL, LU, PS, PP, PE) was not observed under impulse loading.

2.2.4 Conclusions

The limitations of time-independent experiments and analysis presented above set the context for the areas of improvement critical to establishing nanoindentation as a standard tool for obtaining quantitative mechanical data for confined polymeric geometries as well as bulk samples. To this end, careful studies relating mechanical response to physical and structural properties of polymers must be conducted. Alternately, time-dependent mechanical properties must be identified that are independent of or change predictably with experimental conditions. At the very least, standard testing protocols must be established such that nanoindentation data of polymers can be compared within research communities and industry. The absorbed energy per unit volume discussed in the previous section is a model-free metric for the interpretation of nanoindentation response of polymers. These data, published as MRS Proceedings Vol. 841,[1] show through interrelated nanoindentation experiments that energy absorption is strongly dependent on loading rate, deformed volume, and physical / structural characteristics for amorphous and crystalline polymers. These trends are consistent with concepts of threshold strain energy density and activation volume processes of energy dissipation. Although this response is not inconsistent with the spring and dashpot simplification of polymer deformation, these results indicate a crucial volume of material deformed, beyond which elastic and plastic deformation mechanisms change under the confined loading of nanoindentation. Therefore, this investigation of alternative nanoindentation approaches indicates that systematic studies of energy absorption via the experiments outlined above are one option for future, material structure / physical properties-based descriptions of key mechanical properties for polymeric small volume structures.

2.3 CONTACT CREEP COMPLIANCE

The following study was published in 2006[11] with special thanks extended to M. Van Landingham and T. Juliano for providing and discussing experimental data and interpretation and providing epoxy samples.

The creep compliance of viscoelastic materials such as synthetic polymers is an established metric of the rate at which strain increases for a constant applied stress, and can in principle be implemented at the nanoscale to compare quantitatively bulk or thin film polymers of different structures or processing histories. Here, we outline the evolution of contact creep compliance analysis and application for both conical and spherical indenter geometries. Through systematic experiments on four amorphous (glassy) polymers, two semi-crystalline polymers, and two epoxies, we show that assumptions of linear viscoelasticity are not maintained for any of these polymers when creep compliance is measured via conical indentation at the nanoscale, regardless of the rate of stress application (step or ramp). Further, we show that these assumptions can be maintained to evaluate the contact creep compliance $J_c(t)$ of these bulk polymers, regardless of the rate of stress application, provided that the contact strains are reduced sufficiently through spherical indentation. Finally, we consider the structural and physical properties of these polymers in relation to $J_c(t)$, and demonstrate that $J_c(t)$ correlates positively with molecular weight between entanglements or crosslinks of bulk, glassy polymers.

2.3.1 Introduction

As discussed in Section 2.2.1, devices comprising small volumes of time-dependent materials, such as polymeric thin films, hydrated biological scaffolds, and microelectronic packaging, require mechanical characterization not attainable through well-developed methods suitable for bulk materials. Several categories of nanomechanical testing exist, including quasistatic nanoindentation,[3] dynamic nanoindentation,[12,13] nanomechanical contact creep,[14-20] and impulse indentation.[1] However, few analytical methods to interpret time-dependent material responses have been proposed that do not assume the material to be well-described as a linear

viscoelastic solid. Despite frequent application of this assumption, this idealized response is not maintained in most nanomechanical experimental conditions on polymers and this assumption can thus propagate quantitative and qualitative errors in analysis of polymer deformation. Time-dependent materials will behave as linear viscoelastic solids below a material-dependent, limiting elastic strain of approximately 1 - 2%. Stress, and thus strain, imposed on the material under contact loading such as nanoindentation may be reduced by decreasing the magnitude of the applied force P or by increasing the area over which P acts on the material. However, most instrumented nanoindenters have a fixed load range over which data can be acquired accurately, such that the indenter geometry and corresponding shape function are important experimental factors.

Nanomechanical creep testing has significant potential for interpreting the mechanical responses of polymers because the material response inherently includes time-dependent deformation. The shear creep compliance $J(t)$ is strictly defined as the change in strain as a function of time under instantaneous application of a constant stress,

$$J(t) = \frac{\varepsilon(t)}{\sigma_0} \tag{2.3}$$

and provides a means to quantify the capacity of a material to flow in response to a sudden applied stress.[21] Although conventional measurements of $J(t)$ included uniaxial or simple shear stress, researchers have increasingly reported creep compliance interpretations of instrumented (conical and spherical) indentation experiments on bulk or thin film polymers. However, due to the non-linearities in material behavior and contact mechanics, current experimental investigations of creep compliance typically assume particular linear viscoelastic models to fit the creep response. Figure 2.9a schematically illustrates the linear viscoelastic creep response at various applied stresses. The doubling of the instantaneous and constant applied stress σ_1 exactly doubles the strain $\varepsilon(t)$ for any time t during creep. It is well-established that the creep compliance $J(t)$ for a linear viscoelastic material is invariant with applied stress (Fig. 2.9b) due to the linear relationship between stress and strain at any time point for such materials. Referencing

Eq. (2.3), a polymer for which $J(t)$ changes as a function of maximum instantaneous stress σ does not conform to the assumptions of linear viscoelasticity. That is, $J(t) / \sigma(t) \neq k$ where k is a constant, due to the nonlinear constitutive relations of that particular polymer and / or to induced strain in excess of the linear viscoelastic strain limit for that material. In either case, polymers that do not exhibit $J(t) / \sigma(t) = k$ for a given indenter geometry and load / stress range cannot be characterized accurately by models that implicitly assume a purely linear viscoelastic response. Further, the models from which most expressions for creep compliance $J(t)$ expressions are derived were developed to determine the pressure distribution for axisymmetric indenter contact on viscoelastic solids,[21,22] and simplified for the case of step loading. In actuality, few nanomechanical instruments can attain the step-load condition because of limitations in speed of data acquisition and in force resolution. Thus, "quasi-step" loading, where the minimum loading time documented thus far for the step-load experiment is 1 s,[14,16,23] is often employed. Loading rate has been demonstrated to have an effect on the creep response,[16,20] and corrections for ramp loading have been proposed for a specific linear viscoelastic constitutive relation.[18]

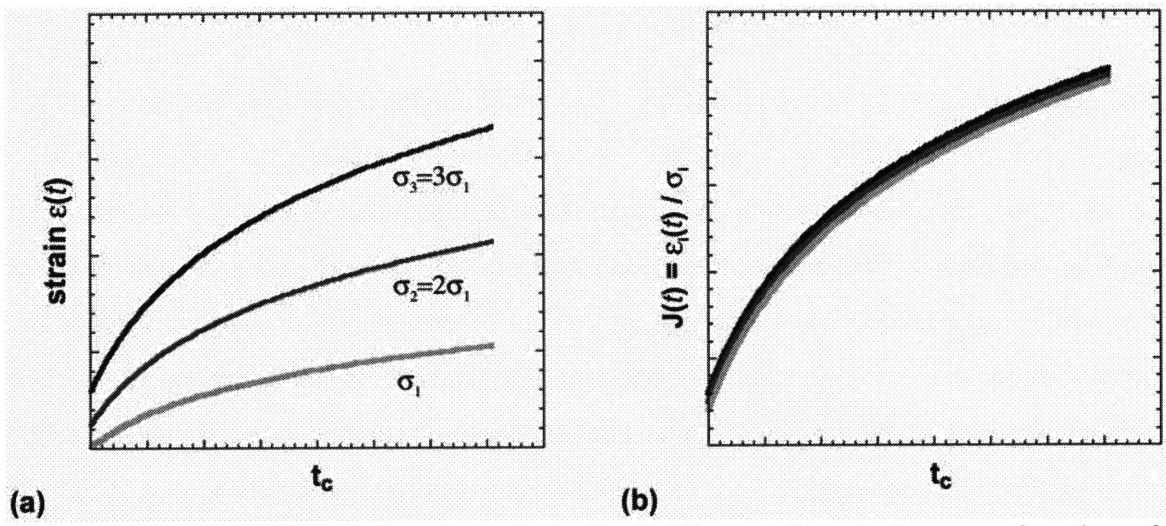

Figure 2.9 (a) Ideal linear viscoelastic behavior is illustrated as strain ε as a function of time during creep t_c for three instantaneous and constant levels of applied stress σ_i. (b) The creep compliance $J(t)$ for a linear viscoelastic material is characteristic of that material and independent of σ_i.

In attempts to attain the linear viscoelastic deformation regime during indentation-enabled creep, several studies have included rounded conical probes (R = 10 μm and 20

μm,[14,19,24]) and spherical probes (R = 3.4 μm[16] to 150 μm[18]). However, it is not generally considered or demonstrated whether polymers conform to the idealized linear viscoelastic response of Fig. 2.9b under the contact creep conditions employed, with notable exceptions.[18,25] Often, $J_c(t)$ is evaluated among polymers for only a single P_{max},[20,24] such that load dependence cannot be ruled out. Lu et al.[16] posited that since indentations below a critical indentation depth are unique to each of two amorphous polymers considered were not observable post-indentation via scanning electron microscopy, recovery implied linear viscoelasticity. However, such indentation recovery does not ensure a linear path in either loading or unloading; linear viscoelastic deformation of these materials under indentation was not proven or disproven. Recent approaches to determination of $J_c(t)$ or linear viscoelastic operators based on the contact creep response are summarized in Section 2.3, including those that also consider the limits of a linear viscoelastic creep response. As $J_c(t)$ is often interpreted within the framework of phenomenological models of linear viscoelastic behavior, for which there can be several distinct forms that reasonably fit a measured contact creep response, it is useful to also consider how $J_c(t)$ can be related to the structure and physical properties of polymers.

The contact creep compliance $J_c(t)$ is calculated herein primarily to demonstrate when the implicit assumption of linear viscoelastic deformation is obtained experimentally, and to consider how the material response changes with both polymer / monomer structure and loading conditions. Creep compliance formulations for conical and spherical indenter geometries are outlined and compared, and recent extensions are discussed. The contact creep compliance of eight bulk (semicrystalline and amorphous) polymers is then characterized with a Berkovich indenter that can be approximated as a conical geometry; none of the polymers behave as linear viscoelastic materials under these conditions. In contrast, the creep compliance of a subset of these same polymers under the same creep loads exhibits linear viscoelastic behavior for a spherical indenter of R = 500 μm. These results illustrate the limit of linear viscoelastic analyses in nanomechanical creep compliance characterization, and also demonstrate the relative effects of monomer

structure, molecular steric hindrance, and microstructure on the contact creep compliance of bulk polymers.

2.3.2 Basis and implementation of contact creep compliance solutions

As demonstrated below, although the conditions required for accurate creep compliance determination according to Eq. (2.3) are typically not maintained in indentation-enabled creep experiments, this characterization of time-dependent flow can be used to compare materials and / or consider the microstructural determinants of polymer deformation. For this reason, we delineate creep measured via instrumented indentation as contact creep compliance $J_c(t)$, underscoring the fact that it is load and not stress that is maintained constant in such experiments. The majority of viscoelastic solutions used to interpret contact creep compliance derive from two, independently obtained derivations to the general problem of contact between a rigid symmetric body and a viscoelastic half-space. These solutions for creep compliance in shear $J(t)$, reported by Lee and Radok (1960) and by Ting (1966), were elegant responses to an analytical challenge: viscoelastic deformation for which the Laplace transform could not be readily applied to predict stress distributions under contact loading (See Appendix A). Here, we state the relevant solutions of Lee and Radok (LR-) and Ting (T-), and summarize recent implementation in experimental investigations of creep for bulk and thin film polymers.

2.3.2.1 Solutions for spherical indenter geometry

The LR-solution for creep compliance in shear under spherical indentation where $a << R$ under a constant applied load P_0 can be stated as:

$$J_c(t) = (1-\nu)J(t) = \frac{8\sqrt{R}}{3P_0}\left[h(t)^{3/2}\right], \tag{2.4}$$

whereas the T-solution for the same condition can be stated as:

$$\phi(t) = \frac{8\sqrt{R}}{3P_0}\left[h(t)^{3/2}\right], \tag{2.5}$$

such that $\varphi(t) = (1 - \nu)\, J(t)$ for constant ν, or $\varphi(t) = 1/2\, J(t)$ for incompressible materials for which $\nu = 1/2$. Ting states that $\varphi(t)$ is of the general form of creep compliance, but does not explicitly equate $\varphi(t)$ to $J_c(t)$. Neither solution of the pressure distribution actually requires step-loading of the viscoelastic material, but both solutions are simplified by this constraint and implicit in the representations of $J_c(t)$ for Eqs. (2.4) - (2.5).

2.3.2.2 Solutions for conical indenter geometry

Lee and Radok did not consider conical indenter geometries, presumably due to the constraint of "small strains" imposed by linear viscoelastic operators. However, Ting presented a general solution for any smooth, axisymmetric indenter profile, and provided specific solutions of total contact pressure for conical, spherical, and paraboloidal (classic sphere for $a << R$) geometries. The T-solution for $\varphi(t) = 1/2J(t) = J_c(t)$ under an instantaneously applied and constant depth h_o is generally given by Eq. (A.11) of Appendix A. For a conical indenter of semi-apex angle $\alpha = \pi/2 - \theta$, where θ is the angle between the material free surface and inclined indenter surface assumed by Ting, contact creep compliance $J_c(t)$ is

$$J_c(t) = \frac{2\pi a^2(t=0)\tan\theta}{P(t)}. \tag{2.6}$$

For the case more accessible to instrumented indentation experiments, an instantaneously applied and constant force P_o,

$$J_c(t) = \frac{2\pi a^2(t)\tan\theta}{P_0} = \frac{8\tan(\alpha)h^2(t)}{\pi P_0}. \tag{2.7}$$

As stated in Eq. (2.7), $J_c(t)$ can be calculated directly from experimentally measured $h(t)$ for a known indenter semi-apex angle α. Although this calculation is straightforward and the average contact stress for a conical indenter is maintained constant by virtue of the

self-similar geometry, the stress singularity at the cone apex immediately violates the assumption of linear (or small strain) viscoelastic deformation.

Equations (2.4) - (2.7) represent the principal relations for determining creep compliance from contact loading, i.e., indentation-enabled creep experiments. Equations (2.5) and (2.7) are used to analyze the experiments in the present study. These equations assume linear viscoelasticity, but do not assume any particular form of the constitutive relation in terms of the nature of the linear viscoelastic operators. More simply, these solutions do not presuppose configurations of springs and dashpot elements that describe phenomenologically the stress or strain of a real polymer at short and long times. However, both Lee and Radok[22] and Ting[21] illustrate an application for indentation of a Maxwell solid. Ting thus shows that a decrease in applied load need not result in a decrease in contact area for a conical indenter geometry -- an analytical prediction of the so-called "nose effect" observed during indentation unloading of polymers under insufficiently rapid unloading rates.[6,26]

2.3.2.3 Extensions and applications of $J_c(t)$ models

Here, we briefly outline the extensions and adaptations of these solutions by others who have subsequently determined $J_c(t)$ via indentation for specific polymers and loading conditions. First, we consider approaches that do not assume a particular form of the linear viscoelastic operators and compare polymer response directly on the basis of measured $J_c(t)$.[16,25] Next, we consider approaches that inherently assume a spring-dashpot constitutive response of the polymer (such as the standard linear solid model[14,18,20,24,27]) from which model-dependent constants can be obtained.[18,20,24] As discussed, it is possible to demonstrate whether the condition of linear viscoelastic deformation is met with either approach.

Lu et al. adapted the solutions of Sneddon,[8]Ting,[21] and Lee and Radok[22] to extract viscoelastic properties from contact creep experiments via spherical and conical indenter geometries.[16] The authors found less than 10% error of $J_c(t)$ calculated during quasi-step loading with conical or spherical indenters (for amorphous poly(methyl methacrylate) or

PMMA and polycarbonate or PC), as compared to $J(t)$the authors measured in separate experiments via conventional uniaxial (PMMA) or shear (PC) creep compliance measurements, although the contact creep conditions were not demonstrated to be independent of creep load P_o. In contrast, Van Landingham et al.[25] have recently applied Ting's solution for a constant applied load P_o to compute $J_c(t)$ for amorphous (glassy) polymers and epoxies under conical indentation-enabled creep experiments. The authors superposed a cyclic load during a dwelling period at each of several distinct P_o to obtain the projected contact area $A_{c(t)}$ for each data point during the dwelling period rather than calculate $J_c(t)$ directly from $h(t)$, and found that none of the polymers analyzed via Berkovich conical indentation and Eq. (2.7) were well-described as linear viscoelastic: $J_c(t)$ was not independent of applied load.

Although $J_c(t)$ can be determined quantitatively without recourse to a particular linear viscoelastic constitutive relation via Eqs. (2.4) – (2.7), the experimentally observed $h(t)$ can also be fit to a particular form of the creep function. Yang et al.[20] did not consider the elastic or viscoelastic contact solutions rigorously, but rather applied the constitutive relations for a Kelvin-type solid (a series of parallelized springs E_i and dashpots η_i of established σ - ε relations) to a flat punch to determine $h(t)$ and thus

$$J(t) = \frac{h(t)}{\sigma_0 h_{in}} = \sum_i J_i \,, \tag{2.8}$$

where h_{in} is an empirically determined length scale, and the form of J_i represents the number of Kelvin-type elements in series that exhibit the characteristic depth decay of (1 - e^{t/τ_i}). The authors considered several amorphous polymers but could not correlate known physical or monomer structure / properties with the creep compliance quantified in this way. In contrast, Cheng et al.[24] and Oyen[18] adapted the LR- solution to interpret spherical indentation creep on the basis of a standard linear solid model (i.e., a spring in series with a Kelvin-Voigt parallel spring and dashpot), via the method of Laplace transforms[16,24] or direct solution of the viscoelastic integral equations.[18] Defining $J_c(t)$ in terms of a constitutive model enables tractable solutions of constants defined by the

model, but it is well understood that the number and magnitude of linear operators (or Prony series constants) is not unique and that several such sets can accurately describe a measured creep response. The resulting constants or material properties extracted from these fits necessarily depend on both the material and the form of the constitutive model that defines the creep function. Within a given study assuming a specific model, results among polymers can be compared, but it is then difficult to compare among studies or interpret $J_c(t)$ as a function of the structure and physical properties of these polymers. Cheng et al. described $J_c(t)$ as

$$J(t) = \sum_{i=1}^{N} J_i e^{-t/\tau_i}, \tag{2.9}$$

where all constants were determined through fits to experimental data and represented rather involved algebraic functions of the simple linear solid constitutive relations from which element constants E_1, E_2 and η could ultimately be determined. The authors found that the indentation elastic modulus E_i agreed well with E_1 extracted from the creep-type experiments for amorphous polystyrene and semicrystalline polymer poly(vinyl alcohol) at very low relative humidity (10%) but to disagree significantly at higher relative humidity, attributing this discrepancy in part to increased viscoelasticity under higher humidity. Oyen[18] tested the applicability of the standard linear solid model to several polymer films by fitting a different linear viscoelastic creep function for a spherical indenter geometry (R = 150 μm) under single-ramp and multi-step ramp loading to extract associated time constants and instantaneous shear modulus G. Successful prediction of $h(t)$ was demonstrated for an order of magnitude increase in loading time (20 s to 200 s) and a factor of two increase in maximum load (50 mN to 100 mN), indicating that this linear viscoelastic material model could be applied to contact creep analysis under specific (loading and environmental) conditions. That is, rather than showing that measured $J_c(t)$ was independent of load, the author demonstrate additivity required of linear viscoelasticity: the creep function form accurately predicted the $h(t)$ response measured at multiple creep loads.

In the present study, we seek to determine the experimental conditions under which the assumptions implicit in Eqs. (2.4) - (2.7) hold, such that $J_c(t)$ can be measured within the linear viscoelastic regime. Further, rather than fit $J_c(t)$ to a particular linear viscoelastic constitutive model, we consider $J_c(t)$ as it relates to the molecular structure and physical properties of a range of well-characterized bulk polymers.

2.3.3 Experiments

2.3.3.1 Materials

Common engineering polymers with relatively simple monomer structures were chosen for these contact creep experiments. These materials included four injection molded, amorphous polymers (polycarbonate (PC); polystyrene (PS); poly(methyl methacrylate) of two different weight-average molecular weights M_w of commercial names Lucite (LU) and Plexiglas (PL)); as well as two epoxies in which the effective structural length scale is the molecular weight between cross links M_c: E3 (M_c = 380 g/mol) and E8 (M_c = 818 g/mol) as reported by Lesser et al.[28] In such chemically cross linked, amorphous polymers, molecular chain mobility, or the ability for a given macromolecular chain to displace with respect to the network, increases with increasing M_c. In addition, two injection molded, semi-crystalline polymers were considered (polyethylene (PE) of ~69% crystallinity and polypropylene (PP) of 58% crystallinity, as determined by small angle x-ray diffraction. The monomer structure, glass transition temperature T_g and M_w for each

Table 2.2 Polymer monomer structure and physical properties

POLYMER NAME	STRUCTURAL FORMULA[1]	T_g [°C]	M_w [g/mol]
Polyethylene PE	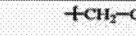	-30	85,195
Polypropylene PP	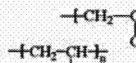	4.6	343,326
Polystyrene PS	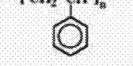	103	248,670
Poly(methyl methacrylate) LU: Lucite®[2]	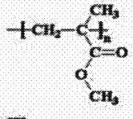	114	1,042,916
PL: Plexiglas®[3]		117	2,588,744
Polycarbonate PC	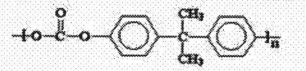	145	18,000
Epoxy E3 E8	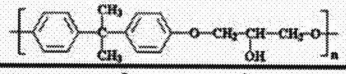	—	M_c: 380 818

[1] Images from http://www.psrc.usm.edu/macrog/index.htm; [2] Rohm and Haas; [3] Ineos Acrylics

polymer are listed in Table 2.2. All polymers were stored and tested at ambient temperature and relative humidity (T = 22.2°C, RH < 55%). The T_g of all polymers excluding epoxies was measured via differential scanning calorimetry (DSC) as reported by the manufacturer (DuPont, Wilmington, DE) and confirmed in the present study, while the M_w was determined by the manufacturer via gel permeation chromatography (GPC).

2.3.3.2 Instrumented indenter-enabled contact creep testing

Nanoindentation-enabled creep experiments were conducted on an instrumented nanoindenter (MicroMaterials, Ltd., Wrexham, UK) to obtain indenter displacement into each polymer surface as a function of maximum load P_{max}, loading rate dP / dt, and indenter geometry. Indenter geometries included a diamond Berkovich (trigonal pyramid) indenter of cone-equivalent semi-apex angle $\alpha = 71°$ and a ruby sphere of radius $R = 500$ μm.

As-processed root mean square sample surface roughness was < 20 nm for all samples, as measured via contact-mode scanning probe microscopy (3DMFP, Asylum Research, Santa Barbara, CA). Samples were stored in desiccators before and after testing, and surfaces were not chemically or mechanically modified prior to experimentation. Polymers were aged 2 hrs prior to testing in an instrument chamber that maintains humidity at 55% RH.

Creep tests were conducted to several P_{max} (1 mN, 5 mN, 10 mN and 15 mN) for each of two dP / dt: ramp loading (0.5 mN/s) and rapid ``quasi-step" loading (0.5 s to P_{max}), and to P_{max} = 30mN for ramp loading only. The quasi-step loading over a constant elapsed time required variation of loading rates to ensure sufficient data point acquisition at increased speeds (2 mN/s, 10 mN/s, 20 mN/s, 30 mN/s). For each pair (P_{max}, dP / dt), constant load $P_{max} = P_o$ was maintained for 10 s, 60 s, or 100 s to acquire $h(t)$. During this holding period approximating creep conditions, P did not vary more than 2%; for ``quasi-step" loads, the overshoot of the desired P_o did not exceed 10% for the range of polymers considered. Indentation depths ranged between 300 nm and 2500 nm for experiments

with the Berkovich indenter geometry and between 50 nm and 300 nm for the spherical indenter geometry. Typical drift in the displacement signal at room temperature was 0.01 nm/s. Each sample was tested at least in triplicate for each loading condition for the Berkovich indenter geometry. The two epoxy samples were tested in triplicate to all loading conditions with both the Berkovich and spherical indenter geometries. Equations (2.5) or (2.7), as appropriate for the indenter geometry used, were fit to the acquired $h(t)$ responses, where t_c is the elapsed time after attainment of the maximum contact load P_o via step or ramp loading; that is, both step and ramp loading creep were evaluated from $h(t_c = 0)$.

2.3.4 Results and Discussion

2.3.4.1 Nanoindentation contact creep with a sharp indenter

2.3.4.1.1 Nonlinear viscoelastic deformation

Eight common engineering polymers, with monomer structures and physical properties outlined in Table 2.2, were evaluated at several distinct P_{max} with a Berkovich (sharp trigonal pyramid) indenter. The contact creep compliance, calculated using the model-independent formulation of $J_c(t)$ in Eq. (2.7), exhibited a positive dependence on increasing P_{max} for all the polymers tested, confirming nonlinear viscoelastic behavior under these contact creep conditions for structurally simple amorphous polymers. Similar values for contact creep compliance of polymeric materials with a Berkovich indenter geometry were found in other recent studies.[20,25] Figure 2.10a shows the typical variation of $J_c(t)$ with P_o ranging from 3 mN to 15 mN, and Fig. 2.10a compares all polymers for P_o = 3 mN and 15mN at $J_c(t$ = 10 s). Note that in response to an increase in P_{max} by a factor of five, all amorphous polymers exhibited a marked increase in $J_c(t)$ at the higher P_{max}, and therefore all amorphous polymers exhibited nonlinear viscoelastic deformation under these conditions. Although $J_c(t)$ can be calculated according to Eq. (2.7), the inherent assumptions of this calculation are not maintained. Therefore, the data are discussed in terms of monomer and microstructural determinants of creep-like resistance to viscoelastoplastic flow in Section 2.3.4.3.

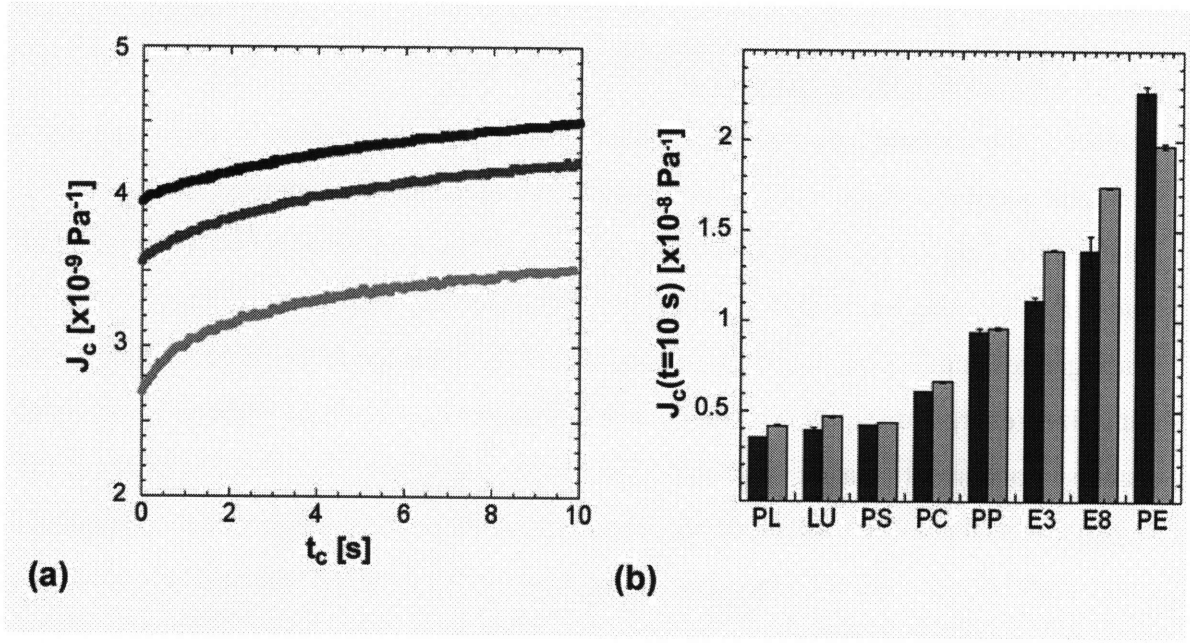

Figure 2.10 Contact creep compliance $J_c(t)$ under ramp loading of 0.5 mN/s via Berkovich (sharp) probe. (a) Plexiglas (PL) shows typical dependence on creep load for P_o: 3 mN (light grey), 15 mN (dark grey) and 30 mN (black). (b) Comparison among all polymers at J_c (t = 10 s) for P_o: 3 mN (black) and 15 mN (grey) indicates increasing J_c (t) with decreasing steric hindrance. Polymer abbreviations are as follows: PMMA Plexiglas (PL), PMMA Lucite (LU), polystyrene (PS), polycarbonate (PC), polypropylene (PP), polyethylene (PE) and two epoxies: E3 and E8.

Plastic flow is also a deformation mechanism under indentation-enabled creep compliance.[29,30] One way to assess the extent of plasticity is to subtract the creep portion of the displacement from the loading-unloading cycle, and determine the extent to which the corrected, final depth of indentation h'_f exceeds the maximum depth of indentation prior to the creep segment h_{max}. The ratio h'_f / h_{max} is proportional to the percent plastic work W_p / W_{total}.[23] We found that, for the Berkovich indenter geometry, h'_f / h_{max} was as great as 62% in the amorphous polymers considered herein, indicating that there was indeed deformation that was not recovered during the unloading cycle of the indentation experiment. As we have shown via scanning probe microscopic examination of post-indentation recovery of Berkovich indentation in these same polymers,[31] although the depth of indentation does continue to recover over the next 48 hrs post-indentation, the volume of indentation does not recover appreciably because the material at the indenter sidewalls (where two facets of the pyramid join) remains plastically deformed over at least 48 hrs post-indentation.

2.3.4.1.2 Effect of loading rate dP / dt

Contact creep experiments conducted with a sharp conical indenter induce not only a load-dependent response, but also loading rate-dependent response. This point is illustrated in Fig. 2.11a where $J_c(t)$ of the low- M_c epoxy E3 is shown for three maximum loads (P_o = 1 mN, 5 mN and 15 mN) for both ramp and step loading. The increase in loading rates induces an increase in $J_c(t)$ at all P_o considered, as rapid loading to P_o minimizes energy dissipation through viscous mechanisms, while slow loading to P_o enables concurrent elastic and viscous responses prior to creep. Figure 2.11b demonstrates the effects of increased chain mobility on this loading rate dependence under conical indentation creep, comparing $J_c(t)$ for E3 (low M_c) and E8 (high M_c) for three P_{max} attained via ramp loading (dP / dt = 0.5 mN/s). As expected from Fig. 2.11b, the increase in M_c causes an increase in the $J_c(t)$ for all conditions. Surprisingly, the polymer of lower M_c, and thus lower molecular chain mobility, exhibits a greater dependence on load. This result is consistent with the pair of amorphous polymers PC (lower M_w) and PL (greater M_w), in which case the polymer with fewer entanglements and greater chain mobility (PC) is affected less by changes in load than the polymer with less chain mobility (PL) during contact creep.

Experiments performed by Van Landingham et al.[25] demonstrated the same trend for PMMA and an epoxy: creep tests were carried out between P_{max} = 0.2 mN and 10 mN on PMMA and epoxy samples (different from the epoxies detailed herein). Although the epoxy was slightly stiffer than the PMMA upon loading, $J_c(t)$ for the epoxy was more sensitive to changes in P_{max}. Together, these results indicate that contact creep compliance of polymers with lower chain mobility is more sensitive to changes in applied load. Here, for the Berkovich indenter geometry, an increase in P_o by an order of magnitude resulted in a maximum increase in $J_c(t$ = 10 s) of 57% (E8 epoxy). However, we note that to support this effect of chain mobility on load dependence rigorously, complementary experiments are required to maintain a constant loading time for a range of loads P_o. More importantly, although trends with monomer rigidity, M_w, and M_c are observed in $J_c(t)$ as measured via a sharp conical indenter geometry, the dependence of

this response on applied load and loading rate indicate highly non-linear behavior that is not interpreted accurately via standard linear viscoelastic analytical functions.

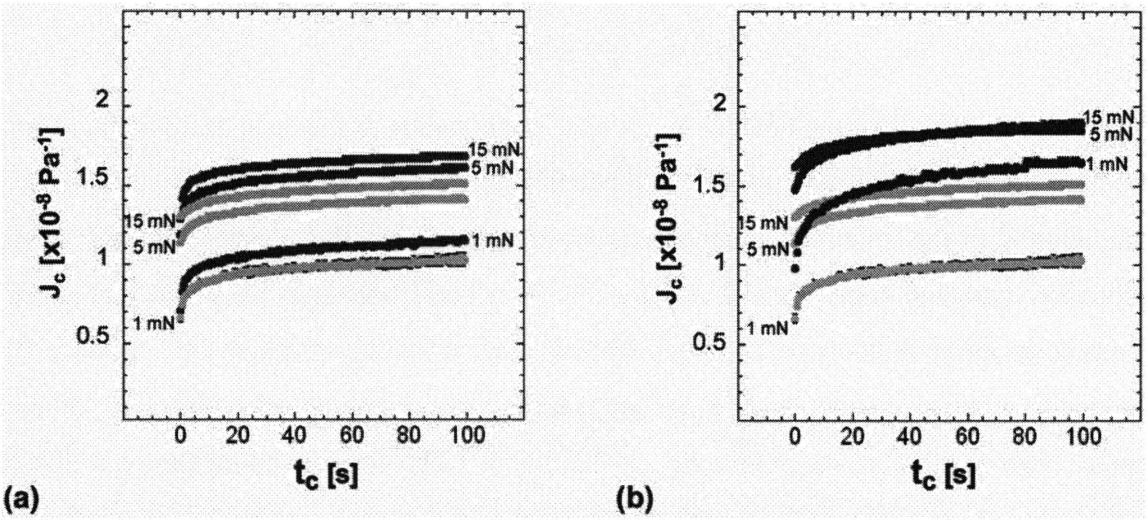

Figure 2.11 Comparison of creep compliance $J_c(t)$ for step (black) and ramp (grey) loading for a single epoxy (E3) indented with a Berkovich indenter at three maximum loads: 1 mN, 5 mN and 15 mN. (b) Comparison of $J_c(t)$ for two epoxies differing in molecular weight between crosslinks M_c ramp loaded with a Berkovich indenter to three maximum loads: 1 mN, 5 mN and 15 mN. The average M_c is twice as high for E8 (black) than for E3 (grey).

2.3.4.2 Nanoindentation contact creep with a spherical indenter

In order to determine whether it is possible to measure contact creep responses within the linear viscoelastic regime of polymer deformation, nanoindentation creep experiments were conducted with a spherical ruby indenter of R = 500 μm to the same five maximum loads as used in conical ramp indentation (P_{max} = 1 mN, 5 mN, 10 mN, 15 mN and 30 mN) via ramp and step loading for the two epoxy samples: E3 and E8. Comparison of the load-displacement P - h response with the Berkovich and spherical indenter geometries to the same P_{max} (15 mN) illustrates the difference between the viscoelastic and the viscoelastoplastic regimes (Fig.2.12). The percent of plastic or absorbed work, expressed as the ratio of final displacement at final unloading h'_f to the maximum displacement h_{max}, was 39.4% for the Berkovich geometry and only 11.6% for the spherical geometry in E3. This confirms that the material response to the spherical indentations was predominantly viscoelastic under the loading rates considered. This conclusion is supported by the Tabor contact strain calculated for this spherical indenter geometry:[32]

$$\varepsilon = 0.2\frac{a}{R}, \tag{2.10}$$

where a is the radius of the contact area and R is the radius of the spherical indenter. For the P_{max} considered, the strains thus calculated ranged between 0.3% and 0.8%, indicating that the spherical indentations were well within the elastic limit for these polymers (typically between 1% and 2%[33]). Van Landingham et al. noted that creep compliance measurements on an epoxy (different from those considered herein) via a 10 μm radius conical tip appeared to be approaching linear viscoelastic behavior for the lowest loads applied in that study (P_{max} = 0.2 mN).[25] The corresponding strains in those experiments were ~ 4%, and thus apparently exceeded the elastic limit of those materials under the conditions cited. Incidentally, for polymers with elastic strain limits near 1% and an instrumented indenter with load resolution on the order of 0.1 mN, a 500 μm radius is one of the smallest indenter radii that can be used while remaining within the elastic deformation regime. (This indenter radius induced contact strains of 0.8% at a maximum depth of 360 nm and load P_o of 1 mN. For the polymers considered herein, indenters of smaller radii would require greater load resolution such that P_o < 1 mN to maintain contact strains \epsilon < 1%.) Although the strains induced by the two indenter geometries cannot be directly compared (the Berkovich induces strains >> 1% at the cone apex), the average applied stresses may be estimated as the quotient of load to projected contact area (σ_e, akin to indentation hardness). Average stress imposed by the spherical indenter ranged 5.5 - 18 MPa (depending on P_{max}), while the average stress imposed by the Berkovich indenter ranged 194 MPa - 470 MPa for the same range of P_{max}. Responses to these applied stress ranges are in agreement with published values of yielding; for example, amorphous polycarbonate has a yield strength of 62.1 MPa, which is well above stresses under the spherical indenter geometry but less than the lowest stress applied by the Berkovich indenter geometry.[34]

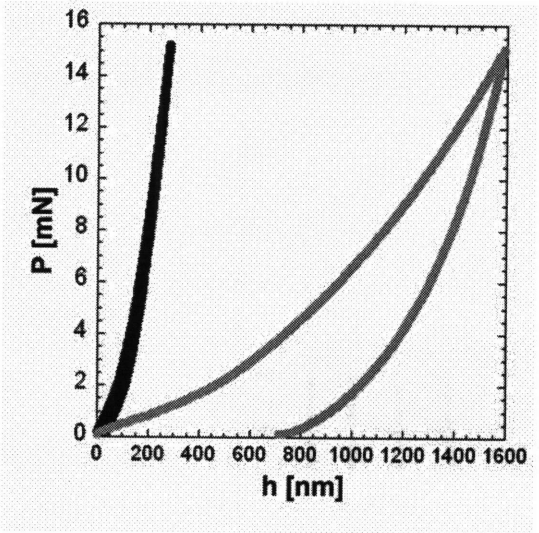

Figure 2.12 Load-displacement response for epoxy (E3) ramp loaded to a maximum load of 15 mN for both a Berkovich indenter (grey) and a spherical indenter of radius R = 500 μm (black). Here, the creep segment at maximum load has been removed.

The low strains attainable with the large spherical indenter geometry enable contact creep experiments within the elastic strain limit of the material. As depicted in Fig. 2.13a, contact creep via the spherical probe demonstrate $J_c(t)$ that is independent of both P_{max} and dP / dt. Additionally, the magnitude of $J_c(t)$ is lower by an order of magnitude as compared with that obtained with a Berkovich indenter geometry for these polymers. Results reported by Van Landingham et al. display a similar trend over the same load range: a decrease in contact creep compliance obtained with a blunted conical indenter as compared with that obtained with a Berkovich indenter for the same polymers.[25] As expected, this decrease in $J_c(t)$ for the blunted cone was more subtle, as σ_e differed by a factor of two, while in the current study σ_e differs by a factor of 10 - 20. In contrast with experiments that employ a Berkovich or conical indenter geometry, for which error in $J_c(t)$ is significantly less than differences in $J_c(t)$ measured at different P_{max} for a given polymer and loading rate, the error obtained on $J_c(t)$ measured with spherical indenter geometries indicates no statistically significant effect of load on $J_c(t)$. Of course, Fig. 2.13 also demonstrates that the experimental scatter in $h(t)$ and thus in $J_c(t)$is increased for spherical indenters of large R, in part because the change in load at the point of initial contact with the surface is less significant than that for a sharp indenter geometry. As noted, clear demonstration of the linear viscoelastic regime implies additivity, i.e., a

given linear viscoelastic model fit to one set of data for a given material can accurately predict the creep response under varied loading times and maximum loads.[18]

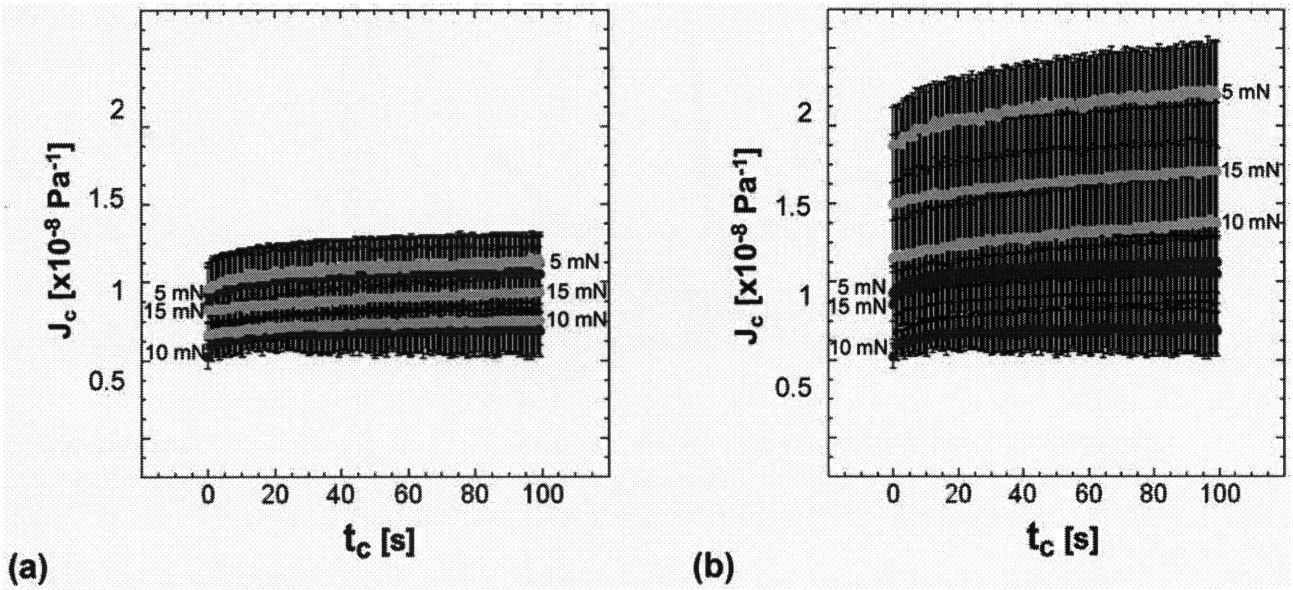

Figure 2.13 (a) Comparison of creep compliance $J_c(t)$ for step (black) and ramp (grey) loading measured with a spherical indenter of radius R = 500 μm for a single epoxy (E3). $J_c(t)$ is not dependent on load or loading rate, as shown in the overlap among step and ramp loading for three maximum loads: 1 mN, 5 mN and 15 mN. (b) Comparison of $J_c(t)$ for two epoxies differing in molecular weight between crosslinks M_c, under ramp loading with a spherical indenter of R = 500 μm to three maximum loads: 1 mN, 5 mN and 15 mN. M_c of E8 (black) is twice that of E3 (grey).

2.3.4.3 Structural and physical determinants of creep compliance

The interdependence of certain synthesis routes, structural characteristics and physical mechanical properties of polymers make correlations of structure-property relations challenging, as demonstrated by the description of deformation states including creep via spring-dashpot continuum models. However, certain subsets of the polymers considered herein enable consideration of structural determinants for $J_c(t)$ when linear viscoelastic deformation conditions are met, as well as speculation of microstructural determinants of creep and creep compliance rates when these conditions are not met.

Figure 2.10b illustrates creep compliance via Berkovich indentation for which the small strain assumptions of linear viscoelasticity are not met. Despite this quantitative limitation, $J_c(t$ = 10 s) of eight polymers at P_{max} = 3 mN and 15 mN correlates most

strongly with monomer steric hindrance at a given load; it should be noted that molecular weight among these polymers also differs. Polyethylene is expected to exhibit the greatest molecular chain mobility per unit length, due to the extremely simple monomer structure of this polymer as shown in Table 2.2, and this correlates with the fact that PE exhibits the greatest $J_c(t)$ at all conditions. Polypropylene (PP) also has a very simple monomer structure, and was the fourth most creep compliant polymer tested. Both the PE and PP samples were semicrystalline and tested above their glass transition temperatures; although it is expected that the amorphous regions of these materials would still creep readily, this microstructural heterogeneity resulted in rather complex behavior. For example, while PP shows a slight increase in $J_c(t)$ with P_{max}, PE is the only polymer to exhibit a decrease in $J_c(t)$ with increasing P_{max}.

Contact creep responses of the six amorphous polymers indicate the relative importance of monomer steric hindrance and molecular weight. The polycarbonate (PC) backbone contains two benzene rings and has significantly reduced chain mobility due to this rigidity. Consequently, amorphous PC exhibits lower $J_c(t)$ than PE or PP, despite the extremely low M_w of PC. This indicates that steric hindrance is more important than M_w in determining the magnitude of contact creep compliance $J_c(t)$ for a given applied contact load P_{max}. However, molecular weight does have a modest effect on $J_c(t)$, as demonstrated by the comparison of the two poly(methyl methacrylates) considered: Plexiglas (PL) and Lucite (LU). The M_w of PL is more than twice that of LU, but otherwise these amorphous polymers are identical; this difference in M_w correlates with an 8% decrease in $J_c(t)$ for PL with respect to LU. In addition, the two epoxies have different molecular weight between crosslinks or entanglement points quantified as M_c, which has a corresponding effect on $J_c(t)$: E3 (M_c = 380 g/mol) exhibited a significantly lower $J_c(t)$ at all loads considered than that of E8 (M_c = 818 g/mol), due to the relatively lower chain mobility of epoxy E3.

The microstructural dependency of $J_c(t)$ is underscored by the rankings of the six glassy network polymers depicted in Fig. 2.14a, considered at the same P_{max}. While $J_c(t = 0)$ simply reflects the relative stiffness of these polymers during the loading phase, the rates

of change in the (steady-state) contact creep compliance do not follow this same trend. Figure 2.14b shows this contact creep compliance rate over a 60 s dwell for polymers listed in order of increasing M_w. Figure 2.14 illustrates two important points. First, the (steady-state or $t > 5$ s) rate of creep compliance is unique to each polymer, as demonstrated by distinct $d[\log(J_c(t))]/d[\log(t)]$ in Fig.2.14b. Second, unlike material responses during the loading phase, which correlate positively with steric hindrance to chain mobility, the primary factor in the rate of creep compliance (and, by definition, the rate of change of contact area) is the M_w or entanglement distance of the polymers.

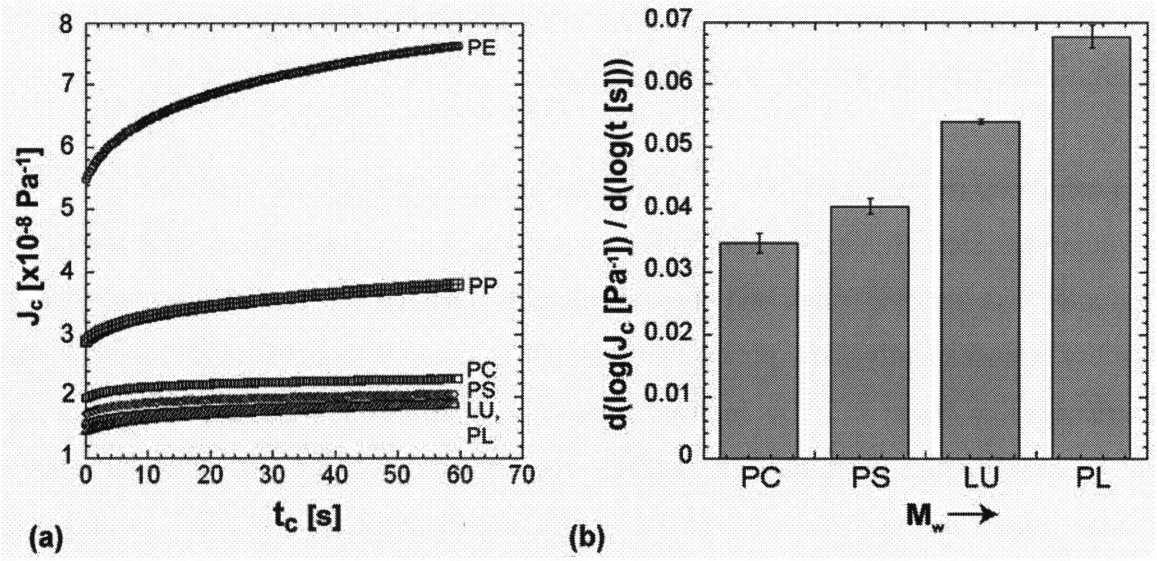

Figure 2.14 a) Contact creep compliance $J_c(t)$ under ramp loading (0.5 mN/s) to 30 mN via Berkovich (sharp) probe for (a) six polymers as a function of t_c. (b) The rate of creep compliance $dJ_c(t))/dt$ increases with molecular weight M_w for the amorphous polymers tested in (a): polycarbonate (PC), polystyrene (PS), Lucite (LU), and Plexiglass (PL). Though monomer structure and physical properties also differ among these polymers, LU and PL differ principally in M_w.

The most striking illustration of this point is the comparison of the two poly(methyl methacrylate) samples, PL and LU. Although PL and LU have the same monomer structure and T_g, the M_w of PL is nearly 2.5 times greater than that of LU. The local steric hindrance of a given polymer segment is equivalent, so these polymers would be expected to deform to approximately the same depth h for a given load P. By extension, the magnitude of $J_c(t = 0)$ would be expected to be quite similar, and this is what is observed experimentally (Fig. 2.14a). However, these polymers of differing M_w show

dramatic differences in the creep compliance rate, with the PMMA of greater M_w demonstrating the higher rate of contact creep compliance. Another clear example of the apparent effect of M_w on contact creep compliance rate is demonstrated by PC: The fourth stiffest polymer tested, PC exhibits the lowest creep compliance rate. We hypothesize that this is due to the low M_w of PC, which signifies very little structural continuity / connectivity between the deformed and undeformed regions of material. As shown schematically in Fig. 2.15, when contact stress is applied to a material comprising many short macromolecules, such as PC, the deformation is likely to translate entire chains to new locations without requiring storage of large internal strains within molecules that bridge deformed and undeformed regions in the material. In contrast, when contact stress is applied to a material comprising long macromolecules, it is likely that a single polymer chain may reside both in surface regions of high strain (near the indenter) and low or zero strain (far from the indenter). In fact, the contact radii a ranged from 0.8 μm to 4.8 μm for contact creep experiments on the amorphous polymers considered herein, while the contour lengths L of the amorphous polymers of highest and lowest M_w were 0.7 μm (PS) and 7.3 μm (PMMA), respectively. (Contour length L [35] was estimated as the product of the number of segments n and monomer length l, given published radii of gyration for PS[36] and PMMA.[37]) While increased M_w causes a modest increase in stiffness during the loading phase, this structural connectivity between highly strained and unstrained material regions has a more dominant effect during contact creep. Under constant applied load, as during indentation creep, it is hypothesized that a long-chained or high M_w material will decrease the intramolecular tension induced by the applied creep load by either displacing the portion of the molecule under low strain toward the highly strained region of the contact zone or by displacing the highly strained region of the molecule toward the ``anchored" region of low strain. In either scenario, the connectivity decreases the resistance of the material to further indenter penetration and results in a faster rate of change in the creep compliance. In the case of the short-chained polymer, such a driving force to reduce intramolecular strain would be decreased by the lack of long-range molecular continuity / connectivity between the highly strained and unstrained material regions.

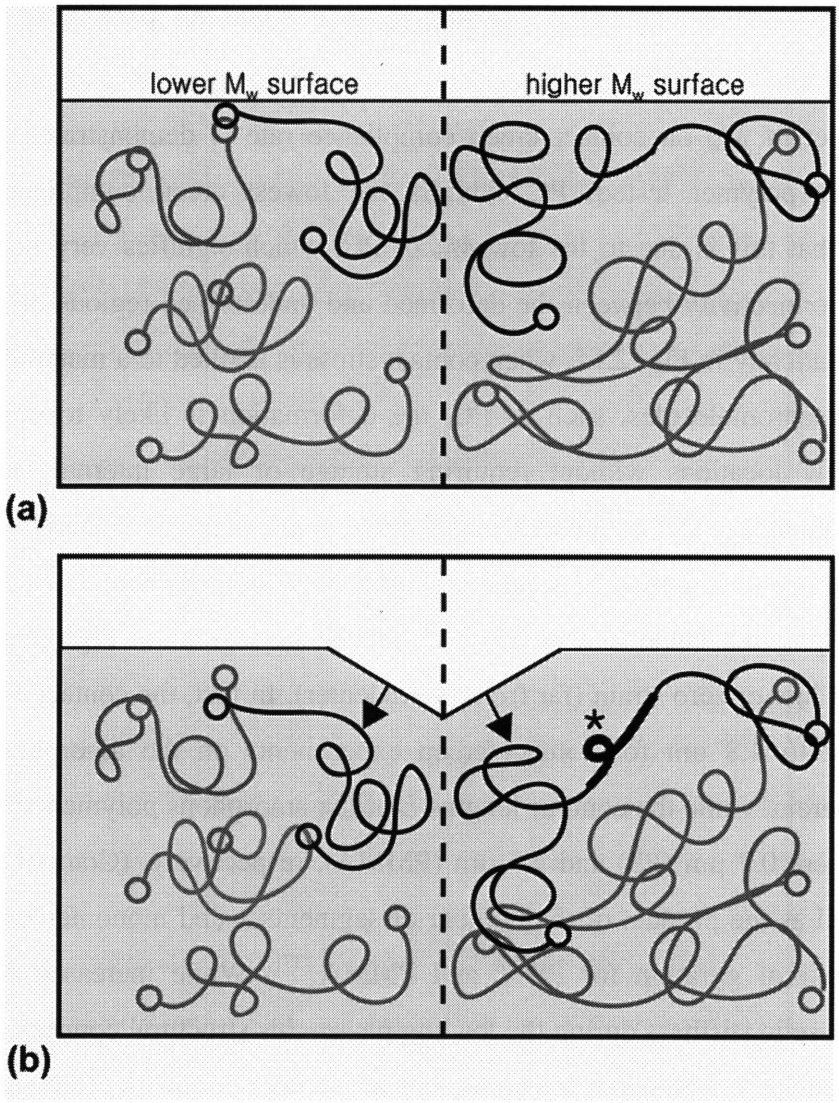

Figure 2.15 Schematic illustrations of high (left) and low (right) molecular weight polymer samples (a) before and (b) after loading via a sharp indenter. Actual contact radii a ranged from 0.8 μm to 4.8 μm, while contour lengths L of the amorphous polymers of highest and lowest M_w were 0.7 μm (PS) and 7.3 μm (PMMA), respectively. The star * in (b) indicates a region of high intramolecular tension, which causes continued molecular displacement to reduce the internal strain.

Although there is no clear dependence of $J_c(t)$ on P_{max} or dP / dt for these polymers evaluated with a sphere of R = 500 μm, there remains a clear effect of polymer structure on $J_c(t)$ within the linear viscoelastic deformation regime. Figure 2.11b compares $J_c(t)$ for epoxies E3 and E8 to P_{max} = 5 mN, 10 mN and 15 mN under ramp loading. Although there is no direct dependence on P_{max} almost all $J_c(t)$ measured for the polymer of greater M_c and thus higher chain mobility (E8) exceeded those of the lower M_c polymer (E3).

This result indicates that the contact creep response of a polymer, measured in the linear viscoelastic regime, will reflect changes in polymer structure while remaining independent of loading conditions.

2.3.5 Conclusions

Contact creep compliance is a useful metric that quantifies a unique mechanical response of time-dependent materials. The analysis of contact creep compliance experiments to quantify the mechanical response of polymers is conceptually straightforward but includes several important experimental and analytical caveats. Herein, we have detailed the evolution and assumptions of the contact creep compliance analysis in the context of linear viscoelastic deformation, and have experimentally determined the conditions under which such analysis may be reasonably applied by identifying contact strains for which $J_c(t)$ is not a function of creep load. In addition, we have considered the extent to which the molecular description of amorphous polymers defines the extent and rate of contact creep compliance.

There are two main conclusions to be drawn from these findings. First, nanoscale contact creep experiments conducted with sharp and / or conical indenter geometries on polymeric surfaces cannot be interpreted accurately through recourse to current linear viscoelastic analyses of contact. However, linear viscoelastic responses may be obtained via a spherical indenter geometry of sufficiently large R to induce maximum strains less than the elastic strain limit. This limitation should be considered for contact creep analysis of thin films, for which finite thickness also requires small indentation depths. (However, we note that analytical separation of nonlinear and plastic deformation from the total creep response would enable application of linear viscoelastic solutions to indentation creep under large strains including via conical indentation.[38]) Second, although monomer steric hindrance correlates strongly with polymer stiffness (and the initial magnitude of the contact creep compliance $J_c(t = 0)$), molecular weight or molecular weight between crosslinks correlates strongly with contact creep compliance rate.

2.4 INDENTATION RECOVERY RATES VIA SCANNING PROBE MICROSCOPY

The following study was published in 2006.[31]

Instrumented indentation-based approaches are frequently implemented to quantify the resistance to permanent deformation of viscoelastic materials via time-independent analyses. Here, we quantify the significant post-indentation recovery of several bulk polymers via time-lapsed scanning probe microscopy under ambient conditions, indicating up to 80% recovery of both indentation depth and volume within 48 h. This viscoelastic response demonstrates that indentation hardness values for these polymers are accurate within 10% for less than 5 min to 3.5 days post-indentation, neglecting any other analytical or experimental errors. Further, although the extent and rates of volumetric recovery depend strongly on loading history and polymer structure / physical properties, deformation resistance inferred from indentation hardness does not quantitatively or qualitatively predict recoverable work or residual deformation of polymer surfaces.

2.4.1 Introduction

As motivated in Sections 2.2.1 and 2.3.1, the interpretation of polymer nanoindentation is often based on a framework developed for time-independent materials. That is, load-displacement data are analyzed following closed-form, semi-empirical equations based in contact mechanics for linear elastic, von Mises yielding materials such as metals.[10,39,40] This compromise is accepted for convenient metrics such as indentation hardness H_i without a quantitative understanding of post-indentation polymer recovery rates at room temperature, which would appraise the applicability of H_i:

$$H_i = \frac{P_{max}}{A_c(h_c)} \tag{2.11}$$

where P_{max} is the maximum load applied during indentation and $A_c(h_c)$ is the calculated contact area at that load.[3] Indentation hardness is therefore dependent on the contact depth, h_c, which is a function of the maximum depth at complete unloading of the surface, h_o. [3]

Recovery of polymer surfaces has been the focus of several previous studies.[41-47] Lorenzo et al. related the change in uninstrumented Vickers microhardness depth ($h_{max} \geq$ 10 μm) determined through interference microscopy post-indentation to variations in weight-average molecular weight, M_w, and %-crystallinity for bulk polyethylene.[43] The authors observed a negative correlation between extent of indentation depth recovery and both %-crystallinity and yield stress. However, these experiments were limited to discrete depth measurements and could not be extended to measure changes in volumetric recovery. Similarly, Low noted for polyacrylics that the diagonal lengths, D, of a Vickers (square pyramidal) microhardness impression remained approximately fixed when measured via optical microscopy over 48 h post-indentation, despite the observed inward sidewall bowing or "pin cushioning" effect.[42] This temporal consistency in D was used to justify Vicker's microhardness, H_V, as a valid metric for polymer mechanical characterization. Of course, although this does satisfy the procedural aspects of measuring microhardness through optical observation of D post-testing, instrumented indentation hardness H_i computed from the continuously measured load-displacement ($P - h$) response is intended to quantify the average effective stress required to plastically deform the material – a metric with units of stress that is load- and loading time-dependent for polymers.[1] Thus, the constancy of position of indentation apices and diagonals measured between those apices need not be synonymous with resistance to plastic deformation of the entire indentation-deformed polymeric volume.

Chang et al. have considered the finite recovery of microscale contact deformation as a function of elevated temperature in order to determine relaxation or recovery kinetics of amorphous polymers such as polystyrene.[41,45-47] By recording a contact profilometry line scan through the Vickers microindentation depth minima at discrete temperatures up to 55 h post-indentation, the authors concluded that microindentations imposed at room

temperature recovered many times faster than those imposed at elevated temperature during a subsequent annealing phase[47] and, as expected, that indentation depth minima recovery rates changed most rapidly near the glass transition temperature.[41]

In the present work, continuous mapping of the evolving indentation topography at room temperature provides fuller understanding of confined polymer recovery, enabling a definitive evaluation of indentation hardness characterization of polymers and a quantitative determination of viscoelastic recovery at deformed surfaces.

2.4.2 Experimental

2.4.2.1 Materials

The volumetric recovery of three bulk, engineering polymers post-indentation was considered: polyethylene (PE), polycarbonate (PC) and polystyrene (PS). The glass transition temperatures, T_g, the weight-average molecular weights, M_w, and the polydispersity indices (PDI) were as follows for the three polymers: PE (T_g = -30°C, M_w = 85,195 g/mol, PDI = 3.10), PC (T_g = 145°C, M_w = 18,000 g/mol, PDI = 1.57), and PS (T_g = 103°C, M_w = 248,670 g/mol, PDI = 3.14). Indentation experiments were conducted at ambient temperature T_a = 22°C, pressure, and humidity RH < 50%. Note that $T_a > T_g$ of PE with a melting temperature T_m of ~125°C (68% crystalline, as quantified by wide-angle X-ray diffraction; data not shown), but that $T_a < T_g$ for PS and PC (fully amorphous). These samples were obtained from DuPont as smooth discs (4-5 nm root mean square surface roughness, as measured via scanning probe microscopy; MFP3D, Asylum Research, Santa Barbara, CA) processed via injection molding into a polished aluminum mold. The T_g was measured via differential scanning calorimetry[35] as reported by the manufacturer and confirmed in the present study, and M_w was determined by the manufacturer via gel permeation chromatography.

These polymers provide a wide range of mechanical response: The varied monomer composition among the three polymers results in persistence lengths, L_p, the length scale over which a polymer chain is effectively rigid,[48] that vary by a factor of six ($L_{p,\,PC}$ = 3 nm,[49] $L_{p,\,PS}$ = 0.9 nm,[48] and $L_{p,\,PE}$ = 0.5 nm[50]). All of these polymer chains are

relatively flexible, as can be characterized by $\chi << 1$, where χ is L_p normalized by polymer chain contour length L_c. However, the values of χ for these polymers varied by orders of magnitude (3.64×10^{-2} (PC), 1.25×10^{-3} (PS), and 1.25×10^{-4} (PE).[36,51,52] Thus, PE is expected to exhibit greater intermolecular motion, despite being semi-crystalline, due to a very simple monomer structure, while PS and PC molecular motion is restricted due to benzene rings present in the monomer side group and backbone, respectively.

2.4.2.2 Indentation, imaging, and image analysis

An instrumented nanoindenter (TriboIndenter, Hysitron Inc., Minneapolis, MN) collinear with a commercial scanning probe microscope or SPM (Quesant Inc., Agoura Hills, CA), pictured in Figure 2.17, was used to indent and acquire the load – depth or $P - h$ response of each sample and then to image the surface topography comprising each indentation at discrete time intervals over 48 h following the indentation experiment. The indenter was a diamond Berkovich (or trigonal pyramid) geometry of included semi-apex angle $\theta \sim 65^\circ$ with nominal apex curvature (tip radius ~ 150 nm as quoted by the manufacturer and estimated via our nanoindentation of quartz). For calculated indentation volumes discussed below, an equivalent cone semi-apex angle of $\theta = 70.3^\circ$ is assumed. To account for measurement drift caused by the piezoelectric actuator in the indenter transducer, each indentation experiment was initiated when this drift was ≤ 0.1 nm/s.

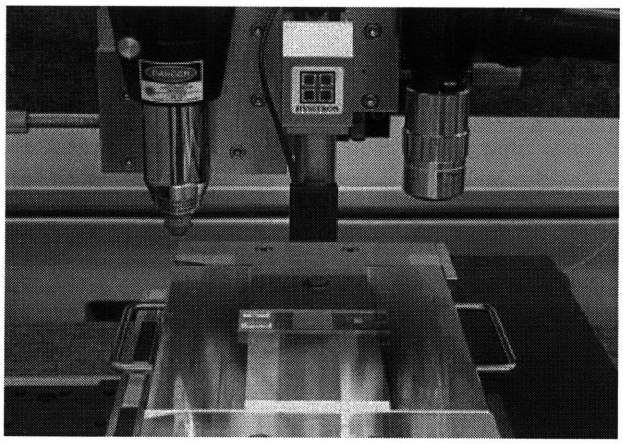

Figure 2.17 Hysitron nanoindenter and Quesant scanning probe microscope (SPM).

Each sample was tested in triplicate under load control to a specific maximum load P_{max} of 7 mN and, in separate experiments, to a specific maximum depth h_{max} of 1200 nm at constant loading and unloading rates of 0.5 mN/s. The latter experiment required material dependent maximum loads (PE: 1.6 mN, PC: 5 mN, PS: 7 mN). The resulting indentations were imaged in intermittent contact mode SPM with a Si cantilevered probe (CSC17; Quesant Inc., Agoura Hills, CA) of radius $r < 25$ nm over 48 h post-indentation t_o at discrete intervals (t_{SPM} = 4 min, 30 min, 1 h, 6 h, 12 h, 24 h, and 48 h). Piezoactuator drift normal to the sample surface that occurred between AFM images did not affect the applied analysis because depth values were calculated relative to a best-fit plane of the undeformed surface surrounding each indentation; this plane was determined individually for each image. Figure 2.18a compares the load-depth responses for PS, PC, and PE tested to the same h_{max}, indicating that PS is more resistant to contact loading than either PE or PC. Figure 2.18b shows the plan-view progression of the indentation surface recovery in PE, as measured via SPM over 48 h post-indentation.

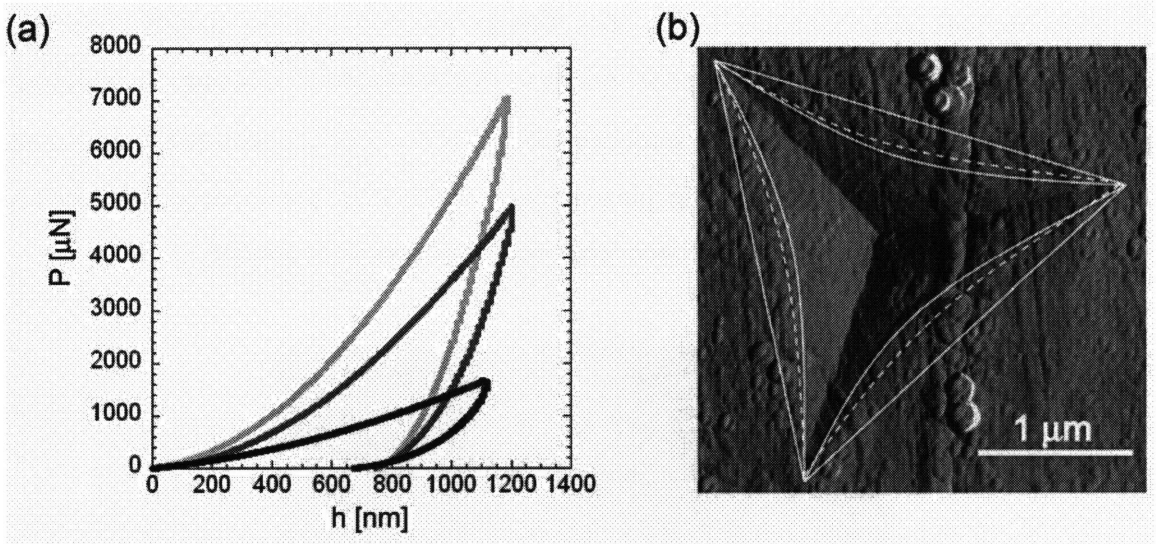

Figure 2.18 (a) Load-displacement curves for indentations in polystyrene (light gray), polycarbonate (dark gray) and polyethylene (black) to approximately the same depth. (b) Tapping mode scanning probe microscopy amplitude image of an indentation in polyethylene to 7 mN at 48 h post-indentation. Sidewall bowing at the surface is delineated at the loss of contact (straight, solid lines), at 4 min (curved, dashed lines), and at 48 h (curved, solid lines) post-indentation.

Three-dimensional graphing and analysis software (DPlot, Vicksburg, MS) was applied to SPM ASCII image data to determine the indentation depth minima (or nadir), $h_n(t)$, and to calculate the indentation volume, $V(t)$. For each image, indentation depth minima were calculated as the difference between the global minimum of all line scans and the averaged, tilt-corrected height of the undeformed surface surrounding the indentation. Indentation volumes were calculated by assigning the best-fit plane of the undeformed surface surrounding the indentation as $h = 0$ and then integrating over the indentation surface for all line scans. Although the first scan was executed immediately after each indentation (t_{SPM} = 4 min for each indentation), subsequent scans were acquired sequentially for indentations conducted in triplicate. Thus, temporal correspondence of acquisition times post-indentation differed by as much as 12 min for $t_{SPM} > 4$ min within an experimental condition, and reporting of averaged t_{SPM} and averaged calculated values would be misleading. Each recovery response $h(t)$ was fit separately to the viscoelastic model discussed below, and the standard deviation of h_n, V, and model parameters among triplicate experiments is reported in figures for the values of t_{SPM} stated above.

In subsequent studies to consider recovery over $0 < t < 4$ min and the separate effects of loading time and unloading time on the extent of recovery, a hold segment at (P_h =100 μN, t_h = 60 s) was introduced prior to full unloading to $P = 0$. The indentation depth $h_n(0 < t < 60$ s) was acquired directly from the upward displacement of the indenter. In the first set of these experiments, all three polymers were deformed to h_{max} = 1200 nm at a loading rate of 0.5 mN/s, duplicating the conditions of Fig. 2.18a that preceded sustained SPM imaging. In the second set of these experiments, PE was deformed to h_{max} = 1200 nm (P_{max} = 1.6 mN) at a loading rate of 0.5 mN/s, and the unloading rate was increased in a geometric series as 0.1, 0.5, or 2.5 mN/s. In the third set of these experiments, PE was deformed to P_{max} = 1.6 mN at a loading rate of 0.5 or 2.5 mN/s, and the unloading rate remained fixed at 0.5 mN/s.

2.4.3 Results and discussion

This systematic study of viscoelastoplastic indentation recovery facilitates consideration of two aspects of polymer characterization: prediction of the extent and timescales of

recovery at deformed polymeric surfaces, and applicability of indentation hardness as a gauge of plastic deformation resistance.

2.4.3.1 Viscoelastic recovery progression

The progression of post-indentation recovery is shown in Fig. 2.19, for the case of polyethylene (PE) at P_{max} = 7 mN (h_{max} = 2.64 μm). In a typical indentation hysteresis, full recovery of the surface is assumed at (P, h) = (0, h_o). However, upon unloading to a small positive load (h_o + 100 μN) as shown in Fig. 2.19a, significant viscoelastic recovery of the indentation depth is measured via upward displacement of the nominally loaded surface over ~1 min post-indentation. In fact, consistent with linear viscoelastic models of recovery, the greatest recovery of indentation depth (~50% for PE) occurs in this interval. Subsequent SPM imaging of the indentation for t > 4 min (the time required for stage translation and initiation of SPM data acquisition) is shown in Fig. 2.19b. This lagging recovery represents an additional ~25 % decrease of the indentation depth between 4 min and 48 h post-indentation and, considered in conjunction with the indentation P-h response, is consistent with an instantaneous change in depth (extrapolation to t = 0) of ~50%. To confirm that this large, rapid change in h_n could not be attributed to calibration inaccuracies either in h_o as reported by the $P - h$ response of the instrumented nanoindenter or in h_n at t = 4 min as reported by the piezo-actuated SPM cantilever, additional experiments were conducted. First, we tested these three polymers under the same conditions with a different instrumented indenter for which indenter displacement can be independently calibrated as a function of displacement sensor voltage (NanoTest600, Micro Materials, Wrexham, UK) and found agreement with h_o within <4%. Second, we recalibrated the SPM displacement as a function of photodiode voltage with a 1 μm step standard and found agreement with the previous calibrations within <5%. Third, we considered a potential offset in the reference position of the undeformed surface between the nanoindenter and AFM, due to variation in contact force sensitivities (i.e., the indenter may displace the surface significantly before detecting contact). However, this disparity was much smaller than the magnitude of recoveries measured: the contact load of the indenter was 1 μN, corresponding to ≤3 nm of surface displacement prior to indentation data acquisition in these polymers. The plane fit to the

undeformed regions of AFM images minimized the effect of nanoscale surface roughness, but RMS roughness was only 4-5 nm on these polymers. Thus, this significant recovery appears to accurately reflect the immediate post-indentation response of the deformed polymer volumes. Clearly, then, there exists a rapid recovery occurring immediately after loss of indenter contact that is not captured by the standard $P - h$ response.

Cross-sections through the minimum of the indentation volume demonstrated recovery of the indentation depth $h_n(t)$, as well as bowing of the indentation sidewalls (Fig. 2.16b). For times $t \geq 4$ min post-indentation, only limited additional bowing of the sidewalls over 48 h was observed. Therefore, although the sidewall bowing predominantly transpired immediately following loss of indenter-material contact, the indentation depth recovered over at least 48 h.

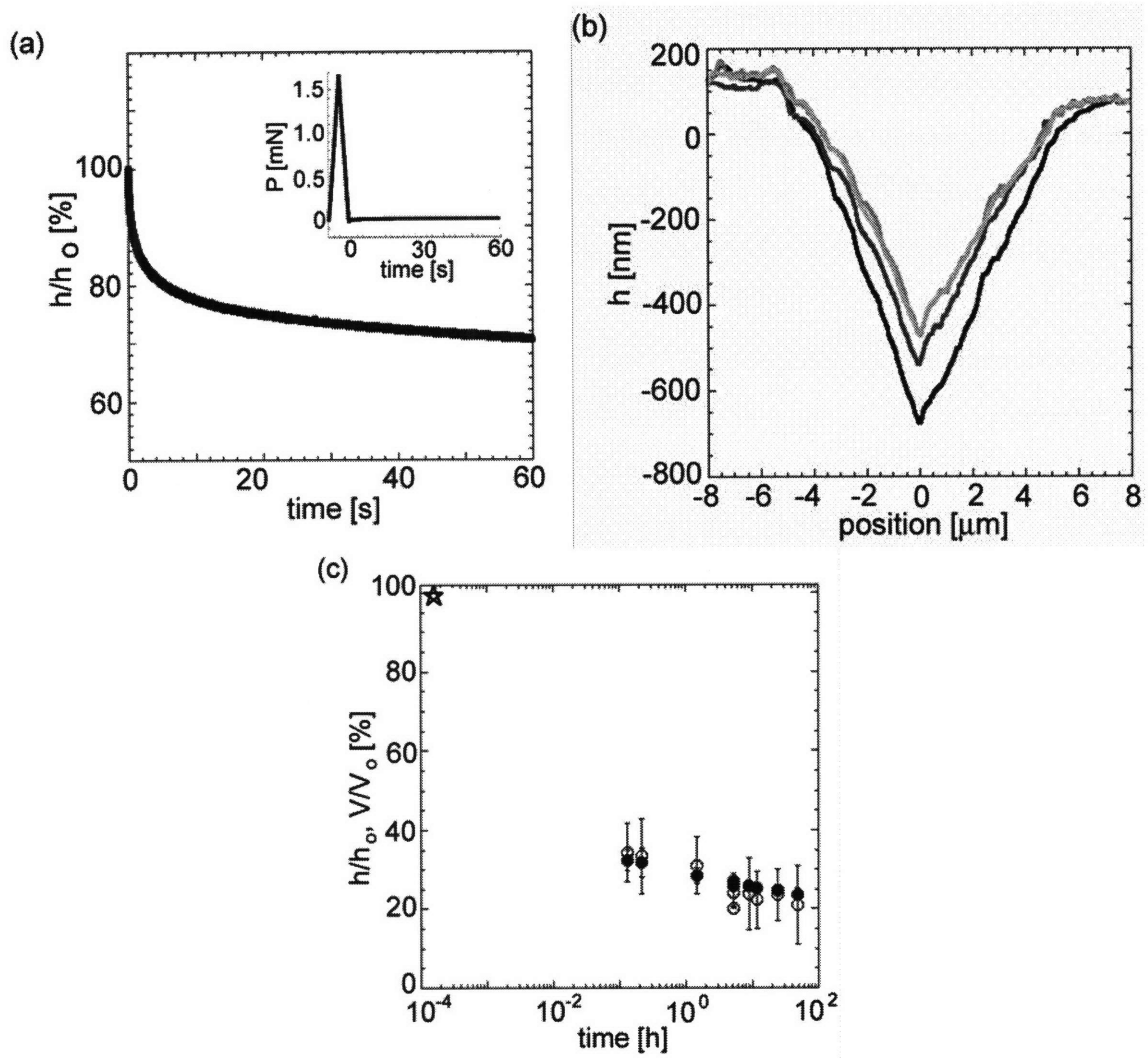

Figure 2.19 Polymer surface recovery is detected immediately upon unloading via a low-load holding phase (loading profile pictured in inset of plot (a)). (a) Normalized depth h / h_o recovery of polyethylene (PE) during hold segment after loading to 1.6 mN. (b) Scanning probe microscopy line traces through the minimum of an indentation to 7 mN in PE at 4 min (black), 136 min (dark gray), 24 h (light gray), and 48 h (lightest gray). (c) Normalized depth h / h_o and volume V / V_o as a function of $t > t_o$ for PE loaded to 1.6 mN. Note: star represents h_o / h_o and V_o / V_o, which are measured and calculated via Eq. 4, respectively, from the last point of indentation unloading. Error bars represent standard deviation among triplicate experiments.

The indentation topology afforded by SPM imaging also illustrates the evolution of volumetric recovery. The normalized recovery of indentation depth h_n / h_o and of indentation volume V / V_o is shown in Fig. 2.19c. Here, instantaneous depth $h_n(t)$ and volume $V(t)$ were acquired via SPM, while h_o was acquired directly from the indentation

$P - h$ response. If the indentation recovered as a self-similar volume of a cone, the corresponding volume V_o could be inferred from idealized conical indenter geometry:

$$V_{o,Berkovich} = 8.2h_o^3 \tag{2.12}$$

However, as Fig. 2.19b illustrates, the apices remain fixed at least for 4 min < t < 48 h, and thus the volume corresponding to h_o may be expected to recover approximately as

$$V_{o,Berkovich} = 8.2h_{max}^2 h_o \tag{2.13}$$

The measured $h_n(t = 0) / h_o$ and calculated $V(t = 0) / V_o$ are unity at time $t = 0$ post-indentation. Although the instantaneous volume, V_o, cannot be measured experimentally, $V(t > 4$ min) calculated directly from the indentation SPM images confirms this proportional decrease in V_o and h_o, indicating that the indentation recovers not as a self-similar volume (see Eq. 2.12), but as a cone with constant base area and decreasing height (Eq. 2.13). This finding is in agreement with results such as Fig. 2.18b, which indicate that the volumetric recovery due to sidewall bowing or apical contraction is negligible during the period captured via SPM. Therefore, from Fig. 2.19b, it is apparent that that the indentation depth and volume recover at the same rate, such that:

$$V(t) = \left(\frac{1}{3}\pi R^2\right) h_n(t) \tag{2.14}$$

where R is the base-radius of the trigonal pyramidal indentation volume, at least for $t > 4$ min post-indentation.

2.4.3.2 Comparison among polymers and loading histories

Comparison of the volumetric recovery of these three polymers deformed to the same maximum depth and maximum volume ($P - h$ responses in Fig. 2.18a) is shown in Fig. 2.20a. A clear material dependence of volumetric recovery from the $t = t_o$ conformation,

ranging from 45% (PC) to 80% (PE), is exhibited over 48 h. As shown in Fig. 2.19c for PE, h / h_o recovers in the same manner as V / V_o for these polymers. Although this recovery is represented on a log(t) scale due to the duration and time intervals of these experiments, the relaxation spectra of all three polymers are well-described through nonlinear regression as a decaying exponential of the form

$$\frac{h_n(t)}{h_o} = c_1 + c_2 e^{-t/\tau}, \tag{2.15}$$

where t here is time post-indentation and τ is the effective retardation time. This is consistent with the recovery of a linear viscoelastic material approximated by a Kelvin model in series with a Maxwell model[35] (also termed a Burgers model[53]), where c_1 represents the normalized depth recovery at $t = \infty$ and ($c_1 + c_2$) represents the normalized instantaneous depth recovery at $t = 0$. Experimental depth recovery data for P_{max} = 7 mN are compared point wise to depth recovery predicted by Eq. 2.15 in Fig. 2.20b.

As discussed below and illustrated in Fig. 2.18b, rapid recovery of the indentation sidewalls implies that the instantaneous indentation depth at t = 0 is typically underestimated, while the recovery rate is overestimated, when measured experimentally via a small contact load (100μN) at $h \sim h_o$. Thus, $h_n(t = 0) = h_o$ was obtained via extrapolation of $h_n(t > 4$ min). We found that $\Delta h_n(t = 0)$ predicted by this material model agrees well with that extrapolated from experimentally measured $h_n(t)$ to t = 0, and that $\Delta h_n(t = \infty)$ agrees closely with that experimentally measured for t = 48 h. This indicates that $h_n(t = 48$ h) and $V(t = 48$ h) well describe the shape of the residual indentation upon the maximum extent of viscoelastic recovery anticipated at room temperature. Considering the range of maximum loads and depths investigated at a single loading rate in these 48 h analyses of indentation recovery, for a given polymer there was no statistically significant difference in the instantaneous and residual indentation depths as a function of (P_{max}, h_{max}). As implied by Fig. 20b, PS and PC exhibit characteristic retardation times (τ = 10.94 ± 0.57 min and 5.69 ± 0.63 min, respectively) that are longer than those of PE (τ = 2.04 ± 0.14 min) for P_{max} = 7mN. However, τ increased with

increasing load for amorphous PC and decreased with increasing load for semi-crystalline PE.

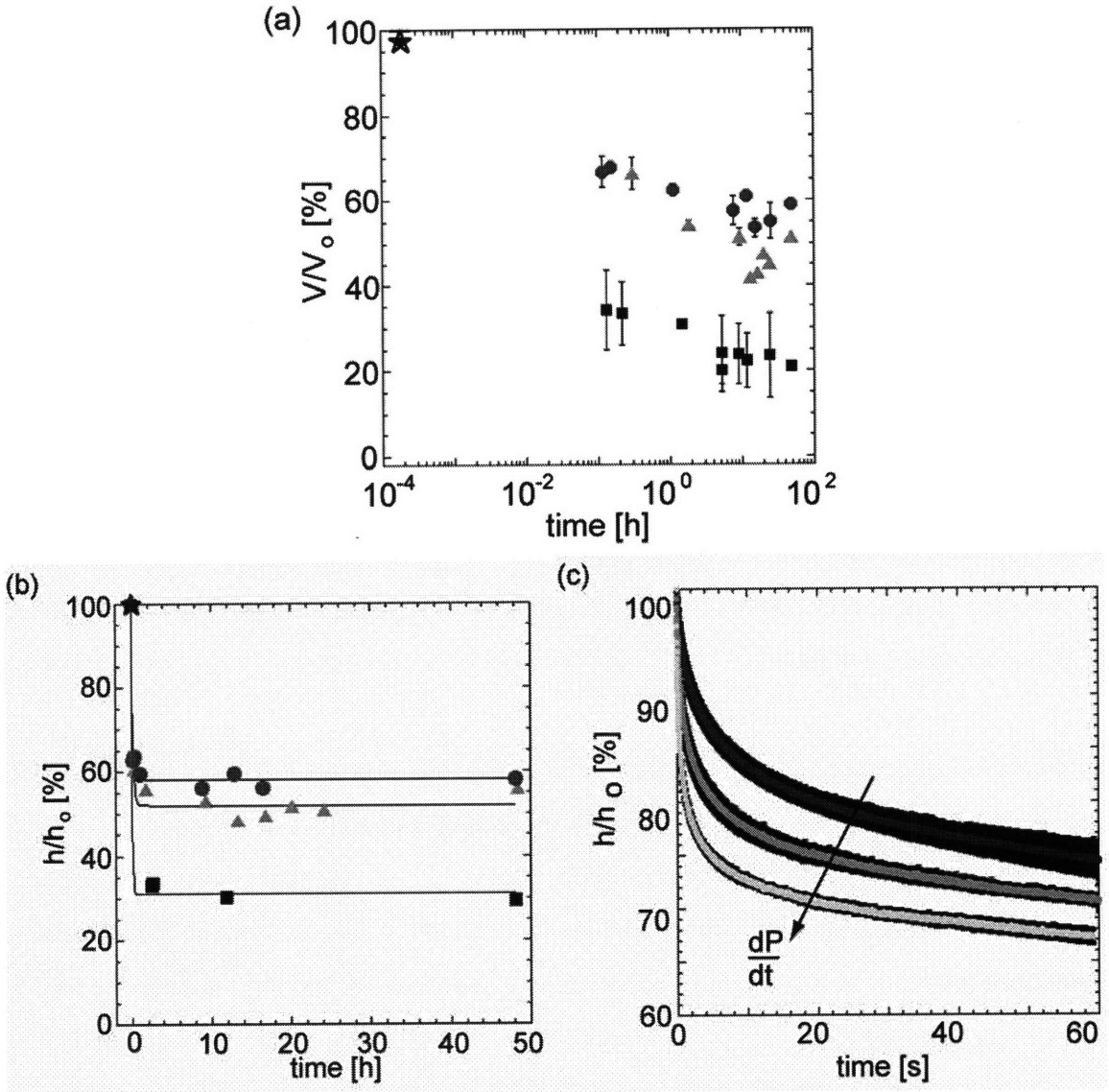

Figure 2.20 (a) Normalized recovered volume V / V_o for indentations to h_{max} = 1200 nm in polyethylene (square), polystyrene (triangle) and polycarbonate (circle). (b) Normalized depth recovery of indentations to P_{max} = 7 mN in polyethylene (square), polystyrene (triangle) and polycarbonate (circle); decaying exponential or Burgers model fit shown as black lines. (c) Normalized depth h / h_o recovery in polyethylene during hold segment for three different unloading rates. The material was loaded to 1.6 mN at 0.5 mN/s and unloaded at 0.1 mN/s (dark gray), 0.5 mN/s (light gray) or 2.5 mN/s (lighter gray). Note: star represents V_o / V_o, where $V(t)$ is calculated via Eq. 4 from the last point of indentation unloading. Error bars represent standard deviation among triplicate experiments.

To further consider the effects of such loading history on the extent and rate of viscoelastic recovery, we measured the upward displacement of the indenter upon unloading to P = 100 μN over 60 s post-indentation. This indenter displacement reflects the limited capacity of this indentation instrument to maintain load control (in open-loop), but is related directly to $h_n(0 < t < 60$ s) and results in a measurable increase in load P due to this material recovery. We found that the rate of instantaneous depth recovery assessed in this manner depended strongly on the magnitude of this dwell load. This rate appeared to be overestimated for small dwell loads due to the rapid recovery of the indentation sidewalls that forced the indenter to lose contact with the indentation depth minimum upon retraction from h_{max}, as well as to inertia of the piezo-actuated indenter during retraction from the surface. The measured extent of recovery was reduced by this counter-loading of the recovering indentation, and thus the progression of $h_n(t < 4$ min) does not coincide quantitatively with $h_n(t > 4$ min). Nevertheless, we note that the ranking of the rapidity and extent of recovery among PS, PC, and PE deformed to the same h_{max} as observed during this dwell segment of recovery is consistent with that measured by SPM for 4 min $< t <$ 48 h.

As would be anticipated for a viscoelastic material under contact loading,[1] we observed that increased unloading time (decreased unloading rate) from a given P_{max} in PE correlated with decreased post-indentation recovery. As shown in Fig. 2.20c, the increased viscous dissipation afforded by greater unloading time resulted in a statistically significant decrease in the extent of instantaneous recovery for a fixed loading rate of 0.5 mN/s. Here, geometric increases in unloading rate (0.1, 0.5 and 2.5 mN/s) correlated with increases in effective τ (0.12, 0.16, and 0.27 min, respectively); as noted above, these τ are exaggerated due to volumetric contraction and expulsion of the indenter during unloading. In contrast, increased loading time to a fixed P_{max} and unloading time in PE resulted in a small but statistically significant increase in instantaneous recovery for loading rates greater than 0.5 mN/s (data not shown). Comparison of $h_n(0 < t < 60$ s) recoveries obtained for identical total times of indentation also indicated that decreases in unloading time more significantly affected this recovery progression than decreases in loading time (data not shown). Thus, the extent and progression of post-indentation

viscoelastic recovery are more pronounced for decreased indentation loading / unloading times. This observation is particularly important with respect to the well-supported convention noted by Cheng and Cheng,[54] as well as others: rapid indentation unloading of a linear viscoelastic material enables reasonable estimation of the instantaneous elastic modulus. However, as a consequence of this rapid unloading, viscoelastic mechanisms and recoverable work that is measurable from the $P - h$ response are significantly suppressed.

2.4.3.3 Implications for indentation hardness of viscoelastic surfaces

These substantial recovery rates demonstrate the fleeting validity of indentation hardness H_i as a metric of plastic deformation resistance for polymers. Clearly, a decrease in h_n over time implies an increase in apparent resistance to permanent deformation. Therefore, if we assume a proportional decrease in contact depth h_c over time, H_i would change by at least 10% within 5 min (PE) to 3.5 days (PC) post-indentation for the range of common engineering polymers considered herein. As illustrated in the previous section, the extent of this error depends directly on loading and unloading times, and increases with loading rate. Thus, if hardness were used even as a quality control metric for which >10% accuracy may be acceptable, note that this error is in addition to that due to measurement precision, systematic analytical errors, and material inhomogeneities. Further, given that this effect is more pronounced for decreasing contact loads for a fixed loading rate, this inaccuracy increases for bulk or thin film polymers indented on the nanoscale – especially if such experiments also include conventional estimation of indentation elastic modulus via rapid unloading.[54] More importantly, H_i so quantified implies a resistance to plastic deformation that does not convey the observed, significant indentation depth recovery up to 80% within 2 days post-indentation. Although H_i should not and does not predict the extent of viscoelastic recovery, these results quantify the extent to which the common application of indentation $P - h$ response (related directly to H_i) fails to predict contact loading resistance afforded by viscoelasticity of polymeric surfaces.

As a result of this truncation of material response, the elastic or recoverable work of indentation W_e, calculable directly from integration of the $P - h$ response,[7] does not

capture the total recoverable energy W_r at $t = \infty$. However, it cannot be assumed that the work recovered per unit material volume is constant during recovery, and therefore it is not straightforward to analytically predict $W_r(t)$ from experimentally determined $h_n(t)$ or $V(t)$.

2.4.4 CONCLUSIONS

In the present work, we have combined instrumented indentation and SPM imaging to formally demonstrate the significance and extent of post-indentation viscoelastic recovery in three common engineering polymers. For the range of indentation loads and rates considered, this recovery results in up to 80% recovery of indentation depth in excess of that measured from the instrumented indentation response. Consideration of a simple, linear viscoelastic model indicates that the extent and retardation time of this recovery vary significantly as a function of the physical / structural properties among these polymers, as well as of the preceding loading histories. Given the increasing application of instrumented indentation to quantify the resistance of (bio)polymeric surfaces to instantaneous loading (e.g., indentation elastic modulus E_i inferred through sufficiently rapid unloading and application of time-independent Oliver-Pharr-type analysis[3,54]) and permanent deformation (e.g., indentation hardness H_i calculated directly from the indentation hysteresis), this time-lapsed imaging of surface recovery illustrates two key points. First, the extent and rates of recovery depend directly on loading time, such that decreased loading time consistent with extraction of E_i from indentation hystereses implies significantly underestimated recoverable work and residual indentation depth. Second, despite the fact that H_i is a target metric for deformation resistance in a wide range of polymer applications including low-k dielectric coatings,[15] comparison among these polymers shows that this parameter is not only (un)loading time-dependent, but also that H_i is not even qualitatively predictive of which polymer is most resistant to permanent deformation. When the mechanical response of interest is best described as (contact) deformation resistance, careful consideration of the loading time with respect to the material retardation time or post-indentation imaging as presented herein is recommended. Although this particular sample set does not elucidate the specific structural determinants of the recovery energetics in confined polymer

volumes, systematic consideration of molecular physical properties on mechanical behavior is explored in Chapter 3.

2.5 CONCLUSIONS

Chapter 2 considered the utility of two established mechanical metrics in terms of experimental parameters and polymer physical / structural properties and presented the specific energy absorption as a model-free metric to characterize viscoelastoplastic materials. Indentation hardness, a metric that does not account for time dependence, is a function of the final depth of deformation at the end of the unloading curve. This depth was found to decrease dramatically over time post-indentation causing the indentation hardness value to only approximate polymer (time-independent) resistance to plastic deformation with ten percent error for minutes or days after the measurement was taken. Contact creep compliance was used to identify the experimental parameters for which common engineering polymers behaved as linear viscoelastic materials. As expected from bulk mechanics, but counter to the assumptions often made within indentation literature, linear viscoelasticity can only be observed for deformation under low strains and never under a sharp probe. Therefore, these classic analyses should be limited to experiments conducted with spherical probes. However, indentations performed with spheres result in a large areas of contact that do not allow for the lateral resolution necessary to mechanically map surfaces with small and complex phase changes such as in nanocomposites. Recent analytical work offers a semi-analytical route to decouple the viscous, elastic and plastic deformations during nonlinear viscoelastoplastic contact and thereby enables such mechanical mapping studies (see Section 5.2.3).

Chapter 3 addresses the challenges related of testing and understanding the nanoscale deformation mechanics of polymer surfaces through experiment and simulation; knowledge that is critical to the future characterization of complex and confined polymeric materials.

REFERENCES

1. Tweedie C.A., Smith, J. F., VanVliet, K. J. Fundamentals of Nanoindentation and Nanotribology III, 2004, pp R5.6.
2. Berry G. In Comprehensive Desk Reference of Polymer Characterization and Analysis; Brady, R. F., Ed.; Oxford University Press: New York, 2003.
3. Oliver W.C., Pharr G.M.; An Improved Technique for Determining Hardness and Elastic-Modulus Using Load and Displacement Sensing Indentation Experiments. *Journal of Materials Research* **1992**; 7, (6), 1564-1583.
4. Briscoe B.J., Sebastian K.S., Adams M.J.; The Effect of Indenter Geometry on the Elastic Response to Indentation. *Journal of Physics D-Applied Physics* **1994**; 27, (6), 1156-1162.
5. Briscoe B.J., Sebastian K.S., Sinha S.K.; Application of the compliance method to microhardness measurements of organic polymers. *Philosophical Magazine a-Physics of Condensed Matter Structure Defects and Mechanical Properties* **1996**; 74, (5), 1159-1169.
6. Briscoe B.J., Fiori L., Pelillo E.; Nano-indentation of polymeric surfaces. *Journal of Physics D-Applied Physics* **1998**; 31, (19), 2395-2405.
7. Dao M., Chollacoop N., Van Vliet K.J., Venkatesh T.A., Suresh S.; Computational modeling of the forward and reverse problems in instrumented sharp indentation. *Acta Materialia* **2001**; 49, (19), 3899-3918.
8. Sneddon I.N.; The relation between load and penetration in the axisymmetric Boussinesq problem for a punch of arbitrary profile. *International Journal of Engineering Science* **1965**; 3, (1), 47.
9. Drechsler D., Karbach A., Fuchs H.; Nanoindentation on polycarbonate polymethyl methacrylate Blends. *Applied Physics a-Materials Science & Processing* **1998**; 66, S825-S829.
10. Klapperich C., Komvopoulos K., Pruitt L.; Nanomechanical properties of polymers determined from nanoindentation experiments. *Journal of Tribology-Transactions of the Asme* **2001**; 123, (3), 624-631.
11. Tweedie C.A., Van Vliet K.J.; Contact creep compliance of viscoelastic materials via nanoindentation. *Journal of Materials Research* **2006**; 21, (6), 1576-1589.
12. Asif S.A.S., Wahl K.J., Colton R.J., Warren O.L.; Quantitative imaging of nanoscale mechanical properties using hybrid nanoindentation and force modulation. *Journal of Applied Physics* **2001**; 90, (3), 1192-1200.
13. Loubet J.L., Oliver W.C., Lucas B.N.; Measurement of the loss tangent of low-density polyethylene with a nanoindentation technique. *Journal of Materials Research* **2000**; 15, (5), 1195-1198.
14. Fischer-Cripps A.C.; A simple phenomenological approach to nanoindentation creep. *Materials Science and Engineering a-Structural Materials Properties Microstructure and Processing* **2004**; 385, (1-2), 74-82.
15. Lu H., Haung G., Wang B., Mamedov A., Gupta S. Fundamentals of Nanoindentation and Nanotribology III, Warrendale, PA, 2005, pp R4.5.
16. Lu H., Wang B., Ma J., Huang G., Viswanathan H.; Measurement of creep compliance of solid polymers by nanoindentation. *Mechanics of Time-Dependent Materials* **2003**; 7, (3-4), 189-207.

17. Ngan A.H.W., Tang B.; Viscoelastic effects during unloading in depth-sensing indentation. *Journal of Materials Research* **2002**; 17, (10), 2604-2610.
18. Oyen M.L.; Spherical indentation creep following ramp loading. *Journal of Materials Research* **2005**; 20, (8), 2094-2100.
19. VanLandingham M.R., Chang N.K., Drzal P.L., White C.C., Chang S.H.; Viscoelastic characterization of polymers using instrumented indentation. I. Quasi-static testing. *Journal of Polymer Science Part B-Polymer Physics* **2005**; 43, (14), 1794-1811.
20. Yang S., Zhang Y.W., Zeng K.Y.; Analysis of nanoindentation creep for polymeric materials. *Journal of Applied Physics* **2004**; 95, (7), 3655-3666.
21. Ting T.C.T.; The contact stresses between a rigid indentor and a viscoelastic half-space. *Journal of Applied Mechanics* **1966**; 88, 845-854.
22. Lee E.H.a.R., J.R.M.; The contact problem for viscoelastic bodies. *Journal of applied mechanics* **1960**; 27, 438-444.
23. Cheng Y.T., Cheng C.M.; Relationships between initial unloading slope, contact depth, and mechanical properties for conical indentation in linear viscoelastic solids. *Journal of Materials Research* **2005**; 20, (4), 1046-1053.
24. Cheng L., Xia X., Scriven L.E., Gerberich W.W.; Spherical-tip indentation of viscoelastic material. *Mechanics of Materials* **2005**; 37, (1), 213-226.
25. VanLandingham M.R., Drzal, P.L., White, C.W. Fundamentals of Nanoindentation and Nanotribology III, Warrendale, PA, 2005, pp R5.5.
26. Cheng Y.-T., Cheng C.-M. Fundamentals of Nanoindentation and Nanotribology III, Warrendale, PA, 2005, pp R5.5.
27. Vandamme M., Ulm F.J.; Viscoelastic solutions for conical indentation. *International Journal of Solids and Structures* **2006**; 43, (10), 3142-3165.
28. Lesser A.J., Calzia K.J.; Molecular parameters governing the yield response of epoxy-based glassy networks. *Journal of Polymer Science Part B-Polymer Physics* **2004**; 42, (11), 2050-2056.
29. Sakai M., Shimizu S.; Indentation rheometry for glass-forming materials. *Journal of Non-Crystalline Solids* **2001**; 282, (2-3), 236-247.
30. Shimizu S., Yanagimoto T., Sakai M.; Pyramidal indentation load-depth curve of viscoelastic materials. *Journal of Materials Research* **1999**; 14, (10), 4075-4086.
31. Tweedie C.A., Van Vliet K.J.; On the indentation recovery and fleeting hardness of polymers. *Journal of Materials Research* **2006**; 21, (12), 3029-3036.
32. Tabor D. The Hardness of Metals: Clarendon, London, UK, 1951.
33. Ferry J.D. Viscoelastic Properties of Polymers; John Wiley & Sons: New York, NY, 1980.
34. Brady R.F. Comprehensive Desk Reference of Polymer Characterization and Analysis; Oxford University Press: Washington, DC, 2003.
35. Young R.J., Lovell P.A. Introduction to Polymers; Chapman & Hall: New York, NY, 1991.
36. Dinelli F., Leggett G.J., Shipway P.H.; Nanowear of polystyrene surfaces: Molecular entanglement and bundle formation. *Nanotech* **2005**; 16, 675.
37. Priestley R.D., Ellison C.J., Broadbelt L.J., Torkelson J.M.; Structural relaxation of polymer glasses at surfaces, interfaces and in between. *Science* **2005**; 309, (5733), 456-459.

38. Oyen M.L., Cook R.F.; Load-displacement behavior during sharp indentation of viscous-elastic-plastic materials. *Journal of Materials Research* **2003**; 18, (1), 139-150.
39. Briscoe B.J., Sebastian K.S.; The elastoplastic response of poly(methyl methacrylate) to indentation. *Proceedings of the Royal Society of London Series a-Mathematical Physical and Engineering Sciences* **1996**; 452, (1946), 439-457.
40. Briscoe B.J., Evans P.D., Biswas S.K., Sinha S.K.; The hardnesses of poly(methylmethacrylate). *Tribology International* **1996**; 29, (2), 93-104.
41. Chang B.T.A., Li J.C.M.; Indentation Recovery of Amorphous Materials. *Scripta Metall. Mater.* **1979**; 13, 51-54.
42. Low I.M.; Effects of load and time on the hardness of a viscoelastic polymer. *Materials Research Bulletin* **1998**; 33, (12), 1753-1758.
43. Lorenzo V., Perena J.M., Fatou J.G., Mendezmorales J.A., Aznarez J.A.; Delayed Elastic Recovery of Hardness Indentations in Polyethylene. *Journal of Materials Science* **1988**; 23, (9), 3168-3172.
44. Lorenzo V., Perena J.M., Fatou J.M.G., Mendezmorales J.A., Aznarez J.A.; Interference Microscopy Measurements of Depth at Vickers Hardness Indentations in Polyethylene. *Journal of Materials Science Letters* **1987**; 6, (7), 756-758.
45. Chang B.T.A., Li J.C.M.; Indentation Recovery of Atactic Polystyrene. *Journal of Materials Science* **1980**; 15, (6), 1364-1370.
46. Kung T.M., Li J.C.M.; Recovery Processes in Amorphous Polymers. *Journal of Materials Science* **1987**; 22, (10), 3620-3630.
47. Yang F.Q., Zhang S.L., Li J.C.M.; Impression recovery of amorphous polymers. *Journal of Electronic Materials* **1997**; 26, (7), 859-862.
48. Brulet A., Boue F., Cotton J.P.; About the experimental determination of the persistence length of wormlike chains of polystyrene. *Journal De Physique Ii* **1996**; 6, (6), 885-891.
49. Bicerano J.; Chain stiffness of liquid crystalline polyesters. 1. Characteristic ratio and persistence length. *Computational and Theoretical Polymer Science* **1998**; 8, (1-2), 9-13.
50. Nikolov S., Doghri I.; A micro/macro constitutive model for the small-deformation behavior of polyethylene. *Polymer* **2000**; 41, (5), 1883-1891.
51. Liu Y.G., Bo S.Q., Zhu Y.J., Zhang W.H.; Studies on the intermolecular structural heterogeneity of a propylene-ethylene random copolymer using preparative temperature rising elution fractionation. *Journal of Applied Polymer Science* **2005**; 97, (1), 232-239.
52. Soles C.L., Douglas J.F., Wu W.L., Dimeo R.M.; Incoherent neutron scattering as a probe of the dynamics in molecularly thin polymer films. *Macromolecules* **2003**; 36, (2), 373-379.
53. Nielson L.E. Mechanical Properties of Polymers and Composites; Marcel Dekker: New York, 1974.
54. Cheng Y.T., Cheng C.M.; Scaling, dimensional analysis, and indentation measurements. *Materials Science & Engineering R-Reports* **2004**; 44, (4-5), 91-149.

CHAPTER 3 CONTACT MECHANICS OF CONFINED POLYMER VOLUMES

3.1 INTRODUCTION

The research studies presented thus far have assumed that polymer properties at the surface are representative of the bulk properties. This holds true except for indentations within 100 nm of the polymer free surface or interface, or for polymeric materials confined at the nm-length scale. This chapter will address the challenges of measuring mechanical properties of small volumes of polymer through contact deformation. The high-mobility (and relatively low-T_g) region of near-surface polymer molecules enables greater orientational flexibility and potential for chemical response. The effect of probe surface chemistry on the mechanical response of the probe-polymer interphase was studied via experiment and simulation through probe surface functionalization.

3.2 ENHANCED STIFFNESS OF AMORPHOUS POLYMER SURFACES UNDER CONFINEMENT OF LOCALIZED CONTACT LOADS

The following study was published in 2007 with coauthors Georgios Constantinides, Karl E. Lehman, Donald J. Brill, Gregory S. Blackman.[1]

Although there is an increasing appreciation that physical properties of amorphous (glassy) polymer surfaces and interfaces can differ substantially from those of the bulk, the mechanisms and implications for mechanical performance of thin films, surfaces of bulk polymers, and nanocomposites are unclear. For example, several natural and synthetic nanocomposites exhibit markedly enhanced stiffness and strength that cannot be explained via two-phase composite rules-of-mixtures. Here we apply recent advances in contact deformation to determine the apparent elastic (or storage) moduli over 5 to 200 nanometers from the free surface of amorphous polystyrene, poly(methyl methacrylate), and polycarbonate. We observe that the apparent stiffness of the surface under contact can exceed that of the bulk by up to 200%, independent of processing scheme, macromolecular structural characteristics, and relative humidity. We attribute this enhanced apparent stiffness at the surface to the contact stress-induced formation of a

mechanically confined phase at the probe-polymer interface. These observations are consistent with the increased macromolecular mobility of glassy polymer free surfaces, and relate directly to the material physics of the interphase in synthetic and biological polymer nanocomposites.

3.2.1 Introduction

Most experimental investigations of amorphous polymer surfaces have focused on thermally activated behavior such as the glass transition temperature T_g[2-4] and structural relaxation.[5,6] However, few overarching conclusions exist regarding surface and interface properties,[7] in large part because experimental and sample preparation capabilities have not yet been optimized for the nanometer-length scales over which these surface-specific phenomena are observed. There are two generally accepted conclusions regarding amorphous polymer surface behavior: that T_g is a function of polymer film thickness t_f for $t_f < 100$ nm, and that the magnitude and direction of the T_g shift depends on the polymer and / or substrate.[8] For example, the T_g of amorphous polystyrene (PS) films has been found to be depressed by 35°C in spin-coated films of $t_f < 20$ nm on Si substrates[2] and by 70°C for free standing films of $t_f < 30$ nm,[3] while amorphous poly(2-vinylpyridine) has demonstrated a 35°C elevation in T_g for $t_f = 10$ nm that is attributed to secondary bonding with the Si substrate.[9]

Here, we sought to consider the consequences of such a physical property variation on the resistance of amorphous polymer surfaces to localized contact deformation. Depression of T_g in polymers such as PS and PMMA suggests that, over distances < 100 nm from the free surface of these so-called glassy polymers, the macromolecular chains are more mobile than those located within the bulk. This conceptualization is consistent with computational simulations of molecular mobility of free surfaces and confined volumes,[10-12] as well as recent experimental observations for PS thin films of $t_f \leq 40$ nm, including broadened structural relaxation times[5] and decreased elastic moduli inferred from film buckling.[13] Such elastic instabilities are important to defining the mechanical behavior of polymer free surfaces; however, the response of mechanically loaded or confined surfaces may differ from that inferred via non-contact experiments, especially

for polymers.[14,15] In fact, several recent contact-based studies of polymer surfaces[16-18] have indicated elastic properties differing from that of the bulk, but both the trends and mechanisms remain unclear. For example, two studies have indicated significant increases in elastic or storage moduli E or E' of copolymer, semicrystalline and amorphous polymer surfaces for indentation depths $h_c < 50$ nm,[16,17,19] but may be attributable at least in part to microstructural inhomogeneities on this length scale or to experimental uncertainties such as incomplete knowledge of the nanoscale probe geometry.[15] In contrast, contact-based rheological studies in other polymers tested[20] or heated[21] above bulk T_g have not identified differences in stress relaxation[20] or JKR adhesion-inferred elastic moduli[21] as a function of distance from the free surface. Here, we propose that the depressed T_g of amorphous polymer surfaces can result in a mechanically distinct region at the probe-polymer interface, resulting in an apparent stiffness that exceeds the elastic response of the bulk polymer.

3.2.2 Experimental

3.2.2.1 Polymer synthesis and characterization

Polymer standards of polystyrene (PS) and poly(methyl methacrylate) (PMMA) were synthesized via anionic polymerization (Polymer Laboratories, Amherst, MA) and processed via three routes by DuPont (Wilmington, DE). Compression molded (CM) samples were heated to ~150°C (above the polymer T_g) and compressed at pressures of 0.3-0.5 ton between polished Al and an extremely smooth disk of float glass to yield samples of 1 mm thickness. Injection molded (IM) samples were extruded above the melting temperature into a mold surface specially polished to reduce surface roughness, while spin coated (SC) samples were spun onto Si wafers at 2000 RPM on a spin coater (PM101D-1790, Headway, Garland, TX) using polymer solutions between 7.47 wt% and 22.4 wt% in 2-ethoxy ethanol for the PMMA, and methyl isobutyl for the PS. Profilometry (P10, KLA-Tencor, San Jose, CA) was used to measure the thickness of the SC PS-12k sample yielding $t_f = 1140 \pm 13$ nm. The SC samples were annealed at T_g + 20°C to control for the effects of residual stress or retained solvent on the surface mechanics. The polycarbonate (PC) sample (Lexan®, DuPont, Wilmington, DE) was injection molded into a smooth Al mold. All polymer sample surfaces were analyzed via

optical profilometry and / or atomic force microscopy (AFM) imaging in tapping mode for surface roughness, and indicated root-mean-square roughness values of $\leq$ 1 nm for compression molded samples for which structural and environmental variables were considered, as well as spin coated samples for which annealing was considered. These polymer surfaces were tested as processed, and any chemical or mechanical treatments post-processing were intentionally avoided. Single crystal, electropolished gold (Accumet Materials Co., Briarcliff Manor, NY) and amorphous borosilicate (glass slide; VWR) served as non-polymeric control materials.

Molecular weight M_w was measured via gel permeation chromatography, while differential scanning calorimetry was used to determine the glass transition temperature T_g of the two PS samples: M_w = 12,450 g/mol; PDI = 1.02; T_g = 96.9°C (or PS-12k) and M_w = 194,000 g/mol; PDI = 1.06; T_g = 106.9°C (or PS-194k), the PMMA sample: M_w = 14,920 g/mol; PDI = 1.04; T_g = 123.9°C (or PM-15k) and the PC sample: M_w = 18, 715 g/mol; PDI = 1.59; T_g = 145 °C (or PC-18k). In addition, the elastic modulus under compression was measured via a uniaxial load frame (Instron Inc., Canton, MA) for the compression molded PS-12k sample (E_c = 2.5 ± 0.4 GPa; n = 3), although elastic moduli extracted from μm-scale contact depths via (multiaxial) indentation loading of compression molded PS are typically closer to 4 GPa.[22]

3.2.2.2 Nanoindentation experiments and analysis

Sample surfaces were probed using an instrumented nanoindentation apparatus (TriboIndenter, Hysitron, Minneapolis, MN) in open-loop feedback mode to five maximum loads corresponding to an indentation contact depth range of approximately 5 nm to 200 nm for both indenter probe radii. This is a rigid load frame, quite distinct in operating principles from the cantilevered loading scheme of an atomic force microscope. Indenters were diamond cones of 60° included angle, terminating in spheres of effective radii R_{eff} = 487 nm and 8724 nm, respectively. The loading profile (2 s loading, 0.5 s unloading) was optimized on the material exhibiting the most creep, PS-12k, according to current nanoindentation analysis theory for viscoelastic materials[23] for the extraction of elastic properties via the Oliver and Pharr method.[24] As discussed in Chapter 2,

polymers are primarily time-dependent materials, however there are applications for which the instantaneous, elastic response is the mechanical metric of interest and the Oliver and Pharr method can be used to extract accurate elastic responses for carefully chosen experimental parameters. All tests were conducted at ambient humidity and at 22°C, unless otherwise noted. The load used to define surface contact in open-loop mode was 0.3 μN; however, control experiments were performed using closed-loop mode and indicated that this variation in the initial point detection method does not change the stiffness trend observed for polymer surfaces (data not shown). Humidity controlled experiments were performed on the PS-12k after 4 h of equilibration at each of three conditions: at 42% RH (both before and after the sample was dried in the oven at 105°C for 2 h) and at 10% RH (immediately after oven drying).

Nanoscale mechanical characterization of polymer surfaces includes several experimental factors that can introduce significant error in the estimation of elastic properties.[15] At the outset of this study, these potential artefacts were addressed as follows: root-mean-square surface roughness of CM samples was ≤ 1 nm as prepared; the indentation contact area A_c as a function of contact depth h_c was constructed directly from AFM imaging of the diamond indenter probes, rather than from assumption of ideal spherical geometry corresponding to an effective radius R_{eff}; the loading rate was optimized for the extraction of the reduced elastic modulus E_r;[23] and a sensitivity analysis was conducted to ensure that the observed trends were not affected by the finite contact load preceding acquisition of the load-displacement ($P - h$) response. Finally, results were quantitatively confirmed by identical experiments on a different instrument (NanoTest600, Micro Materials LLC, Wrexham, UK) for PM-15k with a probe of radius R_{eff} = 3.3 μm.

The apparent elastic modulus E_a is determined via the reduced elastic modulus E_r which is a function of a geometrical constant related to the apex angle of the indenter and the indented material Poisson's ratio β, the unloading slope dP / dh at maximum applied load P_{max}, and the maximum projected indentation contact area $A_{max} = A_c$.[24,25]

$$E_r = \beta \frac{dP/dh\big|_{P_{max}}}{(A_{max})^{1/2}} = \left[\frac{1-\upsilon_i^{\,2}}{E_i} + \frac{1-\upsilon_s^{\,2}}{E_s}\right]^{-1} \qquad (3.1)$$

where the subscripts i and s denote properties of the indenter and the surface of interest, respectively, and ν is the Poisson's ratio. Note that E_s is a weak function of the assumed Poisson's ratio of the polymer surface, and that variation of ν_s from 0.1 to 0.4 incurs a change in E_s of less than 10%.[26] Determination of the storage elastic modulus of PS via indenter enabled nanoscale dynamic mechanical analysis (nano-DMA[27,28]) with the probe of radius R_{eff} = 487 nm also indicated quantitatively comparable stiffening over this same range of h_c (Fig. 2d); for any given h_c, the resulting surface areas of contact was greater for the larger probe.

Two conospherical diamond probes with effective radii R_{eff} of 487 nm and 8724 nm were used for nanoindentation. To approximate indenter size, estimates of the effective radii of the two probes were determined by minimizing the error between the area function as predicted by spherical geometry ($A^{sp} = -\pi h_c^2 + 2\pi R_{eff} h_c$) and the numerically computed area. However, for analysis of $P - h$ responses to extract apparent stiffness E_a via Eq. 3.1, the area function $A_c(h_c)$ was obtained through analysis of AFM image ASCII coordinates (x, y, z) for 1 x 1 μm^2 and 5 x 5 μm^2 scan sizes. Probes were cleaned with acetone and a lint-free swab before experiments to remove in / organic debris; this was verified through phase images of the probe surface. The contact area as a function of contact depth $A_c(h_c)$ was determined directly via Matlab® analysis of AFM tip surface images as motivated and detailed by VanLandingham et al.[29] Note that determination of E_a from $A_c(h_c)$ is accurate for any body of revolution, even if spherical symmetry is not maintained. The contact surface area of the probes as a function of contact depth was also evaluated via Matlab® analysis of AFM tip images by interpolating bilinearly among data points and integrating numerically.

3.2.3 Results and discussion

In this study, we measured the apparent stiffness of several amorphous polymer surfaces at room temperature, in response to five maximum indentation loads imposed through two well-characterized conospherical diamond probes of approximate radii R = 500 nm and 9 μm (Fig. 3.1a). These maximum loads corresponded to indentation contact depths

h_c ranging 5 nm to > 100 nm from the free surface (Fig. 3.1b). To infer the elastic response of the polymer from this contact loading as an apparent elastic modulus or stiffness E_a, we designed these experiments to minimize viscous contributions[23] and account for geometric nonideality of the spherical probes;[29] consideration of these and other potential artefacts in nanoscale contact mechanics are discussed in Methods. We intentionally chose to consider an ensemble of well-controlled, amorphous polymers including PS and PMMA, as the physical and mechanical properties (of the bulk and of thin films) have been determined by us and others using several complementary approaches.[3-5,8,13,14,18,30-34] As described below, in all of these polymers that were considered over a range of processing, loading, and environmental conditions, we consistently observed an increase in apparent stiffness E_a of up to 200% measured close to the surface, relative to that 100s of nanometers from the surface; Fig. 3.1c illustrates this trend for compression-molded PS. At depths > 50 nm, E_a tended toward the elastic moduli of the bulk polymer as measured by indentation[22] or by uniaxial compression; see Methods. We assert that this enhanced apparent stiffness near the surface is the result of an interface formed at the contact surface confined between the polymer and the diamond probe – a region of unique structural and / or physical properties termed the interphase.[35,36] As this phenomenon would have significant implications regarding enhanced mechanical stiffness of nanocomposites and other material systems that are confined or mechanically loaded at the nanoscale, we explored this apparent stiffness as a function of processing and thermal history, polymer structure (molecular weight, monomer structure, and persistence length), relative humidity, and experimental parameters such as probe radius.

To consider whether this surface stiffening was a function of structural attributes of these amorphous homopolymers, we first varied the molecular weight of PS by over an order of magnitude. Nanoindentation of two compression-molded PS samples of molecular weight M_w = 12.45 kg/mol (PS-12k), near the entanglement molecular weight of ~13 kg/mol[13] for PS, and M_w = 194 kg/mol (PS-194k) quantitatively demonstrated the same stiffening at ~5 nm from the free surface (Fig. 3.2a), indicating that this stiffening mechanism is independent of M_w, macromolecule radius of gyration, or chain-end density

at the surface, at least over this range of M_w. In addition, we considered bulk amorphous polymers with significantly different persistence lengths to further probe the effects of monomer structure on this apparent stiffening. Persistence length b, the length scale over which a polymer chain is effectively rigid,[37] was compared for three amorphous polymers: polycarbonate (PC-18k; b_{PC} = 3 nm[38]), PMMA (PM-15k; b_{PM} = 1.3 nm[39]), and PS-12k (b_{PS} = 0.9 nm[37]), over the same range of contact depths, 5 nm < h_c < 200 nm. Although E_a was greatest at the surface for all three polymers, the extent to which the PM-15k surface stiffened was significantly less than that of PS-12k or PC-18k,[59] despite the fact that the persistence length of PMMA is bounded by that of PS and PC. As discussed below, this is consistent with the observation that the depression of T_g observed for PMMA is not as pronounced as in PS of the same molecular weight ranges[40]. Note that the apparent stiffness in Fig. 2a is normalized for all polymers only for visual clarity, and that E_a at h_c > 100 nm was consistent with that of macroscopic volumes for all polymers.[59] Thus, we concluded that molecular weight and persistence length do not strongly contribute to this apparent stiffening of the contact loaded surface.

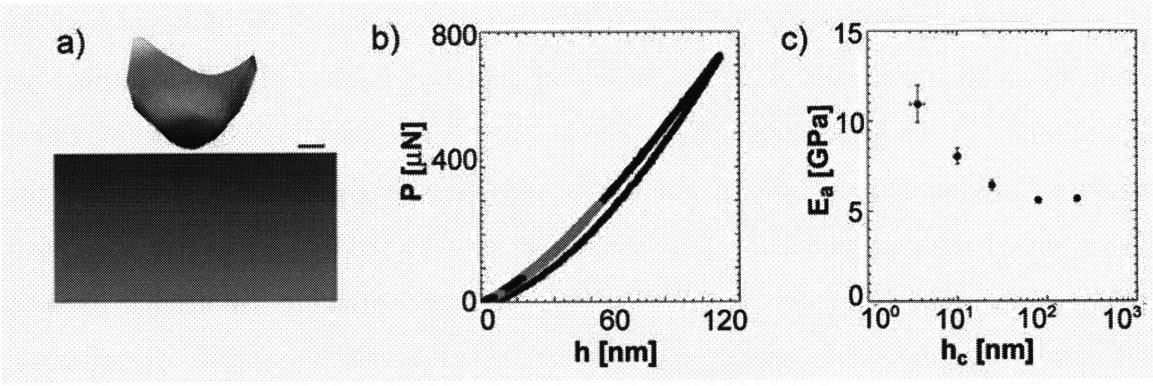

Figure 3.1 Stiffening of polymer surfaces under contact. a) Schematic of a nanoindentation probe (image reconstructed from atomic force microscopy, scale bar = 500 nm) approaching an amorphous polymer surface with higher molecular mobility over the first ~40 nm from the surface. b) Representative indentation load-displacement curves to five maximum loads P corresponding to a range of indentation depths h are displayed alternately in black and grey. c) The indentation elastic modulus E increases with decreasing indentation depth h_c in compression molded polystyrene, molecular weight M_w = 12 kg/mol. Error bars represent one standard deviation and may be smaller than the symbol.

To consider whether this apparent stiffness could be attributed to processing-dependent changes in structural, physical, and mechanical properties at the surface,[41] we employed four different processing and thermal history routes (compression molding (CM), injection molding (IM), spin coating (SC) and annealing after spin coating (SC-A)) for PS and PMMA. These routes were modified to minimize surface roughness to < 1 nm, as confirmed by atomic force microscopy. As shown in Fig. 3.2b for the case of PS-12k, all processing routes resulted in identical increases in E_a at the surface over $5 \leq h_c \leq 200$ nm. For contact depths greater than 20 nm, spin-coated films of ~1 μm thickness appeared stiffer than the compression- or injection-molded samples of mm-scale thickness. We confirmed through finite-element simulation of this experimental system[58] that this transition is expected at such depths due to the mechanical contribution of the underlying, stiff Si substrate. As thin films formed from a solvent and bulk discs formed from a confined melt exhibited the same apparent stiffness at the surface, we concluded that this effect cannot be attributed to processing-induced artefacts at the surface.

To consider whether ambient environmental effects such as relative humidity could induce such a significant mechanical changes at the polymer surface under contact, we evaluated the CM PS-12k surface as a function of % relative humidity (RH). As shown in Fig. 3.2c, this polymer demonstrated no statistical variation in E_a among experiments conducted at 42% RH (before and after drying the polymer for 2 h in a 105°C oven to exceed the boiling point of water) and those conducted within a 10% RH chamber (after drying the polymer). Although it would not be expected that a hydrophobic, amorphous polymer such as PS would be particularly susceptible to the presence of water at the surface, this experiment confirms this intuition over nanoscale distances from the PS free surface, where water meniscus formation[42] or physical adhesion to the probe[1] may be plausible.

---

[1] Data such as in Fig. 1b also demonstrate a lack of significant probe-surface adhesion force (< 0.3 μN for h_c < 50 nm). Further, for our probe radii R and apparent elastic moduli E, and the well-documented surface energy of these polymers γ, the Tabor parameter of adhesion $\mu(R, E, \gamma) < 2$ in all cases: neither JKR nor DMT theories of contact adhesion apply.[61] Even in the case of strong JKR-type contact adhesion for elastomers such as poly(dimethoxysilane) or PDMS, it can be inferred from recent reports that elastic moduli extracted from indentation experiments on materials that exhibit measurable probe-surface adhesion forces (E_{PDMS} < 2.9 MPa)[62] do not necessarily or significantly exceed that of uniaxial measurements on bulk forms of those same polymers ($E_{PDMS} = 3.5 \pm 0.2$ MPa)[63]

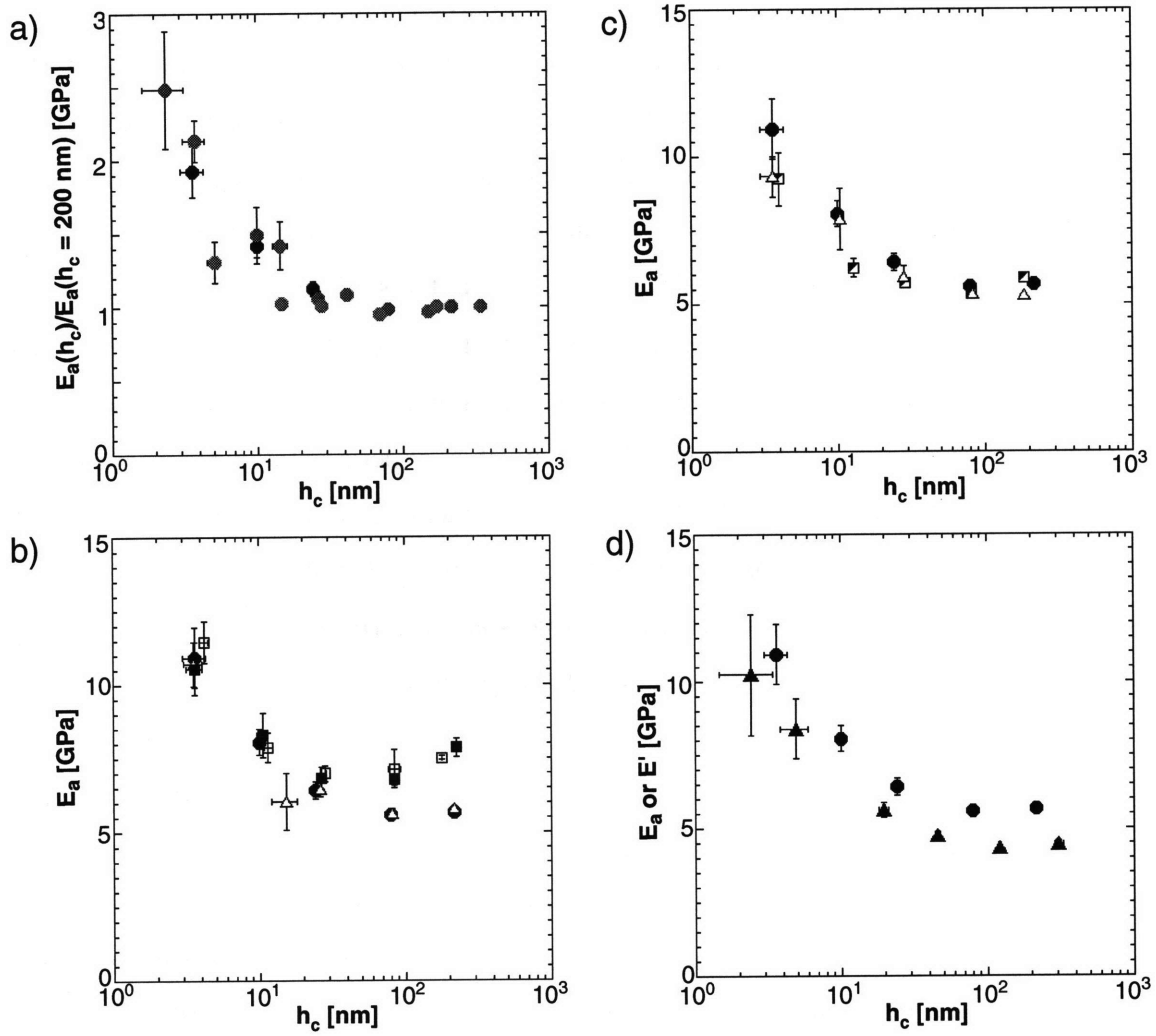

Figure 3.2 Dependence of apparent stiffness under contact loading on polymer processing, structure, and physical environment. a) Compression molded polystyrene (PS) samples with M_w = 12 kg/mol (●) and M_w = 197 kg/mol (●) as well polycarbonate, PC with M_w = 18 kg/mol (●) exhibit statistically equivalent stiffening trends toward the surface, while poly(methyl methacrylate), PMMA with M_w = 15 kg/mol stiffened at the surface to a lesser extent (●). Data are normalized for each material with respect to E_a measured at h_c ~ 200 nm for clarity, as the plateau stiffness of PMMA overlaps with the decreasing stiffness trends of PS and PC. b) Apparent stiffness E_a increases with decreasing contact depth h_c in PS (molecular weight M_w = 12 kg/mol) for compression molded (●), injection molded (Δ), spin coated (□), and annealed / spin coated (■) PS. Both spin coated samples appear stiffer for $h_c \geq 20$ nm than for other processing routes because of the Si substrate contribution to the mechanical response. c) There is no effect of relative humidity (% RH) on the extent of stiffening at the surface of compression molded PS: 42% RH before oven drying (●), 10% RH after oven drying (Δ), 42% RH after oven drying (half-filled square). d) Quasistatic nanoindentation (●) and nanoscale dynamic mechanical analysis at an oscillation frequency of 90 Hz (▲) of polystyrene (PS-12k) both demonstrate significant

stiffening of the amorphous polymer surface for contact deformation experiments. Error bars represent one standard deviation and may be smaller than the symbol.

To consider whether this apparent stiffness under monotonic loading was representative of the storage component of a viscoelastic response, we employed nanoscale dynamic mechanical analysis (nano-DMA[27,28]) for the same probes and range of contact depths. As shown in Fig. 3.2d for the case of PS-12k, we observed quantitatively comparable increases in the apparent storage modulus obtained under oscillatory loading E' and apparent stiffness obtained under monotonic loading E_a. Importantly, DMA includes the viscous response of the polymer that is intentionally minimized in our evaluation of E_a. Nevertheless, over the range of accessible oscillation frequencies ranging from 10 to 250 Hz, E' at $h_c < 50$ nm from surface significantly exceeded that at $h_c > 100$ nm. Finally, none of the inorganic crystalline and amorphous materials (e.g., single crystal gold and borosilicate glass, Fig. 3.3) that were characterized over the same contact depths and range of experimental conditions exhibited an increase in elastic moduli near the free surface.

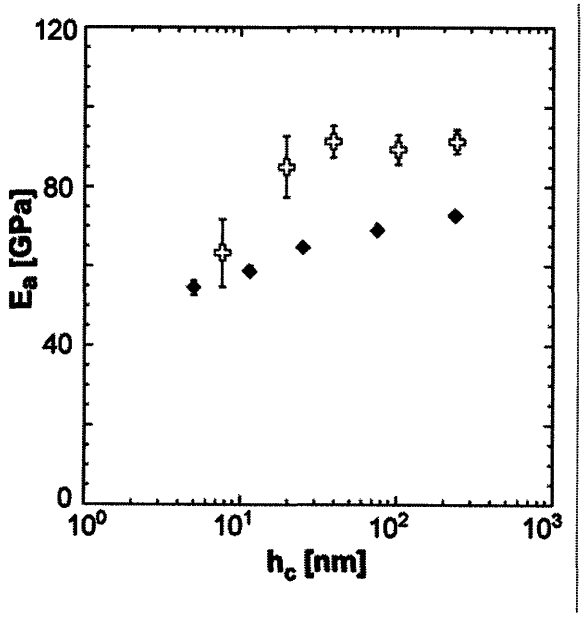

Figure 3.3 Lack of surface stiffening for non-polymeric materials. No increase in elastic modulus E is observed in soft, single crystal gold (open cross) or hard, borosilicate glass (closed diamond) over contact depths ranging 5 nm to 200 nm from the free surface. Note: the decrease in E of the gold surface for the indentation of contact depth ~ 5 nm is likely due to the presence of a well-documented thin organic layer (~ 1 nm) that adsorbs to gold surfaces under ambient conditions.[53]

Observations of enhanced mechanical stiffness of these amorphous polymers over contact depths h_c < 50 nm may appear counter to that expected from a surface of increased molecular mobility. We posited that the marked stiffening of these polymer surfaces could be due to either a thin, mechanically stiff layer spanning the entire polymer surface, or to the formation of a mechanically distinct interfacial region induced under the confined contact loading. Both scenarios can be considered via comparison of the mechanical responses obtained in compression-molded PS-12k for probes of radii differing by over an order of magnitude (R_{eff} = 487 nm and 8724 nm) over the same range of contact depths (5 nm < h_c < 200 nm). For a given contact depth, the larger probe will deform a larger volume of material that can be defined by the radius of contact at the surface a and the surface area of contact between the probe and the polymer SA_c. If a stiff surface layer exists, analytical models of bilayers under contact predict that the elastic response of this composite will be an analytical function of a, but will be independent of probe radius R. However, as shown in Fig. 3.4a, this is counter to what we observed: the apparent stiffness observed for two probe radii does not result in consistent predictions of the stiff-layer modulus E_1 or of the effective layer thickness t.[60] In contrast, the apparent stiffness observed with each probe scales with the contact surface area SA_c, as determined numerically from three-dimensional atomic force microscopy images of the actual probes to the measured contact depth h_c (Fig. 3.4b). This scaling strongly suggests the formation of a mechanically unique interphase induced at the region of the amorphous polymer surface in contact with the mechanical probe.[2]

A range of recent experiments in PS supports this interpretation of a mechanically unique, induced interface during contact deformation of these surfaces. In particular, three distinct observations should be considered. First, although not all polymer free surfaces exhibit a depressed glass transition temperature,[31] a significant depression of T_g (30 K to 70 K for t_f ~ 10 nm) from the bulk value is consistently reported for PS thin

[2] The timescale for this interphase formation is less than seconds, whereas the duration of contact shown in Figs. 1-2 is constrained by the requirements of elastic contact analysis[22] to be ~2 sec; this trend in greater apparent stiffness at the surface is also quantitatively reproduced over a range of dynamic contact frequencies (e.g., Fig. 2d).

films, both those adhered to substrata[2,4] and free standing,[3,33] and over a range of molecular weights. Recent work by Torkelson et al. has demonstrated the equivalence of T_g depression, indicative of molecular mobility, at the surface of "bulk" polymers (films

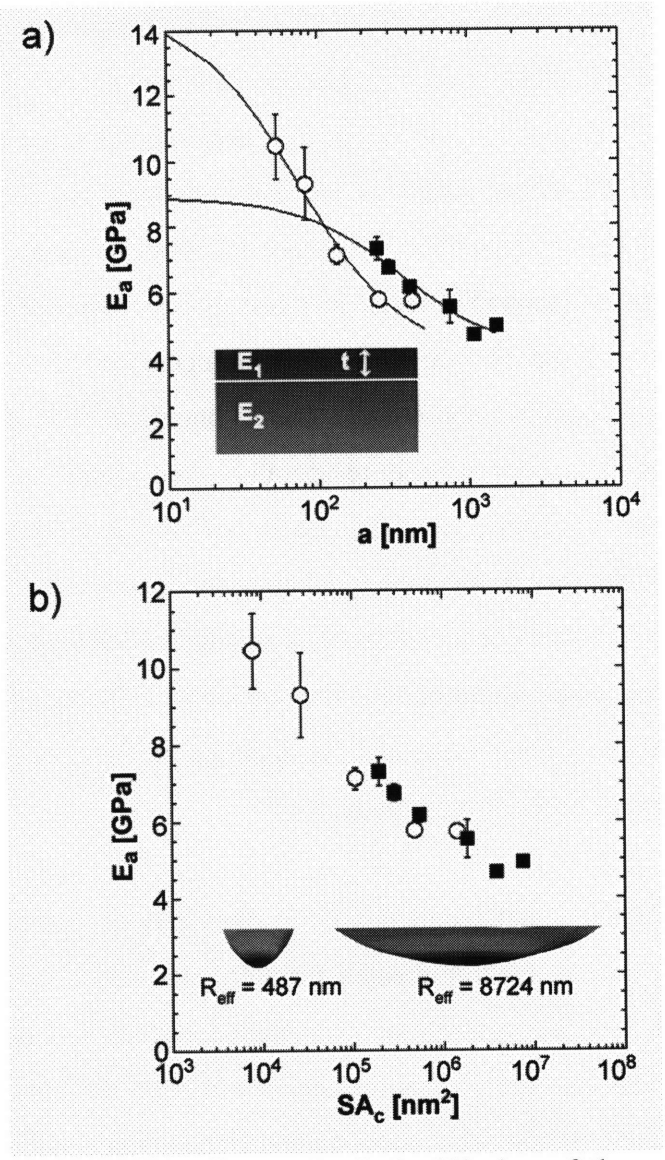

Figure 3.4 Possible mechanisms for mechanical stiffening of the contacted surface. a) The free surface could be a mechanically distinct, thin layer of thickness t. Analytical theory for contact deformation of a bilayer mechanical model (inset) predicts that the composite elastic modulus $E(E_1, E_2, t)$ should vary as a function of contact radius a, but not of indenter radius R. Fits of this model (lines) to experimental data obtained with two probes of effective radii R_{eff} = 487 nm (○) and R_{eff} = 8724 nm (■) for polystyrene (PS-12k) do not coincide and thus do not support this model. b) A mechanically distinct phase could be formed in the material immediately adjacent to the probe surface, scaling with the surface area of contact SA_c for any probe radius R. These data show that E increases with decreasing surface area of contact SA_c for these probes, consistent with the

formation of an interface at the region defined by probe-surface contact. Error bars represent one standard deviation and may be smaller than the symbol.

of at least μm-scale thickness such as those we consider here) and at the surface of thin films (for $t_f > 30$ nm). PS films of $t_f < 30$ nm also exhibited depressed T_g, but no through-thickness gradient in this depression.[2,43] Second, O'Connell and McKenna found this same magnitude of T_g depression (40 K) in free standing PS films of $t_f \sim 20$ nm, and further reported that PS films tested at elevated temperatures in the rubbery state exhibited a film thickness-dependent decrease in rubbery creep compliance. This decreased compliance corresponded to an increase in effective stiffness of the rubbery state from 10^6 Pa to 10^8 Pa as film thickness was decreased to $t_f \sim 13$ nm.[32] Third, Stafford *et al.* recently applied non-contact elastic buckling[33] to determine E_a of PS films on poly(dimethylsiloxane) at room temperature, and found an order of magnitude decrease in E_a of the PS films, from 10^9 Pa to 10^8 Pa as t_f approached 5 nm. To summarize these observations in the archetypal amorphous polymer PS: as film thickness or distance from the surface of observation decreases below ~30 nm, the T_g of both films and free surfaces decreases significantly, the apparent stiffness of the rubbery state increases by two orders of magnitude, and the apparent stiffness as measured by elastic buckling decreases by an order of magnitude.

One possible interpretation that reconciles these observations and is supported by our own findings is that contact loading creates an interfacial region of confined molecular motion and elevated T_g with respect to the uncontacted surface. Extrapolation of reported $T_g(t_f)$ for PS[2] indicates that the T_g at a distance 5 nm from the polymer free surface is ~20°C below room temperature. This suggests that free surfaces and films explored over this length scale at room temperature are effectively in the rubbery regime, which is consistent with the ~0.1 GPa apparent stiffness observed via non-contact creep[32] and buckling[13] of PS films. However, upon contact with another surface such as the spherical diamond probes used in our experiments, this highly mobile region existing within 5 nm of PS free surfaces has the potential for significantly enhanced intermolecular interactions at the geometrically confined interface induced by the indenter probe[44]. Mechanical loading at this interface induces hydrostatic stress beneath

the probe, which is well established to increase T_g by 0.3°C/MPa (for PS and PMMA[7,45]) to 0.4°C/MPa (for PC[46]). For the range of contact pressures in our experiments on these polymers, the hydrostatic stress beneath the spherical probes ranged from 250 to 400 MPa. In contrast to contact experiments on polystyrene in which no external force was applied,[47,48] these hydrostatic pressures indicate an increase in T_g of approximately 50°C – 120°C, which would shift the T_g of this region well above room temperature.

In other words, the uncontacted polymer surface may exhibit T_g near or above room temperature (and therefore an apparent stiffness of ~ 0.1 GPa corresponding to the rubbery state[13]), but the superposed contact stress shifts T_g at the probe-polymer interface upward to at least approach the stiffness of the bulk or glassy state. In addition to this mechanically imposed T_g shift, attraction toward and repulsion from the probe material could restrict molecular mobility in the confined region of mechanical contact adjacent to the probe, either via intermolecular interactions (enthalpic) or via stretching or alignment of macromolecular chains with respect to the probe surface (entropic via reduced conformations)[49]. Significant variation of enthalpic interactions upon contact has been demonstrated by Roth et al. to decrease the molecular mobility of PS through variation of the contacting surface material, as well as in the development of nanoparticle-polymer matrix nanocomposites.[8,9,49,50]

Naturally, the relative volumetric proportion of this confined interfacial region will decrease as the total volume of strained polymer beneath the probe increases with increasing contact depth. As a result, the contribution of this interfacial region to the overall mechanical response will decrease to that of the bulk polymer with increasing contact depth, as observed here for depths h_c > 200 nm. This contribution will be diminished at a given contact depth for larger probe radii, which deform a larger total polymer volume at that depth. This is demonstrated by the comparison of apparent stiffness measured for a given contact depth for different contact surfaces areas (Fig. 3.4b). Thus, contact-based studies of polymer surfaces (tested or heated above bulk T_g) that employ probe radii or contact surface areas SA_c that exceed the range herein by

orders of magnitude would not be expected to exhibit measurable differences in mechanical properties over 10s of nanometers from the free surface.[20,21] For this same reason, the mechanical properties of the interphase region in nanoparticle-polymer nanocomposites will dominate the macroscopic mechanical response only when the volume fraction of the interphase is significant.

3.2.4 Conclusions

In summary, contact deformation to depths of 5 nm < h_c < 200 nm demonstrates as much as a 200% increase in the apparent stiffness of amorphous polymer surfaces, as compared to apparent elastic moduli measured for contact depths > 200 nm from the free surface. For the three amorphous polymers considered, this increase in E_a is independent of processing, thermal history, macromolecular structural properties (molecular weight or persistence length), or relative humidity. The trend in apparent stiffness scales with the surface area of contact, and indicates that the polymer surface stiffening mechanism is related to the creation of a mechanically unique interfacial region between the probe and the polymer surface. These results provide the basis for isolating the effects of mechanical compression / confinement and of probe surface chemistry on the mechanical behaviour of polymer surfaces under localized contact. Our findings relate directly to the mechanical performance of polymers employed as protective barrier coatings. Further, this contact-induced stiffening may control deformation physics at the interphases formed in synthetic composites of amorphous polymer matrices and nanoscale particles,[8,50] as well as in (bio)polymeric surfaces and interfaces that define interphase cell rheology:[51] the unique mechanical properties of such synthetic and biological composites are often not explained by continuum rules of mixing two distinct phases.[35,49] It is plausible that mechanically distinct interphases induced upon contact loading between two phases (e.g., inorganic nanoparticles and an amorphous polymer matrix[52]) are responsible in part for the unexpected mechanical performance of such materials.

Mechanical response to contact deformation on the nm-scale is increasingly understood to be a function of the geometrical loading conditions as well as the interfacial chemistry.[8,49] Section 3.3 develops new experimental techniques to isolate the effect of

chemistry (or probe surface charge) on the dynamic formation of a contact induced interphase.

3.3 MODIFIED PROBE SURFACE CHEMISTRY

Preliminary results from the following study were published in 2007.[53]

Mechanical behavior of polymer thin films and nanocomposites under contact loading is partially controlled by physical confinement and interfacial chemistry.[8,49] Although the contact deformation mechanics of amorphous polymers can be investigated very near the surface, it has become increasingly acknowledged that chemical interactions at the interface between the polymer and probe may play a large role in near-interface mechanical behavior.[8,49,50] Testing of this hypothesis requires nanoscale mechanical testing in which the indenter probe surface chemistry is tunable. Herein, the first chemically functionalized nanoindentation probe is fabricated and used to measure the mechanical properties of an amorphous polystyrene surface. The capability of atomic force microscopy to characterize the mechanical response to deformation with a chemically functionalized contact probe was also investigated.

3.3.1 Introduction

Although size-dependent effects on elastoplastic mechanical behavior of metallic and ceramic structures are increasingly well-studied, relatively little is known about how the deformation of polymers depends on microstructural and physical length scales. In particular, it is not yet clear how the structural and mechanical properties of amorphous (glassy) polymers differ at free surfaces, at interfaces, and within the bulk. Such understanding is important because free surface and interface properties dominate the mechanical behavior of (bio)polymeric thin films and of nanocomposites. Recent experiments have demonstrated significant variation of the glass transition temperature T_g within ~100 nm of the free surface in amorphous polystyrene (PS) thin films.[3,4,6] This indicates possible differences in the macromolecular mobility that induce a mechanical response quite different from that indicated via bulk or μm-scale testing, even at room temperature, within 100 nm of the free surface. Several experiments have characterized aspects of the polymer surface mechanics via non-contact[13] approaches, as well as via contact deformation methods.[16,17] Others have begun to address the influence of the probe surface chemistry on (bio)polymeric surface response in the areas of surface

adhesion studies,[54] compositional surface mapping[55] or single molecule recognition microscopy to image protein distributions on biological surfaces including cells.[56] The importance of surface chemistry on polymer properties has also been studied in the context of thin film / substrate interactions[6,57] as well as nanoparticle / polymer matrix interactions in nanocomposites.[8,49] However, very little has been reported regarding the mechanical behavior of polymeric surfaces via contact deformation using probes of controlled surface chemistry. Such probes enable consideration of the extent to which the chemically defined interphase between the probe and the polymer surface contributes to the mechanical response of the deformed volume.

In this section, a protocol for creating chemically functionalized nanoindentation probes is demonstrated. This approach enables tunable chemistry of the probe surface during controlled mechanical testing over a load and displacement range appropriate for investigating glassy polymeric surfaces. Such probes can be used to study chemically defined adhesion at the nanoscale, to inhibit nonspecific organic adsorption during mechanical experiments, and to consider the formation of chemically distinct interphases under confined loading of polymer surfaces.

3.3.2 Materials and methods

A polystyrene (PS) polymer standard was synthesized via anionic polymerization (Polymer Laboratories, Amherst, MA) and processed via compression molding by DuPont (Wilmington, DE). The compression molded sample was heated to ~150°C above the polymer T_g and compressed at 0.3-0.5 ton pressures between polished Al and an extremely smooth disk of float glass to yield samples of 1 mm thickness and RMS roughness < 1nm. Weight average molecular weight M_w was measured via gel permeation chromatography and was found to be 12,450 g/mol, while differential scanning calorimetry was used to determine the glass transition temperature T_g = 96.9°C. Sample surfaces were probed using an instrumented nanoindentation apparatus, with load range capability appropriate for indentation of glassy polymers over this depth range of 100s nm, as well as using an atomic force microscope, for further investigation despite the limited maximum loads.

The instrumented nanoindentation apparatus (Triboindenter, Hysitron, Minneapolis, MN) was used in open-loop feedback mode to five maximum loads (15 μN, 30 μN, 75 μN, 200 μN, and 500 μN). This load range corresponded to an indentation depth range of approximately 10 nm to 250 nm for the spherical probe of radius R = 2000 nm that was customized through the attachment of functional molecular groups at the surface. In addition, two conospherical, diamond probes with radii R of 500 nm and 9000 nm were used to indent the PS surface to a maximum load of 75 μN for comparison to the customized probe. The loading profile (2 s loading, 0.5 s unloading) was optimized on the PS sample according to current nanoindentation analysis theory for viscoelastic materials[23] for the extraction of elastic properties via the Oliver and Pharr method.[24] This loading profile was shown to produce equivalent elastic modulus values to the storage moduli values determined via nanoDMA (see Fig. 3.2d). All tests were conducted at ambient humidity and at 22.4°C. The load used to define surface contact in open-loop mode was 0.3 μN.

Indentations with the atomic force microscope (MFP-3D, Asylum Research, Santa Barbara, CA) were performed in open-loop feedback mode to five maximum voltages corresponding to displacements ranging from 10 nm to 100 nm. Relatively stiff tipless AFM probes (AppNano ACL-TL, Applied NanoStructures, Santa Cruz, CA) were mounted with borosilicate spheres of R = 2 μm (BioForce Nanosciences, Ames, IA). Calibration of the cantilevers indicated stiffness or spring constant k ranging from 76.5 N/m and 77.6 N/m, resonant frequencies between 189.5 kHz and 191 kHz, and inverse optical lever sensitivities between 126 nm/V and 138 nm/V on this particular AFM laser-photodiode feedback. All tests were conducted at ambient humidity and at 22.4°C, after equilibration of the enclosed testing environment for at least 1 hour.

For all probes, the contact area as a function of contact depth $A_c(h_c)$ was determined directly via Matlab® analysis of atomic force microscopy (AFM) images of the probes, interpolating bilinearly among data points and integrating numerically as detailed in Constantinides et al.[29] Although the effective radius R is noted for reference herein, this

reconstructed $A_c(h_c)$ was used to calculate an effective elastic modulus E from the measured load-displacement (P-h) response.[24]

3.3.3 Experimental protocol

Instrumented nanoindenters, in contrast to commercial AFMs, can induce maximum loads sufficient to investigate contact depths extending < 100s nm from the surface of an amorphous, glassy polymer (Young's modulus E ~ 3 GPa) with < μm-scale spherical probes. Spherical probes are preferable for indentation of polymeric materials because these probes induce continuous, low-strain deformation profiles that can be used to induce elastic as well as viscoelastoplastic polymer responses.[15] Nanoindentation with a chemically controlled probe surface is challenging because most spherical nanoindentation probes are machined from diamond, which is not easily functionalized with small molecules. To create a spherical nanoindentation probe that can be chemically functionalized, a relatively stiff and smooth sphere (preferably with a radius R < 5 μm) must to be positioned and affixed in the center of a nanoindenter load-train fixture that is compatible with the nanoindentation hardware. As individual spheres of this size are difficult to manipulate even with micromanipulators, atomic force microscopy cantilevers (with a sphere of known radius already affixed) were used to build nanoindentation probes with the desired properties. Herein, this experimental technique is discussed in detail as a useful route to control the interface chemistry during contact deformation experiments on (bio) polymeric materials.

3.3.3.1 Design and assembly of spherical, nanoindentation probe

In response to the need for a nanoindentation probe with controlled surface chemistry, a probe was designed (Fig. 3.5a) using an AFM cantilever (length ~ 150 μm, thickness ~ 1 μm) with a borosilicate sphere of R = 2.5 μm already affixed (BioForce Nanosciences). Note that most spherical nanoindentation probes are designed with a conical geometry that evolves into the final probe tip geometry to ensure that only the probe tip touches the surface during indentation experiment. With this design the load-displacement data can be analyzed given the $A_c(h_c)$ for that particular probe.[29]

The challenge of the AFM-cantilever design stems from the deviation from the typical probe base-geometry of a cone. Unlike a cone, when this AFM cantilever-mounted probe is in contact with the sample surface, the 'large' glass surface on to which the AFM cantilever is affixed is only 6 μm from the indentation surface (Fig. 3.5b). Therefore the success of this design is critically dependent on the cleanliness of the sample surface (here, PS) and the probe surface, and on the parallel mounting of the glass relative to the sample surface. The following measures were taken to ensure cleanliness of the probe: all tweezers were rinsed in acetone and dried with clean air before each use, latex gloves were worn at all times, and glass mounting surfaces were cleaned using a Q-tip with acetone, then with methanol, and then dried with clean air. The probes were assembled by hand under an optical microscope using a 30x objective.

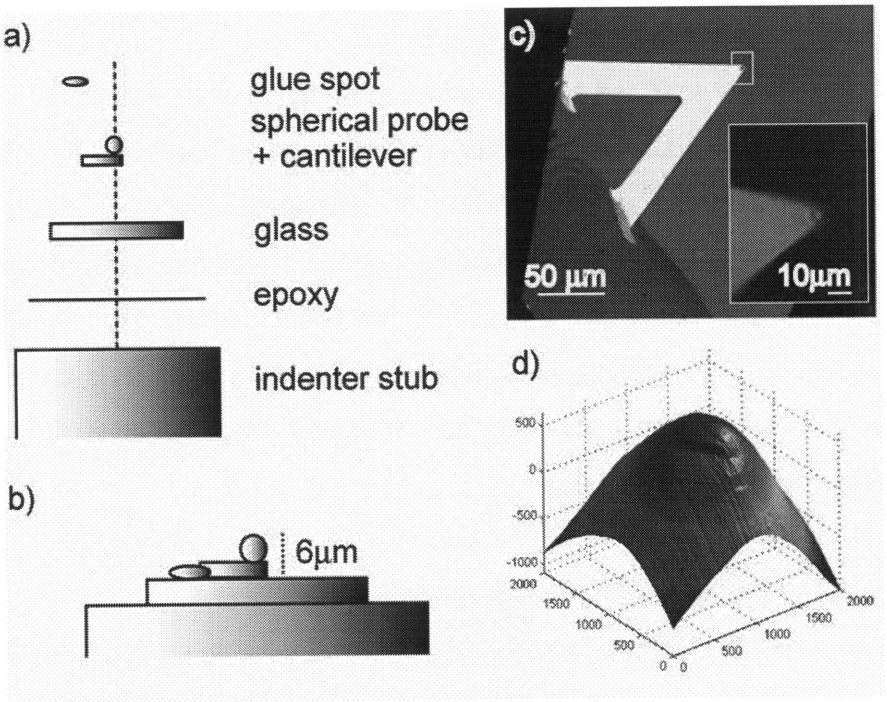

Figure 3.5 a) Schematic of the indenter probe assembly using an atomic force microscopy probe. b) Schematic of the top of the assembled probe. c) Top down optical microscopy image of cantilever glued onto the glass with zoom-in inset of spherical probe. d) Three-dimensional topography from atomic force microscopy image of probe surface.

A complete indentation probe is pictured in Fig. 3.5c, with an inset highlighting the region near the borosilicate probe tip. To confirm the cleanliness of the probe tip and

obtain the contact area function directly, AFM was performed on the indenter probe surface as depicted in Fig. 3.5d.

3.3.3.2 Chemical functionalization

Amine functionalization: Although this probe tip could be functionalized using any molecules that can be bound densely and strongly to borosilicate glass, amine (NH_2) functionalization was chosen for this study. Probe tips that were imaged and screened for performance on the nanoindenter were first cleaned under ultra violet (UV) for 30 min, then derivitized with amine groups through a 2 h chemical vapor deposition of 300 μL N, N diisopropylamine and 900 μL 3-aminopropyltriethoxysilane. When the amine groups gain a hydrogen atom, they present a net positive charge to the polymer surface.

Control tests to confirm surface functionalization of the borosilicate glass probes were performed on borosilicate glass slides and compared via changes in water droplet angle on the material surface (Fig. 3.5c inset). After 30 min of UV cleaning, the contact angle on the borosilicate glass slide was 0.9° ± 0.4° (6 measurements on 2 slides), immediately after amine functionalization the contact angle increased to 54.2° ± 2.0° (6 measurements on 2 slides), and after 48 h the contact angle had decreased by 10% to 48.7° ± 1.4° (Fig. 3.6). Importantly, the indentation experiments take 4 h to set up and complete, over which duration no statistically significant change in contact angle is measured.

Carboxyl functionalization: Polyelectrolyte multilayers (PEMs) were chosen as the most effective route for carboxyl functionalization in this study. PEM assembly has been described previously,[58-60] but in brief: poly(acrylic acid) (PAA, Polysciences) and poly(allylamine hydrochloride) (PAH, Sigma-Aldrich) were used to assemble PAA / PAH polyelectrolyte multilayers (PEMs). The dilute solutions of the polyelectrolytes (0.01M) were prepared in deionized water (Milli-Q, 18MΩ/cm) and a pH of 6.5. This solution pH was used to maximize density and stiffness[12] and minimize the bilayer thickness (1 nm) as deposited on a clean borosilicate spherical probe. Two bilayers were deposited to maximize the purity of the top PAA layer, as there is increased interpenetration in the first bilayer. Polyacrylic acid (PAA) comprised the outmost layer,

which presents carboxyl groups toward the polymer surface and has a net negative charge when in solution.

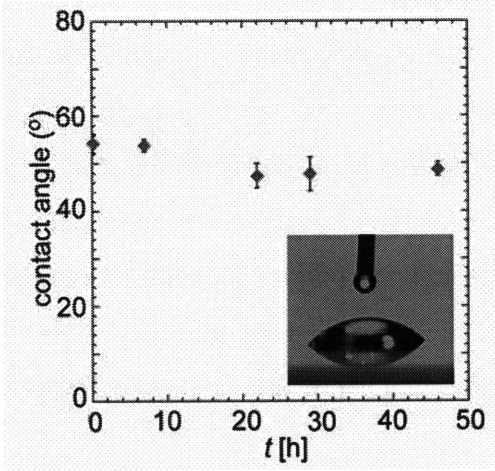

Figure 3.6 Contact angle measurements of a drop of water on a borosilicate glass slide were performed to evaluate stability of the amine functionalization over time.

3.3.4 Results and discussion

Nanoindentation experiments were performed to four maximum loads P_{max} corresponding to a maximum depth range of 10 nm to 250 nm, both before and after chemical functionalization of the probe surface. Figure 3.7 shows a subset of these experiments. Figure 3.7a shows the load-depth (*P-h*) responses of a PS surface indented to the same maximum load P_{max} with three spherical probes of varying effective radii. As expected from the corresponding contact area functions, the response of the customized spherical nanoindentation probe of intermediate radius (R = 2000 nm) is bounded by the responses to the two diamond, conospherical probes of smallest and largest radii (R = 500 nm and 9000 nm). That is, assuming the elastic properties of the PS are invariant with contact depths over this range, the probe of smallest radius should penetrate less deeply than the probe of largest radius. This provides a facile check of probe construction and parallel surfaces; initial contact of sharp AFM cantilever edges instead of the spherical probe would produce an artifactually stiff response.

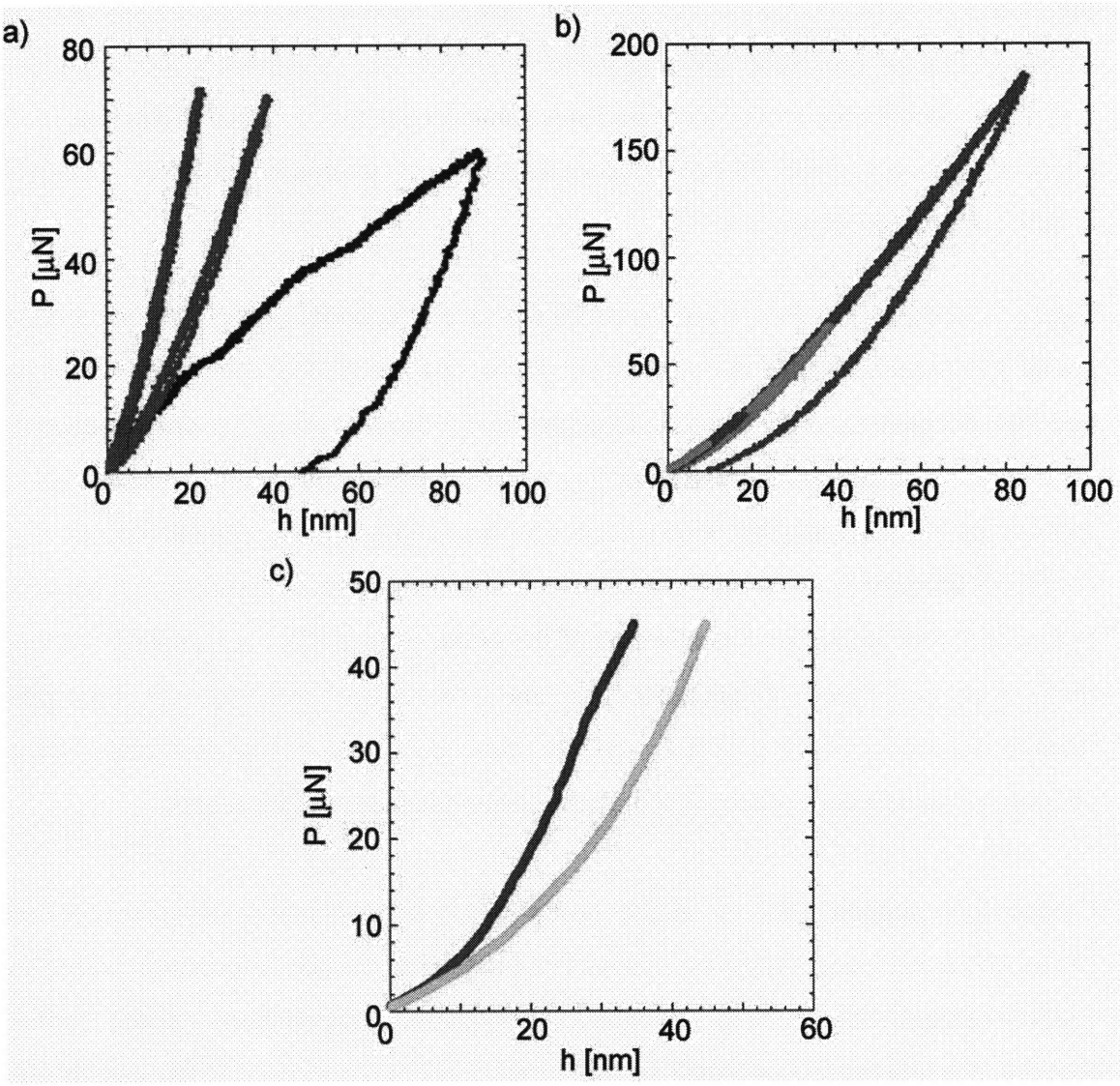

Figure 3.7 a) Load-displacement *P-h* hystereses of amorphous, atactic polystyrene indented by three probes of varying radii. The data for the assembled probe of radius R = 2500 nm (•) is bounded by the induced responses from two conospherical, diamond probes of R = 9000 nm (•) and R = 500 nm (•). **b**) Representative *P-h* responses for contact deformation experiments on an instrumented nanoindenter with an amine group functionalized probe of R = 2500 nm before (•) and after (○) surface chemistry are indistinguishable over this range of loads and depths. *P-h* responses at alternating maximum loads are highlighted (•) such that the smaller maximum loads/depths may be distinguished. **c**) Representative *P-h* responses for contact deformation experiments on an atomic force microscope, with a carboxyl group functionalized probe of R = 2500 nm before (•) and after (•) surface chemistry to P_{max} of 40 μN, demonstrates a stiffer response than the bare borosilicate sphere.

Using the AFM-constructed area function of the customized, unfunctionalized probe and the experimentally measured load-displacement responses (e.g., Fig. 3.7a, corresponding to a maximum contact depth of ~ 40 nm), the calculated E of PS agrees well with

literature values (E ~ 3 GPa). This good agreement confirms the probe construction and functionalization procedure as a reliable approach that contributes no significant, additional compliance to the measured mechanical response. Further discussion of the depth-dependence of the inferred elastic properties of amorphous polymer surfaces is detailed in Tweedie et al.[1]

Figure 3.7b shows the *P-h* responses of PS for several maximum loads, before and after amine functionalization of the customized probe surface. As the *P-h* responses for pre- and post-chemistry nanoindentation experiments lie directly on top of one another, it is clear that the amine functionalization has no effect on the mechanical response of the amorphous PS surface. This experiment was repeated with un / functionalized Si_3N_4 conospherical probes of ~50 nm radius, which also demonstrated identical *P-h* responses before and after amine functionalization of the probe surface (data not shown). Although there was no effect of chemistry on the mechanical response for this probe functionalization / polymer surface system, these data demonstrate that probe surface chemistry can be a controlled variable during nanoindentation experiments.

Contact deformation with an amine group functionalized probe surfaces repeatedly produced no mechanical response change compared with contact deformation with a bare probe surface. In contrast, contact deformation experiments with carboxyl functionalization were performed using atomic force microscopy (AFM) and the load required to achieve a given displacement increased for the carboxyl-functionalized probe relative to that of the bare. AFM was used due to the relative ease of not having to fabricate the indenter probe, but over a smaller range of accessible indentation loads and depths. Figure 3.7c depicts representative loading curves for the polymer responses to the carboxyl-functionalized and bare probes. These results suggest that contact deformation with varied probe surface functionalizations can affect the mechanical response of polystyrene. The change in mechanical response for carboxyl group functionalization as opposed to no change in mechanical response for amine group functionalization may be caused by charge sign, charge density, or controlled by the specific polymer surface under contact deformation. However, due to challenges associated with these experiments,

results in this area are likely to remain sparse and inconclusive, suggesting that atomistically detailed simulations should be utilized to develop broad conclusions regarding chemomechanics of confined polymers. Polystyrene is generally not considered a reactive polymer so its mechanical response is unlikely to be affected by changes in probe surface functionalization, nevertheless, it is valuable for this research to compare the simulated effect to experiment to determine whether experimental results have been influenced by experimental errors. There are a few possibilities as to why more force was required to achieve the same displacement for the functionalized probe than the bare probe: (1) the true radius of the spherical indentation probe may deviate significantly for one or both of the probes used from the manufacturer's reported radius over the surface area of contact. (2) there may have been relatively compliant, but well-adhered, contamination on the bare probe causing the displacement to increase for a given force relative to the functionalized probe.

3.3.5 Conclusions

The design and procedure for producing and testing a chemically functionalized nanoindentation probe was presented. This experimental approach enables tunable chemical probe / surface interactions during nano-scale mechanical testing in a load range appropriate for investigating glassy polymers. This protocol not only provides the basis for isolating the effects of surface charge and compression on polymer surface response to contact deformation, but suggest that specific synthetic interfaces (such as those created in nanocomposites) may be systematically investigated as a function of geometry, material characteristics, and surface chemistry. However, due to complicated nature of these small-scale chemomechanical experiments, this research field will develop most rapidly if atomistically detailed simulations are used to guide specific experimental design choices.

3.4 REACTIVE POTENTIAL MOLECULAR DYNAMICS (MD) OF POLYMER SURFACE INDENTATION

3.4.1 Motivation and background

The near-surface contact deformation experiments described in Sections 3.2 and 3.3 push the length scale resolution limits of the most recent nanomechanical testing technologies. Experimental challenges in nanomechanical testing of polymers lead to experimental observations that are not readily translated into broad trends in material behavior. In this section, computational modeling of atomistic detail allows mechanistic hypotheses of experimental observations to be tested very close to the experimental length scales. Herein, a reactive molecular dynamics potential is utilized to observe any bonding changes that could be induced by mechanical pressure exerted by an indentation probe surface.[61]

3.4.2 Simulation details and analysis

As these simulations are intended to consider bond breaking and bond formation as a possible mechanism for mechanical changes in response to variation of probe surface chemistry, the molecular dynamics package used was one that allowed for chemical reactivity called ReaxFF [California Institute of Technology, Pasadena, CA]. In exchange for this additional capability, simulation calculations become more computationally costly and system sizes must be reduced relative to those possible for standard molecular dynamics simulations.

The polystyrene (PS) thin films were initially constructed and equilibrated for 100 ps using Materials Studio, a standard molecular dynamics simulation and analysis package [Accelrys Software Inc., San Diego, CA]. The unit cell of the film, as indicated in Figure 3.8a was comprised of 16 molecules with 10 monomer units each, with the unit cell containing roughly 2900 atoms in the PS film. These molecules have a molecular weight of 1,040 g/mol while the weight average molecular weight of the polystyrene testing in Section 3.2 was approximately 12,000 g/mol.

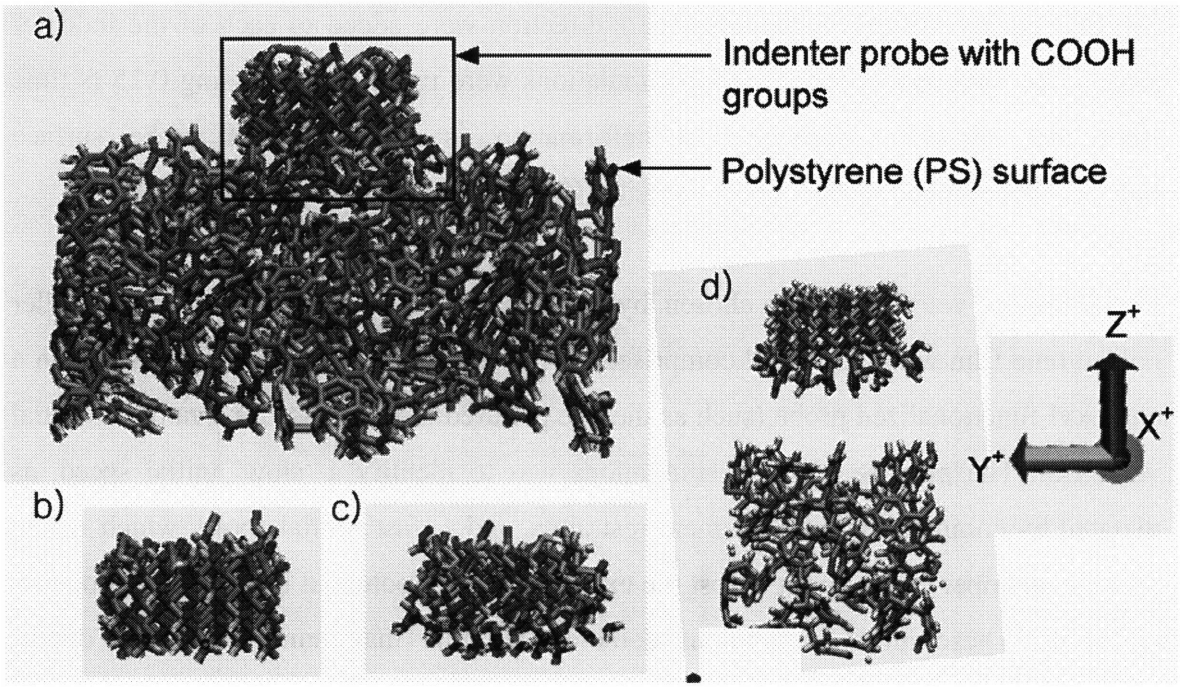

Figure 3.8 a) A polystyrene (PS) thin film surface with periodic boundary conditions in the x-y plane is deformed with an indenter (rigid-carbon lattice) functionalized with carboxyl (COOH) groups that are presented toward the polymer surface. The polymer-indenter simulations were repeated with two other probe surface functionalizations: b) hydrogen-capped and c) amine (NH_2) group functionalized. d) A smaller simulation system was used to determine the range of feasible initial velocities for the approaching indenter.

The film was bounded in the x-y place by periodic boundary conditions, but is fixed on the lower z-axis boundary and had a free surface facing the positive z-direction. The indenter probe was comprised of a rigid, carbon atom lattice with a 10 x 10 angstrom surface area that impacts the surface normally with a velocity in the negative z-direction. The indenter probe surface was functionalized in three ways: carboxyl groups (COOH) (Fig. 3.8a), amine groups (NH2) (Fig. 3.8b), and hydrogen-capped (Fig. 3.8c). To ensure that the three indenter probes could be compared directly, twelve, symmetrically distributed dummy atoms (green atoms in Fig. 3.8b-c) were added to the top surface of each indenter to achieve equivalent total masses for each indenter.

After equilibration in Materials Studio, the simulation system was equilibrated again using the ReaxFF force field for 1.25 ps using 0.25 fs time steps. Following the equilibration period, during which the total energy and temperature settled to constant

ranges, velocity vectors in the negative z-direction were added to each of the indenter probes and then molecular dynamics simulations were run for 2.5 ps using 0.25 fs time steps that allowed comparison of deformation as a function of probe surface functionalization and initial impact velocity (0.5 km/s and 2 km/s).

Initial impact velocities were chosen by running initial test-simulations on a smaller polystyrene film with a unit cell comprised of 4-10 monomer molecules, indented with a carboxyl-functionalized probe (such as the one pictured in Fig. 3.8d) for a range of initial velocities. The purpose of these simulations was to identify a 'slow' initial speed, as dictated by computational requirement restraints, and a 'fast' initial speed, which would provide an upper energy limit to test the extreme case for potential breaking or formation of bonds. These initial simulations demonstrated that maximum indentation depths increased linearly, as expected, until the indenter was directly slowed by the bottom z-axis boundary condition. These initial simulations indicated no change in the number and size of the molecules over the simulation time, until at an initial velocity of 6 km/s the polymer molecules were vaporized. Furthermore, the experiments should be conducted at speeds slower than the longitudinal elastic wave propagation speed through polystyrene (~2.5 km/s for bulk PS).[62] For these reasons, 2 km/s was chosen as the upper impact velocity condition.

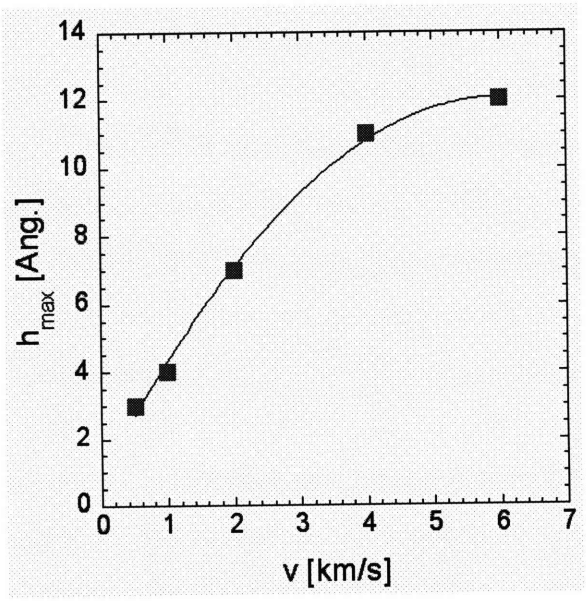

Figure 3.9 Maximum probe indentation depth for a flat probe with carboxyl group functionalization indenting a polystyrene surface (see Fig. 3.8d) as a function of initial probe approach velocity v.

Table 3.1 compares the scaling of the major length and time parameters relevant to this experimental and simulated system. The length scales are only 1-2 orders of magnitude smaller for the simulation than the experiment, but consistent with current modeling literature, the simulation rates for the model by far exceed those of the experiment – in this case by 10 orders of magnitude. Although the polymer film unit cell is too small compared to dimensions of the indenter to accurately simulate the mechanical response to a single indentation on a polymer surface, this simulation does directly address whether bond formation / breakage occurs during contact deformation and whether this effect is a function of for the functional groups considered.

Analysis of the molecular dynamics simulations of polystyrene indentations was performed for three parameters as a function of probe surface functionalization: (1.) molecular integrity during the indentation (formation / breakage of bonds); (2.) maximum indentation depth after impact; and (3.) changes in local molecular orientation. For each time step the ReaxFF MD output reports the number of molecules and the number of each type of element present in each molecule. This output would indicate if any changes in bonding occurred at any point during the simulation.

The maximum indentation depth h_{max} was identified by plotting all z-axis values for all atoms in a simulation and subtracting the height of the indenter, as measured before the indenter touches the surface, from the minimum height of the indenter above the surface after impact. Indenter rotation was constrained during approaches to the surface, eliminating changes in apparent indenter height. However, the analysis does make the reasonable assumption that the carbon network is much more rigid that the polystyrene surface and therefore does not deform during indentation.

The local chain orientation[63,64] P was calculated for each molecule at each time frame via post-simulation script to study the effect of changes in probe surface chemistry

relative to the probe surface. The local chain orientation was studied as an average over all the molecules in a simulation (also averaged over the three repetitions of an experimental condition) and compared for variations in impact velocity and functionalization group. In addition, the local orientation parameter for individual molecules either under or 'far away' from the indenter were averaged over the three repetitions of the simulation to look at changes in local orientation relative to indenter probe surface position.

Table 3.1 Experimental parameter scale comparison between reactive molecular dynamics simulations and physical experiment.

	ReaxFF Simulation	Nanoindentation experiment	Scale difference
Indentation rate [m/s]	10^{3}	10^{-7}	10^{10}
Indentation depth [m]	10^{-10}	10^{-9}	10^{1}
Contact diameter [m]	10^{-9}	$200 * 10^{-9}$	10^{2}
Polymer molecule size [# monomers]	10	113	10^{1}

3.4.3 Results and discussion

The purpose of these chemically reactive molecular dynamics simulations was to test whether bond formation / breakage occurs during near-surface indentation of amorphous polymer surface, and further, whether this occurrence is a function probe surface chemistry. The probe surface chemistry is altered by attaching different short functional groups to the face of the rigid indenter probe that contacts the polymer surface. For all the simulations performed in the study, the number of molecules and the composition of those molecules remained constant for each time-step throughout each simulation. This indicates that for even extreme impact energies, such as an indenter probe traveling at 2 km/s, a polystyrene free surface will not form new bonds with the probe surface nor break intrachain bonds in response to contact deformation.

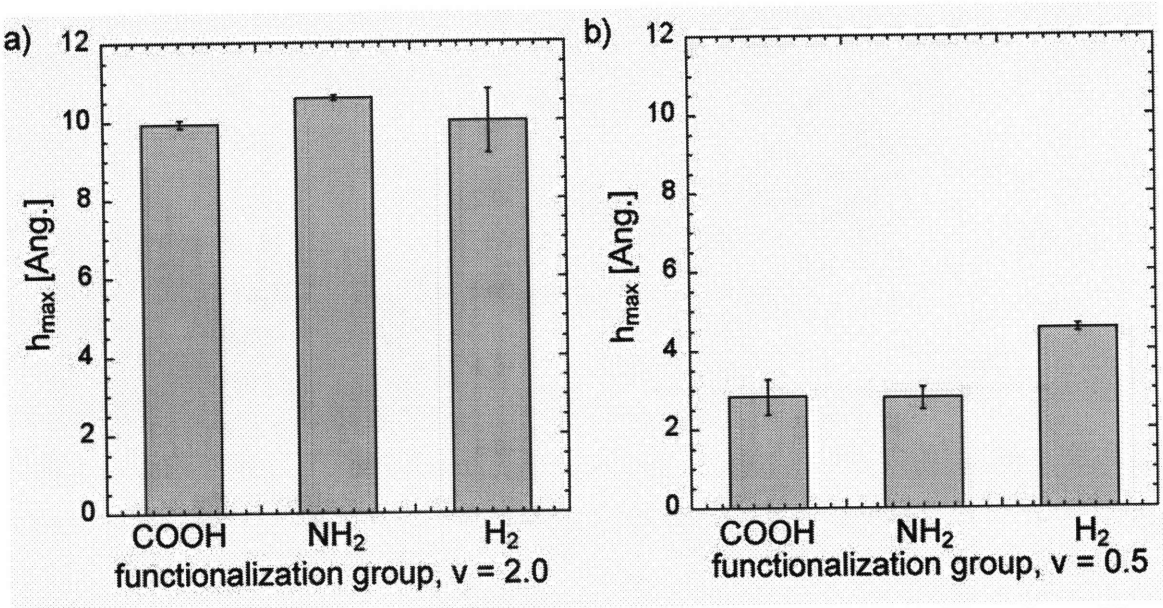

Figure 3.10 Maximum indentation depths h_{max} on a polystyrene surface for probes with three different chemical functionalizations: carboxyl groups (COOH), amine groups (NH_2), and hydrogen atoms. The results are presented for two initial probe velocities: a) 0.5 km/s and b) 2 km/s. Error bars represent one standard deviation among three repeats of the same simulation beginning with different starting structures.

Figure 3.10 illustrates the maximum depth of indentation h_{max}, or the distance into the polymer surface traveled by the indenter probe, as a function of probe surface functionalization and the two impact velocities considered. As seen in Fig. 3.10a, there is no statistical difference between the h_{max} for the three probe functionalizations at an impact velocity of 2 km/s, indicating that for the probe surface chemistries sampled in this study, there is no relative change in the deformation response of the polymer surface quantifiable by h_{max}. For the slower impact velocity of 0.5 km/s, there is a small, but statistically significant, increase in the maximum indentation depth of the hydrogen-capped indenter probe relative to the two probes functionalized with short chemical groups. A possible explanation for this variation at low speeds is that the indenter surface is only weakly interacting with the polymer surface (h_{max} ~ 2-4 Angstroms) and that the hydrogen probe has an effectively smaller contact area than the amine-functionalized indenter probe. This is apparent in a comparison of Figs. 3.8b and 3.8c. This geometrical effect is due to system size restraints that prevent the indenter from more realistically representing a sphere of large radius.

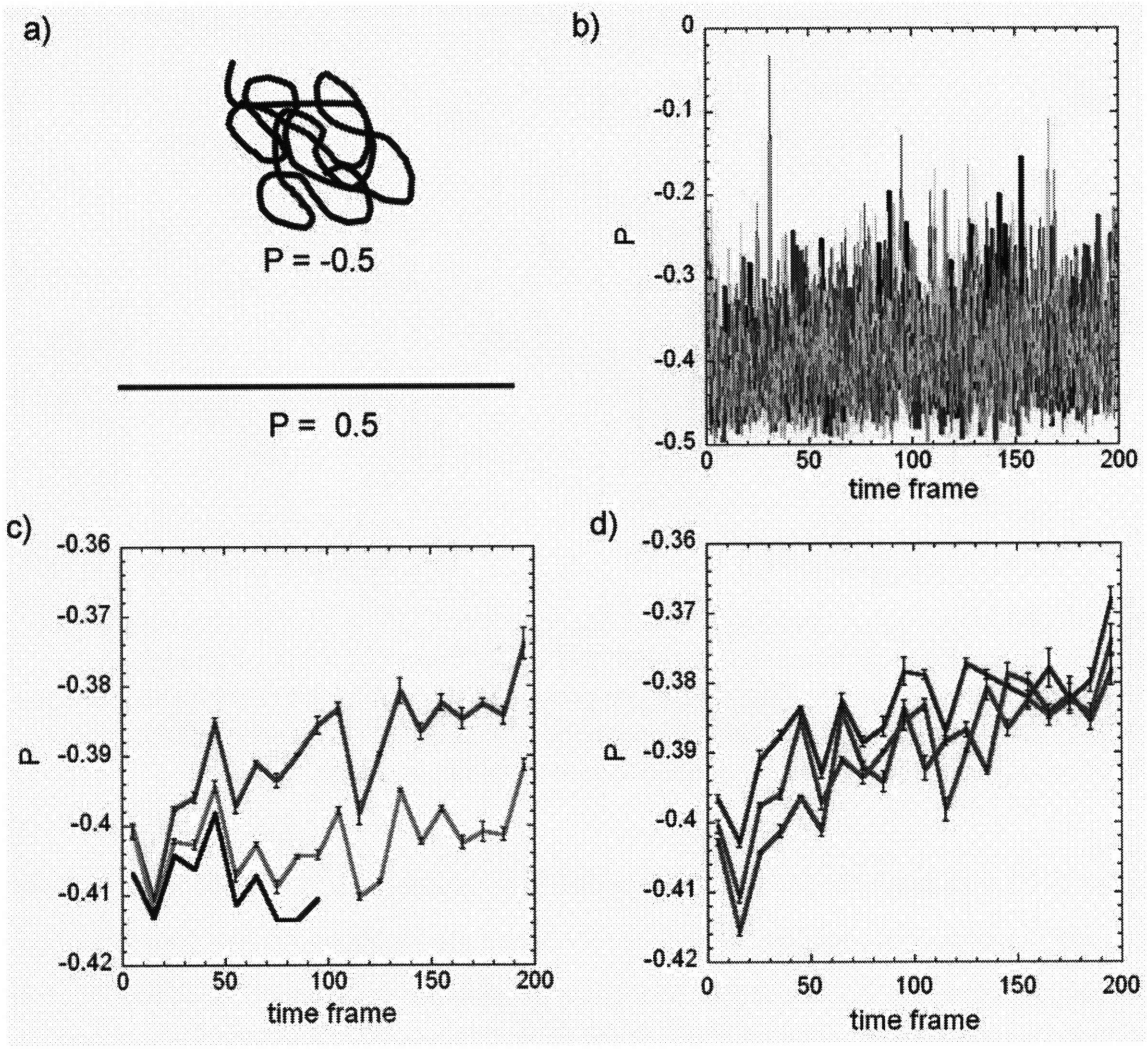

Figure 3.11. The local orientation parameter *P* can range between -0.5 (randomly coiled molecule) and 0.5 (straight molecule). The orientation parameter was calculated for each molecule in each time-frame and is plotted b) for a single indentation simulation with an amine group (NH_2) functionalized probe at an initial velocity of 2 km/s over 200 time frames, equal to 2.5 ps. In c), the time-averaged orientation parameter for the average over all the molecules is shown over 2.5 ps during equilibration (black), indentation with an initial velocity of 0.5 km/s (gray), and indentation with an initial velocity of 2km/s (blue). The d) time-averaged orientation parameter averaged over all the molecules in the simulation and then over the three repetitions of the simulation for three probe surface functionalizations: hydrogen atoms (gray), amine groups (blue), and carboxyl groups (red). Error bars represent one standard deviation among three repeats of the same simulation beginning with different starting structures.

In addition to considering changes in bonding and the extent of deformation in response to changes in probe surface chemistry, the local orientation parameter *P* of individual polystyrene molecules during indentation was considered. The local orientation

parameter as described by Rutledge et al.[63,64] ranges between 0.5 and -0.5, which represents the extent of chain orientation in any direction between two extreme conformational states of the polymer: P = -0.5 represents random bond angles between every C-C bond in the backbone, and P = 0.5 represents a completely straight molecule in one direction (see Fig. 3.11a). In Figure 3.11b, the local orientation parameter is shown for each of 16 molecules in a unit cell indented by an amine-functionalized probe at 2 km/s over 200 time frames, or 2.5 ps. The values for P generally range between -0.5 and -0.2 throughout the entire simulation, not surprisingly suggesting that the polymer molecules remain more clumped than they do linear. However, without any smoothing or averaging over different starting structures, no trend is apparent from this set of data.

When smoothing and averaging over molecules as well as simulation repetitions is taken into account, the local orientation parameter is observed to increase at an increasing rate over time for increased impact energy. In Figure 3.11c, P is averaged over the 16 molecules in a single simulation and then over three repetitions of the simulation with different starting structures for impact velocities of 0.5 km/s, 2 km/s, and no impact. In general, molecules appear to orient faster over time during indentation the faster the indentation velocity. Also, consistent with the statistically equivalent maximum deformation depths for all three probe functionalizations, Fig. 3.11d demonstrates equivalent changes in the local molecular orientation over time for impact simulations with initial velocities of 2 km/s.

To investigate the effect of probe surface functionalization on local molecular orientation as a function of position relative to the indenter probe surface, individual molecules under the indenter and "far" from the indenter were compared. Figure 3.12a illustrates which positions relative to the indenter in the polystyrene film were compared and the corresponding local orientation parameters for the molecules within those regions. No relative difference in orientation over the simulation time was observed for the molecules in different regions relative to the indenter. This indicates that the simulation system is too small to show varied regions of molecular response and therefore that the question of

the whether molecular orientation changes near the probe surface as compared to far away cannot be answered from this set of simulations.

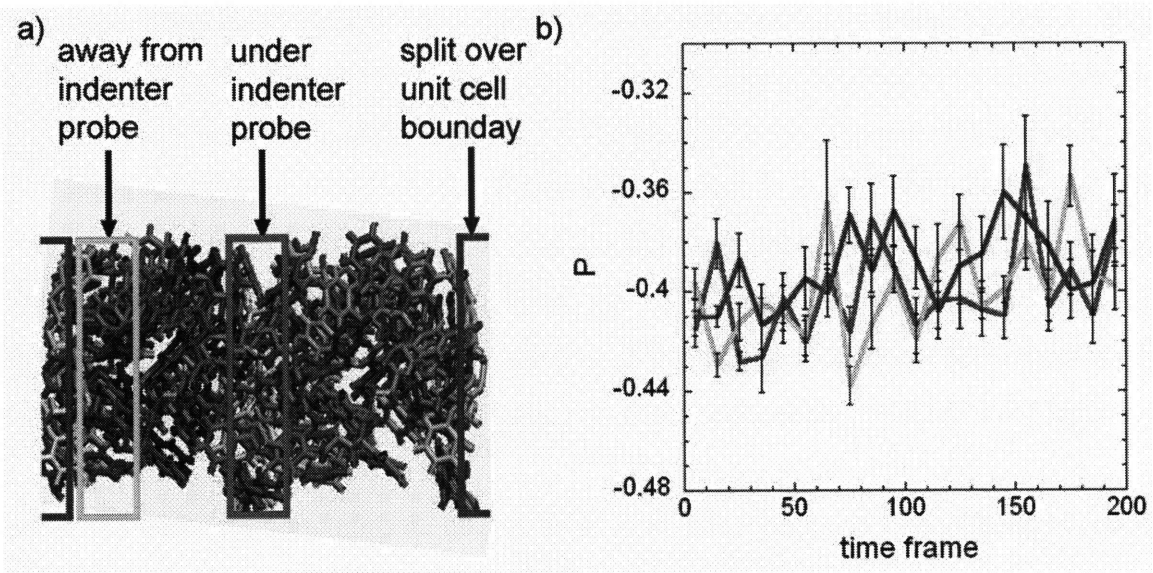

Figure 3.12 a) Side-view of polystyrene film with each molecule depicted in a distinct color. Vertically-long rectangles highlight regions of the film relative to the indenter position within which the local orientation parameter was calculated. b) Depicts the change in the local orientation parameter over time 200 time frames, or 2.5 ps, for three molecules averaged over 3 repetitions of the simulation in different positions in the polymer film relative to the indenter probe: under the indenter (red), away from the indenter (green) and split over the boundary condition (purple).

3.4.4 Conclusions

Chemically reactive molecular dynamics simulations of indentations in polystyrene surfaces with indenter probes of varied surface functionalization indicate that bonds are not broken or formed during contact deformation experiments. These simulations provide a high-velocity limiting case for probe-surface contact and demonstrate that even under high-energy impact with a mechanically confining probe surface the molecules remained in tact. Although the system size for these simulations (~3000 atoms) was too small to extract mechanical properties from the polystyrene surface response, the molecular deformation (extent and orientational quality) could be compared as a function of probe surface chemistry to determine whether this factor affects the stiffening response observed. For the higher initial impact velocity there was no change in maximum indentation depth, while for the slower impact velocity the hydrogen capped indenter probe penetrated the polystyrene surface further than the other functionalized probes.

This variation is attributed to the relatively lower stress applied by the amine and carboxyl functionalized probes since the slightly longer functional groups (amine and carboxyl) effectively increase the contacting surface area. Consistent with these results, studies of the local orientation parameter identified no change in molecular orientation over time in response to changes in probe functionalization. However, the local orientation parameter was observed to increase over time at an increasing rate for increasing impact velocity. While it is true that other polymer surfaces may react chemically to contact deformation, as observed in simulations by Chateauneuf et al.,[61] the focus of this study was to understand the nanomechanical deformation mechanisms of amorphous polymer systems such as polystyrene, and no effect of probe surface functionalization was observed. In summary, (1) probe surface functionalization does not matter to the maximum depth for a given loading, (2) chains do become more stretched during indentation the greater the deformation speed, but (3) chain realignment is not a function of probe surface chemistry.

These simulation results provide new insight into the probe functionalization experimental results presented earlier in this chapter. The simulations demonstrated that indentation with probes functionalized with hydrogen-satisfied groups, including amine and carboxyl groups, does not affect the mechanical response of near-surface polystyrene macromolecules. Meanwhile, experiments suggest that carboxyl group functionalization does affect the extent of deformation in response to loading while the amine group functionalization does not. The reason for this discrepancy may be that although the experimental system is not in solution, the finite humidity in the surrounding air may cause some fraction of the functional groups attached to the probe to become charged. The effect of charged functional groups on simulated mechanical response of polystyrene is the subject of ongoing work.

3.5 CONCLUSIONS

Chapter 3 addressed the challenges related to mechanical testing of confined polymers and explored the chemistry of a mechanically contacting surface as a driver for varied mechanical response. Since the mechanical properties of polymeric materials confined to the nanoscale are incompletely understood, the design of complex nano-scale materials systems has not yet been achieved. To build such an understanding of nanomechanical response for time-dependent materials, contact deformation of homogeneous engineering polymers was use to characterize the near-surface mechanical response. All the polymeric materials tested exhibited significant apparent stiffening for increasingly shallow indentations, independent of polymeric structural factors including molecular weight and monomer-type and environmental factors such as increased humidity. Chemical effects were considered as a mechanism for altered mechanical behavior in response to contact deformation of confined polymers via experiments and simulations. An experimental method was developed to test the nanomechanics of confined polymers as a function of probe surface functionalization using either nanoindentation or AFM. Such experiments demonstrated that probe surface chemistry can have an effect of the mechanical response of amorphous polymer surfaces. However, there are many experimental complications related to these nano-scale mechanical tests, including efficiency of probe surface functionalization chemistry, variation in probe surface functionalization density, identification of contact with the complication of surface functionalization, and the availability of only home-built functionalized probes for nanoindentation. In response to these challenges, a chemically reactive molecular dynamics simulation was used to discover that no bonds are formed or broken under contact deformation of polystyrene and that, within the limitations of the simulation, the molecular response does not vary with probe surface chemistry.

REFERENCES

1. Tweedie C.A., Constantinides G., Lehman K.E., Brill D.J., Blackman G.S., VanVliet K.J.; Enhanced stiffness of amorphous polymer surfaces under confinement of localized contact loads. *Advanced Materials* **2007**; In press,
2. Ellison C.J., Torkelson J.M.; The distribution of glass-transition temperatures in nanoscopically confined glass formers. *Nature Materials* **2003**; 2, (10), 695-700.
3. Forrest J.A., Dalnoki-Veress K., Stevens J.R., Dutcher J.R.; Effect of free surfaces on the glass transition temperature of thin polymer films. *Physical Review Letters* **1996**; 77, (10), 2002-2005.
4. Keddie J.L., Jones R.A.L.; Glass-Transition Behavior in Ultra-Thin Polystyrene Films. *Israel Journal of Chemistry* **1995**; 35, (1), 21-26.
5. Akabori K., Tanaka K., Nagamura T., Takahara A., Kajiyama T.; Molecular motion in ultrathin polystyrene films: Dynamic mechanical analysis of surface and interfacial effects. *Macromolecules* **2005**; 38, (23), 9735-9741.
6. Priestley R.D., Ellison C.J., Broadbelt L.J., Torkelson J.M.; Structural relaxation of polymer glasses at surfaces, interfaces and in between. *Science* **2005**; 309, (5733), 456-459.
7. Alcoutlabi M., McKenna G.B.; Effects of confinement on material behaviour at the nanometre size scale. *Journal of Physics-Condensed Matter* **2005**; 17, (15), R461-R524.
8. Bansal A., Yang H.C., Li C.Z., Cho K.W., Benicewicz B.C., Kumar S.K., Schadler L.S.; Quantitative equivalence between polymer nanocomposites and thin polymer films. *Nature Materials* **2005**; 4, (9), 693-698.
9. Roth C.B., McNearny K.L., Jager W.F., Torkelson J.M.; Eliminating the Enhanced Mobility at the Free Surface of Polystyrene: Flourencence Studies of the Glass Transition Temperature in Thin Bilayer Films of Immiscible Polymers. *Macromolecules* **2007**; 40, 2568-2574.
10. Bohme T.R., de Pablo J.J.; Evidence for size-dependent mechanical properties from simulations of nanoscopic polymeric structures. *Journal of Chemical Physics* **2002**; 116, (22), 9939-9951.
11. Mansfield K.F., Theodorou D.N.; Molecular-Dynamics Simulation of a Glassy Polymer Surface. *Macromolecules* **1991**; 24, (23), 6283-6294.
12. Lichter J., Thompson M., Delgadillo M., Nishikawa T., Rubner M., Van Vliet K.; Substrata mechanical stiffness can regulate adhesion of viable staphylococcus epidermidus bacteria. **2007**;
13. Stafford C.M., Vogt B.D., Harrison C., Julthongpiput D., Huang R.; Elastic Moduli of Ultrathin Amorphous Polymer Films. *Macromolecules* **2006**;
14. Briscoe B.J., Sebastian K.S.; The elastoplastic response of poly(methyl methacrylate) to indentation. *Proceedings of the Royal Society of London Series a-Mathematical Physical and Engineering Sciences* **1996**; 452, (1946), 439-457.
15. VanLandingham M.R., Villarrubia J.S., Guthrie W.F., Meyers G.F.; Nanoindentation of polymers: An overview. *Macromolecular Symposia* **2001**; 167, 15-43.
16. Amitay-Sadovsky E., Ward B., Somorjai G.A., Komvopoulos K.; Nanomechanical properties and morphology of thick polyurethane films under contact pressure and stretching. *Journal of Applied Physics* **2002**; 91, (1), 375-381.

17. Chakravartula A., Komvopoulos K.; Viscoelastic properties of polymer surfaces investigated by nanoscale dynamic mechanical analysis. *Applied Physics Letters* **2006**; 88, (13), -.
18. van Melick H., van Dijken A., den Toonder J., Govaert L., Meijer H.; Near-surface mechanical properties of amorphous polymers. *Philosophical Magazine a-Physics of Condensed Matter Structure Defects and Mechanical Properties* **2002**; 82, (10), 2093-2102.
19. Yang F.Q., Zhou J.Y.Y., Kordonski V., Jacobs S.D.; Indentation size effect of thermoset polymer: Allyl diglycol carbonate (CR-39). *Journal of Materials Science Letters* **1996**; 15, (17), 1523-1525.
20. Houston J.E.; A local-probe analysis of the rheology of a "Solid liquid". *Journal of Polymer Science Part B-Polymer Physics* **2005**; 43, (21), 2993-2999.
21. Mary P., Chateauminois A., Fretigny C.; Deformation of elastic coatings in adhesive contacts with spherical probes. *Journal of Physics D-Applied Physics* **2006**; 39, (16), 3665-3673.
22. Briscoe B.J., Fiori L., Pelillo E.; Nano-indentation of polymeric surfaces. *Journal of Physics D-Applied Physics* **1998**; 31, (19), 2395-2405.
23. Cheng Y.T., Cheng C.M.; Scaling, dimensional analysis, and indentation measurements. *Materials Science & Engineering R-Reports* **2004**; 44, (4-5), 91-149.
24. Oliver W.C., Pharr G.M.; An Improved Technique for Determining Hardness and Elastic-Modulus Using Load and Displacement Sensing Indentation Experiments. *Journal of Materials Research* **1992**; 7, (6), 1564-1583.
25. Sneddon I.N.; The relation between load and penetration in the axisymmetric Boussinesq problem for a punch of arbitrary profile. *International Journal of Engineering Science* **1965**; 3, (1), 47.
26. Constantinides G., Ravi Chandran K.S., Ulm F.-J., Van Vliet K.J.; Grid indentation analysis of composite microstructures: Principles and validation. *Materials Science and Engineering A* **2006**; in press,
27. Asif S.A.S., Wahl K.J., Colton R.J.; Nanoindentation and contact stiffness measurement using force modulation with a capacitive load-displacement transducer. *Review of Scientific Instruments* **1999**; 70, (5), 2408-2413.
28. Asif S.A.S., Wahl K.J., Colton R.J., Warren O.L.; Quantitative imaging of nanoscale mechanical properties using hybrid nanoindentation and force modulation. *Journal of Applied Physics* **2001**; 90, (3), 1192-1200.
29. VanLandingham M.R., Juliano T.F., Hagon M.J.; Measuring tip shape for instrumented indentation using atomic force microscopy. *Measurement Science & Technology* **2005**; 16, (11), 2173-2185.
30. Forrest J.A., Dalnoki-Veress K., Dutcher J.R.; Brillouin light scattering studies of the mechanical properties of thin freely standing polystyrene films. *Physical Review E* **1998**; 58, (5), 6109-6114.
31. O'Connell P.A., McKenna G.B.; Rheological measurements of the thermoviscoelastic response of ultrathin polymer films (vol 307, pg 1760, 2005). *Science* **2005**; 310, (5753), 1431-1431.
32. O'Connell P.A., McKenna G.B.; Dramatic stiffening of ultrathin polymer films in the rubbery regime. *European Physical Journal E* **2006**; 20, (2), 143-150.

33. Stafford C.M., Harrison C., Beers K.L., Karim A., Amis E.J., Vanlandingham M.R., Kim H.C., Volksen W., Miller R.D., Simonyi E.E.; A buckling-based metrology for measuring the elastic moduli of polymeric thin films. *Nature Materials* **2004**; 3, (8), 545-550.
34. Tweedie C.A., Van Vliet K.J.; Contact creep compliance of viscoelastic materials via nanoindentation. *Journal of Materials Research* **2006**; 21, (6), 1576-1589.
35. Ganguli S., Dean D., Jordan K., Price G., Vaia R.; Mechanical properties of intercalated cyanate ester-layered silicate nanocomposites. *Polymer* **2003**; 44, (4), 1315-1319.
36. Richards R.W., Thomason J.L.; Small-Angle Neutron-Scattering Measurement of Block Co-Polymer Interphase Structure. *Polymer* **1983**; 24, (9), 1089-1096.
37. Brulet A., Boue F., Cotton J.P.; About the experimental determination of the persistence length of wormlike chains of polystyrene. *Journal De Physique Ii* **1996**; 6, (6), 885-891.
38. Bicerano J.; Chain stiffness of liquid crystalline polyesters. 1. Characteristic ratio and persistence length. *Computational and Theoretical Polymer Science* **1998**; 8, (1-2), 9-13.
39. Yoon D., Flory P.; Persistence vectors for polypropylene, polystyrene, and poly(methyl methacrylate) chains. *Journal of Polymer Physics* **1976**; 14, 1425-1431.
40. Rittigstein P., Torkelson J.M.; Polymer-nanoparticle interfacial interactions in polymer nanocomposites: Confinement effects on glass transition temperature and suppression of physical aging. *Journal of Polymer Science Part B-Polymer Physics* **2006**; 44, (20), 2935-2943.
41. R.F.Brady. Comprehensive Desk Reference of Polymer Characterization and Analysis; Oxford University Press: Washington, DC, 2003.
42. Major R., Houston J., McGrath M., Siepmann J., Zhu X.; Viscous water meniscus under nanoconfinement. *Physical Review Letters* **2006**; 96, 177803.
43. Jones R.A.L.; Amorphous materials - Glasses with liquid-like surfaces. *Nature Materials* **2003**; 2, (10), 645-646.
44. Peanasky J., Cai L.L., Granick S., Kessel C.R.; Nanorheology of Confined Polymer Melts .3. Weakly Adsorbing Surfaces. *Langmuir* **1994**; 10, (10), 3874-3879.
45. Gacoin E., Fretigny C., Chateauminois A., Perriot A., Barthel E.; Measurement of the mechanical properties of thin films mechanically confined within contacts. *Tribology Letters* **2006**; 21, (3), 245-252.
46. Parry E.J., Tabor D.; Effect of hydrostatic pressure on the mechanical properties of polymers: a brief review of published data. *Journal of Materials Science* **1973**; 8, (10), 1510-1516.
47. Hutcheson S.A., McKenna G.B.; Nanosphere embedding into polymer surfaces: A viscoelastic contact mechanics analysis (vol 94, art no 076103, 2005). *Physical Review Letters* **2005**; 94, (18), -.
48. Sharp J.S., Teichroeb J.H., Forrest J.A.; The properties of free polymer surfaces and their influence on the glass transition temperature of thin polystyrene films. *European Physical Journal E* **2004**; 15, (4), 473-487.
49. Balazs A.C., Emrick T., Russell T.P.; Nanoparticle polymer composites: Where two small worlds meet. *Science* **2006**; 314, (5802), 1107-1110.

50. Mayes A.M.; Nanocomposites - Softer at the boundary. *Nature Materials* **2005**; 4, (9), 651-652.
51. Janmey P.A., Euteneuer U., Traub P., Schliwa M.; Viscoelastic Properties of Vimentin Compared with Other Filamentous Biopolymer Networks. *Journal of Cell Biology* **1991**; 113, (1), 155-160.
52. Lee J.Y., Zhang Q.L., Emrick T., Crosby A.J.; Nanoparticle alignment and repulsion during failure of glassy polymer nanocomposites. *Macromolecules* **2006**; 39, (21), 7392-7396.
53. Tweedie C.A., Constantinides G., Blackman G., Van Vliet K. Surface and interfacial nanomechanics San Francisco, CA, 2007, pp HH06-01.
54. Noy A., Frisbie C.D., Rozsnyai L.F., Wrighton M.S., Lieber C.M.; Chemical Force Microscopy - Exploiting Chemically-Modified Tips to Quantify Adhesion, Friction, and Functional-Group Distributions in Molecular Assemblies. *Journal of the American Chemical Society* **1995**; 117, (30), 7943-7951.
55. Schonherr H., Feng C.L., Tomczak N., Vancso G.J.; Compositional mapping of polymer surfaces by chemical force microscopy down to the nanometer scale: Reactions in block copolymer microdomains. *Macromolecular Symposia* **2005**; 230, 149-157.
56. Van Vliet K.J., Bao G., Suresh S.; The biomechanics toolbox: experimental approaches for living cells and biomolecules. *Acta Materialia* **2003**; 51, (19), 5881-5905.
57. Forrest J.A., Dalnoki Veress K., Dutcher J.R.; Interface and chain confinement effects on the glass transition temperature of thin polymer films. *Physical Review E* **1997**; 56, (5), 5705-5716.
58. Berg M.C., Yang S.Y., Hammond P.T., Rubner M.F.; Controlling mammalian cell interactions on patterned polyelectrolyte multilayer surfaces. *Langmuir* **2004**; 20, (4), 1362-1368.
59. Mendelsohn J.D., Yang S.Y., Hiller J., Hochbaum A.I., Rubner M.F.; Rational design of cytophilic and cytophobic polyelectrolyte multilayer thin films. *Biomacromolecules* **2003**; 4, (1), 96-106.
60. Yang S.Y., Mendelsohn J.D., Rubner M.F.; New class of ultrathin, highly cell-adhesion-resistant polyelectrolyte multilayers with micropatterning capabilities. *Biomacromolecules* **2003**; 4, (4), 987-994.
61. Chateauneuf G.M., Mikulski P.T., Gao G.T., Harrison J.A.; Compression- and shear-induced polymerization in model diacetylene-containing monolayers. *Journal of Physical Chemistry B* **2004**; 108, (43), 16626-16635.
62. Jarzynski J., Ed. Encyclopedia Of Polymer Science and Technology; John Wiley & Sons, Inc., 2002.
63. Ko M.J., Waheed N., Lavine M.S., Rutledge G.C.; Characterization of polyethylene crystallization from an oriented melt by molecular dynamics simulation. *Journal of Chemical Physics* **2004**; 121, (6), 2823-2832.
64. Lavine M.S., Waheed N., Rutledge G.C.; Molecular dynamics simulation of orientation and crystallization of polyethylene during uniaxial extension. *Polymer* **2003**; 44, (5), 1771-1779.

CHAPTER 4 COMBINATORIAL SCREENING OF MECHANICAL RESPONSE

4.1 Motivation and background

Combinatorial screening of mechanical response is a time-effective option for rapid material discovery in both academic and industrial settings while a lack of mechanistic understanding of composite materials systems and confined volumes of time-dependent materials currently prevents predictive design. In this section, a nanomechanical characterization approach capable of precisely screening the mechanical properties of a large, discrete polymer library comprising nL- to μL- scale material volumes will be introduced. In conjunction with the Langer group, a library of 576 photopolymerizable materials was synthesized and mechanical properties identified using an automated nanomechanical screening system within several days. This polymer library was originally developed to quickly asses cell-growth on substrates made of pairings of twenty-four different monomers and was therefore the first discrete polymer library available to test mechanically. It is important to note that these polymers differ from the model materials characterized in Chapter 3; the mechanical properties of these polymers are not readily predicted from their structure as they have complicated monomer units and their mechanical properties have never been of interest to biologists and chemists. Although, this is not the optimal materials set, it is a proof-of-methodology and may become a powerful tool to materials scientists in industry. This method of high-throughput mechanical screening enables the rapid identification of optimal mechanical characteristics for polymer compounds, and correlates these characteristics with polymer composition, processing, and structure.

4.2 High-throughput polymer synthesis and nanomechanical screening

The following study was published in 2005 with coauthors Daniel G. Anderson and Robert Langer.[1] The samples used in this study were made by the Langer lab.[2]

4.2.1 Introduction and enabling experimental technologies

Combinatorial materials science, an experimental concept developed in the 1960s for alloy development, has resurged via advances in materials synthesis.[3] Application of high-throughput syntheses toward the rapid discovery and optimization of functional materials has required parallel advances in materials characterization.[4] In the context of polymer design for applications ranging from biomaterials to microelectronic insulators, combinatorial approaches can enable systematic, high-throughput surveying of structure-processing-property relationships as a function of composition and operating conditions, in nL to μL volumes.[1,5,6] Here, we develop a high-throughput synthesis / nanomechanical profiling approach capable of accurately screening the mechanical properties of a large, discrete polymer library comprising nL-scale material volumes. Within just a few days, a library of over 1,700 photopolymerizable materials was synthesized and then assayed for mechanical properties using an automated nanomechanical screening system. The approach outlined herein enables the rapid correlation of polymer composition, processing, and structure with mechanical performance metrics.

Efficient and accurate quantification of the mechanical behavior of materials is of broad significance to material discovery, characterization, and model validation. In fact, the mechanical properties of small material volumes (nm^3 – μm^3) are increasingly important aspects of performance in non-structural contexts ranging from low-k dielectric thin films and metal interconnect lines in microelectronics;[7] to abrasion resistant palliative coatings;[8] to photonics-compatible adhesives;[9] to polymeric biomaterials.[1,10,11] Conventional materials development and characterization – the serial process of bulk material synthesis, batch sample preparation, and individual sample testing (e.g., uniaxial tensile testing of several material coupons machined to a specific geometry) – typically

occurs over the span of weeks to months. Parallelization of this effort through combinatorial approaches has the potential to not only screen a large number of materials more efficiently, but also to enable material design through systematic variation in composition, processing, and / or microstructure.[12] Thus, we sought to develop an accurate, high-throughput analysis of relevant mechanical properties of polymers, facilitating subsequent correlation of these properties with material composition and functional performance.

To maximize throughput and mechanical property accuracy while minimizing reagent cost, we considered a discrete polymer library as a microarray format of nL-scale material volumes. While combinatorial biomolecular libraries such as DNA microarrays are used commonly, the synthesis of discrete polymer libraries – an array of μm-scale spots, each representing a stepwise change in composition and / or processing of crosslinked molecules– has been a challenge.[6,13] This is due to both polymer physics, in that monomers deposited in solution must polymerize and crosslink within the small reaction volume of the droplet, and technical challenges such as reliable printing of high viscosity (high molecular weight) solutions. Anderson et al.[2] have recently demonstrated this capability in the context of a wide range of acrylate-based crosslinked polymers printed onto glass slides (Fig. 4.1). Semi-quantitative mechanical characteristics of temperature- and composition-gradient polymer libraries have been assessed via pointwise, microscale impact testing of polymer films peeled from deposition substrates, to correlate processing history of a small subset of the gradient library with impact energy and failure modes.[14] However, for reasons related to solution-based materials synthesis, accurate interpretation of nanomechanical experiments, and application-specific assays of material performance, discrete polymer libraries such as in Fig. 4.1 are often preferable to continuous gradient libraries.[5,15]

Nanoindentation, a continuous measurement of load vs. nanometer-scale displacement of a rigid indenter into a material surface, has been proposed as an experimental approach particularly well-suited to rapid mechanical characterization of the small representative volume elements (RVEs) of gradient or discrete material libraries.[3,5] From the load-

displacement (P – h) hysteretic response of the RVE (Fig. 4.2), bulk mechanical properties including elastic modulus E and semi-quantitative mechanical parameters such as hardness H can be estimated in closed-form.[16-19] As nanoindentation inherently probes nm^3 to μm^3 material volumes, it is theoretically possible to mitigate the contributions of adjacent material by restricting the maximum depth of indentation h_{max} to be much less than the RVE diameter and thickness, or to separate these contributions by semi-analytical deconvolution of the responses of the RVE and adjacent material. This is a particularly important consideration in nanoindentation characterization of thin films,

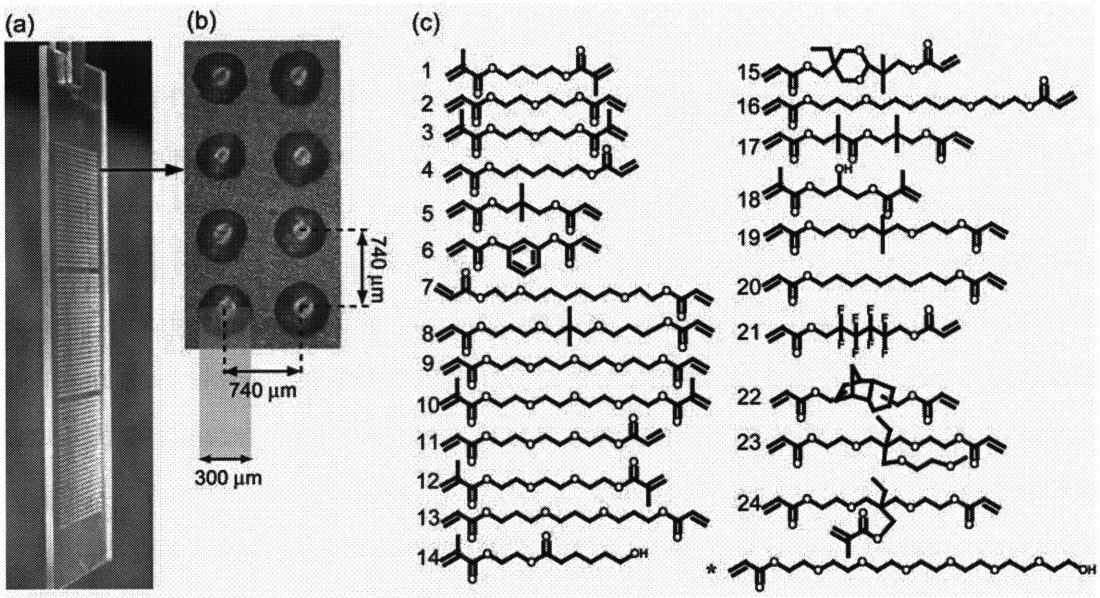

Figure 4.1 Discrete polymer arrays. (**a**) Three 576-spot libraries comprised of pairwise combinations of 24 monomers printed on a glass slide. (**b**) Differential contrast interference image depicts spots of 300 µm diameter and 15 µm thickness printed on a square lattice with 740 µm spacing. (**c**) Monomer unit structure notation. Note that monoacrilate * was added at 30 vol% instead of monomer 17 to increase hydrophilicity.

for which instrumented nanoindentation was originally developed, and has been addressed by several researchers. In fact, nanoindentation has been applied recently to the analysis of gradient libraries of metal alloy thin films: large circular metal films in which the composition is changed continuously as a function of radial distance.[15,20] Technology required to apply this approach to rapid and accurate analysis of large polymer libraries – which unlike metals exhibit large displacements under small applied loads – requires unique considerations. If the rigid indenter geometry can be

approximated as a sharp cone and the indented material can be approximated as a linear elastic-plastic solid, then:

$$E_r = \beta \frac{\left.\frac{dP}{dh}\right|_{P_{max}}}{(A_{max})^{1/2}} \tag{4.1}$$

$$H = \frac{P_{max}}{A_{max}} \tag{4.2}$$

where E_r is the reduced elastic modulus of both the indenter and sample materials, β is a geometrical constant related to the apex angle of the indenter and A_{max} is the maximum projected indentation contact area which can be calculated from the nanoindentation data as a function of h;[18,21] $A_{max} = 24.5h_{max}^2$ assuming ideal geometry of the Berkovich (trigonal pyramid) indenter used herein. The sample elastic modulus E_s can be determined directly as:

$$E_r = \left[\frac{(1-\nu_i^2)}{E_i} + \frac{(1-\nu_s^2}{E_s}\right]^{-1} \tag{4.3}$$

where E_i and ν_i of the diamond indenter are 1100 GPa and 0.07, respectively, and ν_s of the polymer samples is assumed as 0.45. Thus, the applied stress state and calculation of mechanical properties from these data are well defined and validated by applications unrelated to combinatorial materials research.[18,22,23] As discussed in Chapter 2, more complex analyses exist that relate the dynamic $P - h$ response to mechanical properties of time-dependent materials such as polymers. However for this polymer library designed to study cell adhesion - very low stress states - it is the instantaneous, elastic mechanical response that must be correlated with cellular response.

4.2.2 Experimental details

Here, a large array of 1,728 distinct polymer spots was synthesized and analyzed via nanoindentation. In order to determine precision and accuracy of this approach, each sample included arrays printed in triplicate; each of the three arrays comprised 576 unique polymers, arranged in 24 subarrays each comprising 24 polymer spots representing all possible pairwise combinations of 70 vol% major monomer: 30 vol%

minor monomer. Polymer spots were ~300 μm in diameter and ~15 μm in thickness t_p, with 740 μm center-to-center spacing (Fig. 4.1). Monomer structure is shown in Fig. 4.1c.

4.2.2.1 Combinatorial Array Preparation

Polymers were printed in humid Ar-atmosphere on epoxy monolayer-coated glass slides (Xenopore XENOSLIDE E, Hawthorne, NJ[24]) which were first dip-coated in 4 vol% pHEMA, using modifications of robotic fluid handling technology. Spots were polymerized via ~10s exposure to long-wave UV, and dried at < 50 mTorr for at least 7 days prior to nanoindentation array analysis.

4.2.2.2 Nanoindentation

Nanoindentation experiments were conducted on a pendulum-based nanoindenter equipped with a scanning stage (NanoTest600 NT1, MicroMaterials, Wrexham, UK), and fitted with a diamond Berkovich indenter (trigonal pyramid of apex semi-angle ~71°). This instrument has force and displacement resolution of 1.5 μN and better than 0.1 nm, respectively; and force and displacement maxima of 30 mN and 4 μm, respectively. Automated calibration of load and depth transducers requires < 1 hr. All indentations proceeded in load control at a rate of 2 mN/s to a maximum depth of 1.5 μm (or 20 mN, whichever was attained first; the latter condition was attained only for nanoindentations on glass and the stiffest polymers). Positioning of the indenter on the center of the first polymer spot on the array was refined by isoforce profiling of the spot topography via the x-y scanning stage. This approach is similar to scanning probe microscopy, but uses the relatively blunt indenter (radius ~ 100 nm) as the scanning probe. Additionally, conventional profilometry (Tencor P10 Surface Prolifometer, San Jose, CA) was used to determine the average radius of curvature ρ and height t of spots (ρ_{avg} = 1269 μm; t_{avg} = 17 μm). An array of nanoindentations was programmed via stage translation, based on the polymer library spacing (740 μm inter-indentation spacing). Load – depth indentation data were analyzed for E via the method of Oliver and Pharr,[18] which neglects material viscoelasticity and / or pile-up of the indented material, where the unloading portion of the data was analyzed to obtain $dP / dh|_{Pmax}$ by fitting the conventional power law form

from $0.90P_{max}$ to $0.20P_{max}$. The calculation of material stiffness is appropriate for this polymer library because the application space – cell substrates – involves minimal stress levels.

Although nanoindentation is an increasingly automated experiment that is possible using instrumentation ranging from commercial machines to home-built atomic force microscopes, application of this approach for combinatorial materials science – particularly of discrete polymer libraries – requires unique considerations. First, the instrument must include a sample translation stage that facilitates rapid motion among array positions, as well as sufficient load and displacement resolution / maxima to reliably contact relatively soft materials. Secondly, both the load / displacement transducers and the sample translation stage should be stable against thermal / electronic drift, so that no post-test data correction is required and so that every element in the combinatorial array is accessed with high positional accuracy. The absence of piezocrystal-actuation in the load frame of the indenter used herein resulted in frame compliance and load / displacement signals that were extremely stable and repeatable. Third, in experiments different from these that consider microstructurally heterogeneous polymers (e.g., crystalline domains in an amorphous matrix), the maximum indentation volume will dictate whether the calculated properties represent the composite or minor-phase response. Although the solution is not straightforward or general, it is advisable to restrict indentation depths to < 1/10 of minor-phase diameter (typically via sharp geometries) to capture this response and at least 10 times the minor phase diameter (typically via blunt / spherical geometries) to capture the composite mechanical response of the material.

4.2.3 Results and discussion

The triplicate array (1,728 polymer spots) was printed on a standard glass slide in less than 24 hrs via a modified robotic fluid handling system. Upon automated calibration of nanoindenter (MicroMaterials Limited, Wrexham, UK) load and depth transducers (as a function of signal voltages) and readily implemented modifications of translational stage displacement maxima and inter-indentation delay, the entire array (representing 576

unique polymer compositions) was mechanically characterized in 24 hrs of continuous, automated acquisition and analysis of nanoindentation $P - h$ responses (Fig. 4.2), with maximum indentation depths h_{max} = 1.5 μm (~10% t_p) as shown for one of the three arrays in Fig. 4.3. As the array was regularly spaced, automated data acquisition required simply that the first indentation occurred near the center of any spot in a subarray, which could be achieved visually or via profilometric scanning across a polymer spot with the indenter. To establish precision of the approach as well as material uniformity, adjacent subarrays of major monomers 1, 2, 5, and 6, each with 24 individual polymer spots, were

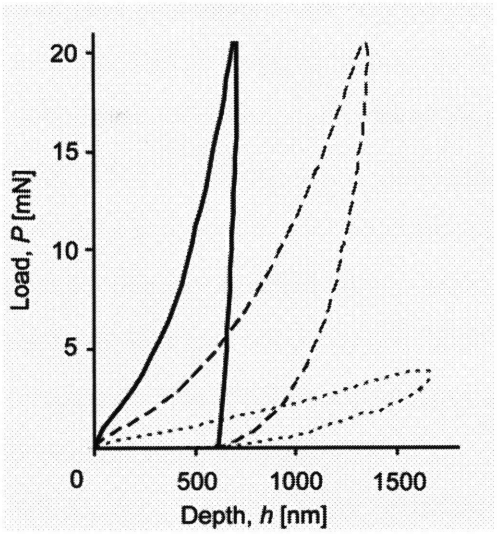

Figure 4.2 Load-displacement (P – h) responses from the borosilicate glass (solid line); a stiff polymer spot (dashed line) and the most compliant polymer spot (dotted line).

nanoindented on each of the triplicate arrays. Under the loading rate and stage displacement rates implemented, a single subarray could be automatically nanoindented and analyzed for E and H in about 1 hr, such that the entire array could be completely and automatically analyzed in a 24 hr cycle. Although cycle time could be decreased considerably and easily through more rapid sample actuation and / or increased loading rates, the nanoindentation analysis employed herein assumes quasistatic loading. This approach is experimentally and analytically simpler to implement than dynamic loading methods that idealize the polymer as a configuration of springs and dashpots, which is an important consideration for robust combinatorial approaches. However, Kossuth et al. have implemented simplifying assumptions to achieve parallel dynamic testing of small, discrete polymer composite libraries (96 sample films of μL-scale volumes and mm-scale

diameter on a flexible polyimide substrate) with reasonable repeatability of estimated complex modulus E_c over different temperatures (standard deviation / mean ranging 11% - 125% for identical polystyrene samples). The speed of this testing was not reported.[25]

Representative results for E for the entire array (576 spots) and a key subset are shown in Fig. 4.3. Several trends are immediately apparent. First, E measured for any particular major monomer is not strongly affected by the addition of a minor monomer. That is, the standard deviation of the average E in a subarray comprising a given major monomer is typically $\leq$ 2 GPa, regardless of minor monomer structure. Thus, although the minor monomer structure clearly modulates E of the copolymer in a consistent fashion, in general the major monomer more strongly influences copolymer stiffness. Secondly, certain minor monomers significantly and consistently affect E within this library. Specifically, when monomers 8 and 11 are the minor components (30 vol%), the resulting copolymers are the most compliant observed within any given major monomer subarray (Fig. 3(b)). Thirdly, the mechanical properties of a copolymer are not necessarily consistent with those of the bulk counterparts. In fact, although polymers with 30 vol% monomer 8 were identified as the most compliant polymers in 92% of the subarrays, the subarray comprising 70 vol% monomer 8 exhibited an average E = 5.7 +/- 0.7 GPa, ranking 12th in compliance among the 24 major monomer combinations. In contrast, polymers comprising a major volume fraction of monomer 11 (70 vol%) resulted in the most compliant subarray of the 24 considered. This finding, which would not be expected solely from consideration of monomer structure and volume fraction, indicates that there is a critical volume fraction of monomer 8, beyond which there exists a microstructural and / or phase change concomitant with a significant increase in mechanical stiffness.

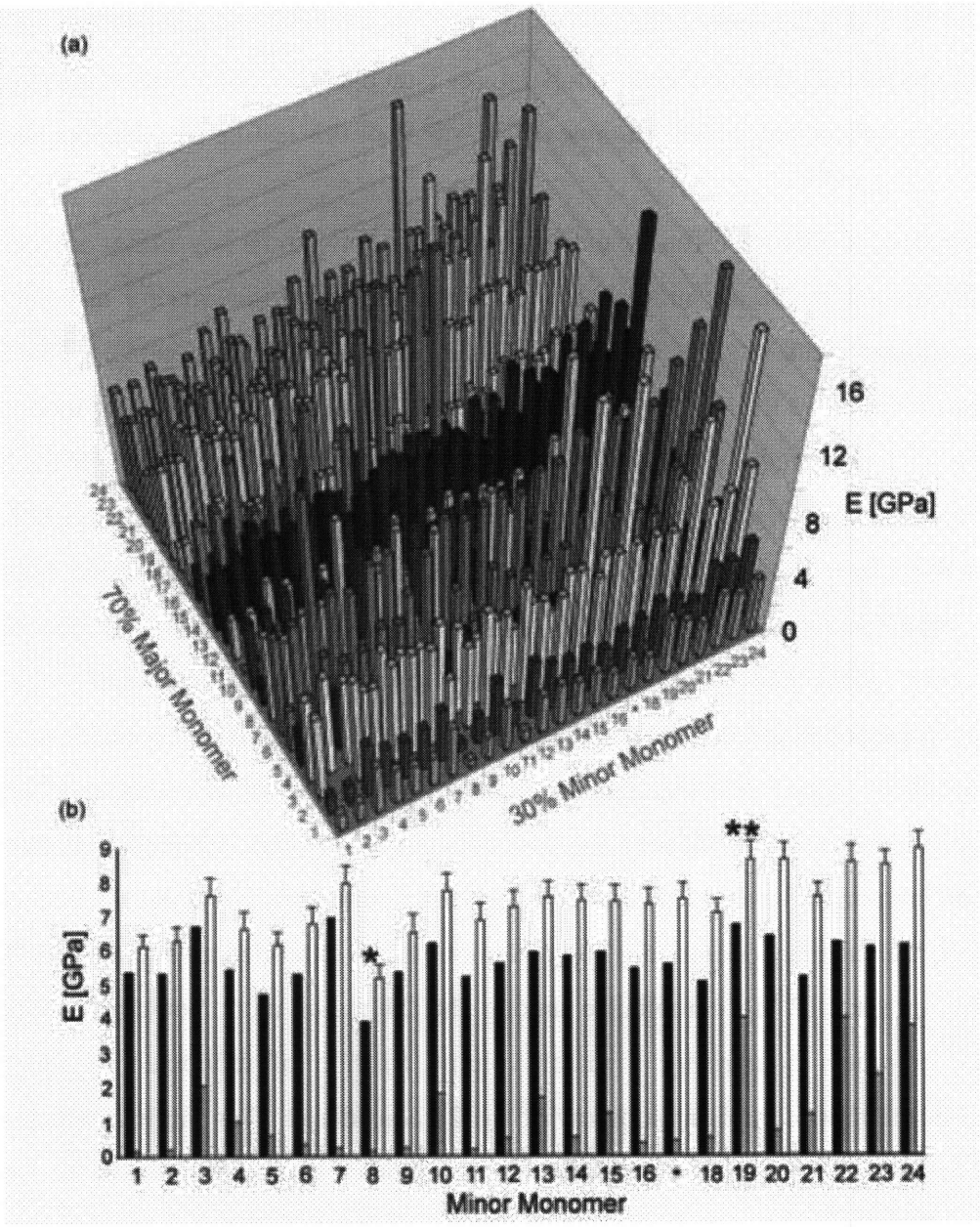

Figure 4.3 Nanoindentation determination of elastic modulus *E* for 576-spot array. (a) Nanoindentation data was acquired in 48 hrs with precision and accuracy. (b) Subarrays of major monomer 8 (black); monomer 11 (grey); and monomer 22 (white). Error bars represent the maximum observed standard deviation of 7.5% among the triplicate subarrays (shown only on major monomer 22). Asterisks mark polymer spots with minimum and maximum *E*.

Importantly, the error bars in Fig. 4.3(b) represent the standard deviation among the triplicate arrays – incidentally acquired on three separate days – and are not greater than 10% for any specific polymer spot. This level of repeatability is comparable to the

standard deviation observed for an array of nanoindentations on a single, bulk metal sample of homogenous microstructure.[26] This underscores the high reliability of the discrete polymer library deposition approach, as well as the precision of the nanoindentation approach used herein.§ Further, the accuracy of this approach is demonstrated by analysis of the nanoindentation response of the glass slide. A series of experiments was conducted in which the inter-indentation spacing was decreased by a factor of two, such that polymer spots and the glass slide were nanoindented alternately. From these data it was found that E_{glass} = 67 +/- 2 GPa, which is consistent with bulk measurements of E_r for borosilicate glass.[27,28] Finally, a small subset of polymer spots was indented to two different h_{max} (1 μm and 1.5 μm) at the same loading rate of 2 mN/s, and the calculated E was found to vary no more than 6.5% as a function of maximum depth / applied load.

4.2.4 Conclusions

In summary, automated array synthesis and indentation analysis provides a general, rapid, precise, and accurate mechanical characterization of discrete material libraries. Automated analysis of a large library of acrylate-based materials demonstrates a range of mechanical properties that are affected by polymer composition in unexpected ways. These studies provide the first large scale analysis of structure / property relationships governing the mechanical response of combinatorial, acrylate-based materials. These methods are suitable for the analysis of crosslinked polymers for functional applications such as biological substrata, enabling studies of mechanical cues on cell behavior.[11,29] Likewise, this approach can be applied to the discovery of new materials that require dual optimization of mechanical and other functional properties, such as environmentally inert

§ Calculated values of H showed similar trends and repeatability (< 8% standard deviation among triplicates), but data are not shown as hardness – the resistance of a material to permanent deformation as quantified by Eq. (2) – is not a true mechanical property, is a poor metric of mechanical behavior in time-dependent materials such as polymers,[19] and is not particularly relevant to the present application of this polymer library.

structural coatings and insulating films in microelectronics. Beyond the immediate utility of material screening and discovery, the experimental capability demonstrated herein could accelerate the development of accurate material models relating monomer structure, microstructure, and mechanical response.

4.3 Combinatorial screening of mechanical response case study: photocrosslinkable and degradable materials

The following case study is part of a publication from 2006 with coauthors Daniel G. Anderson, Nashaud Hossain, Sergio M. Navarro, Darren M. Brey, Robert Langer, and Jason A. Burdick.[30] The Langer Lab developed the material library and characterized the degradation rates.

The rapid mechanical screening method for combinatorial polymer libraries demonstrated in Section 4.2 was applied to a library of photocrosslinkable and degradable polymers - a materials set of increasing importance throughout the field of biomaterials. Biodegradable polymer application fields include dentistry, bone-replacement, and containment and controlled release of biological molecules.[31,32] In addition to systems requiring specific degradation properties, photoinitiated control of polymerization enables complex patterning and processing which is critical for fields such as microfluidics.[33,34] Although specific photopolymerizable and degradable materials have been developed,[35-38] desired properties such as degradation rate and mechanics cannot be predicted from the composition and structure of the polymer constituents.

4.3.1 Methods and materials

4.3.1.1 Macromer synthesis and characterization

To address this needs for biomaterials discovery Dan Anderson in the Langer Lab synthesized degradable photocrosslinkable macromers through the conjugate addition of primary or bis(secondary) amines to diacrylates in a 10 ml scintillation vial (Figure 4.4) to form functionalized poly(β-amino ester)s. The vial was reacted while stirring at 90°C overnight. Samples were stored at 4°C prior to analysis. The chemical structures and molecular weights of several polymer systems were verified with gel permeation

chromatography and ^{1}H-NMR (data not shown). The benefits of this polymer library are that: i) amine and diacrylate monomer reagents are inexpensive and commercially available, ii) polymerization can be accomplished without the need for additional protection / deprotection schemes because amines participate directly in the bond-forming processes in these reactions, iii) no byproducts are generated during synthesis which eliminates the need for purification steps, and iv) the conjugate addition reaction is generally tolerant of additional functionality such as alcohols, ethers, and tertiary amines, which further expands the available amines and diacrylates available for the library.

4.3.1.2 Polymerization and degradation

The library of 120 diacrylate terminated poly(β-amino ester) macromers was synthesized using the reagents shown in Figure 4.2. The macromers were mixed with the photoinitiator 1,1-dimethoxy-1-phenyl acetophenone (DMPA, Sigma, dissolved 10 wt% in methylene chloride) and placed in a vacuum desiccator overnight for solvent removal. The macromer / initiator mixture was placed between two glass slides separated with a 1mm spacer and polymerized with exposure to ~10 mW/cm^2 ultraviolet light (Blak-Ray® UV lamp, 365 nm) for 5 minutes. These reagents were chosen to provide chemical diversity, including variations in hydrophobicity.[39] The GPC results indicate that macromer molecular weights are ~2-3 kDa with polydispersities of ~1.5. Eighty-nine liquid macromers from this library were polymerized into crosslinked and degradable networks of approximately 200 mg, and the degradation behavior was monitored by the Langer Lab over several months in triplicate. We characterize degradation as the ability to cleave ester linkages in the polymer networks, which releases network components (i.e., crosslinks, kinetic chains) when immersed in 150 mM phosphate buffered saline while rotating. Polymer slabs (~0.8 cm×1.2 cm, 3 per macromer) were cut from the samples, weighed, and placed in tissue culture cassettes. The cassettes were submerged in 150 mM phosphate buffered saline (PBS) and placed on an orbital shaker in a 37°C incubator for degradation. At each time point, samples were removed, dried and weighed to determine the mass loss. A3, A5, A10, A12, B3, B9, B12, C5, C7, C9, D3, D5, D9, D10, D12, E10, F3, F5, F8, F9, G3, G8, G10, G12, I3, I9, J5, J7, J9, J10, J12 crosslinked during the polymerization process and were not evaluated in the degradation study.

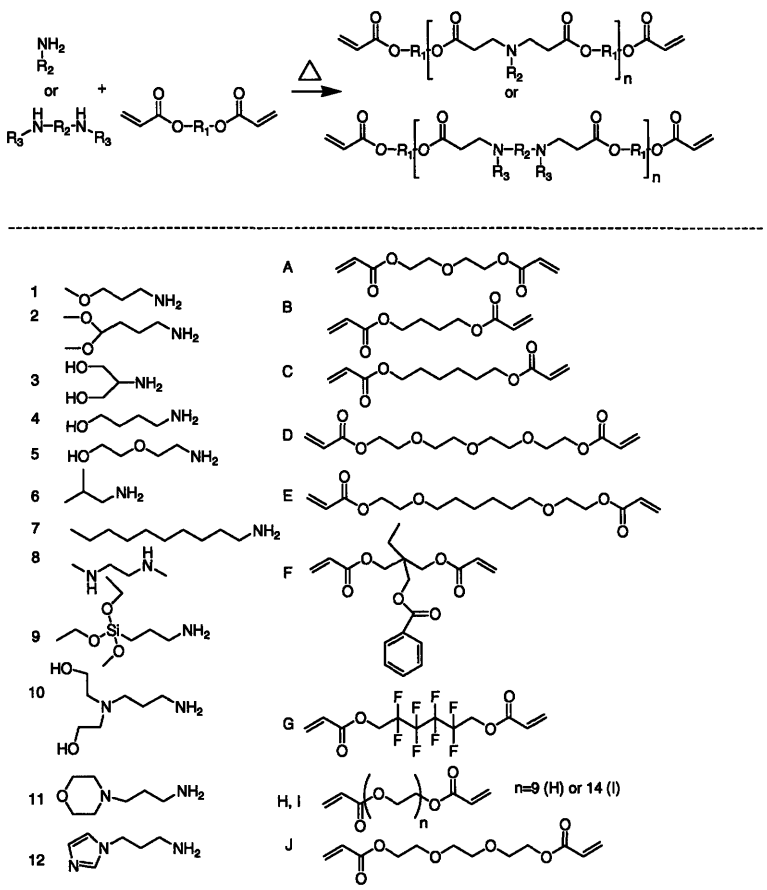

Figure 4.4 General polymerization scheme and chemical structures. Diacrylated macromers were synthesized by the condensation polymerization of an amine with a diacrylate (top). The various monomers used included 12 amines and 10 diacrylates (bottom) to produce a library of 120 photopolymerizable macromers. The macromers were crosslinked into polymers with exposure to ~10 mW/cm^2 ultraviolet light (365 nm) for 5 minutes.

4.3.1.3 Mechanical properties characterization

To create a grid of polymer spots of systematically varied properties for mechanical testing macromers were dissolved at 1:2 v:v ratio in tetrahydrofuran containing 2 wt% DMPA and a spot volume of 10 µl was pipetted onto the surface of an epoxy monolayer-coated glass slide (Xenopore XENOSLIDE E, Hawthorne, NJ) (~18 spots per slide). The THF was allowed to evaporate for 30 - 60 minutes at room temperature. The deposited macromer was then polymerized by exposure to long-wave UV (Blak-Ray®) for 10 minutes in the presence of argon. They were again vacuum desiccated for at least 7 days prior to analysis. Polymer spot thickness was analyzed via contact profilometry (Tencor

P10 Surface Profilometer, San Jose, CA) and was > 200 μm for all spots. Nanoindentation was conducted on a pendulum-based nanoindenter (force resolution: 1.5 μN, displacement resolution: 0.1 nm, force maxima: 30 mN, displacement maxima: 4 μm) equipped with a scanning stage (NanoTest600 NT1 and NT0, Micro Materials, Wrexham, UK) and fitted with a spherical indenter of radius R = 500 μm. For this contact-based approach, it was necessary that polymers adhered well to the underlying slide substrate; polymers not meeting this criterion upon photocrosslinking were excluded from this analysis. Indentations were conducted in load control at a rate of 5 μN/s to a maximum depth of 600 nm, resulting in maximum loads ranging from 20 μN to 800 μN and contact strains < 1%. This method was previously described in detail.[1] Load-depth responses were analyzed for E via the method of Field and Swain.[40] Each of the 79 polymers was synthesized and analyzed in triplicate, with three indentations conducted per spot or a total of nine indentations per polymer.

4.3.2 Results and discussion

As the mechanical properties of biomaterials are typically important for medical applications, the library was also mechanically characterized. The elastic modulus (E) was determined for ~80 members of the polymer library using a rapid nanoindentation technique, displayed in Figure 4.5.[1] Within this library subset, E varied from ~4 to ~350 MPa with an average modulus of 21.2 MPa (standard deviation of 5.3% among experiments on an individual polymer). Approximately 95% of the polymers exhibited E within the range of 4 to 25 MPa, which is on the order of moduli for elastomers and non-biodegradable polyurethanes. However, several polymers (e.g., F4, G9, H9) exhibited significantly greater E, on the order of moduli for nylon and high-density polyethylene.[41] [42] Although it would have been difficult to predict a priori that these specific polymers would exhibit superior elastic stiffness, especially since polymers with similar chemistry had moduli that were much lower, this property may be desirable for certain load-bearing or stress-matching applications. Importantly, mechanical stiffness does not correspond directly with degradation rate, demonstrating the potential to derive materials from this library with optimal stiffness and degradation behavior independently.

In summary, the first library of degradable photocrosslinked materials was synthesized and characterized. The large diversity in degradation profiles and elastic moduli demonstrates the potential of this approach in the rapid optimization of material properties. Since crosslinking is radically initiated, these materials may also find non-medical uses as degradable plastics. The chemical diversity presented by these materials could offer other advantages, including potential for specific cellular interactions, [2] modification of toxicity, and the facilitation of drug delivery.[2] [43] We believe this combinatorial approach will provide a new method for identification and optimization of degradable and photopolymerized materials.

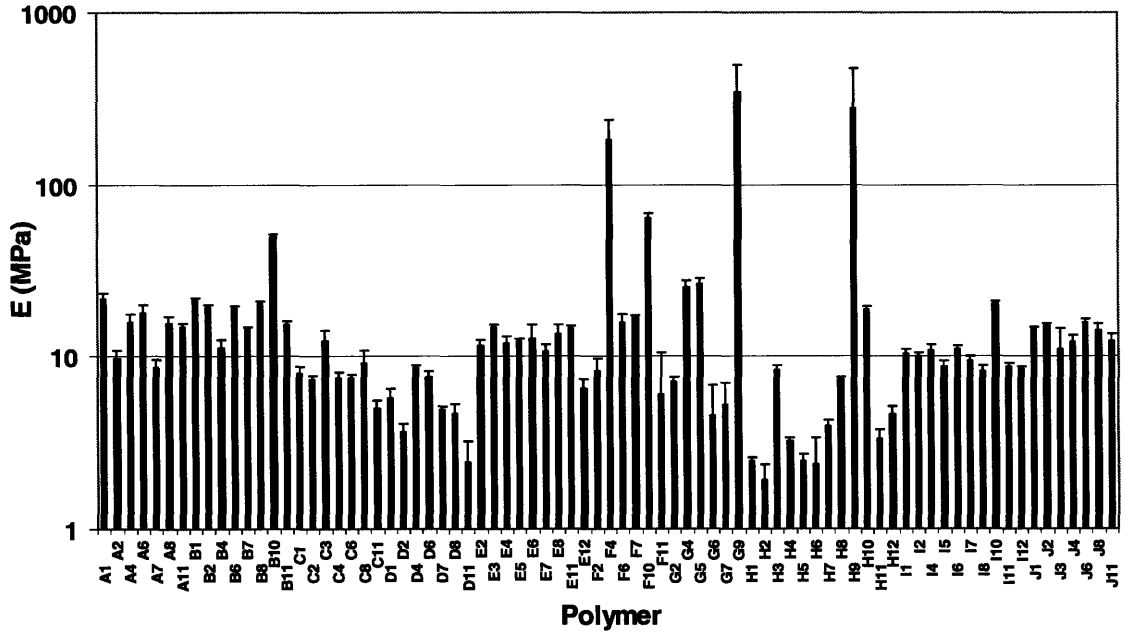

Figure 4.5 Mechanical behavior of polymers fabricated from the macromer library. The elastic modulus (*E*), determined with a nanoindentation method, is reported for 79 of the candidate polymers from the macromer library. These polymers exhibit a range of E ranging from ~4 to ~350 MPa (note the log scale on the y-axis).

4.4 CONCLUSIONS

The two case studies presented in this chapter are ideal for rapid mechanical screening of the polymer libraries when the instantaneous, elastic response is the primary mechanical design parameter. However, for most polymer applications it is important to consider the time-dependent mechanical behavior, resistance to plastic deformation, or response to high-velocity impact testing. To address the development of such application spaces, the next step in the contact deformation characterization of arrays of functional polymers is to characterize viscoelastoplastic responses via high-throughput, automated instrumented indentation.

REFERENCES

1. Tweedie C.A., Anderson D.G., Langer R., Van Vliet K.J.; Combinatorial material mechanics: High-throughput polymer synthesis and nanomechanical screening. *Advanced Materials* **2005**; 17, (21), 2599-+.
2. Anderson D.G., Levenberg S., Langer R.; Nanoliter-scale synthesis of arrayed biomaterials and application to human embryonic stem cells. *Nature Biotechnology* **2004**; 22, (7), 863-866.
3. Stafford C.M., Harrison C., Beers K.L., Karim A., Amis E.J., Vanlandingham M.R., Kim H.C., Volksen W., Miller R.D., Simonyi E.E.; A buckling-based metrology for measuring the elastic moduli of polymeric thin films. *Nature Materials* **2004**; 3, (8), 545-550.
4. Schmatloch S., Schubert U.S.; Techniques and instrumentation for combinatorial and high-throughput polymer research: Recent developments. *Macromolecular Rapid Communications* **2004**; 25, (1), 69-76.
5. Meredith J.C., Karim A., Amis E.J.; Combinatorial methods for investigations in polymer materials science. *Mrs Bulletin* **2002**; 27, (4), 330-335.
6. Stoykovich M.P., Cao H.B., Yoshimoto K., Ocola L.E., Nealey P.F.; Deformation of nanoscopic polymer structures in response to well-defined capillary forces. *Advanced Materials* **2003**; 15, (14), 1180-+.
7. Itano K., Choi J.Y., Rubner M.F.; Mechanism of the pH-induced discontinuous swelling/deswelling transitions of poly(allylamine hydrochloride)-containing polyelectrolyte multilayer films. *Macromolecules* **2005**; 38, (8), 3450-3460.
8. Hsing A.W., Gao Y.-T., Wu G., Wang X., Deng J., Chen Y.-L., Sesterhenn I.A., Mostofi F.K., Benichou J., Chang C.; Polymorphic CAG and GGN repeat lengths in the androgen receptor gene and prostate cancer risk: a population-based case-control study in China. *Canc. Res.* **2000**; 60, 5111-5116.
9. Yacobi B.G., Martin S., Davis K., Hudson A., Hubert M.; Adhesive bonding in microelectronics and photonics. *Journal of Applied Physics* **2002**; 91, (10), 6227-6262.
10. Engler A.J., Richert L., Wong J.Y., Picart C., Discher D.E.; Surface probe measurements of the elasticity of sectioned tissue, thin gels and polyelectrolyte multilayer films: Correlations between substrate stiffness and cell adhesion. *Surface Science* **2004**; 570, 142-154.
11. Thompson M., Berg M., Tobias I., Rubner M., Van Vliet K.; Tuning compliance of polyelectrolyte multilayers to modulate cell adhesion. *Biomaterials* **2005**; in press,
12. Meier M.A.R., Schubert U.S.; Combinatorial polymer research and high-throughput experimentation: powerful tools for the discovery and evaluation of new materials. *Journal of Materials Chemistry* **2004**; 14, 3289-3299.
13. Leugers A., Neithamer D.R., Sun L.S., Hetzner J.E., Hilty S., Hong S., Krause M., Beyerlein K.; High-throughput analysis in catalysis research using novel approaches to transmission infrared spectroscopy. *Journal of Combinatorial Chemistry* **2003**; 5, (3), 238-244.
14. Sormana J.-L., Meredith J.C.; High-Throughput Screening of Mechanical Properties on Temperature-Gradient Polyurethaneurea Libraries. *Macromolecular Rapid Communications* **2003**; 24, 118-122.

15. VanLandingham M.R., Chang N.K., Drzal P.L., White C.C., Chang S.H.; Viscoelastic characterization of polymers using instrumented indentation. I. Quasi-static testing. *Journal of Polymer Science Part B-Polymer Physics* **2005**; 43, (14), 1794-1811.
16. Venkatesh T.A., Van Vliet K.J., Giannakopoulos A.E., Suresh S.; Determination of elasto-plastic properties by instrumented sharp indentation: Guidelines for property extraction. *Scripta Materialia* **2000**; 42, (9), 833-839.
17. Kaddurah-Daouk R., Papoulas O., Greene J.M., Baldwin A.S., Kingston R.E.; Activation and repression of mammalian gene expression by the c-*myc* protein. *Genes Dev.* **1987**; 1, 347-357.
18. Oliver W.C., Pharr G.M.; An Improved Technique for Determining Hardness and Elastic-Modulus Using Load and Displacement Sensing Indentation Experiments. *Journal of Materials Research* **1992**; 7, (6), 1564-1583.
19. Doerner M.F., Nix W.D.; A method for interpreting the data depth-sensing indentation instruments. *Journal of Materials Research* **1986**; 1, 601-609.
20. Rar A., Frafjord J.J., Fowlkes J.D., Specht E.D., Rack P.D., Santella M.L., Bei H., George E.P., Pharr G.M.; PVD synthesis and high-throughput property characterization of Ni-Fe-Cr alloy libraries. *Measurement Science & Technology* **2005**; 16, (1), 46-53.
21. Sneddon I.N.; The relation between load and penetration in the axisymmetric Boussinesq problem for a punch of arbitrary profile. *International Journal of Engineering Science* **1965**; 3, (1), 47.
22. Van Vliet K.J., Li J., Zhu T., Yip S., Suresh S.; Quantifying the early stages of plasticity through nanoscale experiments and simulations. *Physical Review B* **2003**; 67, (10),
23. VanLandingham M.R., Villarrubia J.S., Guthrie W.F., Meyers G.F.; Nanoindentation of polymers: An overview. *Macromolecular Symposia* **2001**; 167, 15-43.
24. Xenopore. Xenopore, Hawthorne, NJ, 2005.
25. Kossuth M.B., Hajduk D.A., Freitag C., Varni J.; Parallel dynamic thermomechanical measurements of polymer libraries. *Macromolecular Rapid Communications* **2004**; 25, (1), 243-248.
26. Van Vliet K.J., Prchlik L., Smith J.F.; Direct measurement of indentation frame compliance. *Journal of Materials Research* **2004**; 19, 325-331.
27. http://www.matweb.com/search/SpecificMaterial.asp?bassnum=BGLAS0.
28. http://www.sas.org/E-Bulletin/archive/reference/material/byMaterial.html. 2005.
29. Shukla A., Dunn A.R., Moses M.A., Van Vliet K.J.; Endothelial cells as mechanical transducers: Effects of cyclic strain on enzymatic activity and organization. *Mechanics and Chemistry of Biosystems* **2004**; 4,
30. Anderson D.G., Tweedie C.A., Hossain N., Navarro S.M., Brey D.M., Van Vliet K.J., Langer R., Burdick J.A.; A combinatorial library of photocrosslinkable and degradable materials. *Advanced Materials* **2006**; 18, (19), 2614-+.
31. Anseth K.S., Burdick J.A.; New directions in photopolymerizable biomaterials. *MRS Bulletin* **2002**; 27, 130-136.
32. Fisher J.P., Dean D., Engel P.S., Mikos A.G.; Photoinitiated polymerization of biomaterials. *Annual Review of Materials Research* **2001**; 31, 171-181.
33. Eddington D.T., Beebe D.J.; Flow control with hydrogels. *Adv Drug Deliv Rev* **2004**; 56, (2), 199-210.

34. Khademhosseini A., Yeh J., Jon S., Eng G., Suh K.Y., Burdick J.A., Langer R.; Molded polyethylene glycol microstructures for capturing cells within microfluidic channels. *Lab Chip* **2004**; 4, (5), 425-430.
35. Anseth K.S., Shastri V.R., Langer R.; Photopolymerizable degradable polyanhydrides with osteocompatibility. *Nat Biotechnol* **1999**; 17, (2), 156-159.
36. Elisseeff J., Anseth K., Sims D., McIntosh W., Randolph M., Langer R.; Transdermal photopolymerization for minimally invasive implantation. *Proc Natl Acad Sci U S A* **1999**; 96, (6), 3104-3107.
37. Fisher J.P., Holland T.A., Dean D., Engel P.S., Mikos A.G.; Synthesis and properties of photocross-linked poly(propylene fumarate) scaffolds. *J Biomater Sci Polym Ed* **2001**; 12, (6), 673-687.
38. Smeds K., Grinstaff M.; Photocrosslinkable polysaccharides for in situ hydrogel formation. *JOURNAL OF BIOMEDICAL MATERIALS RESEARCH* **2001**; 54, (1), 115-121.
39. Anderson D.G., Lynn D.M., Langer R.; Semi-automated synthesis and screening of a large library of degradable cationic polymers for gene delivery. *Angew. Chem. Int. Ed. Engl.* **2003**; 42, 3153-3158.
40. Field J.S., Swain M.V.; A Simple Predictive Model for Spherical Indentation. *Journal of Materials Research* **1993**; 8, (2), 297-306.
41. Wang Q., Gao J., Wang R., Hua Z.; Mechanical and rheological properties of HDPE/graphite composite with enhanced thermal conductivity. *Polymer Composites* **2001**; 22, (1), 97-103.
42. Unal H., Mimaroglu A.; Influence of filler addition on the mechanical properties of nylon-6 polymer. *Journal of Reinforced Plastics and Composites* **2004**; 23, (5), 461-469.
43. Leach J.K., Mooney D.J.; Bone engineering by controlled delivery of osteoinductive molecules and cells. *Expert Opin Biol Ther* **2004**; 4, (7), 1015-1027.

CHAPTER 5 CONCLUSIONS AND DIRECTIONS FOR FUTURE RESEARCH

5.1 THESIS SUMMARY

This thesis has presented mechanical testing techniques that measure key aspects of polymer response for bulk as well as confined sample geometries. Several nanoindentation enabled experiments, including creep compliance and relaxation studies were used to characterize the time-dependent responses of glassy and rubbery polymers as well as identify the limitations of traditional experimental practices and analyses. The contact mechanics of near-surface polymer indentations were investigated for a set of model glassy polymers as a function of polymer structure and environmental conditions. An interphase was found to be induced by nanoscale contact deformation of amorphous polymers and was studied as a function of probe surface charge through both experiment and simulation. Further, a proof-of-principle study on high-throughput characterization of combinatorial polymer libraries was demonstrated and applied to a biodegradable polymer library.

Chapter1

Chapter 1 motivated this thesis research by briefly introducing well known bulk polymer characterization techniques and explaining why bulk mechanical testing techniques are not applicable to very small volumes of material. Nanoindentation experiments and analysis were summarized and defended as a potential route to quantify the mechanical properties of polymers confined to small length scales. This chapter also discussed current experimental and analytical alternatives to nanoindentation, and provided background in the areas of polymer molecular dynamics simulations and combinatorial screening of mechanical properties.

Chapter 2

In Chapter 2 the nuances of contact deformation of time-dependent materials were explored through several alternative nanoindentation-enabled experimental techniques. These experiments demonstrated the utility of specific energy absorption as a model-free

analysis to characterize polymer deformation as a function of experimental factors such as loading rate and polymer properties such as Mw and monomer structure. The evolution of the analytical expression for creep compliance was summarized and experimental results sharp and spherical creep data on both thermoplastic and thermoset materials are presented and discussed. An extensive set of amorphous and semi-crystalline polymers, some rubbery and some glassy, were characterized. None of the samples were found to respond linear viscoelastically under indentation with a sharp probe, while the creep compliance measured under a spherical indenter (low strain) was independent of load and loading rate. Further, the recovery of glassy polymer surfaces post nanoindentation were investigated using atomic force microscopy and the value of indentation hardness as a metric for polymeric materials was shown to be limited.

Chapter 3

Glassy polymer surfaces were mechanically probed through contact deformation to indentation depths between 5 nm and 250 nm from the polymer surface. The apparent stiffening of the polymer surface response was studied as a function of polymer molecular weight, monomer type (persistence length) and environmental factors (humidity) after experimental artifacts were thoroughly taken into account. For all control experiments the stiffening trend as indentation depths become shallower persisted; only the magnitude changed for a change in monomer type. Chemically modified spherical probes were used to test polymer mechanical response as a function of the probe surface charge. These functionalized probes were used to test glassy polystyrene via nanoindentation as well as atomic force microscopy. The amine functionalization (net positive charge) showed no deviation from bare probe response while the carboxyl functionalization (net negative) revealed a stiffer response. To more efficiently attain broad conclusions about the effect of probe surface charge on polymer surface mechanics, reactive molecular dynamics simulations were used to robustly conclude that changes in probe functionalization do not cause a change in mechanical response through the breaking or formation of bonds.

Chapter 4

In Chapter 4 combinatorial nanomechanics was introduced as a rapid, high-throughput mechanical screening technique directly applicable to material discovery in material classes where structure-composition-property relationships are not yet fully understood. In this chapter, a proof-of-principle study was presented in which a 576-spot acrylate library was automatically characterized within 24 hours of instrument time. In addition, the technique was applied to a discrete biodegradable materials library that resulted in discovery of a wide range of mechanical and degradation property combinations relevant to a range of application spaces.

5.2 CORRELATION OF MECHANICAL AND STRUCTURAL PROPERTIES

In Section 2.2 the primary challenges of relating polymer mechanical properties quantitatively to polymer physical / structural properties included: 1. many interdependent polymer structural variables, the individual effect of which was difficult to isolate and 2. mechanical metrics that either assume time-independence or linear viscoelasticity. In this thesis, several small-scale experimental approaches have been investigated in terms of polymer physical attributes.

Table 5.1 summarizes the **type of correlation** [*positive or negative*] and **strength of correlation** [*strong, medium, weak or none*] between the **polymer physical properties** [*molecular weight (radius of gyration), monomer type, persistence length, crystallinity and glass transition temperature*] and **polymer mechanical properties** [*elastic (bulk stiffness, surface stiffness), viscoelastic (creep compliance), and viscoelastoplastic (recovery)*] and also includes the **weight of the conclusion** based on the results in this thesis [*confident or tentative*].

Table reading guide: the persistence length L_p was found to have a WEAK and INDIRECT relationship to the contact creep compliance L_p. This indicates that when the persistence length increased, the creep compliance would be expected to decrease because increased inflexibility of the molecule resists deformation. However, J_c did not

always decrease for increased L_p, and therefore L_p exerts a weak effect on the contact creep compliance. However, this conclusion in tentative because a change in L_p was never isolated from all other physical parameters.

Table 5.1 Synthesis of polymer property data for the mechanical metrics studied rigorously in this thesis.

	Elastic	Elastic	Viscoelastic	VE-plastic
	Apparent stiffness E (bulk)	Apparent stiffness E_s(surface)	Creep compliance J_c	$\Delta h(t) / h_{max}$
Molecular weight M_w (Radius of gyration, R_g)	WEAK Positive CONFIDENT	NONE CONFIDENT	Mw: STRONG Negative Mc: STRONG Positive CONFIDENT	WEAK Positive TENTATIVE
Monomer	WEAK Changes CONFIDENT	WEAK Changes CONFIDENT	STRONG Changes CONFIDENT	STRONG Changes CONFIDENT
Persistence length L_p (aspect of monomer)	NONE TENTATIVE	NONE TENTATIVE	NONE TENTATIVE	NONE / WEAK Negative TENTATIVE
Time constant τ	NONE TENTATIVE	NONE TENTATIVE	NONE TENTATIVE	WEAK Negative TENTATIVE
T_g ($T_{test} < T_g$)	NONE TENTATIVE	NONE TENTATIVE	NONE CONFIDENT	NONE CONFIDENT
T_g ($T_{test} > T_g$) Semi-crystalline vs. amorphous	STRONG Positive CONFIDENT	No DATA	STRONG Negative TENTATIVE	STRONG Negative TENTATIVE

Figures 5.1 - 5.4 summarize the data from this thesis that support each of the observed correlations in Table 5.1 that relate polymer structural length scales, time scales, and

physical properties to changes in mechanical behavior (elasticity, viscoelasticity, and viscoelastoplasticity). Although monomer choice is contained in Table 5.1, the effect of this variable on mechanical response is not associated with a single, measurable metric, but is influenced by several factors including monomer steric hindrance and chemical composition. Therefore the structural and physical properties discussed below and described by Figures 5.1-5.4 are comprised of those variables that can be measured and are of interest in terms of nm- and μm-scale contact deformation.

Figure 5.1 considers changes in the bulk elastic modulus E as inferred from instrumented indentation on the μm-scale in terms of polymer structural and physical properties. Figure 5.1a) depicts E as a function of molecular weight for five common engineering polymers, described further in Table 2.1. Among the polymers tested$E$ appears to have a weak positive correlation with molecular weight M_w. This correlation is most apparent when the M_w is less than the entanglement molecular weight M_e. For those polymers for which $M_w >> M_e$, including PS, LU, and PL, only a mild positive correlation is implied by the comparison of the low M_w (LU) and high M_w (PL) poly(methyl methacrylate) samples. The two semicrystalline polymers, PP and PE, are below their glass transition temperature and are more compliant than the glassy polymers of equivalent M_w. The persistence length L_p, defined in Chapter 2, describes the length scale over which the polymer macromolecule can bend. PC has the greatest L_p of the polymers considered because it has a long and rigid monomer unit containing two benzene rings along the monomer backbone. No correlation is observed between L_p and E (Fig. 5.1b), which makes sense since L_p describes the ability for a polymer to deform via molecular motion, - a process that is minimal in glassy polymers - making this structural length scale L_p irrelevant to the instantaneous elastic response. Since the characteristic time of retardation τ trends with the persistence length, there was no correlation between E and τ (Fig. 5.1c). This decoupling is not surprising since the elastic modulus measures the instantaneous response while τ describes a time-dependent response. Finally, the dependence of the bulk elastic modulus on the difference between the testing temperature T_{test} and the glass transition temperature T_g was considered. As T_g becomes increasingly < T_{test}, the polymeric response becomes increasingly fluid, causing a strong positive

correlation between T_g and E. However, for $T_g >> T_{test}$, the glassy modulus is nearly constant and no correlation is observed (Figure 5.1d). In short, even though the T_g is representative of several structural / physical polymer properties, there is no dramatic effect on mechanical response beyond whether the testing temperature is above or below the glass transition temperature.

Figure 5.2 focuses on the apparent instantaneous response to contact deformation E_s within 200 nm from the free surface - a length scale comparable to the macromolecular chain dimensions. The near-surface apparent stiffness was measured on well-characterized engineering polymers described in Chapter 3. Figure 5.2a depicts E_s at two indentation depths (5 nm and 200 nm) for two PS samples of significantly varied M_w. As explored in Chapter 3, there is an increased apparent stiffness for shallower indentation depths but no change in stiffness was observed for changes in M_w. The lack of change in response to varied M_w somewhat surprising because 12 kg/mol is close to the M_e of PS, but it is likely that E_s would decrease for a further decreased M_w. No correlation was identified between E_s and either L_p (Fig. 5.2b) or τ (Fig. 5.2c) for the same reasons discussed for Figs. 5.1b-c. Further there is no correlation observed between the glass transition temperature and the apparent elastic response near the surface for $T_g >> T_{test}$,, Fig. 5.2d. Near-surface experiments were not conducted for semi-crystalline polymers for which $T_g < T_{test}$,, although the confined mechanical response of such heterogeneous materials will be an area of future interest for this field.

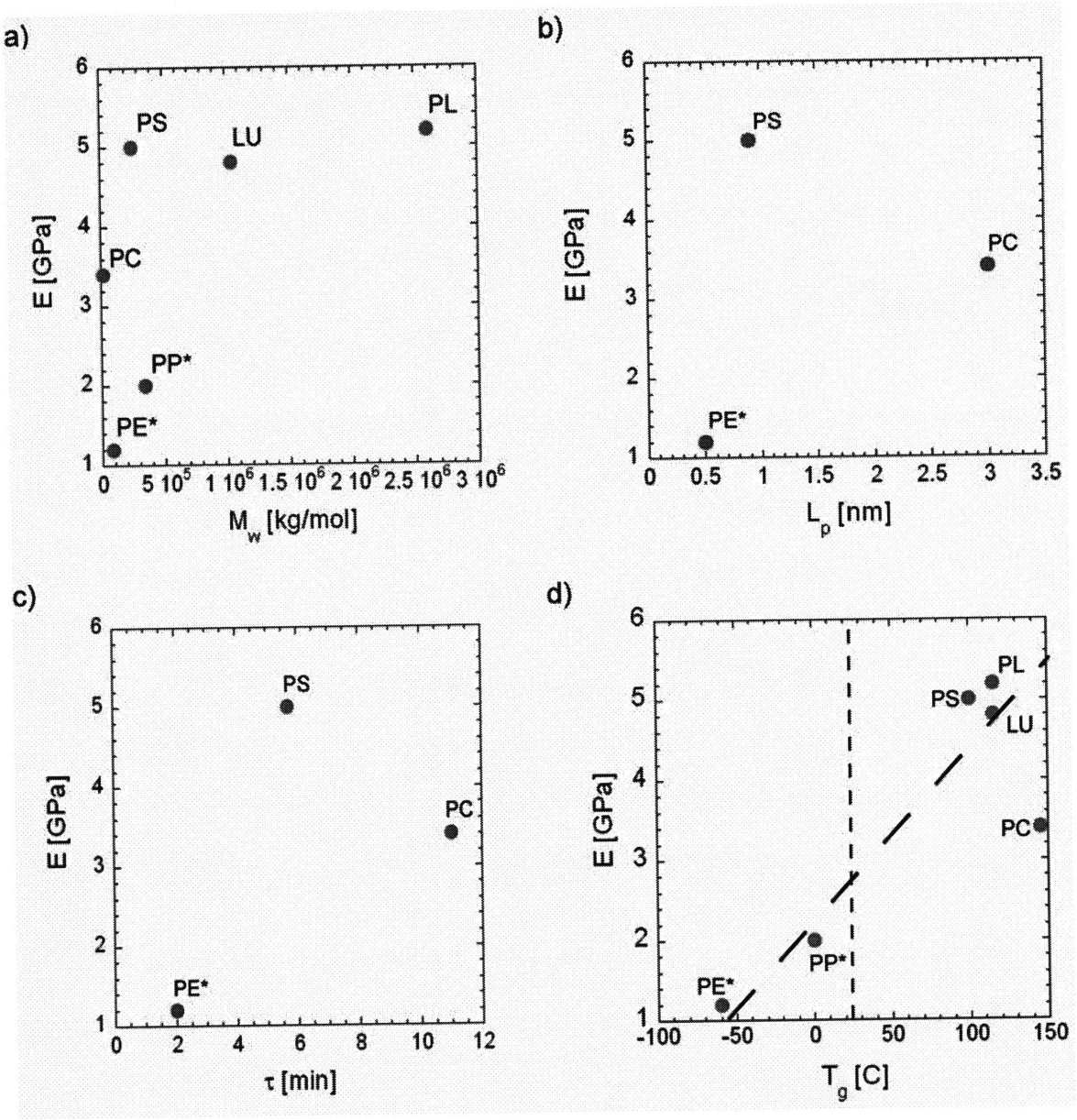

Figure 5.1 Elastic modulus E as inferred from instrumented indentation on the μm-scale as a function of polymeric structural length-scales, time-scales, and physical properties. Data for E as a function of weight average molecular weight (M_w), persistence length (L_p), characteristic retardation time (τ), and glass transition temperature (T_g) is given as available for an array of amorphous (polystyrene (PS), poly(methyle methacrylate) (LU and PL), polycarbonate (PC)) and semi-crystalline (polyethylene (PE), polypropylene (PP)) polymers.

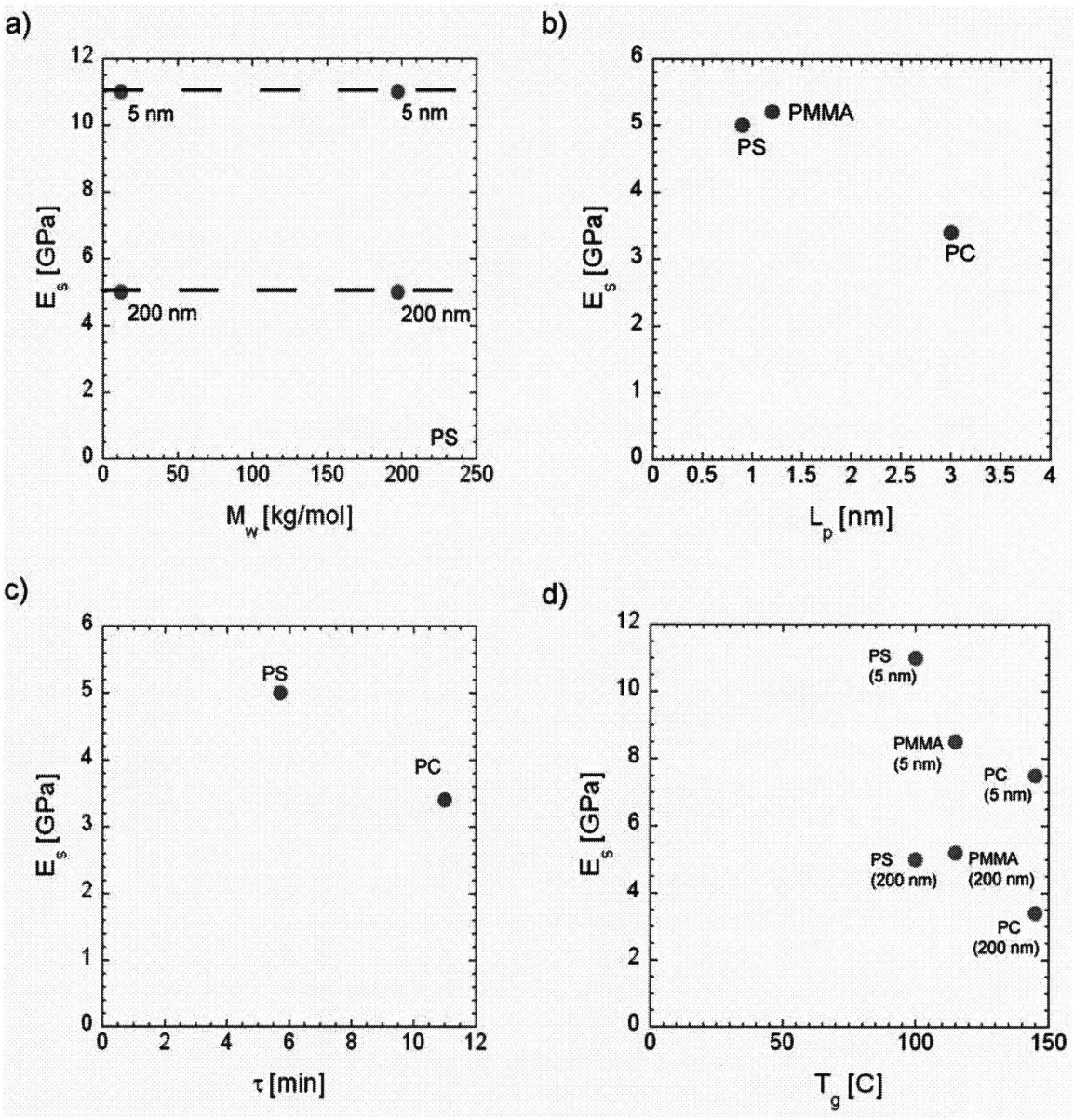

Figure 5.2 Apparent elastic modulus of near-surface polymeric material E_{surf} as inferred from instrumented indentation on the nm-scale as a function of polymeric structural length-scales, time-scales, and physical properties. Data for E_{surf} as a function of weight average molecular weight (M_w), persistence length (L_p), characteristic retardation time (τ), and glass transition temperature (T_g) is given as available for an array of amorphous (polystyrene (PS), poly(methyle methacrylate) (LU and PL), polycarbonate (PC)) and semi-crystalline (polyethylene (PE), polypropylene (PP)) polymers.

Figure 5.3 considers the time-dependent responses using the contact creep compliance metric J_c as defined in Section 2.3 of a range of polymers described in Table 2.2. Figure 5.3a suggested a weak negative correlation between molecular weight and creep compliance at 10 s post-loading to a specific load for glassy polymers, $T_g >> T_{test}$,.

Polymers such as PE and PP, for which $T_g < T_{test}$, creep significantly more because macromolecules can shift more easily relative to one another in response to the applied load. Neither, persistence length nor characteristic retardation time appear to correlate with creep compliance. Intuitively, a weak negative correlation would be expected since the smaller the persistence length and the retardation time, the greater the expected mobility of the macromolecule chains, thereby increasing J_c (Figs. 5.3 b-c). However, as noted in the discussion of Figs. 5.1b-c, these polymers are primarily glassy and are not expected to flow. The glass transition temperature was observed to have a strong negative correlation with the creep compliance, a trend that is intensified for polymers tested above the T_g. For amorphous polymers tested well blow the glass transition temperature, the creep compliance is varies only slightly.

The fractional depth recovery $\Delta h / h_{max}$ is a measure of the resistance to plastic deformation. It measures the extent to which a polymer will recover in response to contact deformation. There is tentatively a weak positive correlation between M_w and $\Delta h / h_{max}$, however no significant changes in the recovery properties are expected from variations in $\Delta h/h_{max}$, for $M_w >> M_e$ (Figure 5.4a). Weak negative correlations were observed for the dependence of $\Delta h / h_{max}$ on the persistence length and the characteristic retardation time (Figs. 5.4b-c), suggesting that structural factors and properties related to molecular mobility are more dominant factors during deformation recovery than during creep under a specific load. Polyethylene, the only polymer tested above the glass transition temperature, was able to recover the most post-unloading. Finally, the glass transition temperature is negatively correlated to the fractional depth recovery for the same reasons cited in the discussion of 5.3d.

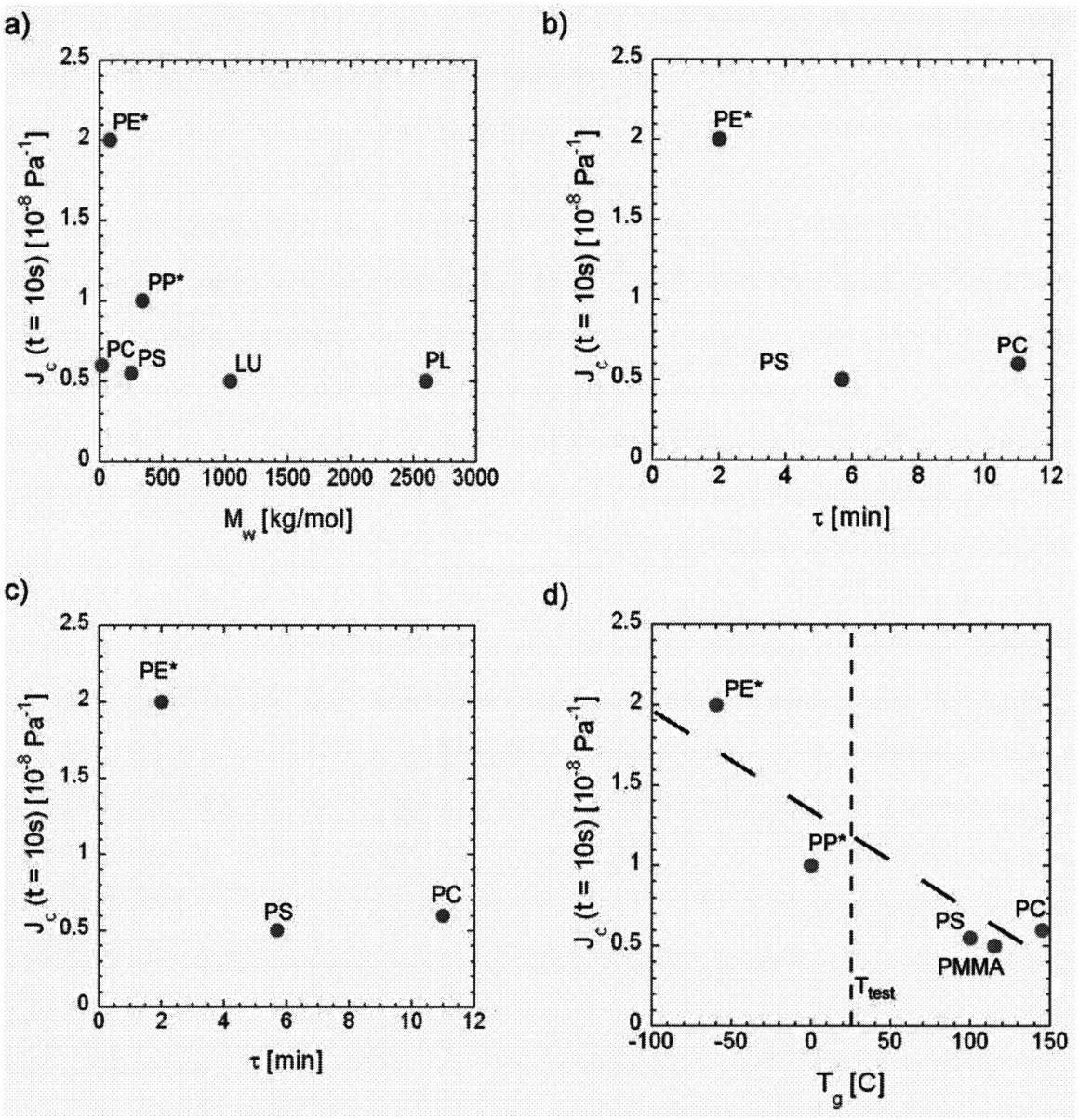

Figure 5.3 Contact creep compliance J_c as a function of polymeric structural length-scales, time-scales, and physical properties. Data for J_c as a function of weight average molecular weight (M_w), persistence length (L_p), characteristic retardation time (τ), and glass transition temperature (T_g) is given as available for an array of amorphous (polystyrene (PS), poly(methyle methacrylate) (LU and PL), polycarbonate (PC)) and semi-crystalline (polyethylene (PE), polypropylene (PP)) polymers.

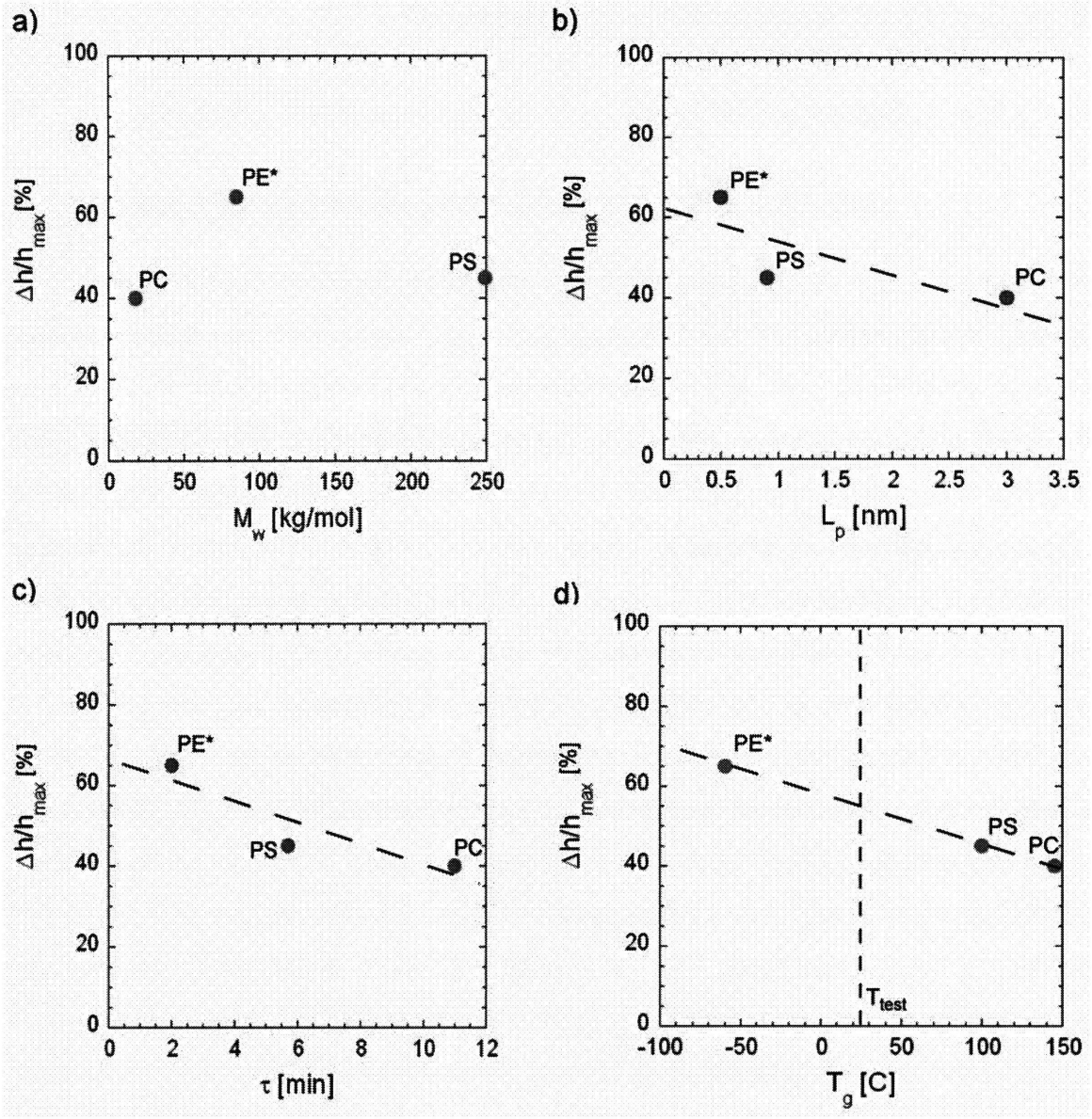

Figure 5.4 Extent of recovery post indentation $\Delta h / h_{max}$ as a function of polymeric structural length-scales, time-scales, and physical properties. Data for $\Delta h / h_{max}$ as a function of weight average molecular weight (M_w), persistence length (L_p), characteristic retardation time (τ), and glass transition temperature (T_g) is given as available for an array of amorphous (polystyrene (PS), poly(methyle methacrylate) (LU and PL), polycarbonate (PC)) and semi-crystalline (polyethylene (PE), polypropylene (PP)) polymers.

5.3 SUGGESTIONS FOR FUTURE RESEARCH

In this section, the most natural extensions of this thesis research are discussed.

5.3.1 Larger molecular dynamics studies on polymer surface mechanics

In Section 3.3, the effect of probe surface charge on the mechanical response of an amorphous polymer surface was investigated using a reactive molecular dynamics (MD) package, ReaxFF. Reactive MD was used because we were testing whether the stiffening observed at the surface was the result of new bond-formation at the probe-polymer interface with a positively, negatively or neutrally charged probe surfaces. The reactive simulations, performed at much higher impact energies than the corresponding experiments, established that bond breaking and reforming does not appear to control the elevated mechanical stiffness measured at the surface-probe contact interface. Therefore, in future simulations of the molecular response of amorphous polymer surfaces to mechanical deformation non-reactive molecular dynamics should be used to simulate larger systems closer in scale to experiment. As illustrated in Table 3.1, for the size and speed of simulation to begin approaching experiment a much less computationally costly simulation route is required. As illustrated in Figure 5.5, non-reactive MD simulation utilizing a united atom force field on parallel processors would greatly increase the potential system size as well as the possible simulation run-time. Larger system sizes would allow nm-scale understanding of how molecular motion determines mechanics. This knowledge could then be transferred to more complex systems of industrial interest as discussed in Section 5.2.2.

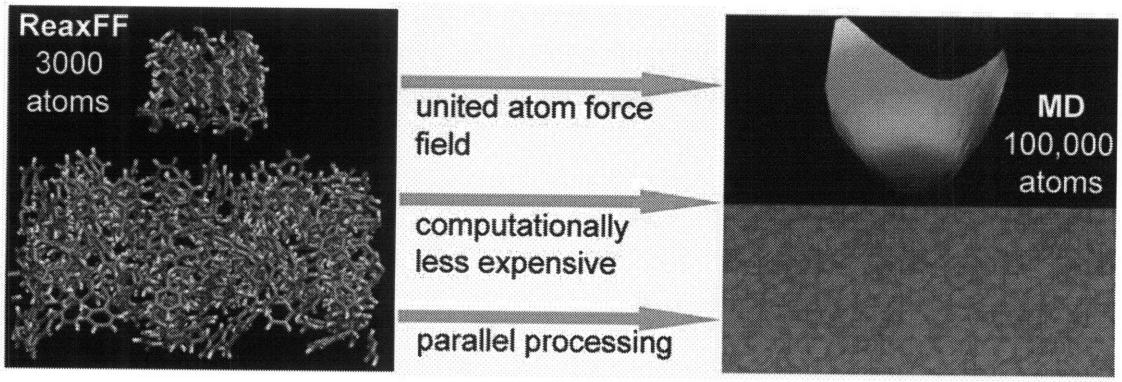

Figure 5.5 Much larger system sizes can be simulated with united atoms molecular dynamics (MD) run on parallel processes than for all-atom reactive MD (ReaxFF) simulations that allow for bond breaking and reforming.

5.3.2 Model nanocomposite interfaces using molecular dynamics

Once the contact deformation of amorphous polystyrene PS is understood on the nano-scale, this knowledge can be extended to the study of more complex confined-material systems. For example nanocomposites can be simulated to understand how the polymer matrix-nanoparticle interphases can be engineered to improve mechanical performance by examining critical nanoparticle / polymer length scales (see Fig. 5.6). These simulations may have the greatest impact be executed in parallel with experiments on specific nanocomposite systems of commercial interest.

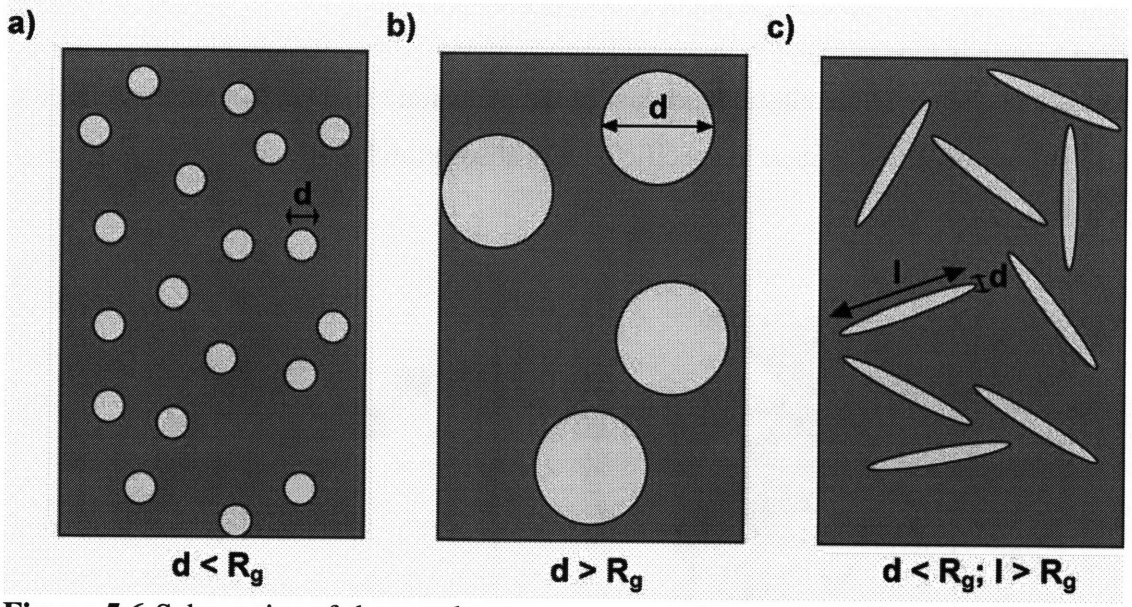

Figure 5.6 Schematics of three polymer nanocomposites systems. In each schematic the yellow color represents the nanoparticle and the blue represents the surrounding amorphous polymer matrix. In a) the thickness d of the nanoparticle is less than the radius of gyration R_g of the polymer matrix, while in b) the thickness d exceeds R_g. In c) the asymmetric nanoparticle has one dimension greater than R_g and another smaller than R_g.

5.3.3 Nonlinear viscoelastoplastic analysis of model nanocomposites materials

An outstanding challenge in nano-scale contact mechanics bas been transitioning from hardware and analysis developed for metals and ceramics to standardized mechanical characterization of time-dependent materials. Often the analysis of indentation experiments approximates time-dependence of polymers and biomaterials by assuming linear viscoelasticity. For this assumption to be realistic, spherical probes must be employed to maintain induced strains < 1%. However spherical probes have much larger contact areas than sharp probes, which is a significant impediment to characterizing the mechanical surface properties of nanocomposites with nm-scale resolution. For this reason, we propose the use of Oyen et al.'s visco-elasto-plastic VEP model[1] that also utilizes linear viscoelastic elements but explicitly includes a plastic deformation term. The implementation of this analysis on nanoindentation or AFM indentation data will allow mapping of these mechanical parameters over a complex sample surface such as in nanocomposites, where the polymer matrix surrounding the nanoparticles may form an interphase of altered mechanical properties, as suggested by Figure 5.7. Initial studies on a silicate particle / acrylic matrix nanocomposites, manufactured by DuPont, demonstrate no statistical change in the elastic modulus for the inclusion of 10 vol % nanoparticles, but do indicate a 10 % increase in specific energy absorption for 10 vol % nanoparticles plus a dispersion agent.

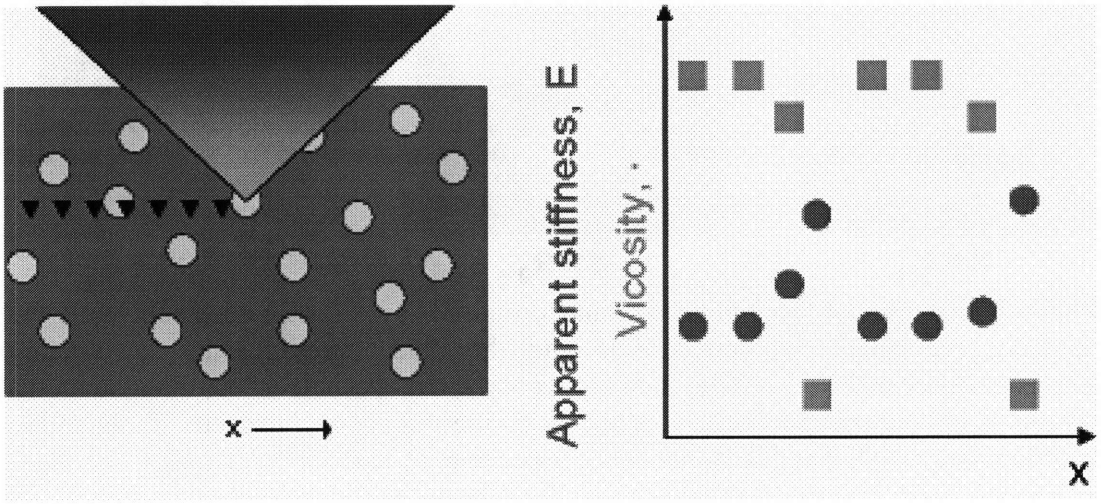

Figure 5.7 Mapping of nanocomposites through sharp probe contact deformation, schematically represented in a), may provide multi-dimensional mapping of several mechanical parameters. In b), the apparent stiffness and viscosity are represented as a function of mechanical mapping in the x-direction.

5.3.4 Contact deformation of hydrated (biological) materials using fluid cell

Mechanical testing resolution allows direct characterization of biological tissues and even single cells, which until recently was necessarily performed in air. These experiments, while very interesting, contributed limited understanding of mechanical properties in natural operating environments. Our research laboratory has recently developed the capability of hydrated nanoindentation on bio(materials) (see Fig. 5.8a) and other materials in solution, enabling characterizations that will dramatically improve development of in-solution mechanical applications. Figure 5.8b depicts an elastomeric material indented with a spherical probe after 1 h and 17 h in solution, demonstrating the clear change in mechanical response.

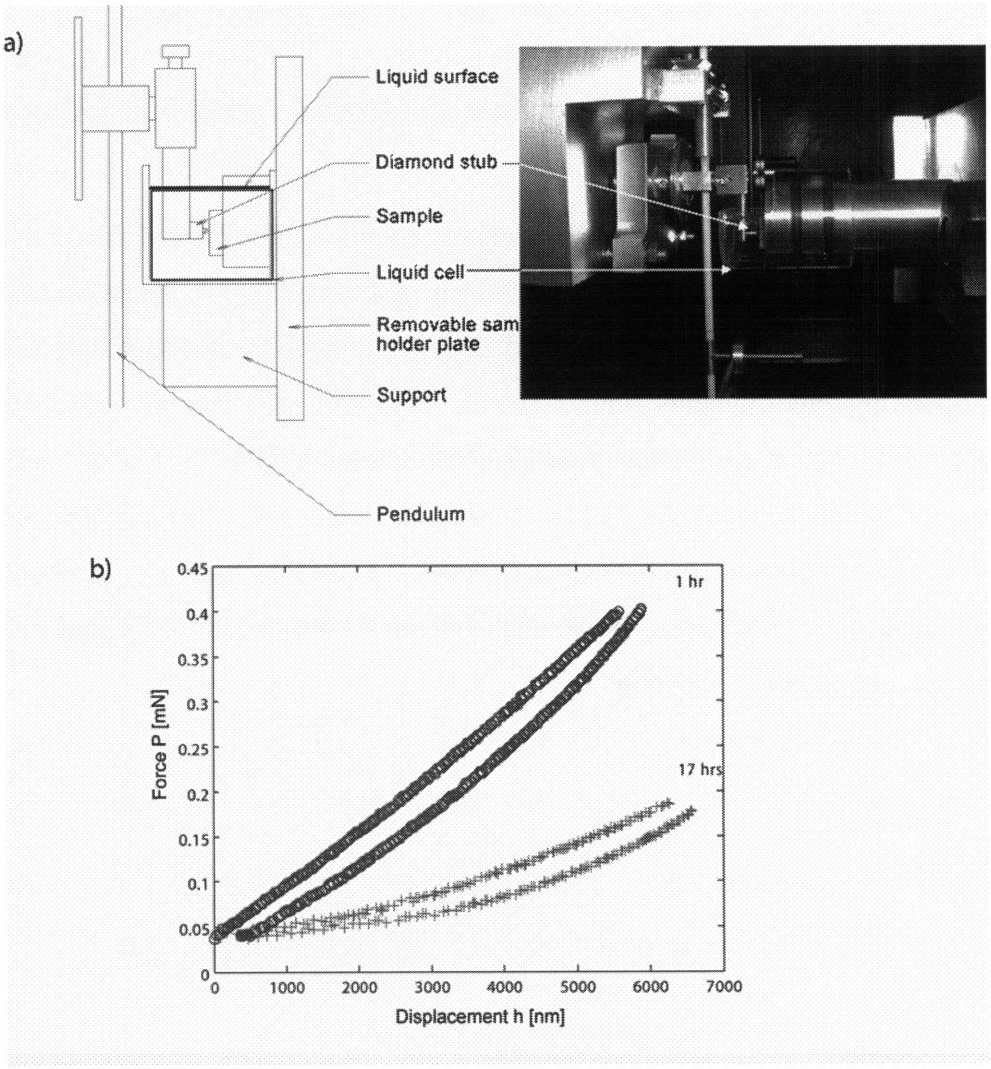

Figure 5.8 a) Schematic and image of nanoindentation fluid cell installed on the Van Vliet Lab MicroMaterials Ltd. instrumented nanoindenter. b) Change in load-displacement response for a viscoelastic material as a function of hydration time.

5.3.5 Apply impulse experimental technique to develop protective / barrier coating materials

Measured mechanical properties should depend on the end-use parameters of the application. In the case of barrier coatings and other protective devices, energy damping and resistance to cracking are primary success criterion. Polymer behavior depends strongly on experimental testing conditions, indicating that comparison of two polymers from one mechanical test may not indicate anything about the same two polymers in a second mechanical test. For example, neither quasistatic indentation data nor long-time

creep data can indicate the relative impact resistance of a material. As summarized in Figure 5.9, impulse testing was developed and tested on metals and later refined for polymeric materials. Additionally, impulse testing can be combined with high temperature testing capabilities to study changes in mechanical metrics such as the coefficient of restitution as a function temperature relative to the glass transition temperature (shown in Figure 5.10).

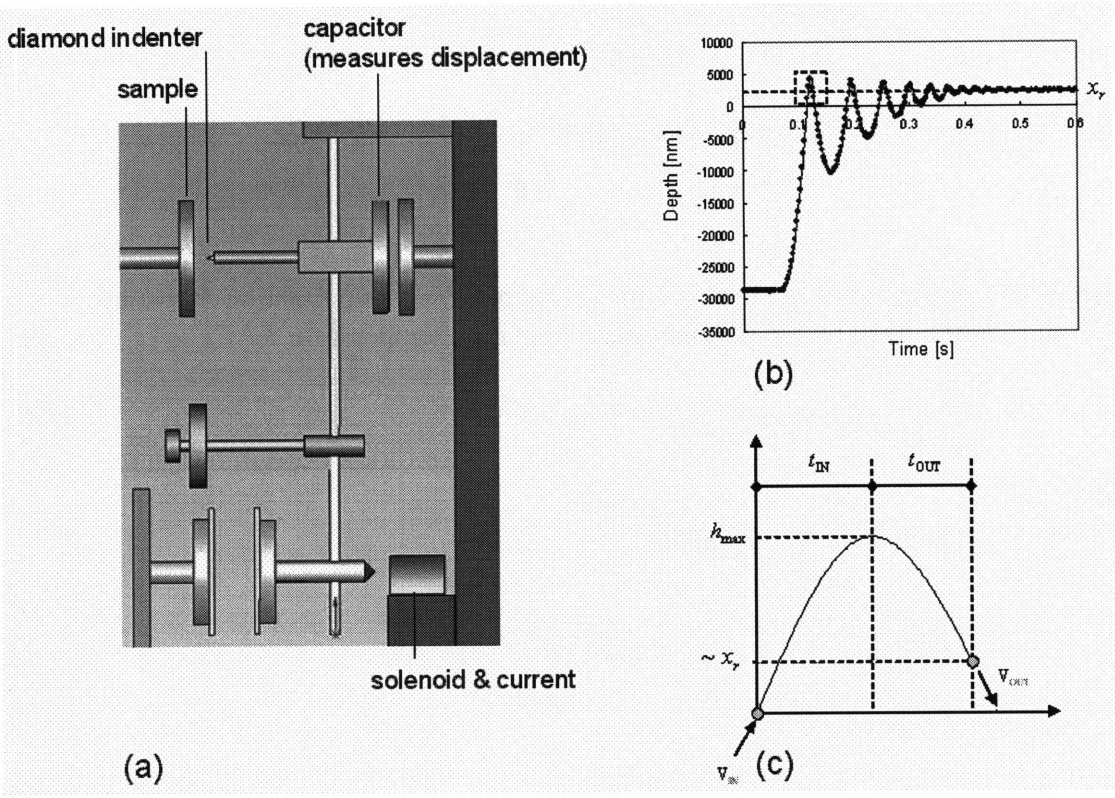

Figure 5.9 a) Schematic of impulse experimental apparatus as installed on the Micro Materials Ltd. instrumented nanoindenter. b) Representative impulse response on glassy polymeric material, where c) diagrams the important parameters measured during the first contact with the surface.

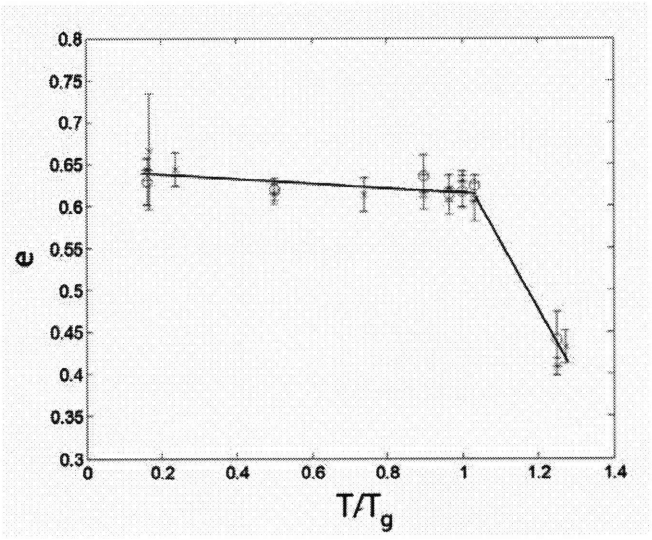

Figure 5.10 Coefficient of restitution e for glassy polymers as a function of testing temperature normalized by the polymer glass transition temperature T / T_g.

REFERENCES

1. Oyen M.L., Cook R.F.; Load-displacement behavior during sharp indentation of viscous-elastic-plastic materials. *Journal of Materials Research* **2003**; 18, (1), 139-150.

APPENDIX A: GENERAL FRAMEWORK OF EXISTING SOLUTIONS FOR $J(T)$

Lee and Radok first recognized the difficulty in obtaining a solution to calculate the stress distribution for Hertzian (elastic, spherical) contact between a rigid indenter and a viscoelastic body. This complication arises because conventional approaches to linear viscoelastic deformation had applied the Laplace transform (i.e., solving for linear operators) to map this time-dependent solution to the corresponding elastic solution.[1] Although this approach could be used to determine, for example, the viscoelastic solution to creep of a viscoelastic material under a uniform uniaxial stress (Fig. 1a), the Laplace transform is not necessarily valid when both the boundary position and boundary conditions change with time -- as is characteristic of spherical or conical contact for increasing / decreasing displacement -- because neither the stress nor the strain can be uniquely determined at each deformation time point and thereafter transformed to time-space.

Lee and Radok proposed to instead adopt a single elastic solution for the boundary conditions of the actual viscoelastic problem, and then substitute elastic constants with viscoelastic operators. They verified this approach for the specific problem of spherical elastic contact loading, i.e., increasing contact area as would be expected during loading or creep. As Ting's more general analysis -- the linear viscoelastic analogue to the solutions of Sneddon[2] -- extends this approach to other indenter geometries and loading conditions, it is necessary to outline the assumptions common to both solutions, hereafter referred to as the LR- or T-solution. Both the LR- and T-solutions assume linear viscoelasticity, in that the functions that define the constitutive relation of the viscoelastic material are linear operators:

$$As_{ij} = Be_{ij} \quad , \tag{A.1}$$

$$A'\sigma_{ii} = B'\varepsilon_{ii} \quad , \tag{A.2}$$

where s_{ij} and e_{ij} are the deviatoric stress and strain components, respectively, and σ_{ij} and ε_{ij} are the total stress and strain, respectively. This restriction enables mapping of a linear elastic solution or inversion of integral forms of such solutions, where the shear elastic modulus G is exactly equal to B / $2A$ for an incompressible material (i.e., ν = 1/2), and implies several characteristics of material behavior and of $J(t)$ as a function of loading conditions. LR then adopt the solution of Hertz[3] for a contact pressure distribution that varies not only with radial distance from the central loading axis r but also with time t:

$$p(r,t) = \frac{4Q}{\pi R} f(r) \quad , \tag{A.3}$$

where $f(r)$ is the indenter shape function relating $h(r, a)$ (see Appendix B) and $a(t)$ is the contact radius at the free surface of the indented material. The assumption of ν = 1/2 is assumed by LR for simplicity but is not required of the solution. The LR-solution determines $J(t)$ based on the deviatoric strain e_{ij}. The two key equations of the LR-solution are the inverse transform to real time of the total indentation force P:

$$A[P(t)] = \frac{8B[Rh(t)]^{3/2}}{3R} \quad , \tag{A.4}$$

where A and B are the linear viscoelastic operators and R is the spherical indenter radius, and the creep compliance in shear is determined as a function of the transform of deviatoric strain e_{ij} in terms of the transform variable s:

$$\overline{A} = \frac{1}{2} J(s) s, \overline{B} = 1 \quad . \tag{A.5}$$

For any given $P(t)$ such that $a(t)$ is increasing, $J(t)$ can then be determined as

$$\int_0^t \frac{1}{2} J(t-\tau) \frac{dP}{dt} d\tau = \frac{8}{3} \sqrt{R} [h(t)]^{3/2} \quad . \tag{A.6}$$

In contrast, the T-solution maintains and inverts the integral form of $p(r, t)$ in terms of elastic indentation depth $h(t)$. As a result, this is a more general viscoelastic solution of contact pressure distribution that can be expressed for any loading history ($a(t)$ increasing or decreasing) and indenter geometry; Ting explicitly demonstrates that the pressure distribution solution of Lee and Radok[4] is recovered for identical conditions. The two key equations of the T-solution are the relation between surface displacement along the loading axis $u(z = 0)$ and the first of two linear viscoelastic operators Ting calls $\varphi(t)$:

$$u(r,0,t) = \int_{0-}^{t} \phi(t-s) \frac{\delta}{\delta s} \int_{0}^{a(t)} \beta(r,x) x p(x,s) ds d\tau \quad , \tag{A.7}$$

where β is a Bessel function of the first kind (typically denoted by J but modified here to avoid confusion with $J(t)$) and r is radial distance along the free surface. The elastic solution to Eq. (A.7) is

$$u(r,0,t) = h(t) - f(r)H(t) = \frac{1-\nu}{G} \int_{0-}^{a(t)} \beta(r,x) x p_e(x,t) dx \quad , \tag{A.8}$$

where $f(r)$ is the indenter shape function relating $h(r, a)$ (see Appendix B), and $H(t)$ is the Heaviside step function defining the edge of the contact zone. By separating any loading history into integrals of the form of Eq. (A.8), the solution for the actual pressure distribution $p(r, t)$ can be determined as a function of the elastic solution and $\psi(t)$, the second of Ting's linear viscoelastic operators. Ting notes that for constant Poisson's ratio ν, $\psi(t)$ has the form of the relaxation modulus in shear $G(t)$:

$$p(r,t) = f\left[\frac{1-\nu}{G} p_e(r,t) \psi(t)\right] \quad . \tag{A.9}$$

and $\varphi(t) = 1 / \psi(t)$ has the form of creep compliance in shear $J(t)$. Ting states that for a monotonic increase in contact radius $a(t)$, $\varphi(t)$ can be related to the elastic expression of total pressure $(1 - \nu)P_e(t) / G$ as

$$\frac{(1-\nu)P_e(t)}{G} = P(0)\phi(t)H(t) \quad , \tag{A.10}$$

where G is the shear elastic modulus. Then, for a constant and instantaneously applied load $P(0) = P_0$, the left hand side of Eq. (A.10) can be expressed as an integral of the shape function $f(r)$ (see Eq. 25c from Ting et al.[5]), such that $\varphi(t)$ can be determined generally as

$$\phi(t) = \frac{4\int \frac{r^2}{\sqrt{a^2(t)-r^2}} \frac{d}{dr} f(r)dr}{P_0 H(t)} \quad . \tag{A.11}$$

For this constant load and changing contact area, $\varphi(t)$ does not identically (or necessarily) represent $J(t)$ which assumes a constant applied stress σ_0, but rather the history of this contact area evolution. In fact, $\varphi(t) = (1 - \nu)J(t)$ for constant ν (See Eqs. (2.3.2) - (2.3.3)). Here, we denote this as contact creep compliance $J_c(t)$. As creep compliance implies deformation in the linear (visco)elastic regime and we discuss deviation from this response for a range of indentation-enabled measurements of creep compliance, $J_c(t)$ is more generally an apparent creep compliance.

APPENDIX B: INDENTER SHAPE FUNCTIONS AND $H(A)$

As stated by Ting, the displacement along the loading axis u_z can be expressed as:

$$u_z = h(t) - f(r)H(t) \quad , \tag{B.1}$$

where $f(r)$ is an indenter shape (or geometric) function that relates the depth of indentation $h(t)$ to $a(t)$ under the condition that Eq. (B.1) is zero at $r = a(t)$. (Note that $h(t)$ is actually the contact depth of indentation, typically denoted as $h_c(t)$.) As a result, the relationship between $h(t)$ and $a(t)$ includes but not is identical to $f(r)$. For example, for a spherical indenter of radius R,

$$f(r) = R - \sqrt{R^2 - r^2} \tag{B.2}$$

and reduces to $f(r) = r^2 / 2R$ for $r << R$ as is typically assumed for "small strain" applications, such that

$$h(t) = \frac{[a(t)]^2}{R} \quad , \tag{B.3}$$

and thus there is a difference of a factor of 2 between $f(r)$ and $h(t)$ in this particular case. This point must be considered when applying solutions expressed in terms of $a(t)$ which must be calculated from instrumented indentation data as a function of $h(t)$ which is measured experimentally.

REFERENCES

1. Lee E.H.; Stress analysis in visco-elastic bodies. *Quart. Appl. Math* **1955**; 13, (183),
2. Sneddon I.N.; The relation between load and penetration in the axisymmetric boussinesq problem for a punch of arbitrary profile. *International Journal of Engineering Science* **1965**; 3, (1), 47.
3. Hertz H.R. On the contact of two elastic solids; MacMillan, 1882.
4. Lee E.H.a.R., J.R.M.; The contact problem for viscoelastic bodies. *Journal of applied mechanics* **1960**; 27, 438-444.
5. Ting T.C.T.; The contact stresses between a rigid indentor and a viscoelastic half-space. *Journal of Applied Mechanics* **1966**; 88, 845-854.